

**PHOTOCATALYTIC HYDROGEN PRODUCTION IN A UV-IRRADIATED FLUIDIZED BED
REACTOR**

by

Kevin Reilly

B.A.Sc., The University of British Columbia, 2008

A THESIS SUBMITTED IN PARTIAL FULFILLMENT OF
THE REQUIREMENTS FOR THE DEGREE OF

DOCTOR OF PHILOSOPHY

in

THE FACULTY OF GRADUATE AND POSTDOCTORAL STUDIES

(Chemical and Biological Engineering)

THE UNIVERSITY OF BRITISH COLUMBIA

(Vancouver)

June 2016

© Kevin Reilly, 2016

Abstract

Growing global energy demands and an increased environmental awareness have resulted in a demand for renewable energy sources. Photocatalytic water splitting has long been explored as a direct solar-to-chemical energy conversion method in the hopes of creating a sustainable, emissions-free hydrogen production process. In this thesis we present the first focused effort on hydrogen production via photocatalytic water splitting in a UV-irradiated fluidized bed reactor. This novel approach was taken to address the mass-transfer effects, poor radiation distribution, parasitic back-reaction and photocatalyst handling difficulties that limit the efficiency and scalability of existing water splitting systems.

By fluidizing platinum-deposited TiO_2 spheres in a 2.2M Na_2CO_3 solution, steady hydrogen production rates of 211 $\mu\text{mol/hr}$ with an apparent quantum efficiency of 1.33% were achieved upon UV-irradiation. This represents a marked 44% increase in efficiency when compared to results obtained by suspended slurry TiO_2 photocatalysts in the same reactor. A mathematical model describing the performance of the fluidized bed water splitting system was derived and then employed to estimate several key parameters. From the model, it was found that high rates of mass transfer in the separator unit could minimize the negative effects of the parasitic back reaction and greatly improve the overall rate of hydrogen evolution. Indeed, it was demonstrated experimentally that slight modifications to the liquid-gas separator to improve mass transfer resulted in a 350% increase in the rate of hydrogen evolution. The application of the model to the design of fluidized bed water splitting systems is described.

Advanced, fluidizable nanowire and nanorod photocatalysts that can withstand the rigors of fluidization are described here for the first time. We present two novel, scalable methods that allow for the growth of anatase nanowires or rutile nanorods on porous glass particles, whose deep surface features protect the nanostructured films from mechanical attrition. It was found that the photocatalytic activity of anatase nanowires grown via a chemical bath deposition process was over three times greater than that of

hydrothermally grown rutile nanorods when employed for photocatalytic hydrogen production and degradation of a model contaminant (Rhodamine B). The factors controlling nanowire growth and performance are discussed.

Preface

All the data presented in this thesis was obtained by the author of this PhD thesis under the supervision of Professors Dr. David P. Wilkinson and Dr. Fariborz Taghipour at the University of British Columbia. The novel fluidized bed water splitting employed for the purpose of this PhD thesis was designed and built by the author of this thesis.

The results detailed in Chapter 2 were presented, in part, at the *Hydrogen + Fuel Cells 2011: International Conference and Exhibition* in Vancouver, B.C on May 15-18, 2011; the 9th *World Hydrogen Energy Conference (WHEC 2012)* in Toronto, ON on June 3-7, 2012; the *62nd Conference of the Canadian Society for Chemical Engineering (CSCChE)* in Vancouver, B.C. on October 14-17, 2012; and at the *Hydrogen + Fuel Cells 2013: International Conference and Exhibition* in Vancouver, B.C. on June 16-19, 2013. As a result of my participation in *WHEC 2012*, part of the findings reported in Chapter 2 were published as part of the conference proceedings:

Reilly, K., Taghipour, F. & Wilkinson, D. P. Photocatalytic hydrogen production in a UV-irradiated fluidized bed reactor. in *Energy Procedia* **29**, 513–521 (Elsevier BV, 2012).

During my studies I collaborated with colleagues to investigate TiO₂ microspheres for CO₂ reduction. The TiO₂ spheres used in the study were based on the catalysts I developed and presented in Chapter 2. I produced the TiO₂ spheres used for the experiments that led to the publication of:

Fang, B. *et al.* Large-Scale Synthesis of TiO₂ Microspheres with Hierarchical Nanostructure for Highly Efficient Photodriven Reduction of CO₂ to CH₄. *ACS Appl. Mater. Interfaces* **6**, 15488-15498 (2014). doi:10.1021/am504128t

All other work presented in this thesis (Chapters 3-5) has not yet been published and is currently in preparation for submission. All of the research and writing with regards to these chapters and the data presented therein are entirely of my own efforts and work and was conducted under the supervision of Professors Dr. David P. Wilkinson and Dr. Fariborz Taghipour at the University of British Columbia.

Table of Contents

Abstract	ii
Preface	iv
Table of Contents	vi
List of Tables	xi
List of Figures	xii
Nomenclature	xviii
Acknowledgements	xxiii
Dedication	xxiv
Chapter 1: Introduction	1
1.1 Thesis Layout	8
1.2 Literature Review	11
1.2.1 Semiconductor Theory	11
1.2.2 Introduction to Titanium Dioxide	15
1.2.3 Sol-Gel Synthesis and Precursors	17
1.2.4 Platinum Loading	20
1.2.5 Influence of Operational Parameters	23
1.2.5.1 Pressure and Mass Transfer	23
1.2.5.2 Temperature	24
1.2.5.3 Solution pH and Additives	24
1.2.6 Fluidizable Particle Design	26
1.2.7 Nanowire Photocatalysts	29
1.2.8 Nanorod Growth	34
Chapter 2: Photocatalytic Hydrogen Production in a UV-irradiated Fluidized Bed Reactor	36
2.1 Introduction	36

2.2	Experimental	40
2.2.1	Reactor and System Design	40
2.2.2	TiO ₂ Sol-gel Composite Preparation	44
2.2.3	Chitosan Polymer Solution Preparation	44
2.2.4	TiO ₂ Sphere Formation.....	44
2.2.5	Preconditioning.....	46
2.2.6	Platinum Deposition	46
2.2.7	Actinometric Measurements.....	47
2.2.8	Suspended Slurry Baseline Measurement	48
2.2.9	Experimental Procedure	49
2.2.10	Characterization.....	49
2.2.11	Safety Considerations	50
2.3	Results and Discussion	50
2.3.1	TiO ₂ Photocatalyst Particle Properties.....	50
2.3.2	Surface “Pleating” Effect.....	52
2.3.3	Particle Attrition	54
2.3.4	Platinum Deposition	55
2.3.5	Baseline Slurry Photocatalyst Performance	59
2.3.6	Typical Fluidized Photocatalyst Performance.....	61
2.3.7	Effect of Na ₂ CO ₃	67
2.3.8	Over-stoichiometry	72
2.4	Conclusions.....	74
Chapter 3: Modeling the Behavior of Water Splitting in a Photocatalytic Fluidized Bed System		75
3.1	Introduction.....	75
3.2	Fluidized Bed Theory and Fundamentals	75

3.3	Mass Transfer.....	80
3.4	Optical Model and Direct Rate of H ₂ Evolution.....	85
3.5	Back Reaction.....	87
3.6	Overall Rate of H ₂ Evolution.....	89
3.7	Discussion.....	92
3.7.1	General Model Behavior.....	94
3.7.2	Effect of Bed Height.....	95
3.7.3	Back Reaction and Mass Transfer Effects.....	97
3.7.4	Effect of Photocatalyst Concentration on Photon Absorption.....	99
3.7.5	Effect of Particle Size and Density.....	101
3.7.6	Other Fluidization Effects.....	104
3.8	Conclusions.....	105

Chapter 4: Scalable Anatase Nanowire Growth for Water Splitting and Photocatalytic

Degradation.....	108	
4.1	Introduction.....	108
4.2	Experimental.....	110
4.2.1	Substrate Preparation.....	110
4.2.2	Growth of Anatase Nanorod Arrays via Chemical Bath Deposition.....	110
4.2.3	Hydrothermal Growth of Rutile Nanorod Arrays.....	111
4.2.4	TiO ₂ Nanoparticle (P25) Deposited Slides.....	111
4.2.5	Characterization.....	112
4.2.5.1	Hydrogen Evolution.....	113
4.2.5.2	Photocatalytic Performance.....	114
4.3	Results and Discussion.....	115
4.3.1	XRD.....	116

4.3.2	UV-Vis-DR Analysis.....	118
4.3.3	XPS Analysis.....	120
4.3.4	Thermogravimetric Analysis.....	124
4.3.5	Growth Mechanism.....	125
4.3.5.1	Effect of Acid Concentration.....	125
4.3.5.2	Role of Melamine.....	127
4.3.5.3	Effect of H ₂ O ₂ ratio.....	132
4.3.6	Photoelectrochemical Characterization.....	133
4.3.7	Photocatalytic Water Splitting.....	138
4.3.8	Photocatalytic Degradation of Model Organic Compound.....	139
4.4	Conclusions.....	141
Chapter 5: Advanced Fluidizable Nanowire Photocatalysts for Water Splitting and Water		
Decontamination..... 143		
5.1	Introduction.....	143
5.2	Experimental.....	145
5.2.1	Materials.....	145
5.2.2	Anatase Nanowire-coated Particles.....	146
5.2.3	Rutile Nanorod-coated Particles.....	147
5.2.4	UV-irradiated Fluidized Bed Reactor System.....	148
5.2.5	Attrition Resistance.....	149
5.2.6	Characterization.....	149
5.3	Results and Discussion.....	151
5.3.1	Anatase Nanowire Growth.....	151
5.3.2	Rutile Nanorod Growth.....	154
5.3.3	Characterization.....	161

5.3.4	Attrition Resistance	164
5.3.5	Comments on H ₂ Evolution Performance.....	166
5.4	Conclusions.....	167
Chapter 6: Conclusions and Recommendations		169
6.1	Conclusions.....	169
6.1.1	Photocatalytic Water Splitting in a UV-irradiated Fluidized Bed Reactor	169
6.1.2	Mathematical Model and Understanding of Performance Determining Factors.....	170
6.1.3	Effect of Na ₂ CO ₃ on the Performance of Photocatalytic Water Splitting	173
6.1.4	Fluidizable Photocatalyst Design and Manufacturing.....	174
6.2	Future Work and Recommendations.....	175
Bibliography.....		183
Appendices.....		202
Appendix A – Publications.....		202
Appendix B - Engineered Drawings		203
B.1	Fluidized Bed Reactor.....	203
B.2	Gas-Liquid Separator	209
Appendix C – Supplementary Figures		211

List of Tables

Table 1: Comparison of existing water splitting photocatalyst methods.....	6
Table 2: Reactor conditions, H ₂ evolution rates and Apparent Quantum Efficiencies for various fluidized photocatalyst mass loadings.	63
Table 3: Nomenclature	76
Table 4: Possible reaction steps for the back reaction of H ₂ and O ₂ (i.e., hydrogen oxidation reaction, HOR) over platinum surfaces.	88
Table 5: Fitted parameter values for R _{net} as a function of photocatalyst mass, W, and bed height, H _{ex} , and relevant fluidization parameters.	92
Table 6: Equivalent circuit used for modeling the photoanode in 3-electrode configuration and corresponding fitting parameters for dark conditions at 0.4V vs RHE.	137
Table 7: Summary of hydrothermal growth conditions and resulting nanorod dimensions.....	156

List of Figures

Figure 1: Band energy diagram showing (1) the promotion of an electron to the conduction band, (2) the recombination of e^-/h^+ , and (3) charge separation arising from band bending (V_B) in the depletion layer (of width, W)	12
Figure 2: Crystal structures of a) anatase, b) rutile, c) brookite, and d) the lepidocrite-like structure of protonated titanates ($H_2Ti_3O_7$ shown).....	16
Figure 3: Sol-gel hydrolysis and condensation mechanism	18
Figure 4: Representation of photocatalytic water splitting over Pt-deposited TiO_2 nanoparticles and simultaneous Pt-catalyzed back reaction	21
Figure 5: Idealized schematic detailing a) light absorption and charge transport in a nanowire, and b) the improved light scattering and absorption by nanowire films.	30
Figure 6: Photograph of the annular fluidized bed reactor	41
Figure 7: Schematic diagram of the fluidized bed photoreactor system	42
Figure 8: XRD pattern for the TiO_2 photocatalyst particles. The anatase peaks (A) and rutile peaks (R) are as indicated.	51
Figure 9: SEM image of a self-supported photocatalyst particle displaying the “pleating” effect	53
Figure 10: a) Detail and b) high- magnification views of the surface pleats.....	53
Figure 11: SEM image displaying the pleats of a self-supported photocatalyst particle following 1 hour of conditioning	54
Figure 12: Depth profiles of Ti, O and Pt (along with the observed Si and Al impurities) as a function of sputter depth for the 0.5 mm particles	56
Figure 13: Relative Intensity ratio of Pt_{195}/Ti_{48} as a function of sputter depth for the 0.5 mm particles.....	57
Figure 14: Photocatalytic water splitting performance for P25 nanoparticles suspended in Solution. a) The gas evolution rates for hydrogen and oxygen, and b) the stoichiometric ratio of hydrogen to oxygen are	

shown with respect to time. The P25 nanoparticles (containing 0.7wt% Pt) were suspended in a 2.2M aqueous Na₂CO₃ solution at a concentration of 1 g/L.60

Figure 15: Photocatalytic water splitting performance for 80g of 1.1 mm diameter fluidizable photocatalyst particles. a) The gas evolution rates for hydrogen and oxygen, and b) the stoichiometric ratio of hydrogen to oxygen are shown with respect to time. The particles were fluidized in a 2.2M aqueous Na₂CO₃ solution.62

Figure 16: The a) volumetric, and b) specific rates of hydrogen evolution with respect to the mass of photocatalyst particles fluidized in the reactor.65

Figure 17: The rate of hydrogen and oxygen evolution over time for 60g of 1.1 mm diameter photocatalyst fluidized in deionized water only. The light was turned on and off to determine whether the photocatalyst deactivation was a photo-induced effect.67

Figure 18: a) The rate of hydrogen and oxygen evolution over time for the same 60 g sample of photocatalyst shown in Figure 17 after dissolving Na₂CO₃ into the solution at a concentration of 2.2M, b) the stoichiometric ratio of hydrogen to oxygen are shown with respect to time.69

Figure 19: The stoichiometric ratio of hydrogen to oxygen with respect to time for various amounts of 1.1 mm diameter photocatalyst particles fluidized in the photoreactor. The ratio for 100 g of 0.5 mm diameter particles when using a modified separator configuration (denoted as ‘Turbulent’) is discussed in more detail later.72

Figure 20: The stoichiometric ratio of hydrogen to oxygen with respect to time for 60 g of the 1.1 mm diameter photocatalyst particles fluidized in the photoreactor. The lamp was turned off and on to observe whether the effect of Na₂CO₃ was photo-induced.73

Figure 21: Schematic diagram of photocatalytic hydrogen generation at the fluidized particle surface and the various mass transfer steps involved in the water splitting process.80

Figure 22: Correlation of predicted hydrogen evolution rates with the experimental data presented in Chapter 2 as a function of photocatalyst mass.93

Figure 23: The relative and overall contributions of photon absorption, mass transfer and the back reaction to the apparent quantum efficiency as a function of photocatalyst mass.....	95
Figure 24: a) The overall rate of hydrogen evolution and b) the rate of evolution per centimeter of bed height as a function of photocatalyst mass, W , and bed height, H_{ex} . All other model parameters are held constant at the values presented in Table 5.	97
Figure 25: The overall rate of hydrogen evolution as a function of photocatalyst mass for various values of a) the back reaction rate constant, k_r' , and b) the mass transfer constant, k_L'' for an expanded bed height, H_{ex} , of 24 cm. All other model parameters are held constant at the values presented in Table 5. The units of k_r' and k_L'' are $(\text{cm}^3/\text{g}\cdot\text{min})$ and $(\text{cm}^3/\text{min})^{0.5}$, respectively.....	98
Figure 26: The overall hydrogen evolution rate as a function of photocatalyst mass for various values of the attenuation coefficient, α , for an expanded bed height, H_{ex} , of 24 cm. All other model parameters are held constant at the values presented in Table 5. The units of α are (cm^3/g)	100
Figure 27: The rate of hydrogen and oxygen evolution over time for a 100 g sample of 0.5 mm photocatalyst particles when using a) the normal separator configuration, and b) the modified separator configuration intended to improve turbulence and liquid-gas contact. The particles were fluidized with the same 2.2M aqueous Na_2CO_3 solution at an expanded bed height of 24 cm.....	102
Figure 28: The stoichiometric ratio of hydrogen to oxygen with respect to time when using a modified separator. The particles for 0.5 mm particles were fluidized in a 2.2M aqueous Na_2CO_3 solution at an expanded bed height of 24 cm.	104
Figure 29: a) cross-section and b) top-view SEM images of CBD-A nanowires grown in peroxotitanium solution containing 0.46M HNO_3	116
Figure 30: a) cross-section and b) top-view SEM images of CBD-N nanowires grown in peroxotitanium solution containing 0.31M HNO_3	116
Figure 31: a) Narrow-angle XRD pattern of CBD-A nanowires calcined at 80 °C, 250 °C and 350 °C for 1 hour. b) XRD patterns of CBD-A nanowires calcined at temperatures ranging from 350 °C to 750 °C. .	117

Figure 32: a) Diffuse reflectance UV-Vis absorption spectra for CBD-A samples calcined at temperatures between 350 °C and 750 °C and b) Band gap energies for CBD-A and CBD-N versus temperature.	119
Figure 33: Tauc plots for CBD-A samples calcined at 550 °C and 650 °C	120
Figure 34: High resolution XPS spectra for a) Ti 2p, b) O 1s, c) Pt 4f, d) C 1s, and e) N 1s	121
Figure 35: Chemical structures of melamine and its condensation products: melam, melem and melon.	123
Figure 36: TGA/DTGA curves for a) CBD-A and b) CBD-N	124
Figure 37: FESEM a) cross-section and b) top-view images of nanowires grown in peroxo-titanium solution containing 45 mM urea	128
Figure 38: Narrow-angle XRD pattern for nanowires grown in peroxo-titanium solutions containing 15 mM melamine and 45 mM urea.....	130
Figure 39: XRD patterns of CBD-A nanowires grown in peroxo-titanium solutions of varying H ₂ O ₂ concentrations, with [H ₂ O ₂]/[Ti] ratios ranging from 1:1 to 1000:1	133
Figure 40: Comparison of the I-V characteristics of CBD-A-550 nanowire, HTV nanorod and P25 films irradiated with 254 nm irradiation in 1M KOH electrolyte.....	134
Figure 41: Chopped-light I-V curves for a) anatase CBD-A-550 nanowires and b) rutile HTV nanowires. Samples were irradiated with 254 nm irradiation in 1M KOH electrolyte. The light was chopped at a frequency of 0.5 Hz. Linear voltage sweeps in light and dark conditions are included for clarity.	135
Figure 42: a) Nyquist plots of CBD-A, HTV and P25 taken in dark at 0.4V vs RHE and b) Mott-Schottky plots for CBD-A, HTV and P25 at 4.8 kHz.....	136
Figure 43: a) Pressure increase with time due H ₂ evolution and b) H ₂ evolution rates for CBD-A and CBD-N nanowire films calcined at temperatures ranging from 350 °C to 750 °C.....	138
Figure 44: a) Photodegradation of Rhodamine B (RhB) in the presence of P25 and CBD-A-550 films with and without stirring, b) Photodegradation of RhB in the presence of CBD-A films calcined at temperatures varying from 350 °C to 750 °C and c) the corresponding pseudo-first order fits, and d)	

Comparison of the photodegradation performance of CBD-A and CBD-N nanowires calcined at temperatures varying from 350 °C to 750 °C.....	140
Figure 45: SEM images of the porous Siran glass particles	146
Figure 46: SEM images of nanowire-deposited deposited particles grown at $[M_{cat}]/[V_{sol}]$ ratios of (a-c) 5×10^{-4} , (d-f) 2.5×10^{-3} , (g-i) 5×10^{-3} , (j-l) 0.025 and (m-o) 0.05 g/ml.....	152
Figure 47: Nanowire length and diameter dependence on $[M_{cat}]/[V_{sol}]$	153
Figure 48: Examples of nanorod films exhibiting (a) Class I (good), (b) Class II (moderate) and (c) Class III (poor) quality	156
Figure 49: Nanorod film quality classification versus R_q	158
Figure 50: Nanorod-deposited particles grown in (a,b) 1:1 HCl/H ₂ O solution with 12 ml TTIP and (c,d) 3:1 HCl/H ₂ O solution with 20 ml TTIP (corresponding to HTV-14 and HTV-18 in Table 7, respectively)	159
Figure 51: TEM image of graphitic contamination layer of nanorod surface	160
Figure 52: (a) X-Ray diffraction patterns of (i) TiCl ₄ -treated seed particles, (ii) nanowire-deposited particles and (iii) nanowires grown on FTO glass slides. (b) X-Ray diffraction patterns of the TiO ₂ -composite seed particles and the nanorod-deposited particles.	161
Figure 53: TEM images of (a) hydrothermally grown nanorods and (b) the lattice fringes. (c) The SAED pattern for the nanorod shown in (b).	162
Figure 54: (a) Tauc plots for the nanowire- and nanorod-deposited particles and (b) UV-Vis diffuse reflectance absorption spectra for bare, seeded and nanowire-/nanorod-deposited particles.....	163
Figure 55: SEM image of an anatase nanowire-deposited particle after 40 hours of fluidization. Nanowires were grown on the porous particles using a $[M_{cat}]/[V_{sol}]$ ratio of 0.025 g/ml.	165
Figure 56: Attrition resistance as determined by the concentration of ablated TiO ₂ in solution (g_{TiO_2}/L) for TiO ₂ Solid Spheres (•) and Nanorod-deposited samples (◦)	166
Figure 56: Schematic view of assembled fluidized bed test station	206

Figure 58: XRD patterns of CBD-N nanowires calcined at temperatures ranging from 350 °C to 750 °C.
.....214

Figure 59: Tauc plots for P25 powder, P25 film and HTV rutile nanorods214

Figure 60: Color shift of the growth solution during the growth of nanowires in a) 0.46M HNO₃ and b)
0.31M HNO₃ solutions215

Nomenclature

a	liquid-gas interfacial area (cm^2/cm^3)
A	cross section area (cm^2)
A_c	reactor cross-section area (cm^2)
Ar	Archimedes number (unitless)
B_{ex}	bed expansion (unitless)
c	speed of light (m/s)
C_{cat}	mass concentration of photocatalyst particles (g/cm^3)
C_F	hydrogen concentration in the liquid bulk within the fluidized bed reactor (mol/cm^3)
C_L^*	hydrogen concentration at the liquid-gas interface (mol/cm^3)
C_s	hydrogen concentration in the liquid bulk within the separator (mol/cm^3)
d_p	particle diameter (cm)
d_p^*	dimensionless particle diameter (unitless)
D	diffusion coefficient of gas species in the liquid phase (cm^2/s)
D_0	conduction band electron diffusion coefficient (cm^2/s)
D_p	hole diffusion coefficient (cm^2/s)
D_w	nanowire diameter (cm)
e	unsigned charge of an electron (coulombs)
E_c, E_v	conduction and valence band energies, respectively (eV)
E°	electrochemical potential (eV)
E_G	band gap energy (eV)
g	gravitational acceleration constant (cm/s^2)
Ga	Galileo number (dimensionless)
$\Delta G_{f,H_2O}^\circ$	Gibbs free energy of evolving 1 mole of hydrogen from water (kJ/mol)

h	Planck's constant (eV s)
H	Henry constant (M/atm)
H_{bed}	static bed height (cm)
H_{ex}	expanded bed height (cm)
I	light intensity (einstiens/min·cm ²)
I_A, I_R	XRD peak intensities for anatase and rutile, respectively
k	Absorption coefficient (m ⁻¹)
k_B	Boltzmann constant (eV/K)
k_L	mass transfer coefficient (cm/min)
$k_{L,a}$	overall mass transfer coefficient (min ⁻¹)
k'_L	mass transfer constant (min ⁻¹ cm ⁻³) ^{0.5}
k''_L	aggregate mass transfer coefficient (cm ³ /min) ^{0.5}
k'_r	back reaction rate constant (cm ³ /g.min)
k_s	solid-liquid mass transfer coefficient (m/s)
L	crystallite size (m)
L_n, L_p	effective electron and hole diffusion lengths, respectively (cm)
m	a constant (unitless)
M_{cat}	mass of photocatalyst substrate (g)
M_v	Mass number (dimensionless)
n	expansion coefficient (unitless)
N_D	donor density (cm ⁻³)
N_G	interface-to-gas mass transfer rates (mol/min.cm ²)
N_L	liquid-to-interface (mol/min.cm ²)
N_S	solid-to-liquid (mol/min.cm ²)
p_{H_2}	hydrogen partial pressure (atm)

P_{abs}	overall rate of photon absorption (einstien/min)
P_i	total rate of photons entering the reaction volume (einstien/min)
P_{sys}	total power input into a system (W)
P_{tot}	total incident solar power (mW/cm^2)
q	volumetric flow rate (cm^3/s)
q_e	elutriation flow rate (cm^3/s)
q_{mf}	flow rate at minimum fluidization (cm^3/s)
r_d	rate of hydrogen generation ($\text{mol}/\text{min cm}^3$)
r_{net}	net rate of hydrogen generation ($\text{mol}/\text{min cm}^3$)
r_p	particle radius (cm)
r_r	rate of back reaction ($\text{mol}/\text{min.cm}^3$)
R_d	total rate of hydrogen generation by a fluidized bed of photocatalyst (mol/min)
R_i	radius of the inner annulus (cm)
R_{net}	net observed rate of hydrogen evolution (mole/min)
R_o	radius of outer reactor wall (cm)
R_q	quality factor (g/L)
s	Scattering coefficient (m^{-1})
S	photocatalyst surface area (cm^2/g)
S_L	rate of photons entering the reaction volume per centimeter of lamp length (ein/min/cm)
Sc	Schmidt number (unitless)
Sh	Sherwood number (unitless)
T	absolute temperature (Kelvin)
U	superficial velocity (cm/s)
U_e	particle settling velocity (cm/s)
U_t	terminal velocity (cm/s)

U^*	dimensionless terminal velocity (unitless)
V_B	band banding (eV)
V_{bed}	volume of expanded bed (cm^3)
V_s	separator volume (cm^3)
V_{sol}	solution volume (L)
W	depletion layer width (cm)
W_{cat}	photocatalyst mass (g)
W_{max}	maximum mass of catalyst (g)
X_A	weight fraction of anatase phase (unitless)
α	photon attenuation coefficient (cm^3/g)
β	corrected full width at half maximum height (FWHM)
ε	bed voidage (unitless)
ε_0	relative dielectric constant, voidage of the static bed (F/cm), (unitless)
η	overall energy conversion efficiency (unitless)
θ	angle of diffraction (degrees)
θ_c	“contact time” of a packet of fluid at the liquid-gas interface (min)
λ	wavelength (m)
μ	fluid viscosity (cP)
μ_p	hole mobility
ν	photon frequency (Hz)
ρ_p	bulk particle density (g/cm^3)
ρ_f	fluid density (g/cm^3)
σ	aggregate attenuation cross section (cm^2/g)

$\sigma_{\text{abs,l}}$	probability of photon absorption by the liquid phase (cm^2/g)
$\sigma_{\text{abs,p}}$	probability of photon absorption by the particles (cm^2/g)
σ_{scatter}	probability of photon scattering by the particles (cm^2/g)
τ_e	conduction band electron lifetime (s)
τ_F	residence time of a fluid parcel in the fluidized bed (min)
τ_p	valence band hole lifetime (s)
τ_S	separator residence time (min)
ϕ	sphericity (unitless)
Φ	photochemical efficiency (moles/einstein)
Φ_{app}	apparent quantum efficiency (moles/einstein)
ψ	function of the hydrodynamic parameters of the model
[X]	concentration of species X (mol/L)

Acknowledgements

When I look in the mirror today, I can hardly believe the person looking back is the same one who embarked on this journey several years ago. My Ph.D. experience has taken my life to new heights that I had never thought possible. I will be forever grateful to my supervisors Dr. David Wilkinson and Dr. Fariborz Taghipour for providing me with this tremendous opportunity and for their encouragement, patience, and guidance along the way. Their support in allowing me to pursue my passions, both within and beyond the walls of the university, has allowed me to become the person I am today.

I would like to acknowledge the Natural Sciences and Engineering Research Council (NSERC) and Trojan Technologies for their valuable financial support that made this research possible.

My sincere appreciation goes to my colleagues Dr. Arman Bonakdarpour, Babak Adeli, Greg Afonso, Dr. David Bruce and Dr. Gustavo Imoberdorf. Your friendship, expertise and advice were invaluable in being able to find the path forward whenever I felt lost, was stumped with a challenge or foiled by broken equipment. I would like to thank all of my fellow labmates for the interesting discussions and entertainment that brought color to my day.

My heartfelt gratitude goes to my family - I would not be here today were it not for the endless love, support and opportunities you have given me and for all of the encouragement when I needed it most. My father and grandfather have been great mentors that have taught me to know that whenever I am faced with a challenge, no matter how big or small, I can roll up my sleeves and say, "I can do that" – a mentality that was critical at every step of this thesis.

Finally, to Emme – you have been my cheerleader, my support crew and have made sure that I would stop working every once in a while to remember the world was still here (and to eat while I was at it). Your love, patience and support know no bounds! You are the most important person in my life and have been on this journey with me since the beginning. We achieved this together.

Dedicated to my family

Chapter 1: Introduction

The global energy demand is projected to increase by 37% by 2040 ¹ as the world's population and economic activity continue to grow. This unprecedented growth is creating a tremendous market pull for both new power generation capacity and new technologies. Current trends in rising oil and gas prices, falling renewable energy technology costs, and an increasing public environmental awareness have resulted in a preference toward renewable energy sources as the world expands its energy production. In 2014, renewable energy sources comprised almost half of all new power generation capacity ², with solar contributing approximately one-third of this new capacity ³. This trend is expected to continue as total global energy production from renewable sources is projected to grow to over 25% in the United States and Asia, and to 50% in the European Union by 2040 ².

Hydrogen has long been touted as the clean fuel of the future, boasting zero emissions when used in combustion engines and fuel cell systems. However, the majority of the 254.5 billion cubic meters of hydrogen produced globally in 2013 ⁴ was produced via methane steam reformation as electrolysis remains prohibitively expensive. While hydrogen-based energy technologies may indeed be efficient and low-carbon emitting, their cumulative ecological impact will be significant if hydrogen production from conventional fossil fuel sources continues, especially as adoption of these technologies grows.

Solar energy is one of the most abundant renewable energy sources yet its market adoption has been slow compared to other renewable energy technologies due to the relative high cost of photovoltaic technology and the difficulty in storing large quantities of solar energy to meet night-time, seasonal and transportation-related energy demands. Success, however, may be realized through the marriage of solar energy and hydrogen production, giving rise to the creation of a Solar-Hydrogen Economy ⁵⁻⁷. While high efficiency photovoltaic cells and electrolyzers may be combined to produce hydrogen in a truly clean,

efficient process –thus expanding the applicability of solar energy through the use of hydrogen as an energy carrier – the cost of such a system remains prohibitively high ^{8,9}.

Heterogeneous photocatalytic water splitting over *semiconductor* materials has been identified as a potential low-cost and environmentally friendly alternative for solar hydrogen production ^{7,10,11}. When semiconductors are illuminated with *photons* having energies equal to or greater than the *band gap* of the semiconductor, *electrons* (negative charge carriers) are excited from the *valence band* (VB) to the *conduction band* (CB), resulting in the formation of *holes* (positive charge carriers) in the valence band. An electric-field gradient in the semiconductor (referred to as the space charge) results in the separation of the electron/hole pairs. This separation process is critical in reducing the *recombination* of electrons and holes, which is greatest source of inefficiency in all semiconductor-based photocatalytic water splitting processes. Electrons and holes that have migrated to the semiconductor/electrolyte interface are then able to participate in electrochemical reactions. If the conduction and valence bands of the semiconductor are situated at potentials sufficiently negative and positive, respectively, water can be electrolysed, or “split”, to evolve hydrogen and oxygen.

Metal oxide semiconductors, which are typically employed as *nanoparticles*, have been the most widely studied photocatalysts for water splitting. Among these, the most popular and heavily researched has been *titanium dioxide* (TiO₂) due to its abundance, low cost and stability in solution (i.e., does not undergo photocorrosion). Titanium dioxide has also gained significant attention in air/water treatment processes as the potential of its valence band results in highly oxidizing photogenerated holes that can decompose even the most persistent contaminants ¹². Indeed, photocatalytic water splitting via TiO₂ may even be combined with other processes, such as wastewater treatment, as the photocatalytic decomposition of organic pollutants can be used to enhance the rate of hydrogen evolution ^{13,14}.

Titanium dioxide is typically found in one of three common crystalline structures: anatase, rutile and brookite. Anatase TiO₂ (band gap ~ 3.2 eV) is typically reported to have superior photocatalytic properties to rutile (band gap ~ 3.0 eV), particularly for water splitting^{11,15-21}, though anatase can be more challenging to synthesize as rutile is the thermodynamically favored phase. While water splitting can occur over TiO₂ photocatalysts, the observed rate of hydrogen evolution over bare TiO₂ is often low. This may be remedied by depositing a co-catalyst, such as platinum^{22,23}, on the surface of the TiO₂. It has been shown that platinum deposited on the surface of TiO₂ behaves as a “sink” and effectively withdraws photoelectrons from the conduction band, which reduces electron/hole recombination²⁴. The presence of platinum, however, catalyzes the thermal back reaction of hydrogen and oxygen (to form waste heat and water), thus reducing the overall efficiency and introducing a complication to the system design (in that the hydrogen must be quickly separated from the platinum-loaded catalyst). In spite of these drawbacks, Pt/TiO₂ has been demonstrated to be effective and has become the *de facto* standard in water splitting research.

The principle disadvantage of TiO₂ is that its large band gap limits the use of TiO₂ to the ultraviolet (UV) range of light (3.2 eV ≈ 387 nm), thus reducing its performance in solar applications. According to the Shockley-Queisser limit²⁵, a single-junction photovoltaic device under 1 sun of illumination is limited to a maximum energy conversion efficiency of 30% at an optimum band gap of 1.4 eV. The theoretical energy conversion efficiency decreases sharply beyond this optimum band gap value, reaching a maximum efficiency of 5% for the 3.2 eV band gap of TiO₂. It should be noted that while the Shockley-Queisser limit was developed for *p-n* junction photovoltaic devices and its results may not directly apply to water splitting materials (i.e. semiconductor nanoparticles suspended in water), it serves as a useful approximation of the maximum efficiency that might be achieved for a given material and band gap.

Much of the recent research in water splitting has focused heavily on improving the *solar-to-hydrogen* (STH) energy conversion efficiency and extending water splitting activity into the visible region of the solar spectrum through alternative photocatalyst materials^{11,26-32}, the modification of TiO₂^{10,11,33-36}, and high-efficiency photoelectrochemical cell (PEC)-type water splitting systems³⁷⁻³⁹. The solar-to-hydrogen efficiency may be defined as:

$$STH = \frac{R_{\text{net}} \Delta G_{f, H_2O}^{\circ}}{P_{\text{tot}} A} \quad (1)$$

where R_{net} is the net rate of hydrogen evolution, $\Delta G_{f, H_2O}^{\circ}$ is the Gibbs free energy of evolving 1 mole of hydrogen from water (237 kJ/mol) and P_{tot} is the total incident solar power (mW/cm²) entering a reaction space of cross section area A (cm²). Though the Shockley-Queisser limit states that maximum energy conversion efficiency is achieved at a band gap of 1.4 eV, which provides a photopotential greater than the 1.23 V required to electrolyze water, additional voltage needs to be generated to overcome the electrochemical losses arising from the oxidation and reduction reactions. In practice, this requires semiconductors with band gaps greater than 2.0 eV and, in turn, limits the maximum practically attainable STH efficiency of water splitting systems to 10% or less²⁸.

Despite the incredible progress in water splitting materials research, little attention has been given to the design of solar-to-hydrogen systems. Indeed, few unique photocatalytic water splitting systems have been demonstrated at bench-^{14,28,40-43} or pilot-scale⁴⁴⁻⁴⁸. Moreover, none of the pilot scale demonstrations could carry out *direct water splitting* and thus required the use of sacrificial reagents, such as methanol, as hole scavengers. One group of researchers has argued that – through intelligent, low-cost system design – it may be possible to produce hydrogen at a cost competitive to gasoline (on an energy basis) via photocatalytic water splitting at STH efficiencies of 5-10% (and possibly lower)⁴⁹⁻⁵¹. As these STH

efficiencies are within the reach of current water splitting photocatalysts, there is a strong impetus to explore and develop new, low-cost and scalable water splitting reactor designs.

Scaling photocatalytic reactors is inherently challenging because in addition to the typical technical challenges encountered when scaling any chemical process – be it kinetic, thermodynamic or fluid dynamic – the need for effective radiation distribution throughout the reactor places additional constraints on the physical dimensions of the reactor⁵². Similarly, the type of photocatalyst employed will dramatically affect the range of possible designs. Nearly all water splitting photocatalysts employed to date (including TiO₂-based photocatalysts) can be classified as either *Immobilized Thin-Film* or *Suspended Slurry* photocatalysts. In photocatalytic reactors employing immobilized films, the photocatalyst is affixed either to a stationary media or to the walls of the photoreactor itself. Conversely, in photocatalytic reactors utilizing suspended slurries, the photocatalyst particles (typically as nanoparticles) are dispersed in the liquid phase (i.e., water). The nature of the photocatalyst type presents its own strengths and challenges when scaling to large photoreactor designs (summarized in Table 1).

As immobilized photocatalysts are deposited on substrates as films, only a limited amount of the photocatalyst surface area is in contact with the liquid phase. Moreover, immobilized films may be hindered both by mass transport at both the liquid/film interface (i.e., boundary layer) and diffusion in the pores of the film^{53,54}. Mass transfer *to* the film is of concern when a sacrificial reagent is employed, while poor mass transfer of the evolved hydrogen and oxygen *from* platinum-loaded photocatalyst films may result in the exacerbation of the back reaction of hydrogen and oxygen. Once the product gases have been removed from the immobilized films, however, they may be swept away from the reactor volume quickly without further back reaction. This is in contrast to suspended slurry photocatalysts, where the product gases remain in contact with the platinum-loaded photocatalyst particles for extended periods of time.

Indeed, Escudero et al.⁵⁵ demonstrated that, while solid-to-liquid mass transfer may be high for suspended slurry photocatalysts, the liquid-to-gas mass transfer step is rate limiting and that low liquid-to-gas mass transfer rates result in reduced hydrogen evolution due to the platinum-catalyzed back reaction.

Table 1: Comparison of existing water splitting photocatalyst methods

	Immobilized Thin Film Photocatalyst (ITP)	Suspended Slurry Photocatalyst (SSP)
Radiation Distribution	Poor	Excellent, when SSP concentration optimized
Mass Transfer	Poor	Excellent, though L → G mass transfer may be limiting
Photocatalyst Surface Area to Reactor Volume	Low	High
Photocatalyst Design Flexibility	Advanced, nanostructured film possible	Limited
Separation of photocatalyst from reaction products	Excellent	Challenging
Scalability	Poor	Poor

Suspended slurry photocatalysts, typically have both excellent radiation distribution and high surface area-to-reactor volume ratios, provided that the concentration of the photocatalyst is optimized for the given design. If the photocatalyst concentration is too low, photons may simply pass through the reactor volume to be absorbed at the outer reactor wall. If the concentration is too high, light will be unable to penetrate throughout the reaction volume. This becomes particularly problematic when using photocatalysts containing platinum deposits since the photocatalyst particles in the shaded regions of the reactor only serve to promote the parasitic back reaction of hydrogen and oxygen. Unlike suspended slurries, the radiation distribution on immobilized films is often poor due to scattering and reflection of incident light from the film surface. However, as the photocatalyst is anchored to a substrate, it is possible to reduce this effect and improve the performance of the immobilized photocatalysts through the use of

nanostructured films^{28,56,57}. Vertically-aligned nanowires, grown on the immobilized substrate with their long-direction collinear with the direction of incident light, allow for rapid charge transfer in their short radial direction while providing maximum light absorption along their length⁵¹. Similarly, films of nanowire arrays are able to scatter light horizontally *into* the film (rather than *away* like a planar surface), thus further reducing losses due to scattering. While it may be possible to employ unique photocatalyst particle shapes in suspended slurries for improved performance^{19,58-60}, it is impossible to hold them in a fixed orientation to enhance both light absorption and charge transfer in the same manner as nanostructured films. Scaling systems that utilize suspended slurries of shape-engineered photocatalyst particles may also prove to be challenging as it has been shown that high shear stresses – such as those developed by stirring, pumping and high flow rates – can result in the damage/destruction of nanoparticles⁶¹.

Photocatalytic fluidized bed reactors were initially developed as an alternative to suspended slurry photocatalysts used in water treatment as the fluidizable photocatalyst particles can be easily separated from the liquid phase (much like immobilized thin-film photocatalysts). These fluidized bed reactors function by suspending (i.e., fluidizing) particles throughout the reactor volume by the upward flow of a liquid phase, resulting in excellent mass transfer, good radiation distribution, and high photocatalyst surface area-to-volume characteristics approaching those of suspended slurry photocatalysts⁶²⁻⁶⁴. Indeed, UV-irradiated photocatalytic fluidized bed reactors employing TiO₂-coated particles have demonstrated contaminant decomposition performances equal to or exceeding those of suspended TiO₂ nanoparticles slurries; quantum yields as high as 37% have been reported, indicating that fluidized beds may be the most efficient among competing photoreactor designs⁶⁵⁻⁶⁷. Several researchers have developed a number of excellent models describing the complex fluid dynamics, reaction kinetics and radiation propagation occurring within the bed of fluidized photocatalyst particles^{62,63,68-70}, allowing for systems to be designed and scaled with relative ease. To date, a number of pilot-scale fluidized photocatalytic water-treatment

systems have been successfully developed using both UV lamps⁷¹⁻⁷³ and natural sunlight⁷⁴⁻⁷⁶ to demonstrate their economic and technical feasibility.

We hypothesize that a UV-irradiated fluidized bed reactor employing Pt-TiO₂ photocatalysts may serve as an efficient platform for the future design of photocatalytic hydrogen production systems. Photocatalytic fluidized bed reactors are expected to allow hydrogen and oxygen evolved through water splitting to be quickly and easily separated from the photocatalyst particles, thus reducing efficiency losses through the platinum-catalyzed back reaction. At the same time, these photoreactors are thought to offer excellent mass transfer, good radiation distribution, and high surface area-to-volume characteristics similar to those observed with suspended slurry photocatalysts. Therefore, it can be anticipated that photocatalytic fluidized bed reactors may yield hydrogen evolution performance similar to, or greater than, that achieved by suspended slurry Pt-TiO₂ photocatalysts. Finally, as the photocatalyst particles can be produced by depositing the semiconductor material into inert, fluidizable supports (in a similar fashion to immobilized thin-film photocatalysts), it may be possible to design advanced photocatalyst particles with nanostructured features, such as vertically aligned nanowires and -rods, that are otherwise impossible with suspended slurries. To date, no known attempt toward photocatalytic hydrogen production in a UV-irradiated fluidized bed reactor has been reported in literature. Moreover, no reports regarding the application of robust, fluidizable nanowire-deposited photocatalysts, nor a method for their large-scale manufacture, have ever been reported.

1.1 Thesis Layout

The focus of this thesis is to develop a UV-irradiated fluidized bed reactor system for photocatalytic hydrogen production, with a goal being to improve upon issues currently limiting the efficiency and scalability of classic approaches (such as suspended slurry TiO₂ photocatalysts). The key objectives of this work are to:

1. Develop and demonstrate a photocatalytic fluidized bed reactor system for hydrogen production

- The design and fabrication of the experimental equipment and setup
- Achieve hydrogen evolution performance comparable or equal to that of existing approaches to photocatalytic water splitting

2. Develop functional TiO₂ water splitting photocatalysts suitable for use in fluidized beds reactors

- Produce a fluidizable photocatalyst that is mechanically stable and active over an extended period of time.
- Develop up to three photocatalyst designs that may yield high performance and/or strength.

3. Identify the primary factors determining the operation and performance of the fluidized bed reactor and photocatalyst

- Factors such as photocatalyst design and fluidization characteristics, the design of the fluidized bed system and operating conditions will be considered.

In Chapter 1, a background on titanium dioxide photocatalysts and their synthesis is presented. The effect of several operational parameters, their effects on water splitting performance, and the design of fluidizable TiO₂ photocatalyst particles is then discussed. Considerations regarding the design and synthesis of advanced nanostructured photocatalysts are presented.

In Chapter 2, the behavior and water splitting performance of a UV-irradiated fluidized reactor is presented. It is shown that simple, fluidizable TiO₂ photocatalysts (having a structure consisting entirely of porous TiO₂) are able to evolve hydrogen at steady rates up to 211 μmol/hr and exhibit a 44% improvement in efficiency over that observed for a suspended P25 TiO₂ photocatalyst slurry employed in the same reactor system. The material in this chapter is currently in preparation for journal submission.

In Chapter 3, a discussion on the theoretical aspects of fluidized bed operation is presented and a mathematical model that defines the critical parameters determining the rate of hydrogen evolution is derived. It is shown that the model fits closely with the data presented in Chapter 2. Through analysis of the model and experimentation, it is revealed that the rate of liquid-to-gas mass transfer in the separator unit has a significant impact on the observed rate of hydrogen evolution. The material in this chapter is currently in preparation for journal submission.

In Chapter 4, a novel method for the low-temperature growth of 2.45 μm long anatase nanowires is presented. The photocatalytic performance of the anatase nanowires is compared with that of P25 TiO_2 films and hydrothermal-grown rutile nanorods. The material in this chapter is currently in preparation for journal submission.

In Chapter 5, the synthesis of nanostructured photocatalysts on porous, fluidizable particles is demonstrated for the first time. In this chapter, two methods for the production of fluidizable nanowire- and nanorod-deposited particles, and their photocatalytic water splitting performance are presented. The use of porous, fluidizable particles was highly effective in preventing attrition of the nanowire/rod films during fluidization. The material in this chapter is currently in preparation for journal submission.

In Chapter 6, the research outcomes, significance and ultimate impact of the work presented in Chapters 3-6 are summarized, and recommendations for further research are proposed.

1.2 Literature Review

1.2.1 Semiconductor Theory

In 1971, Fujishima and Honda presented the first known example of photoelectrochemical water splitting using a TiO₂ electrode⁷⁷. The following year they described the minimum requirements needed for water splitting, indicating that it was possible for the reaction to occur without the need for an external bias potential⁷⁸, thus marking the beginning of photocatalytic water splitting.

In semiconductors there exists a region in the energy band structure, called the *band gap*, where *electrons* are forbidden to propagate due to a lack of energy states. However, when the semiconductor absorbs *photons* of sufficient energy, electrons are excited across the band gap region from the *valence band* (low energy state) to the *conduction band* (high energy state). More specifically, the energy of the photon must be equal to or greater than the band gap energy, E_G :

$$\frac{hc}{\lambda} \geq E_G \quad (2)$$

where h is Planck's constant (4.135×10^{-15} eV.s), c is the speed of light ($\sim 3 \times 10^8$ m/s) and λ is the wavelength of the photon (m). When an electron is promoted to the conduction band, a positively charged site, referred to as a "*hole*", is formed in the valence band. The holes may be treated as *positive charge carriers* – much in the same way electrons are *negative charge carriers* – that can undergo transport through the valence band. For n-type semiconductors that have an excess of electrons, such as TiO₂, electrons are the *majority charge carrier* while holes are the *minority charge carrier*. The free electrons in the conduction band and the holes in the valence band are capable of participating in electrochemical reactions, such as the electrolysis of water.

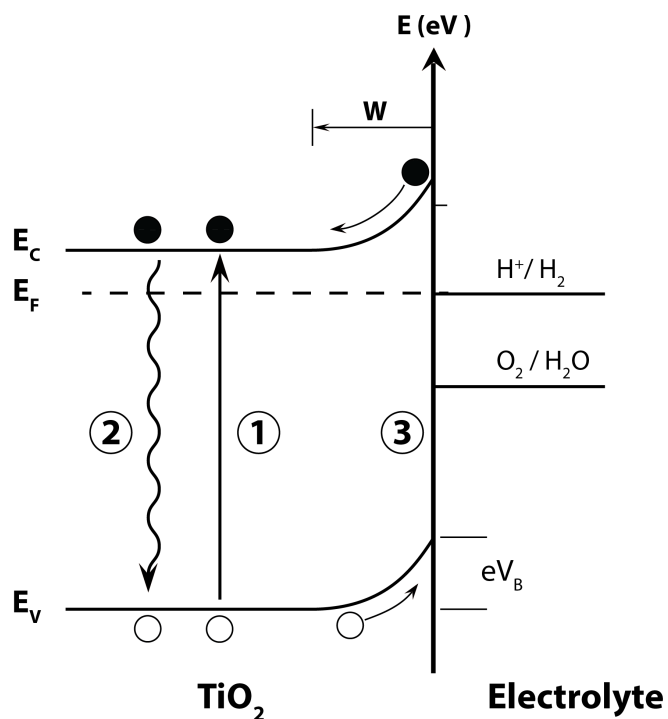


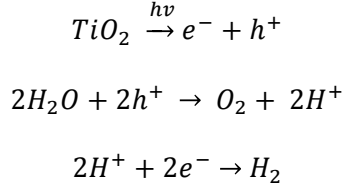
Figure 1: Band energy diagram showing (1) the promotion of an electron to the conduction band, (2) the recombination of e^-/h^+ , and (3) charge separation arising from band bending (V_B) in the depletion layer (of width, W)

The Fermi energy of a semiconductor represents an energy level where an electron's potential energy is equal to its chemical energy or, alternatively, the Fermi energy may be thought of as the energy level that has a 50% probability of being occupied by an electron. For n-type semiconductors, the Fermi energy is situated slightly below the conduction band energy. When a semiconductor and an electrolyte are brought into contact, they tend toward electrochemical equilibrium. If the Fermi energy of the semiconductor is at a higher energy than the redox potential of the electrolyte, there is a transfer of charge from the semiconductor to the electrolyte until the Fermi energy and redox potential are equal. This charge transfer results in the formation of a *depletion layer*, a positive space charge region, in the semiconductor and an *electric double layer* in the electrolyte at the semiconductor-electrolyte interface. As a result, there exists an *electric field* in the semiconductor that locally alters the conduction and valence band edge energies

near the interface; the band gap energy remains the same but the conduction and valence edge energies are shifted with respect to their level throughout the bulk of the semiconductor.

This process, known as *band bending*, is greatly important to photocatalytic water splitting as the electric field created by the depletion layer results in the separation of electrons and holes. If photogenerated electrons and holes are not separated, they undergo *recombination* to produce waste heat. The recombination process occurs at a rate several orders of magnitude higher than that of the water splitting reaction⁷⁹, and is the greatest source of inefficiency limiting performance. If photons are absorbed within the depletion layer, the electrons drift toward the bulk of the semiconductor while holes percolate to the semiconductor-electrolyte interface. If photons are absorbed in the free-field region, where there is no band bending, or if the semiconductor is fully depleted (i.e., it lacks sufficient majority charge carrier concentration to support an electric field), there is no electric field present to separate the photogenerated electrons and holes, and thus they rapidly recombine. The degree of band bending, V_B , and the physical width of the depletion layer, W , are important considerations in the design of photocatalyst particles at the nano- and micro-scale level, as will be discussed later.

Electrons and holes that avoid recombination are able to migrate to the surface of the semiconductor where they may drive electrochemical reactions, provided the conduction and valence band energies are ideally situated (Figure 1). If the valence band energy, E_V , of the semiconductor is lower than the oxidation energy of water, $E^\circ(\text{O}_2/\text{H}_2\text{O}) = -1.23 \text{ eV}$, electrons will be transferred from water molecules to the valence band holes, evolving oxygen and protons. Similarly, if the conduction band energy is greater than the hydrogen evolution energy, $E^\circ(\text{H}^+/\text{H}_2) = 0.00 \text{ eV}$, electrons will be transferred from the conduction band to reduce protons, thus evolving hydrogen. The absorption of photons by TiO_2 and the subsequent water splitting steps may be written as:



From the mechanism above, it can be seen that two electrons and two holes are required for each H₂ and O₂ evolved, respectively (however, there have been recent reports suggesting O₂ evolution requires four-hole chemistry⁸⁰). While the above mechanism is commonly presented in literature, it should be understood that this mechanism is only valid in acidic conditions (whereas basic conditions are typically employed in practice) and the true mechanism under different reaction conditions is poorly understood at the present time. The effect of reaction conditions on the mechanism and possible reaction steps are discussed further in Section 1.2.5.3 and Chapter 3.

The *quantum efficiency* of the process may be defined as the ratio of the number of reacted electrons to the number of absorbed photons. However, determining the actual quantity of photons absorbed by a photocatalyst is challenging, and it is common for the overall efficiency of a water splitting process to instead be quantified by the *Apparent Quantum Efficiency* (AQE), defined by^{26,81}:

$$\phi_{AQE} = \frac{\# \text{ of electrons reacted}}{\# \text{ of incident photons}} \times 100\% \quad (3)$$

The apparent quantum efficiency is an important figure of merit for making accurate comparisons with other reported results. The *overall energy conversion efficiency* of the water splitting process, particularly in systems that utilize artificial light sources, may be defined as the ratio of energy output as hydrogen to the energy input required by the system:

$$\eta_{overall} = \frac{R_{net} \Delta G_{f,H_2O}^{\circ}}{P_{sys}} \quad (4)$$

where R_{net} is the net rate of hydrogen evolution, $\Delta G_{f,H_2O}^{\circ}$ is the Gibbs free energy of evolving 1 mole of hydrogen from water (237 kJ/mol), and P_{sys} is the total power input to the system. For most systems, P_{sys} is simply the energy input required by the light source, while for larger systems this value would include the energy requirements for pumps, etc. It should be noted that overall water splitting efficiency is of the same form as the *solar-to-hydrogen efficiency* (STH) defined in the previous section.

1.2.2 Introduction to Titanium Dioxide

Titanium dioxide (TiO_2) is an abundant, low-cost *metal oxide* semiconductor that gained its initial popularity due to the pioneering work by Fujishima and Honda^{77,78}, who used TiO_2 for the first demonstration of photocatalytic water splitting. Titanium dioxide has since become one of the most widely used and studied photocatalysts for a large number of applications^{79,82-85}, with the treatment of air and wastewater being chief among them.

While TiO_2 may exist in a number of crystalline structures⁸⁶⁻⁸⁸, it most commonly occurs as anatase (tetragonal, Figure 2a), rutile (tetragonal, Figure 2b) and, to a lesser extent, brookite (tetragonal, Figure 2c). Of the three, anatase is typically reported to have the highest band gap energy at ~ 3.2 eV while rutile has the lowest at ~ 3.0 eV. The reported band gap energies for brookite range from 3.14 eV to 3.26 eV⁸⁹. Anatase and brookite are both meta-stable phases and will transform to rutile⁸⁹, the thermodynamically stable phase⁸², upon heating.

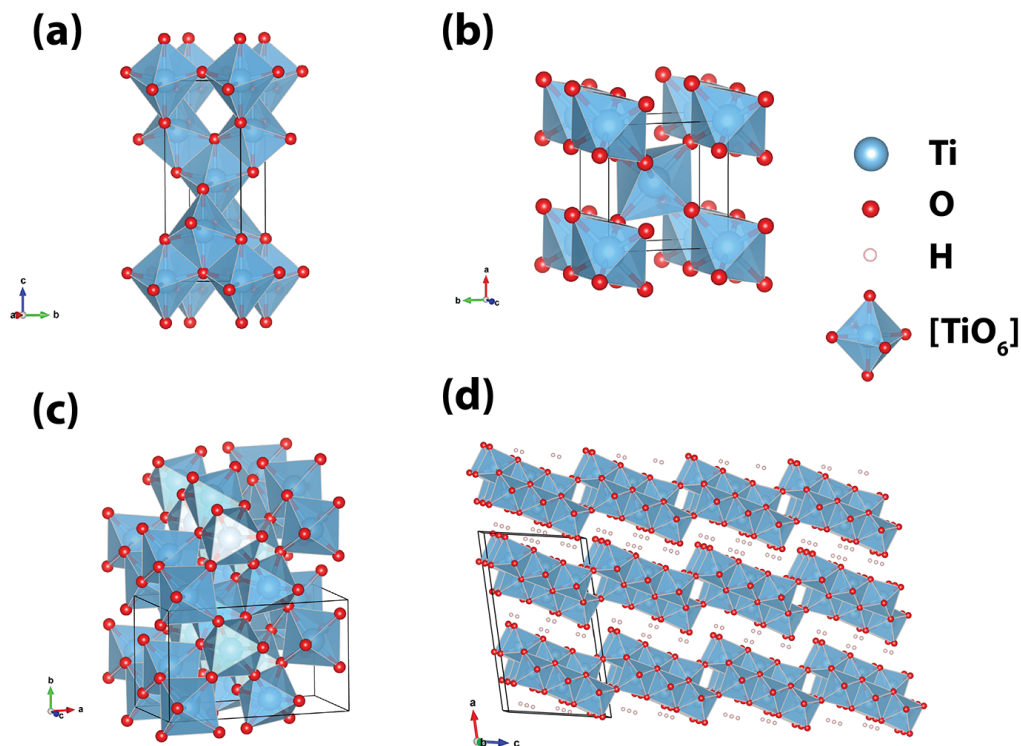


Figure 2: Crystal structures of a) anatase, b) rutile, c) brookite, and d) the lepidocrite-like structure of protonated titanates (H₂Ti₃O₇ shown)

Despite having a larger band gap, which pushes the minimum photon energy further into the UV region (~387 nm), anatase TiO₂ is typically reported to have superior photocatalytic properties to rutile, particularly so for water splitting^{11,15-21}. Experimental evidence initially found the flat band potential of anatase to be situated ~0.2V more negative than that of rutile, thus implying that the positioning of the anatase conduction band energy yields a greater electrochemical driving force for proton reduction in water splitting⁹⁰. While this fact has been hotly debated, it has become the widely accepted understanding amongst researchers to explain the observed difference in photocatalytic performance between anatase and rutile. Recent evidence has argued the contrary and has shown that the conduction band of rutile may in fact be situated ~0.4V *more* negative than anatase, and that the observed difference in performance arises from differences in bulk properties^{21,91}. Nonetheless, anatase is still typically found to be the more active phase for a number of applications.

Protonated and ion-exchanged titanates (Figure 2d) are a unique form of titanium oxides having a layered structure. Titanates are of particular interest because in addition to their own unique properties – such as the ability to be used for ion-exchange⁹² – they can be modified under hydrothermal conditions or by heating to form rare or metastable phases such as anatase^{93,94}, brookite^{93,95} and TiO₂(B)^{96,97}. This ability makes titanates excellent precursors for producing shape-controlled particles with a desired phase, as the low-temperature crystallization of titanate does not result in changes in the morphology of the particles. Moreover, titanates provide an alternate synthesis route to other methods where rutile would be thermodynamically favored. Brookite is one of the least studied TiO₂ crystalline structures largely due to the difficulty in preparing phase-pure samples. *Zhao et al.* demonstrated a facile method to produce brookite^{93,98,99}. It was shown that layered titanates that were either fully protonated or fully intercalated by NH₄⁺ would produce anatase TiO₂ upon calcination or hydrothermal treatment, whereas titanates partially intercalated by both NH₄⁺ and Na⁺ would result in brookite. It was reported that the difference in deintercalation rates of NH₄⁺ and Na⁺ induced a lattice shear during the collapse of the titanate layers, causing a reorientation of TiO₆ octahedra, leading to the formation of brookite.

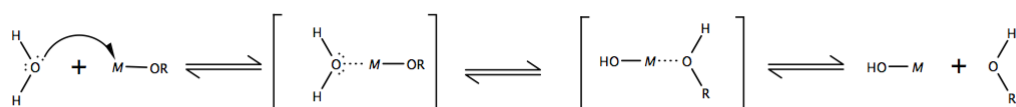
1.2.3 Sol-Gel Synthesis and Precursors

The sol-gel process originated in the mid-1800s through the initial studies of the acidic hydrolysis of tetraethylorthosilicate (TEOS) to form glass-like SiO₂¹⁰⁰. This low-temperature technique gained popularity in the early 1970s for the production of glass/ceramics¹⁰¹, high-performance optics^{101,102}, protective coatings^{103–105} and hybrid materials¹⁰⁶.

The sol-gel process involves the evolution of inorganic polymer networks through the generation of a colloidal suspension (a sol), followed by the gelation of the sol to form a network in a continuous liquid phase (a gel)^{101,107}. The evolution of these inorganic polymer networks proceeds through the hydrolysis and condensation of metal precursors¹⁰⁸. Inorganic metal salts are commonly employed low-cost

precursors; however, they are often difficult to control as they are highly reactive toward water. In contrast, metal-organic precursors tend to be preferred over the inorganic metal salts for the manufacture of porous solids, powders, thin films and ceramics¹⁰⁸. The hydrolysis of metal organics can be easily controlled via their ligands and reaction conditions^{107,109} and their hydrolytic products (typically alcohols) are easy to remove from the metal oxide network upon drying, resulting in high-purity products. The high degree of control afforded by the metal-organic precursors allows for the morphology, porosity, particle size, and resulting crystal phase of the product to be tailored for a desired application^{110,111}, which has led to the sol-gel process becoming the preeminent method used for the production of nanoparticulate photocatalysts. The flexibility of this process even allows for the sol-gel to be reacted with –OH groups on the surface of preexisting TiO₂ particles, to form strong composite materials¹¹², or on the surface of silica particles, resulting in a strong chemical bond between the sol-gel coating and the particle¹¹³.

Hydrolysis



Condensation

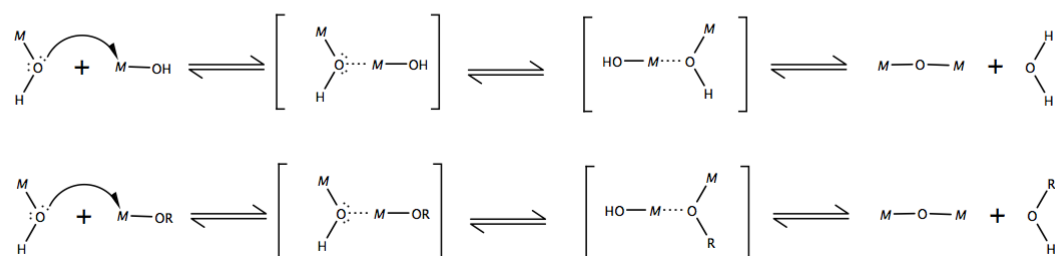


Figure 3: Sol-gel hydrolysis and condensation mechanism

The hydrolysis and condensation of metal alkoxide precursors proceeds through nucleophilic substitution (Figure 3), resulting in the evolution of water and alcohol. The rate of hydrolysis may be controlled

through the water content and pH of the solution, thus most sol-gel reactions are typically carried out in non-aqueous solvents as a means to control the resulting phase and morphology of the product. Over the past decade, a substantial body of work involving ‘green’ chemistries and softer processing conditions has been amassed, with techniques being developed with a greater attention toward low-cost, low-energy and low-waste ¹¹⁴. As a result, a number of non-toxic, water-soluble metal precursors have been discovered ¹¹⁵.

Metal precursors using lactic and citric chelating ligands have been shown to be water-soluble and stable over a wide pH wide range, allowing for safer and easier handling than the highly reactive metal salt and metal alkoxide precursors. According to Livage’s Partial Charge Theory ¹⁰⁷, hydrolysis of a metal precursor continues until the mean electronegativity of the product *is equal to the mean electronegativity of water* ($X_r = 2.49$). If the ligands surrounding a metal center, for example Ti, are replaced with highly stable chelates such as lactate, the partial charge on the Ti atom decreases, resulting in a reduced interaction between the coordinated Ti center and O atoms in water. For our example, using the lactate coordinate $[\text{Ti}(\text{la})_3]^{-2}$ results in the mean electronegativity changing from ($X_r = 2.85$) for hydrated Ti in solution, $[\text{Ti}(\text{H}_2\text{O})_6]^{4+}$, to ($X_r = 2.39$) ¹¹⁵. The introduction of lactate ligands thus drastically suppresses hydrolysis, allowing the complex to remain stable in water.

Titanium precursors derived from these highly stable, water-soluble complexes may be reacted with H_2O_2 to produce peroxo-titanium complexes ^{114,116–120}. The peroxo- ligands that coordinate with the Ti center take on different behaviors with varying pH and, depending on the nature of their coordination, result in steric constraints that encourage the octahedral growth units to link together through shared apical edges (resulting in anatase) or through equatorial edges (resulting in rutile) ¹¹⁹. At certain pH values, a mixture of both apical and equatorial edge sharing can be achieved, resulting in the formation of brookite TiO_2 .

The ligands employed in the water-soluble titanium complexes have been shown to also play an important role during hydrolysis as their hydrolytic products can bind to specific facets of the TiO₂ crystallite and reduce growth in those directions, resulting in anisotropic growth of nanorods and –wires^{118,120}.

Furthermore, hydrolysis of these water-soluble complexes in peroxide solutions containing suitable cations, such as NH₄⁺, results in the formation of layered titanate sheets which can spontaneously stack into nanowire shapes^{121,122}; these morphologies can then be easily converted to a wide range of TiO₂ crystalline structures. In summary, the modern ‘green’ precursors combined with well-known sol-gel processes holds great potential for the low temperature formation of TiO₂. Moreover, by utilizing titanates as a synthesis pathway, it may be possible to achieve a wider range of crystalline structures not currently possible with other techniques.

1.2.4 Platinum Loading

It has been demonstrated that the presence of metal deposits – particularly Pt, Pd, Rh, Au and Ag – onto the surface of TiO₂ results in a significant increase in the rate of hydrogen evolution^{10,22–24,42,123–125}. When metal nanodeposits, typically noble metals, are placed on the surface of TiO₂, the high work function²⁴ and lower Fermi energies¹⁰ of the metals result in a withdrawal of electrons from TiO₂. This charge redistribution creates localized Schottky Barriers⁸² that effectively trap the excited electrons and slow the recombination of electrons with holes. Moreover, the metal nanodeposits behave as “sinks” and withdraw photogenerated electrons from the conduction band, thus improving the charge separation and reducing electron/hole recombination²⁴.

The addition of platinum nanodeposits (34 Å to 2nm)^{22,123} onto the surface of TiO₂, typically at loadings of 0.5 wt% to 1 wt%^{22,42}, was found to be effective at increasing the efficiency of the photocatalyst. The effect of metal nanodeposits has been reported to be size dependent as small Au nanodeposits produced shifts in the Fermi energy that resulted in higher efficiencies than larger nanodeposits¹²⁵.

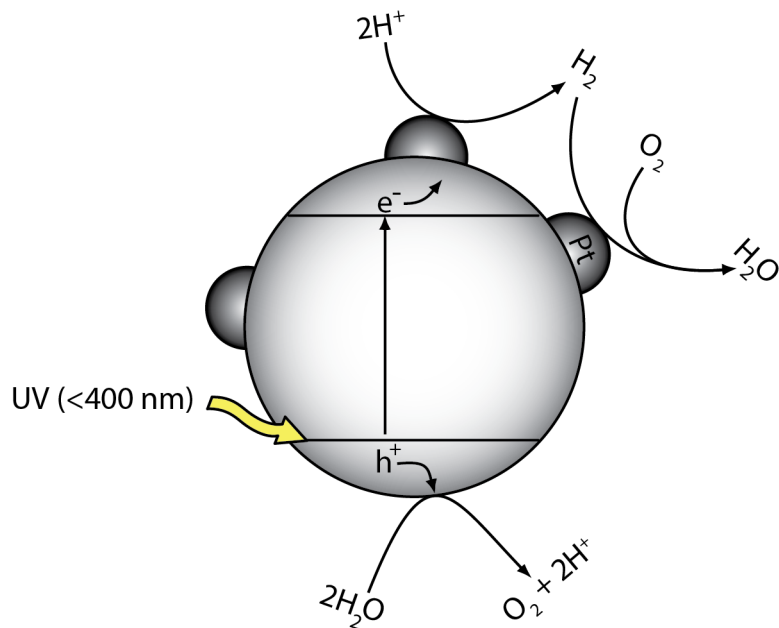
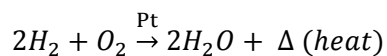


Figure 4: Representation of photocatalytic water splitting over Pt-deposited TiO₂ nanoparticles and simultaneous Pt-catalyzed back reaction

While metal deposits typically result in increases in photocatalyst efficiency, they may also display deleterious effects. It has been demonstrated that the oxidation of Au nanodeposits disrupts the metal/TiO₂ interface, resulting in the deposit behaving as electron-hole traps that promote recombination. Similarly, platinum and rhodium, which are often found to be some of the best material choices, are known to promote the thermal back reaction of hydrogen and oxygen to form water and waste heat. The back reaction is assumed to follow that of the combustion of hydrogen and oxygen over platinum (or Rh):



A schematic diagram demonstrating the water splitting reaction over a Pt-deposited TiO₂ particles and the simultaneous back reaction is shown in Figure 4. It should be noted that the platinum-catalyzed back reaction has not been well studied in water splitting systems, and so the mechanism of this process is

poorly understood. A more thorough discussion of the possible back reaction steps is presented in Chapter 3. It has been demonstrated that platinum loadings beyond 1 wt% decrease the overall rate of hydrogen production^{22,42}; it is suspected that this effect is due to the promotion of the back reaction of hydrogen and oxygen with increasing amounts of platinum on the TiO₂ surface. Recent research has seen the use of Cr₂O₃ to form shell structures over noble metal deposits, which results in the effective suppression of the back reaction²⁷.

The most common techniques employed for the incorporation of metal deposits have been impregnation^{22,126,127}, deposition-precipitation^{126,127} and photodeposition¹²⁶⁻¹³¹, with the photodeposition method being the best among them. It is classically assumed that in the photodeposition method, photogenerated electrons reduce platinum (or other metal) precursors onto the TiO₂ surface. However, evidence¹³⁰ has been shown that suggests that some platinum precursors, when exposed to UV light, will form platinum metal nanoparticles in solution which then deposit onto the TiO₂ surface.

While the photodeposition of metal nanodeposits often results in excellent results, its performance can be highly dependent on preparation conditions. Sacrificial reagents, such as ethanol, are typically added to the solution as hole-scavengers in order to achieve higher photo-metalization rates. It was demonstrated that photodeposition carried out in solutions containing high amounts of ethanol result in CO contamination of the Pt deposits with subsequently low performance¹²⁹; solutions that were comprised mostly of water, however, avoided this issue and yielded far greater performance. Senevirathna et al.¹²⁸ demonstrated that TiO₂ photodeposited in a iodoplatinic acid solution yielded hydrogen evolution rates twice as great as samples photodeposited in a chloroplatinic acid solution. This difference was attributed to the iodoplatinic acid adsorbing more strongly to TiO₂ which resulted in the formation of ultrafine Pt nanodeposits.

1.2.5 Influence of Operational Parameters

1.2.5.1 Pressure and Mass Transfer

As discussed previously, acceptable rates of photocatalytic water splitting necessitate the use of platinum nanodeposits on the TiO₂ surface. The presence of platinum, however, catalyzes the back reaction of H₂ and O₂ to produce waste heat and water. One group of researchers demonstrated in several reports^{132–135} that in closed, batch systems containing Pt-deposited photocatalysts, the overall rate of hydrogen evolution decreased gradually as the evolved product gases accumulated and the system pressure increased. Moreover, it was observed that system pressures as low as 35 torr were required to achieve high hydrogen evolution rates and that hydrogen evolution ceased at pressures greater than 250 torr; high hydrogen evolution rates could be restored by periodically pumping the system to 35 torr. It was found that artificially increasing the system pressure with either oxygen or argon resulted in the same reduction in the rate of hydrogen evolution. It was hypothesized that increasing system pressure resulting in decreased mass transfer from the liquid to gas phase, which in turn promoted the parasitic back reaction of H₂ and O₂ over the deposited platinum sites, as well as the photoadsorption of O₂ (which serves as a recombination pathway for e⁻/h⁺).

Indeed, Escudero⁵⁵ demonstrated that the rate of mass transfer from the liquid to gas phase was the rate determining step for photocatalytic hydrogen evolution over Pt-TiO₂ through the use of a photoreactor system that was continuous with respect to the gas phase. It was shown that bubbling a sweep gas through the solution, thus increasing the liquid-gas interfacial area and the overall rate of liquid-to-gas mass transfer, resulted in an increase in hydrogen evolution. Escudero then demonstrated that, for a continuous photoreactor system, the rate of hydrogen evolution was independent of the gas-phase hydrogen partial pressure. It was thus concluded that the reduction in hydrogen evolution observed in *closed systems* was due a reduction in the driving force for the rate of mass transfer (from the liquid to gas phase) due to the accumulation of photoproducts in the gas phase and increasing system pressure. Karakitsou¹³⁶ observed a

similar effect in that an increase in the stirring rate (and therefore, mass transfer) resulted in an increased rate of hydrogen evolution. It was, however, later argued that this was not due to liquid-to-gas mass transfer but rather that increased stirring led to increased uniformity of the solution and contact of the photocatalyst particles with the light.

1.2.5.2 Temperature

The rate of hydrogen evolution from a Pt-TiO₂ system was demonstrated¹³⁶ to be of the form:

$$r = k_1 e^{-E_a/RT} \quad (5)$$

where the activation energy, E_a , was 21 ± 2 kJ/mol and the pre-exponential factor, k_1 , was a function of the solution pH and varied from 930 to 5800 $\mu\text{mol/hr.mg}$. It can then be expected that the hydrogen evolution rate will increase with temperature. Therefore, the system temperature should be held constant with a heat-exchanging device or be allowed to reach a thermal equilibrium before beginning experimental runs.

1.2.5.3 Solution pH and Additives

It has been observed by several researchers that the rate of hydrogen generation is strongly dependent on the pH of the system and that the rate increases in an exponential fashion with pH^{22,132,133,136}. Kiwi²² suggested that the optimal pH of the system should be pH 14; however, some solutions employed to obtain such high pH values observed the formation of a precipitate in the solution that resulted in decreased performance due to optical impedance of the photons¹³³. As such, it is generally found that the best performance is obtained in the pH range of 11 to 14. It was proposed that at high pH, the high concentration of surface hydroxyl groups play a role in scavenging holes (thereby reducing recombination) and preventing the uptake of O₂ by the TiO₂ surface which would otherwise produce peroxy groups that reduce the photocatalyst's performance²².

It has been reported by a number of researchers that no oxygen evolution was detected during photocatalytic water splitting over Pt-TiO₂^{22,55,80,137,138}. Moreover, the initial rate of hydrogen production was observed to be high, but then decreased with time to a pseudo-steady state. In the classical model for photocatalytic water splitting presented earlier in this section (including the back-reaction of hydrogen and oxygen), oxygen is both produced and consumed at a 1:2 stoichiometric ratio with hydrogen, thus there is reason to suspect that there are intermediate reactions and species involved in the water splitting process that may account for the missing oxygen.

Several reports demonstrated that hydrogen peroxide forms readily on the surface of TiO₂ under UV irradiation in water. Moreover, it has been demonstrated by nearly all reports of hydrogen peroxide generation on TiO₂ surfaces that the formed peroxide species are not detected in solution, suggesting that the peroxides do not readily desorb from the TiO₂ surface^{22,123,139-142}, and even remain chemically bound to the TiO₂ surface long after the light source had been removed¹⁴⁰. Harbour et al. observed that titanium dioxide nanoparticles were capable of containing over 22 chemisorbed H₂O₂ molecules per square nanometer of photocatalyst surface area; for titanium dioxide photocatalysts, having an average specific surface area of 50 m²/g, this represents a significant capacity for adsorbed peroxides¹⁴¹. Abe et al. also demonstrated that TiO₂ particles that had been irradiated in pure water for 600 hours as part of a water splitting experiment showed a remarkable decrease in performance over time and were eventually completely deactivated and could not evolve hydrogen; it was postulated that this was due to modification of the photocatalyst surface¹³⁹. The creation of peroxo-titanium compounds on the surface of the photocatalyst may result in a loss of surface area and eventual deactivation.

Arakawa and Sayama demonstrated¹³²⁻¹³⁴ that the addition of chemical additives, such as Na₂CO₃ at a concentration of 2.2M, would not only yield stoichiometric evolution of hydrogen and oxygen but would increase the hydrogen evolution rates by nearly 600 fold. The researchers hypothesized that this

remarkable increase in performance and appearance of stoichiometric evolution may be due to a carbonate layer forming over the platinum nanodeposits^{133,134}, which reduces the parasitic back reaction of hydrogen and oxygen. An alternate explanation was offered that hypothesized that carbonate species scavenge holes from the TiO₂ surface, which in turn may reduce the photoadsorption of O₂ (which act as a recombination pathway for e⁻/h⁺) and the formation of peroxo-titanium species (which reduce the number of active sites). The true cause of the dramatic increase in hydrogen evolution and the appearance of stoichiometric evolution of oxygen and hydrogen was not satisfactorily explained.

As there is a high potential for the non-stoichiometric evolution of hydrogen and oxygen due to unknown processes, particularly in experiments where no performance enhancing additives are used, the composition of the outlet gas stream **must** be monitored at all times in order to determine the true hydrogen evolution rate. This may be accomplished by a dedicated on-line gas chromatography system or mass spectrometer.

1.2.6 Fluidizable Particle Design

The design of the fluidizable photocatalyst particles is of great importance as the high mechanical stresses experienced by the particle during fluidization often leads to the ablation of the photocatalyst from the supporting substrate. A number of efforts have been made to produce stable TiO₂ coatings on substrate surfaces. Techniques such as *vapor deposition and sputtering*^{64,66,143,144} typically result in the deposited film having low porosity and surface area, with subsequently poor photocatalytic performance, as well as limited adhesion of the photocatalyst to the support. The *thermal adhesion* of TiO₂^{143,145-148} involves nanoparticles, typically commercially available Degussa/Evonik P25, being mixed into a slurry and deposited on the substrate by dip-coating; the TiO₂-coated particles would then be calcined at high temperatures. This technique was often met with limited success as the TiO₂ films were typically ablated from the surface within hours to a few days of operation. The strength of the TiO₂ films could be

improved with higher calcination temperatures, although this resulted in a reduction of surface area and photocatalytic activity.

Sol-gel coated substrates have demonstrated improved adhesion and stability over that of thermally deposited TiO₂ films^{64,113,145,149,150}, however reported results have been highly substrate dependent. Titanium dioxide sol-gels were prepared through the hydrolysis of typical Ti precursors (alkoxides, TiCl₄, etc), applied to the substrate by dip-coating and then calcined to form crystalline TiO₂. Qiu and Zheng¹¹³ reported that the adhesion of both sol-gel and thermally-deposited P25 films on hydroxylated glass beads was poor, with ~30% and ~40% of the TiO₂ particle mass, respectively, being removed from the glass beads after 2 hours of fluidization. Qiu and Zheng observed the particle loss to substantially decrease to 11% when the sol-gel was applied to silica beads; the high density of –OH groups on the silica surface allowed the sol-gel to chemically bind to the surface. Fernandez et al.¹⁴⁹ observed good adhesion of a sol-gel coating applied to quartz and glass, though the substrates were planar substrates and not fluidized. The researchers found that the photodegradation rate of malic acid over the quartz-supported TiO₂ to be an order of magnitude greater than that of the glass-supported TiO₂; this difference in performance was attributed to the diffusion of Na⁺ and Si⁴⁺ from the glass into the TiO₂ during calcination, which acted as electron/hole recombination centers. Ma et al¹⁵⁰ deposited TiO₂ on to clean glass, indium tin oxide-coated glass (ITO), and p-type monocrystalline silicon (p-Si) via sol gel coating. It was found that each substrate type not only affected the resulting surface structure, but also the semiconductor behavior of ITO and p-Si altered the performance of the TiO₂. When used for the photocatalytic degradation of Rhodamine B (RhB), the ITO- and p-Si –supported TiO₂ displayed an ~5 times increase in performance over the glass-supported samples as photoelectrons could be transferred from the TiO₂ layer to the ITO and p-Si substrates, thus improving charge separation.

Keshmiri et al.¹¹² saw remarkable improvements in both photocatalytic performance and mechanical strength with the development of TiO₂-composite coatings and self-supporting “bulk bodies”. The composite coatings and bulk samples were prepared by mixing 5 wt% and 15 wt% TiO₂ powder into a sol-gel solution, respectively; the bulk samples were prepared by casting the powder/sol-gel mixture into plastic dishes. Both samples were found to have high surface areas and exhibit photocatalytic activity comparable to that of the free powders. Balasubramanian^{151,152} and Chen^{153–155} applied a similar concept by forming composites of sol-gel solution and P25 powder. Balasubramanian found that the composite coating had excellent adhesion to both glass and steel with high photocatalytic activity compared to sol-gel only coatings; it was found that the sol-gel only coatings lacked porosity and had low surface area, both of which were increased markedly by the addition of the P25. Chen found that composite solutions containing 10-50 g/L P25 exhibited excellent adhesion, porosity and surface area; P25 content beyond 50 g/L resulted in a reduction in the strength of the composite film. Both researchers found that the strength of the composite films increased with increasing calcination temperature, though Chen observed diffusion of ions from the stainless steel substrate at 600 °C, and thus stated 500 °C provided a better balance between strength and performance.

Vega et al.¹⁵⁶ expanded on the composite TiO₂ approach by developing a process to cast the composite solution into spherical, self-supporting particles without the need for any supporting substrate; this approach removed the weak TiO₂-support entirely and displayed excellent attrition resistance. The TiO₂-composite solution was mixed with an acidic chitosan component, which was then dispersed drop-wise from a burette into a basic bath solution; the high pH of the bath caused the chitosan to undergo rapid gelation, encasing the composite solution into spherical particles. The particles were then allowed to dry – during which time they underwent a 90% volume reduction to produce solid TiO₂ spheres ~1 mm in diameter – and then calcined at high temperature (>450 °C). This drying step has an added effect in that any variations in particle diameter during the forming step become largely negligible in the dry particles,

yielding a very uniform size distribution. The resulting particles showed excellent photocatalytic activity and high attrition resistance.

While Vega's self-supported particle design¹⁵⁶ was highly effective in reducing attrition, the surface of the photocatalyst is exposed to the bed and thus the particles experience a constant erosion. The research group of Langford and Kantzas^{71-73,157,158} employed an alternative particle design by supporting a TiO₂ photocatalyst onto a porous glass substrate. The porous network of the particle created a rough, dimpled surface into which the photocatalyst could be placed. The particle design was likened to the dimpled surface of a golf ball, which protected the photocatalyst from ablation, and was found to be very effective in mitigating photocatalyst attrition. Kanki et al.⁶⁵ applied a similar concept with the use of porous ceramic particle, which was again, found to be highly attrition resistant. Both research groups found that the photodegradation performance of the porous particle design was excellent and comparable to that of suspended slurries of P25 powder.

1.2.7 Nanowire Photocatalysts

Nanostructured semiconductor films with one-dimensional (1-D) morphologies such as nanowires offer interesting properties not possible with nanoparticles or planar films¹⁵⁹, especially when the nanowires are oriented to be collinear with the incident light¹⁶⁰. The high aspect ratio morphology of the nanowires is intended to overcome limitations of other designs through several advantages:

- **Improved Charge Carrier Pathways**

As the bulk of the nanowire mass is distributed in the vertical direction, it provides a large depth of material with which to absorb incident photon, while the narrow diameter of the nanowires provides a short pathway for photogenerated charges to pass to the semiconductor-electrolyte interface^{32,161} (Figure 5a). Moreover, as the nanowires tend to be single crystalline along their

length, many of the grain boundaries present in nanoporous films that serve as charge trap/recombination centers are removed, yielding improved charge transport and reduced recombination¹⁶². Indeed, nanowire-structured rutile TiO₂ films have demonstrated electron diffusion coefficients up to 200 times greater than that of nanoporous TiO₂ films¹⁶³.

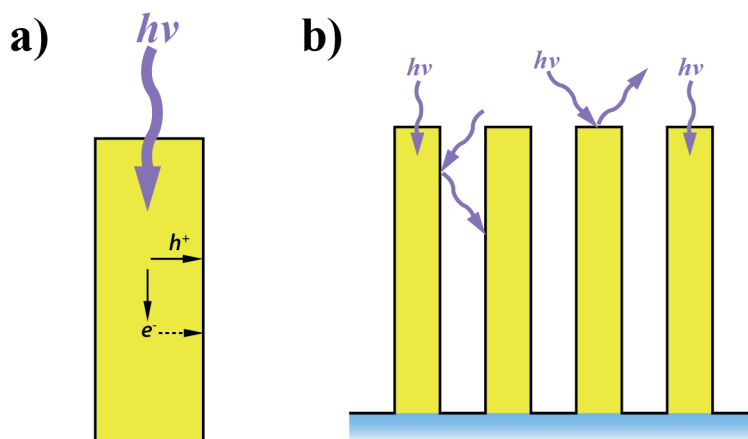


Figure 5: Idealized schematic detailing a) light absorption and charge transport in a nanowire, and b) the improved light scattering and absorption by nanowire films.

- **Improved mass transfer**

As nanowire films are structured longitudinally, the largely straight, open spaces between the nanowires allows for reduced mass transport in the vertical direction¹⁶⁴. In contrast, mass transport resistance in nanoporous films results in reduced reaction rates further into the bulk of the film⁵³; This observation is due to the diffusion of reactants not being rapid enough to scavenge charge carriers and reduce recombination.

- **Improved Light Distribution**

In addition to their vertical alignment allowing maximum photon absorptions, the amount of light reflected from a nanowire-structured surface is significantly reduced (Figure 5b). Photons incident on the nanowire film surface at an oblique angle are scattered into the film rather than

away^{32,161} (as is common with planar films). This aspect of nanowire films has led to their use as anti-reflective coatings⁵⁷.

- **High surface area**

The narrow diameters of the nanorods yield high surface area and, unlike nanoporous films where surface area can be lost due to particle sintering, most of the entire nanorod surface area is in contact with the electrolyte. This not only increases the number of available reaction sites but also allows for charge transfer between the semiconductor and electrolyte to occur at low current densities³². As resistive and overpotential related losses are proportional to the current density, the high surface area/low current density should allow for these losses to be minimized.

Foley et al.¹⁶¹ and Osterloh³² both highlight a common fallacy among researchers, where researchers seek to ‘nanostructure’ a particular material as a ‘magic bullet’ that can convert a low-cost, low-grade semiconductor into behaving like an expensive, high efficient material. While the nanostructuring approach may indeed yield excellent results for some materials, the effort to do so for others may be unfounded, and possibly deleterious, as some of the drawbacks of nanostructures may not be compatible with the given material’s properties. Some of the disadvantages that may arise from nanostructured semiconductors are:

- **Reduced particle diameters**

The diameters of the nanowires may be reduced to a size where they are no longer able to support a space charge, resulting in a lack of an electric field to drive the separation of electrons and holes – in this condition, the nanowires are said to be ‘fully depleted’. Nanowires will be fully depleted if their depletion layer width is greater than the nanorod radius. More specifically, a nanorod is depleted if:

$$2W \geq D_W \quad (6)$$

where D_W is the diameter of the nanowire and W is the depletion layer width. The depletion layer width may be calculated by:

$$W = \left(\frac{2\epsilon_0 V_B}{eN_D} \right)^{1/2} \quad (7)$$

where ϵ_0 is the relative dielectric constant of the semiconductor, V_B is the amount of band bending in the nanowire, e is the unsigned charge of an electron, and N_D is the dopant density ^{165,166} ($\sim 10^{16} - 10^{22} \text{ cm}^{-3}$ for TiO_2 nanowires/nanorods ^{34,58,167}). If a nanowire is in a fully depleted state, the lack of an electric field to separate electrons and holes may yield high rates of recombination. In addition, fully depleted nanowires lack sufficient electron density for electron transport to occur through *drift* and instead transport occurs through slower electron diffusion.

A depleted nanorod may avoid high rates of recombination provided that the effective diffusion length of the charge carriers, L , is much greater than the nanowire radius (i.e., $2L \geq D_W$). This may be understood as, for a given nanowire radius, the rate of diffusion of charge carriers to the semiconductor-electrolyte interface may be sufficient to avoid high rates of recombination. For n-type semiconductors, such as TiO_2 , the diffusion coefficient for holes is less than that of electrons and thus the effective diffuse length of holes is the limiting factor (as $L_n > L_p$). The effective hole diffusion length, L_p , may be calculated by:

$$L_p = \sqrt{D_p \tau_p} = \sqrt{k_B T \mu_p \tau_p} \quad (8)$$

where D_p is the hole diffusion coefficient, τ_p is the hole lifetime, k_B is the Boltzmann constant, T is the absolute temperature, and μ_p is the hole mobility¹⁶⁵. In order to counteract recombination and low band bending (or lack thereof), Foley et al. suggest that when developing nanostructured films, the primary design objective should be to make the magnitude of minority carrier diffusion length greater than the nanowire radius¹⁶¹.

- **Shape Effects**

As an extension of the preceding discussion, the shape of a nanowire may produce some additional effects. As a result of the nanowire growth method, the nanowire may develop a tapered profile – possibly coming to a point at the end. The radius of a tapering nanowire may reduce below the depletion layer width and thus recombination will dominate in this region. Foley et al.¹⁶¹ modeled tapering nanowires and found that a 33% loss in efficiency may result. This matter may be exacerbated when utilizing short wavelength light (such as UV light); as the absorption coefficient for low wavelength photons is expected to be high, the majority of the photons will be absorbed at the tip of the nanowire in the depleted region – thus the efficiency and performance will be severely impacted.

- **Increased Surface Recombination**

Defects at the surface of semiconductors result in the formation of energy levels within the band gap region. These energy levels, known as *surface states*, act to trap both electrons and holes, thus resulting in an increased rate of recombination^{165,168–172}. As the number of surface states increase in proportion to surface area, the high surface area of the nanowires may result in large surface state effects reducing the surface concentration of charge carriers or promoting recombination to such a degree that the photocatalytic activity is severely suppressed or lost. Foley et al.¹⁶¹ note that the effective hole diffusion length, L_p , must be made sufficiently large,

such that depletion layer recombination is no longer the limiting factor, before any attempts at addressing surface state issues are made.

In spite of these potential drawbacks, it has been noted that semiconductors with low charge carrier mobilities will benefit from nanostructuring efforts and, therefore, TiO₂ (having a low intrinsic hole mobility) may be expected to benefit from such a treatment. Indeed, it has been observed in a number of reports that both photocatalytic hydrogen production^{59,173–175} and water remediation^{176–178} were greatly enhanced by the application of nanostructured photocatalysts. It was observed that, even for nanowires suspended in solution (where no benefit arising from the nanowires being collinear with the incident light could be realized), the nanowires evolved hydrogen from a methanol/water solution at a rate ~10 times greater than P25¹⁹. In another report, a suspended slurry of Pt-TiO₂ nanowires (aspect ratio 5.9:1) were found to evolve hydrogen at a rate 1.6 times greater than Pt-TiO₂ nanospheres⁵⁹. In both of the reports, the improved crystallinity and reduced charge transfer resistance were attributed to the increased performance.

1.2.8 Nanorod Growth

One-dimensional nanostructured TiO₂ films have been synthesized via a number of methods^{86,159,179}, however, hydrothermal growth has proven to be the most facile and popular^{167,174,180–188}. Hydrothermal reactions are typically carried out in PTFE-lined steel reactors called hydrothermal vessels (HTV) or autoclaves. The sealed vessel allows for the reactor temperature to be taken beyond the boiling point of water, permitting the ability to carry out reactions at high temperature and pressure.

One of the first hydrothermal methods popularized was the TiO₂ nanotube method described by Kasuga et al.¹⁸⁹. This process involved the treatment of TiO₂ powders in 10M NaOH at 100 °C for 20 hours, followed by washing with HCl. However, this only produced nanotubes in solution. In 2009, Liu and

Aydil¹⁶² presented a hydrothermal growth method that allowed for rutile nanorods to be grown from a substrate surface and has since become one of the most popular and highly cited methods due to its relative simplicity. This method employs a solution containing 30 ml H₂O, 30 ml HCl and 1 ml of titanium tetraisopropoxide (TTIP), a titanium alkoxide. This solution is placed in a hydrothermal vessel along with a suitable substrate, and then heated in an oven at temperatures ranging from 150 °C to 200 °C for up to 24 hours. The resulting nanorods are of high quality and are mostly single crystalline along their length. It is believed that the nanorods grow anisotropically due to the fact that rutile crystals grow fastest in the [001] direction while, at the same time, Cl⁻ ions bind to certain crystal faces and limit diameter growth¹⁹⁰.

Hydrothermal growth of nanowires is seen as promising for growing nanowires from the surface of fluidizable particles as the solution-based method allows even nanorod growth over the entire particle surface, whereas other deposition methods (such as thermal or vacuum methods) are more directional and may be challenged by irregular substrate surfaces. The drawback to Liu and Aydil's method is that the nanorods grow as rutile TiO₂ and not the desired anatase phase. Recent research, however, has demonstrated excellent progress in the development of an anatase nanowire method^{184-186,191}.

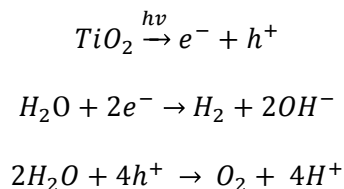
Chapter 2: Photocatalytic Hydrogen Production in a UV-irradiated Fluidized Bed Reactor

2.1 Introduction

Photocatalytic water splitting has long been sought after as a direct solar-to-chemical energy conversion process, with much of the focus on creating a sustainable and emissions-free source of hydrogen.

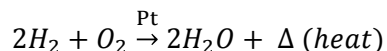
Titanium dioxide (TiO₂) has been one of the most widely researched photocatalyst materials due to its low-cost and high stability when irradiated in solution^{136,137,192}. Though the application of pure TiO₂ is limited due to its wide band gap, thus limiting its use to the ultraviolet spectrum, it remains a popular candidate as a water splitting photocatalyst as the wide band gap provides abundant potential to drive the photocatalytic decomposition of water.

The photocatalytic splitting of water over titanium dioxide under UV irradiation can be described by the simplified reaction mechanism below:



Though the above reaction is possible over pure TiO₂ surfaces, the rate of reaction is severely limited due to a high hydrogen evolution overpotential; however, the hydrogen evolution over potential can be reduced by depositing platinum nanodeposits (34 Å to 2nm)^{22,123} onto the TiO₂ surface, typically at loadings of 0.5 wt% to 1 wt%^{22,42}. While decorating the TiO₂ with platinum allows the hydrogen evolving reaction to proceed, the platinum sites also catalyze the parasitic back reaction of hydrogen and

oxygen to form water and waste heat, thus reducing the overall efficiency of the system. The back reaction is assumed to follow that of combustion of hydrogen and oxygen over platinum:



It has been demonstrated in the literature that platinum loadings beyond 1 wt% decrease the overall rate of hydrogen production^{22,42}; it is suspected that this effect is due to the promotion of the back reaction of hydrogen and oxygen with increasing amounts of platinum on the TiO₂ surface.

Interestingly, while the addition of platinum to the titanium dioxide surface allows the hydrogen evolution reaction to proceed (albeit at low rates), it has been demonstrated in a number of publications that, in pure water, little to no oxygen is detected throughout the course of the experiment^{22,55,80,138,139,192}. The absence of stoichiometric oxygen evolution suggests that parasitic or side reactions, not accounted for in the simplified mechanism presented above, are “trapping” the oxygen and otherwise hindering the reaction. Sayama and Arakawa demonstrated^{133,134} that when photocatalytic water splitting over TiO₂ was carried out in a 2.2M Na₂CO₃ solution, not only was stoichiometric evolution of hydrogen and oxygen observed, but the hydrogen evolution rate increased by nearly 600 times. The researchers hypothesized that this remarkable increase in performance may be due to a carbonate layer forming over the platinum nanodeposits^{133,134}, which reduces the parasitic back reaction of hydrogen and oxygen, or an alternate, more favorable reaction mechanism for water splitting in which carbonate species scavenge holes to prevent the photoadsorption of O₂ and the formation peroxy-titanium species. The true cause of this impressive increase in the rate of hydrogen evolution and appearance of stoichiometric evolution was not determined or explained in full.

Since photocatalytic water splitting over TiO_2 was the first demonstrated by Fujishima and Honda^{77,78}, TiO_2 photocatalysts have typically been deployed as either suspended nanoparticle or as immobilized films. From a reactor design point-of-view, suspended nanoparticle photocatalysts offer good radiation distribution throughout the reaction volume, excellent mass transfer and a high photocatalyst surface area with respect to the reactor volume. In a suspended nanoparticle system, however, the evolved hydrogen and oxygen remain in contact with the platinum-loaded photocatalyst particles for extended periods of time, thus exacerbating the parasitic back reaction. From a system design point-of-view, the inherent issues of nanoparticle photocatalyst handling and the potential environmental impact of nanoparticles¹⁹³ limit the scalability and practicality of suspended nanoparticle systems. Immobilized thin film photocatalysts address some of these design issues in that they offer the practicality of simple photocatalyst handling, and reduce losses to the parasitic back reaction (as the products and platinum-loaded photocatalyst are easily separated). However, immobilized film photocatalysts tend to suffer from poor radiation distribution, limited rates of mass transfer and low photocatalyst surface area (with respect to the reactor volume)⁵⁴; all of which limit the performance and scalability of immobilized film systems. It may be possible to combine the advantages of both approaches, while minimizing their inherent disadvantages, through the use of a fluidized bed reactor.

Fluidized bed reactors operate by suspending particles (larger than the nanoparticles typically employed) throughout the reactor volume by the upward flow of a liquid phase. When used for photocatalytic processes, fluidized bed reactors offer improved mass transfer, excellent radiation distribution, and a photocatalyst surface area-to-volume ratio approaching that of suspended nanoparticle systems⁶²⁻⁶⁴. This approach also yields fast and simple separation of the reaction products from the platinum-loaded photocatalyst particles as the products are carried from the reactor by the fluid flow while the photocatalyst particles are retained in the reactor; the product gases can then be separated from the fluid by downstream separation processes. Fluidized bed reactors are inherently easy to scale, offer various UV

lamp configurations, as well as the possibility of using natural sunlight, thus potentially allowing for a flexible, industrial scale photocatalytic hydrogen production method that can be incorporated into existing processes or be employed as a stand alone system. A more thorough discussion on the theoretical aspects of fluidized bed operation and their relation to the observed rate of hydrogen evolution is presented in Chapter 3.

Fluidization does, however, introduce the issue of mechanical stability, as the photocatalyst particles must be able to withstand particle-to-particle and particle-to-wall collisions. To our knowledge, there have been no other reported attempts of photocatalytic water splitting in fluidized beds by other researchers; however, there have been several endeavors to employ fluidized TiO₂ photocatalysts for both air and water treatment^{62,64–66,71–73,113,156–158,194–198}. Previously reported attempts of producing fluidized photocatalysts employ sol-gel^{62,64,65,113,156,194–196}, slurry dip-coating^{71–73,157,158,197}, or CVD methods^{66,146,147,198} to fix the photocatalyst material onto fluidizable substrates, such as glass beads, though this was often met with limited success. In most instances, the adhesion of the photocatalyst material to the fluidizable supports was not great enough to withstand the rigors of fluidization and significant attrition of the TiO₂ photocatalyst from the fluidizable support material was often observed; in most instances, the photocatalyst material would be ablated from the substrate surface in a short period of time.

From the literature, the critical failure point for supported titanium dioxide films are at the support/TiO₂ film interface, where the TiO₂ film is attached by weak Van der Waals forces, or at fractures and stress points induced by shrinkage during the drying process^{101,112}. One research group attempted to improve the performance of a fluidizable photocatalyst by improving the strength of the TiO₂-substrate interface; by hydroxylating the surface of soda glass beads with a strong NaOH bath such that residual OH⁻ surface groups could chemically bind with a TiO₂ sol-gel¹¹³. While this did achieve an improvement over slurry deposited films, the mechanical strength of the film was still limited and unsuitable for fluidization.

Keshmiri et al.¹¹² developed of a novel TiO₂-TiO₂ composite film where commercially available Degussa P25 nanoparticles were combined with a TiO₂ sol-gel binder. The sol-gel binder caused the P25 nanoparticles to bond to each other, and to a supporting substrate; this resulted in a remarkable improvement in the adhesion of the TiO₂ photocatalyst to the supporting substrate. Vega¹⁵⁶ further developed this TiO₂-TiO₂ composite technique to form self-supported spherical beads of pure TiO₂, which were formed by combining the still wet composite solution with a polymer matrix and cast into spheres by a drop forming technique. By removing the weak TiO₂-support interface entirely, the TiO₂ particles demonstrated dramatically improved attrition resistance and outstanding performance when used for the degradation of model water contaminants in a fluidized bed reactor.

We herein explore the concept of photocatalytic water splitting in a UV-irradiated fluidized bed for the first time. In this research, we present a special designed fluidized bed reactor system and fluidizable, platinum-deposited TiO₂ photocatalyst. This study is intended to develop the fluidized photocatalytic water splitting approach and take steps toward creating an efficient and scalable hydrogen production process.

2.2 Experimental

2.2.1 Reactor and System Design

Pozzo et al.¹⁴⁷ reported previously that an annular fluidized bed with a UV lamp situated in the inner annulus (Figure 6) (as opposed to lamps positioned externally around the periphery of the reactor) will yield the most efficient use of the ultraviolet radiation. As such, a fluidized bed reactor with an inner annulus comprised of a quartz glass tube, containing a low-pressure mercury vapor ultraviolet (UV) lamp (Emperor Aquatics, 50W, 254 nm), and a polycarbonate outer reactor body was employed in these experiments. The photocatalytic reaction zone, formed between the quartz glass tube and the outer

polycarbonate wall, has an inner radius of 1.41 cm, an outer radius of 2.54 cm, and an effective length of 32.76 cm, yielding a total fluidized reactor volume of 0.45 L. The lower inlet portion of the reactor was conically shaped and contained a flow distributor consisting of a packed bed of glass beads (2mm average diameter) supported between two stainless steel mesh sheets; this was necessary in order to avoid jetting and to ensure even fluidization within the reactor. The upper outlet portion of the reactor contains dual outlet ports and was designed such that no gas bubbles can be trapped; this ensures that all product gases are removed from the reactor volume so as to provide accurate measurement of the gas evolution rates.



Figure 6: Photograph of the annular fluidized bed reactor

The fluidized bed reactor formed part of a larger system as shown in Figure 7. The dual outlet ports of the fluidized bed reactor were connected directly to a separator unit (total volume of 0.40 L), which was designed with a headspace for the dissolved hydrogen and oxygen gases to separate from the liquid stream. A gas sparge (fitted with a stainless steel frit) was submerged in the liquid portion of the separator and was used to purge the reaction solution with nitrogen gas before experimental runs (to remove any

dissolved oxygen that would skew results or effect performance). The sparge was also employed as a gas sweep during experiments to continuously carry samples to a gas chromatography system for analysis; an electronic mass flow controller was employed to ensure accuracy. The top of the separator was also fitted with a thermocouple, a digital pressure gauge, a pressure relief valve and a number of auxiliary ports for other measurements, such as liquid sampling. The outlet of the separator was covered by a mesh screen as a precaution to filter any particles that may be eluted from the reactor and prevent them from being carried into the pump (where they would be macerated by the impeller). Technical drawings of both the fluidized bed reactor and separator unit are presented in Appendix B.

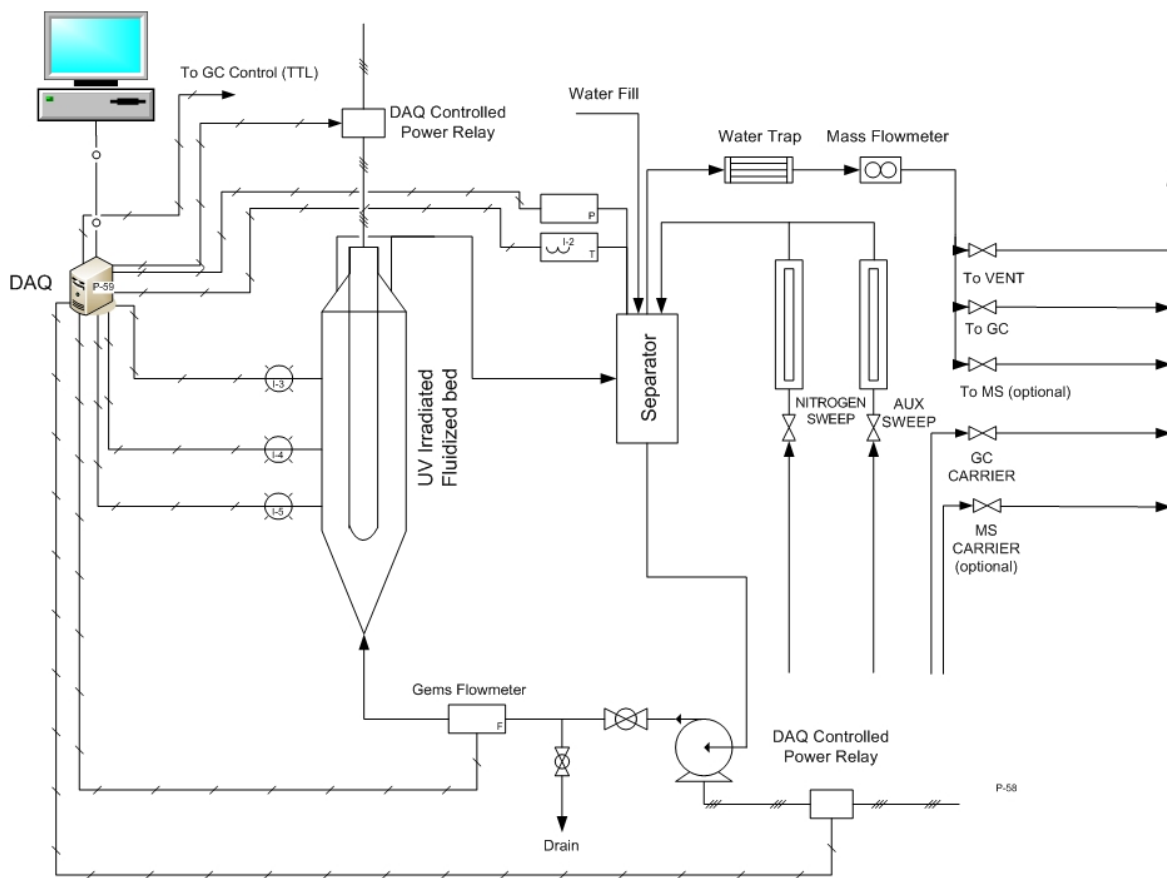


Figure 7: Schematic diagram of the fluidized bed photoreactor system

A PanWorld NH-100PX centrifugal pump was used to circulate a 2.2M aqueous Na_2CO_3 solution through the system at flow rates ranging from 2 L/min to 10 L/min to fluidize the photocatalyst particles. For some experiments, a Gems Sensors FT-110 electronic turbine flow sensor was used to measure the liquid flow rate; the electronic flow meter was not used for all experimental runs as its reliability was affected by sediment from photocatalyst particle attrition and small eluted particles, thus requiring constant repair.

The use of a gas chromatograph is critical to the research as stoichiometric water splitting cannot be assumed; hydrogen/oxygen stoichiometric ratios other than 2 indicate the presence of unwanted processes in the system such as the formation of intermediate species, parasitic side reactions, and system leaks. An Agilent 7890A gas chromatograph (GC) fitted with two thermal conductivity detectors (TCD) was employed in these experiments. The use of dual TCDs, each with separate helium and nitrogen carrier gases, allowed the GC system to be configured to allow lower detection limits and improved measurement accuracy of oxygen and hydrogen (respectively). This configuration also allowed the nitrogen sweep gas from the separator unit to be used as an internal standard; as the nitrogen sweep flow rate could be tightly controlled, it, along with the stream composition, could be used to determine the evolution rates of hydrogen and oxygen. The nitrogen gas flow was measured at the outlet of the GC using a bubble flow meter to ensure accuracy and no system leaks.

A National Instruments USB-6212 Data Acquisition (DAQ) card was used to provide direct control of the GC operation, UV lamp, and centrifugal circulation pump, as well as to record the temperature, flow rate and pressure data. The system control structure and user interface were constructed using National Instruments LabView Version 9.

2.2.2 TiO₂ Sol-gel Composite Preparation

Fluidizable photocatalyst particles were produced via the method first described by Vega et al¹⁵⁶. A TiO₂ sol-gel was first prepared by acid hydrolysis of titanium tetraisopropoxide. Briefly, 6.4 ml of deionized water was added to 96 ml of denatured ethyl alcohol (Fisher, A407-20) in a 500 ml sealable glass jar and stirred for 10 minutes. Hydrochloric acid (Fisher, 37%) (16 ml) was then added and allowed to stir for an additional 10 minutes. To this solution, 120 ml of titanium tetraisopropoxide (TTIP) (Sigma Aldrich, 97%) was added slowly while the solution was stirred vigorously so as to prevent fast gelation and precipitation of the TiO₂. The solution was then stirred at 400 rpm for 2 hours. The resulting sol-gel solution should be clear and pale-yellow in color. Degussa P25 nanoparticles (38 g) were then added to the sol-gel solution and the bottle was sealed so as to prevent the solution from drying on the walls of the jar, which would result in large, solid chunks in the solution. The resulting composite mixture was stirred overnight (approximately 14 to 16 hours).

2.2.3 Chitosan Polymer Solution Preparation

A polymer forming solution (1% w/w) was prepared by adding 3.56 ml of glacial acetic acid (Fisher, 99.7%) to 900 ml of deionized water; 9g Chitosan (Sigma Aldrich, medium molecular weight) was then added while the solution was stirred vigorously. The solution thickens dramatically with the addition of Chitosan and typically requires stirring up to 24 hours for the Chitosan to be completely dissolved. This solution could be stored at room temperature for several months without any change in behavior or performance.

2.2.4 TiO₂ Sphere Formation

The Chitosan polymer solution was first added to a large beaker and stirred vigorously, followed by the addition of the TiO₂ sol-gel-composite solution at a ratio of 1 part to 2 parts Chitosan solution. The

solution was then stirred for 2 hours; the beaker was again covered to prevent the solution from drying on the walls of the beaker and producing large particles in the solution.

TiO₂ spheres were produced by the drop-wise addition of the Chitosan/TiO₂ from a burette into a basic NH₄OH (Fisher, 30%) solution (6:94% v/v NH₄OH/H₂O). Chitosan undergoes fast-gelation on contact with the basic solution, causing the droplets to instantly harden and maintain their spherical shape. The final diameter of the TiO₂ spheres could be widely altered by changing the size of the droplets entering the basic solution. For example, slow drop-wise addition from a burette with an enlarged tip opening can in spheres with a large diameter (1.5-3 mm). To produce smaller TiO₂ spheres (0.5-1.5 mm), the TiO₂-Chitosan solution was released from the burette in a thin, fast flowing stream; Plateau-Rayleigh instability pulled the thin stream into a series of small droplets before coming in contact with the basic solution. Before drying, the large TiO₂ particles had an average diameter of 2.2 mm, while small TiO₂ particles with an average diameter of 1 mm were possible using the fast stream method.

The resulting particles were then dried for several days at room temperature, during which time the diameter reduced dramatically; the dried photocatalyst particles were spherical with an average diameter of 1.1 mm and 0.5 mm, respectively. The photocatalyst particles were then calcined at 500°C for three hours in air. This calcination step causes the amorphous TiO₂ sol-gel to transform to crystalline TiO₂ and serves to burn away the Chitosan polymer used in the forming process. The calcination temperature was chosen to be below the anatase-to-rutile transition temperature of 550°C so as to maintain a high percentage of the anatase phase in the final samples. The calcined photocatalyst particles were pure TiO₂ throughout the entire particle, and were bright white and matte in appearance.

2.2.5 Preconditioning

Following calcination, the photocatalyst particles were preconditioned for 48 hours in a lapidary tumbler (Lortone Model 3A). Though the calcined particles were mechanically strong and attrition resistant, their surfaces contained loose TiO₂ “dust” and fine, easy to remove surface features that would cause the reaction solution to become translucent white; it is imperative to remove these features before depositing platinum on the TiO₂ surface to reduce the number of free nanoparticles in the reactor system and to minimize platinum loss due to attrition. The photocatalyst particles were calcined in air to 500°C for one hour following the precondition process so as to remove contaminants that may have been imparted by the rubber drum of the lapidary tumbler. The photocatalyst particles become glossy in appearance after physical conditioning due to a reduction in surface roughness.

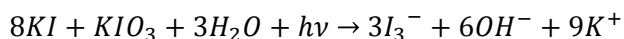
2.2.6 Platinum Deposition

Platinum was deposited into the outer, photoactive region of the photocatalyst particles by a photodeposition method. The photoactive region is the thin outer photocatalyst layer in which photons are absorbed and the charge carrier concentration is great enough to carry out chemical reactions. The calcined and physically conditioned photocatalyst particles were placed into the reaction volume of the UV-irradiated fluidized bed reactor with 1 L of water and a measured amount of chloroplatinic acid hexahydrate (CPA) (Sigma). For the larger 1.1 mm particles, CPA was added to the solution in the amount of 0.0107 grams per gram of photocatalyst particles; while for the 0.5 mm particles, the CPA was added to the solution in the amount of 0.0214 grams per gram of photocatalyst on account of the increased surface area of the smaller particles. These concentrations were employed as they were estimated to yield platinum loadings between 0.5 wt% and 2 wt% in the outer photodeposited layer. The system was then sealed and the solution was circulated through the system at a low flow rate (avoiding fluidization of the particles). The reactor was purged with nitrogen until oxygen was present only in trace amounts. The solution circulation rate was then increased until the photocatalyst particles fluidized to an

expanded bed height of 21.5 cm (bed voidage, $\epsilon \approx 0.78-0.89$). The UV lamp was then turned on for a 3-hour period, during which time the photocatalyst particles darkened to a tan/grey colour. The system was then drained and the photocatalyst particles were then removed from the reactor, washed thoroughly with deionized water, and dried at 100°C overnight. The dried platinum-loaded particles were then placed into a tube furnace under a hydrogen atmosphere (10% H₂ in Ar, 50 cc/min) for 2 hours at 450°C. This additional calcination step in a reducing atmosphere served to ensure that all the platinum was completely reduced to Pt⁰.

2.2.7 Actinometric Measurements

In order to accurately determine the apparent quantum efficiency of the fluidized photocatalytic water splitting system, it was imperative to determine the total radiant power of the low-pressure mercury UV lamp used in the reactor. For ease and simplicity, the iodide-iodate actinometer method¹⁹⁹⁻²⁰¹ was employed. The iodide-iodate actinometer forms triiodide on exposure to UV radiation according to:



The triiodide concentration can then be determined spectrophotometrically, which then allows for the calculation of the photon fluence rate. As this method is optically transparent to wavelengths greater than 330 nm, it is possible to perform actinometric experiments without the need for a darkened room or darkroom safe light. The iodide-iodate actinometric method was, however, designed only to measure wavelengths less than 290 nm; this is not a major concern as low-pressure mercury lamps have a very discreet major emission peak at 254 nm, a minor emission peak at 185 nm, and very minor (mostly undetectable) peaks at 313, 365, 404, 436, 546 nm. The minor emission peaks greater than 390 nm bare no relevance in the performance of the photocatalyst.

The actinometer solution was prepared by first mixing a 0.01M sodium borate (Fisher, 99.5%) buffer solution (pH 9.25), to which potassium iodate (Sigma Aldrich, 99.5%) (in the amount of 0.1M) was added. This solution could be stored for several weeks without any significant change in performance. Immediately before an actinometric measurement, potassium iodide (Sigma Aldrich, 99.5%) was added to the borate-iodate solution in the amount of 0.6M and stirred for 30 minutes. The solution was then placed into the reaction volume of the fluidized bed reactor and the low-pressure mercury UV lamp was turned on for 10 minutes, during which time the solution gradually turned yellow; the lamp was turned on and allowed to reach a stable operating temperature outside of the reactor before the measurement was taken. The solution was then removed from the reactor and stirred in a beaker for an additional 10 minutes. Absorbance measurements were made before and after irradiation using a Cary 100 UV-Vis spectrophotometer. The initial concentration of potassium iodide was determined by the absorption at 300 nm and, by determining the absorbance at 352 nm, it was possible to determine the amount of potassium triiodide formed during the time course of the actinometric measurement. From this it was possible to determine the radiation dose delivered to the actinometric solution during the time course measurement.

2.2.8 Suspended Slurry Baseline Measurement

To provide a baseline performance comparison, a suspended slurry photocatalyst was employed in the reactor system following a procedure similar to that outlined by Sayama and Arakawa^{133,134}. Degussa P25 nanoparticles were suspended in a 2.2M Na₂CO₃ solution at a concentration of 1 g/L (as per Karakitsou and Verykios¹³⁶, and Kiwi and Gratzel²²). Chloroplatinic acid (0.7 wt% Pt to TiO₂) was added to 1L of the solution, which was then sealed in the reactor. The reactor was purged with nitrogen at 100 cc/min overnight until oxygen was at amounts less than 2.5 ppm. The solution was circulated at 7.6 L/min, the nitrogen purge was reduced to 50 cc/min and the UV lamp was turned on. The reaction was then allowed to proceed for up to 200 hours. Gas samples were analyzed at approximately 12-hour intervals.

2.2.9 Experimental Procedure

The 1.1 mm diameter platinum-deposited fluidizable photocatalyst particles were added to the UV fluidized bed in amounts of 60, 80, 100 and 120 grams, and freshly made batches of photocatalyst particles were used for each experimental run. The 0.5 mm photocatalyst particles were used in a separate experiment in the amount of 100 g to demonstrate the effect of particle density and fluidization velocity. The reactor system was then filled with 1 liter of 2.2M Na₂CO₃ in water (pre-heated to 35°C) and sealed. The solution was circulated throughout the reactor system at low flow rates, taking care to avoid fluidization, while purging with nitrogen at 100 cc/min for several hours (until oxygen was detectable to amounts less than 2.5 ppm). The nitrogen flow rate was then decreased to 50 cc/min and the solution circulation flow rate was increased until the bed reached an expanded bed height of 24 cm; the flow rates ranged from 5 L/min to 8 L/min, depending the mass of photocatalyst particles loaded into the reactor. The UV lamp was then turned on and the photocatalytic reaction was allowed to proceed for 24 hours. The GC system was remotely triggered by the USB-6212 DAQ to analyze the composition of the product gas stream from the system at 8-minute intervals. The product gas stream was allowed to vent and was not collected. The system consistently stabilized at a constant temperature of 35°C throughout all experiments.

2.2.10 Characterization

The specific surface area of the photocatalyst particles was measured using the single-point Brunauer-Emmett-Teller (BET) method. The TiO₂ crystal phases present in the photocatalyst particles were characterized by X-ray diffraction (XRD) using a Bruker D2 Phaser desktop X-ray diffractometer using Cu-K α radiation (1.5418 Å). SEM imaging and energy-dispersive X-ray spectroscopy (EDX) were conducted on both the Hitachi S-2600N Variable Pressure Scanning Electron Microscope (VPSEM) and the Hitachi S3000N VP-SEM with EDX. Transmission Electron Microscopy (TEM) imaging was conducted on a FEI Tecnai G2 200kV Transmission Electron Microscope. The photocatalyst samples

were analyzed by dynamic secondary ion mass spectroscopy (D-SIMS) using a Cameca IMS-3f ion microprobe using a positive cesium beam and monitoring various negative secondary ions of interest. The depth scales are approximate and were determined by measuring the sputter rate on a cross-sectioned sample.

2.2.11 Safety Considerations

As hydrogen and oxygen are evolved together from the fluidized bed system, precautions were taken to reduce the risk of explosion. The nitrogen sweep gas flow rate was chosen such that the evolved hydrogen was highly diluted and well below the explosion limit. The product stream was vented into a well-ventilated area. All electronic equipment near the reactor system was grounded to reduce the chance of electric spark.

2.3 Results and Discussion

2.3.1 TiO₂ Photocatalyst Particle Properties

The crystalline phase and crystallite size of the as-synthesized TiO₂ photocatalyst particles were characterized by XRD measurement. The diffraction peaks of the TiO₂ photocatalyst particles shown in Figure 8 were consistent with mixed anatase and rutile phases; no other phases or impurities were observed. The weight fraction of the anatase phase was estimated by the following equation²⁰²:

$$X_A = \frac{1}{1 + 1.26 \frac{I_R}{I_A}} \quad (9)$$

where I_A and I_R are the intensities of the most intense XRD peaks for anatase and rutile, respectively. In Figure 8, I_A and I_R correspond to the intensities of the peaks located at 25.5° and 27.6° respectively. The weight fraction of the anatase phase was calculated to be 84%, with the remainder being entirely rutile. This corresponds well with the expected anatase-to-rutile phase composition of 80:20 for the Degussa P25²⁰³ used in the production of the TiO₂ spheres, and suggests that the TiO₂ sol-gel employed as a

binder in the composite primarily forms anatase particles upon calcination. Though the above equation has become the accepted standard as a reasonable method to estimate the anatase and rutile content of a sample, Ohtani²⁰⁴ cautions that this equation was determined empirically and the coefficient “1.26” will change with the equipment used.

The average crystallite sizes of the TiO₂ nanoparticles was calculated by using Sherrer’s equation²⁰⁵:

$$L = 0.891\lambda/\beta\cos\theta \quad (10)$$

where L, λ , β and θ are the crystallite size, wavelength of the X-ray, corrected full width at half maximum height (FWHM) of the XRD peak, and the angle of diffraction, respectively. The XRD apparatus used in these experiments utilizes Cu-K α radiation (1.5418 Å), and thus the anatase and rutile crystallite sizes were determined to be 19 nm and 75 nm, respectively.

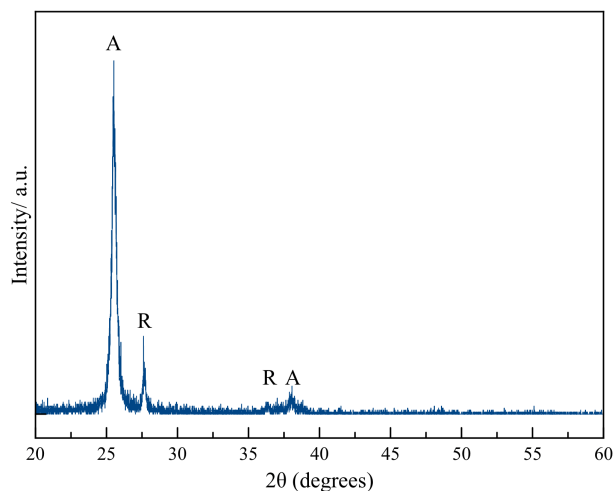


Figure 8: XRD pattern for the TiO₂ photocatalyst particles. The anatase peaks (A) and rutile peaks (R) are as indicated.

The specific surface area of the photocatalysts was determined by BET analysis. The finished particles were measured to have a surface area of 31.4 m²/g. The measured surface area is less than that of the measured 54 m²/g for Degussa P25 as a free powder, indicating a partial reduction of surface area. This is likely due to particle-to-particle necking and sintering due to the sol-gel binder and calcination, respectively, and not crystal growth (which would be expected at calcination temperatures above 550°C).

The mean particle diameter of the calcined photocatalyst particles was found to be 0.5 mm and 1.1 mm, indicating the particles underwent a significant 87.5% volume reduction during the drying process. It was found that the calcined photocatalyst particles have a bulk density of 3500 kg/m³ and a packed bed density of 1200 kg/m³ (thus giving a voidage of 0.34). These physical characteristics place the particles in Geldart class B (sand-like) and D (spoutable)²⁰⁶, and yield estimated minimum fluidization velocities of 0.0018 m/s (~0.15 L/min) and 0.008 m/s (~0.67 L/min) for the 0.5 mm and 1.1 mm particles, respectively.

2.3.2 Surface “Pleating” Effect

While the interior of the photocatalyst particles is pure TiO₂ and without any remarkable features or defects, SEM imaging of the particle exterior revealed a unique, pleated surface around the equator of all particles (Figure 9). This pleating effect is a result of the manufacturing process and is consistent with Vega’s observations¹⁵⁶. The force of the droplets impacting the surface of the basic solution while the chitosan polymer matrix is gelling (during the particle forming process) causes the resulting particles to be more ellipsoidal in shape. As the particles undergo their significant volume change during the drying process, internal stresses pull the particles into a more spherical shape. This causes the excess of material around the equator of the particles to pleat. An interesting feature to note in Figure 9 is the circular indentation on the top of the photocatalyst particles. This feature is induced by the by the backjet, the

column of liquid that shoots upward when the droplet of sol-gel composite solution enters the basic solution in the forming process.



Figure 9: SEM image of a self-supported photocatalyst particle displaying the “pleating” effect

In Figure 10, the pleats and fine surface features can be seen in greater detail. The pleats are surprisingly consistent around the entire equator of the particle and are on average 15 μm across (taken from trough to trough) and approximately 300 μm in length. Despite the pleated surface features, the particles do not show any cracks or defects resulting from the manufacturing process.

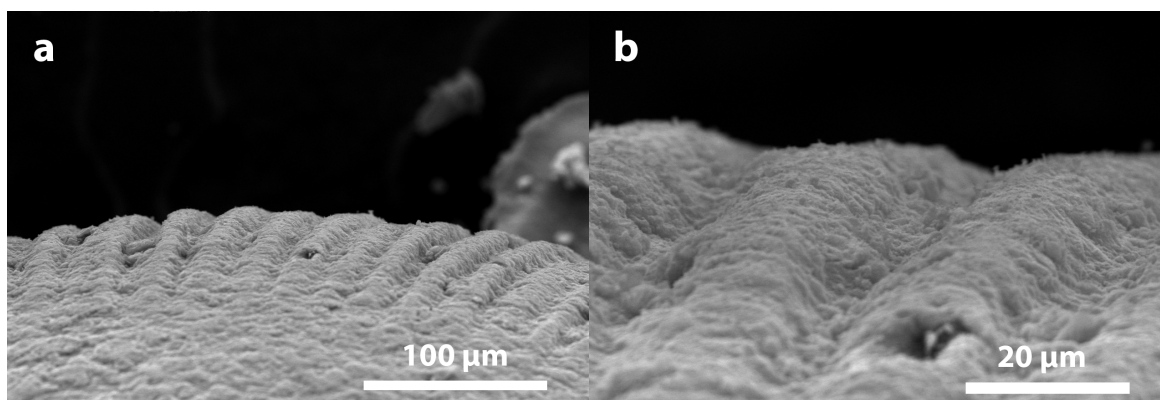


Figure 10: a) Detail and b) high- magnification views of the surface pleats

2.3.3 Particle Attrition

Though the TiO₂ composite particles greatly improve the mechanical strength of the photocatalyst particles, attrition is not eliminated entirely. The initial attrition rate of freshly calcined particles was observed to be high, which was suspected to be due to easy-to-ablate fine surface features being removed in the initial stages of use. A sample of 120 g of the TiO₂ photocatalyst particles were placed in the rubber drum of a lapidary tumbler for 1 hour, after which time they were washed and dried; the physically conditioned particles were then observed with SEM analysis (Figure 11). It was found that the fine features exposed to particle-to-particle contact, such as the surface roughness seen on both the smooth and pleated surfaces of the particle in Figure 10, had been removed quickly, resulting in a smooth outer surface.

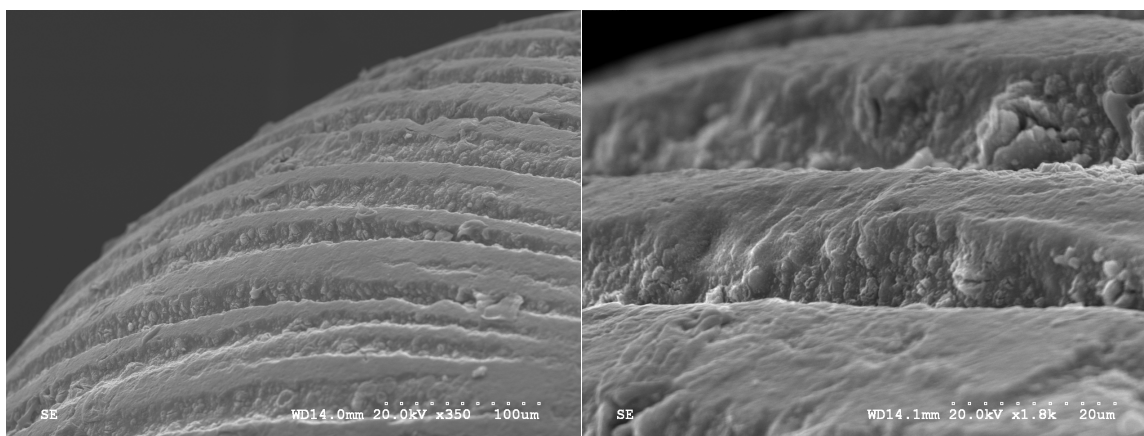


Figure 11: SEM image displaying the pleats of a self-supported photocatalyst particle following 1 hour of conditioning

The most notable areas of attrition were observed on the aforementioned surface pleats. As seen in Figure 11, 1 hour of physical conditioning resulted in the crests of the pleats being ablated away, leaving the pleats with a truncated appearance. Fine surface features can still be seen in the troughs between the pleats as they are protected from direct contact. After several hours of physical conditioning the pleats had largely eroded away, leaving the particles with a flat, polished surface and a spherical appearance

around the entire surface: i.e., only minor striations could be seen where the pleats once stood. Indeed, the appearance of the particles to the naked eye changed from a matte surface to a highly polished, glossy finish through the time course of the physical conditioning. The observed attrition of the physically conditioned particles was markedly reduced when compared to that of freshly calcined particles.

These results underscore the importance of physically pre-conditioning the photocatalyst particles before any use - either in the fluidized bed reactor or in platinum deposition. It is not only important to minimize attrition before use so as to minimize the effects of free photocatalyst particles suspended in the reaction solution during experimental runs, but to also prevent the loss of the critical and expensive platinum deposits. As a precaution, all photocatalyst particles were preconditioned in the lapidary tumbler for 48 hours prior to platinum deposition and use in the fluidized bed reactor.

2.3.4 Platinum Deposition

During the platinum photodeposition process, the color of the photocatalyst particles changed from their natural bright white to a light yellow-brown. Once the photocatalyst particles had been subjected to the final H₂-reduction step in the tube furnace, their color changed to a dark grey, suggesting the platinum particles had indeed been reduced to Pt⁰. Bisection of the photocatalyst particles revealed that the inner core of the particles remained the natural bright white of TiO₂, and that only the outer surface layer of the particles displayed the characteristic grey color of the Pt-deposited TiO₂.

In order to determine the concentration of platinum on the TiO₂ surface, both XRD and EDX analyses were first employed; however, neither method could detect Pt on the TiO₂ surface. The presence of platinum was later confirmed by XPS analysis; however, the results were not consistent enough to provide a reliable estimate of the Pt surface concentration. TEM imaging was used in an attempt to

identify platinum particles deposited on the TiO₂ particles; however, despite extensive work with the TEM equipment, no platinum deposits could be identified.

To reduce the amount of platinum-free TiO₂ from the inner core being incorporated into the samples, sections of the Pt-deposited layer were bisected from the photocatalyst particle using a fine surgeon's blade and were subsequently ground with a fine agate mortar and pestle to prepare samples for TEM; however, the high strength of the photocatalyst particles caused them to fracture into large pieces still containing a large portion of the platinum-free inner core of the particles, and it was, again, impossible to identify platinum deposits. It is suspected that either, once the photocatalyst particles had been ground to prepare samples for TEM, the concentration of Pt-deposited TiO₂ particles became too low due to the Pt-deposited layer being mixed with the platinum-free inner core of the particle, or that the platinum deposits were smaller than the resolution of the TEM equipment. It is suspected that the latter may be probable as some sources^{123,207,208} suggest that the platinum deposits may be 2 nm or less in size; this is below the 5 nm resolution limit of the TEM equipment used.

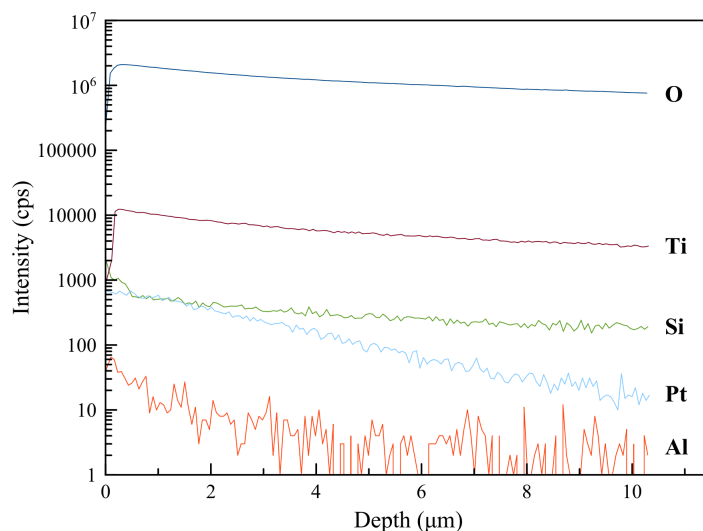


Figure 12: Depth profiles of Ti, O and Pt (along with the observed Si and Al impurities) as a function of sputter depth for the 0.5 mm particles

In order to better understand how Pt deposited throughout the three-dimensional TiO₂ structure, the depth profile of the particles was analyzed using dynamic secondary ion mass spectroscopy (D-SIMS). Due to the tendency of the photocatalyst particles to charge during analysis, the ion beam would often deflect away from the target area, thus resulting in a glancing blow through the side of the particle rather than achieving a bore straight down into the bulk of the particle; the smaller 0.5 mm particles demonstrated less charging behavior and were thus easier to analyze. The D-SIMS depth profile results (shown in Figure 12), clearly demonstrates the presence of platinum incorporated into the TiO₂ matrix. Interestingly, both silicon and aluminum were detected in the sample as impurities (for which the source could not be identified); the signal intensities for both oxygen and titanium, however, did not vary with fluctuations in either the silicon or aluminum signal intensities, suggesting that the impurities are dilute.

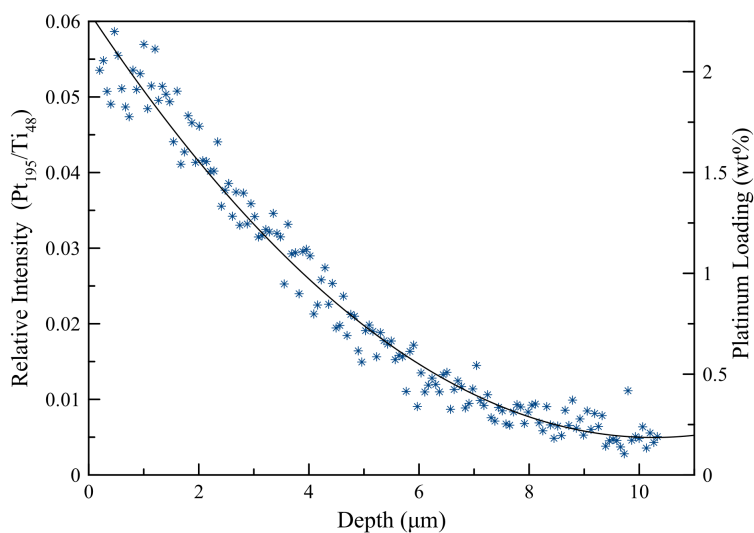


Figure 13: Relative Intensity ratio of Pt₁₉₅/Ti₄₈ as a function of sputter depth for the 0.5 mm particles

The relative intensity ratio of the platinum to titanium signals can be used as a reference for the platinum concentration through the photocatalyst bulk. As seen in Figure 13 below, the relative intensity ratio, and thus the Pt concentration, decays in an exponential manner with increasing depth into the TiO₂ bulk. While it was not possible to achieve reliable measurements of the Pt concentration at the outer TiO₂ surface, it is possible to approximate the Pt loading. If it is assumed that all platinum present in solution

was deposited onto the TiO₂ photocatalyst particles (as no residual Pt could be detected through ICP-MS measurement), we can calculate the effective Pt loading at the outer surface and average loading in the photodeposited layer by integrating the relative intensity ratio over the sputter depth. The Pt concentration at the outer photocatalyst surface was estimated to be 2.27wt% and 2.22wt% and the average Pt loading in the photodeposited layer to be 0.88wt% and 0.86wt% for the 0.5 mm and 1.1 mm photocatalyst particles, respectively.

From Figure 13 above, it is possible to estimate the effective diffusion length for photoexcited electrons through the bulk TiO₂. The probability that an electron will be captured by either a recombination process or through a reaction with a H₂PtCl₆ molecule during photodeposition, p , at a given distance, x , from the photon absorption site (i.e., the outer particle surface) can be written as²⁰⁹⁻²¹¹:

$$p(x) = e^{-\frac{x}{L_n}} \quad (11)$$

where the effective electron diffusion length, L_n , may be estimated by the conduction band electron diffusion coefficient, D_0 , and the conduction band electron lifetime, τ_e :

$$L_n = (D_0\tau_e)^{1/2} \quad (12)$$

If it is assumed that Pt will only deposit as deep into the TiO₂ bulk as electrons can diffuse from the photon absorption sites at the outer particle surface, and that the local platinum concentration is approximately proportional to the probability of electron capture/reaction, the data shown in Figure 13 can be fitted to an exponential function having the form shown in equation 11. The effective electron diffusion length is estimated to be 3.7 μm and it can be seen that the Pt concentration approaches

negligible levels near a depth of 10 μm . Leng et al.²¹¹ observed that, in a photoelectrochemical water splitting experiment, the effective electron diffusion length into a TiO_2 film was approximately 10 μm and that the effective diffusion length varied only slightly with an applied bias potential. The effective electron diffusion length estimated in this work is expected to be less than that observed by Leng et al.²¹¹ as Pt deposits and surface reactions with H_2PtCl_6 molecules act to capture electrons, thus limiting their effective electron diffusion length. It should be noted that the above approach assumes that the structure and porosity of the particles does not vary significantly with depth, and that the particles are porous enough such that the diffusion resistance of Pt ions into the TiO_2 bulk is small. High mass transfer resistances or variations in the pore structure with depth could result in the majority of the platinum depositing near the outer surface of the particles, thus making the effective diffusion length appear smaller than its true value, or causing the platinum depth profile to deviate significantly from the expected exponential curve shape and making curve fitting unreliable.

2.3.5 Baseline Slurry Photocatalyst Performance

Figure 14a below shows the time dependence of hydrogen and oxygen evolution from a 2.2M Na_2CO_3 solution containing platinized P25 nanoparticles (1 g/L); the solution was circulated through the reactor system at a flow rate of approximately 7.6 L/min. It was observed that the rate of hydrogen evolution increased steadily over 200 hours, eventually reaching a steady-state rate of 204 $\mu\text{mol/hr}$ after 215 hours of operation; this is in agreement with observations by Sayama and Arakawa^{133,134}, where the rate of gas evolution increased steadily during operation and reached a maximum steady state rate after approximately 198 hours of operation.

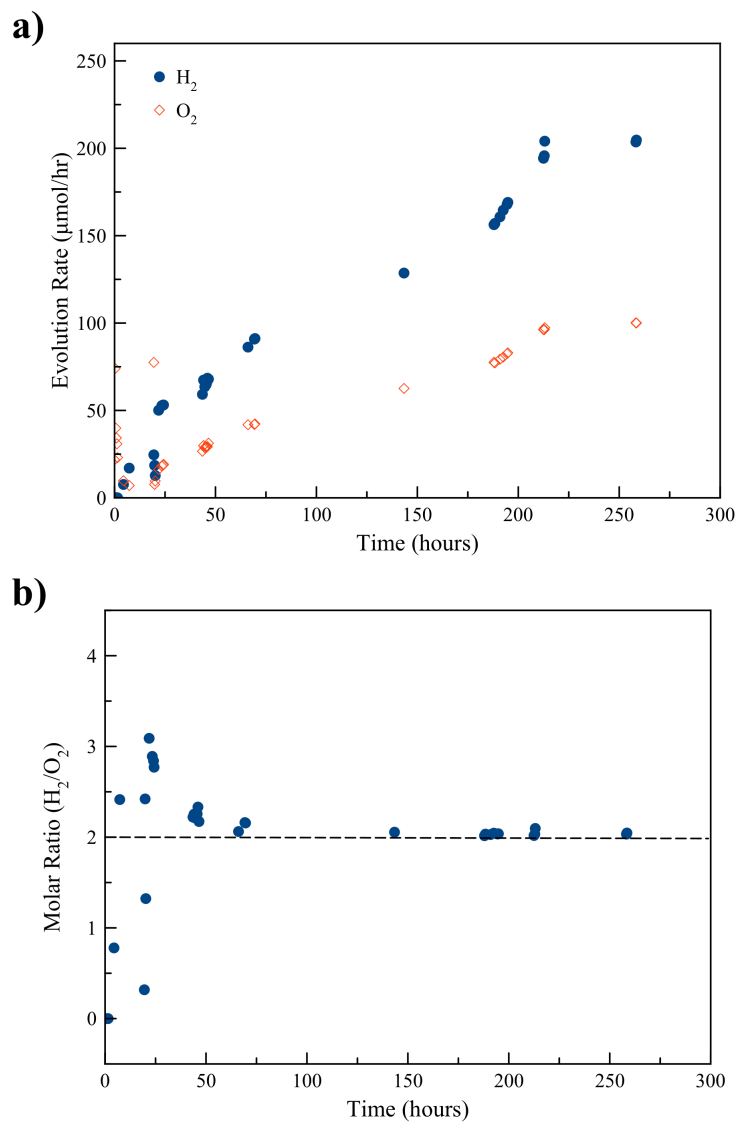


Figure 14: Photocatalytic water splitting performance for P25 nanoparticles suspended in Solution. a) The gas evolution rates for hydrogen and oxygen, and b) the stoichiometric ratio of hydrogen to oxygen are shown with respect to time. The P25 nanoparticles (containing 0.7wt% Pt) were suspended in a 2.2M aqueous Na₂CO₃ solution at a concentration of 1 g/L.

It should be noted that the maximum rate of hydrogen evolution over suspended P25 nanoparticles observed by Sayama and Arakawa (568 μmol/hr) is 2.8 times greater than the maximum observed in this study – this is due to several notable differences between the two reactor systems which prevent direct comparison of the evolution rates. First, Sayama and Arakawa utilized a 400W high-pressure Hg lamp, which has a higher radiant flux in the ultraviolet region than the lamp employed for this study. Second,

unlike the reactor employed by Sayama and Arakawa, where the entire reactor volume was irradiated, the reactor system used in this study had an irradiated reactor volume of 0.45L and a total solution volume of 1L. As such, 55% of the Pt-deposited P25 particles were contained in “dark” (non-irradiated) regions of the reactor system (i.e., the separator, recirculation pump and piping) and were serving to only promote the back-reaction. Finally, our reactor was operated continuously at a pressure of 1 psig. In contrast, the reactor in Sayama and Arakawa’s study was operated in batch-mode under vacuum pressures as they had observed that the rate of evolution was greatly affected by the reactor pressure. Sayama and Arakawa correctly conclude that the reactor pressure affects the rate of mass-transfer of the evolved hydrogen and oxygen from the liquid to gas phase.

As seen in Figure 14b, hydrogen and oxygen are evolved at a molar ratio of 2 for much of the time-course of the experiment. It should be noted that during the initial hours of the experiment, the H₂/O₂ ratio exceeded the expected stoichiometric ratio and decreased with time, eventually settling to a value of 2 and remaining steady after 50 hours of operation. This effect is discussed further in section 2.3.8.

2.3.6 Typical Fluidized Photocatalyst Performance

Figure 15a shows the time dependence of hydrogen and oxygen evolution from a 2.2M Na₂CO₃ solution containing 80 g of 1.1 mm diameter photocatalyst particles and is representative of the typical time course for all experiments employing the 1.1 mm TiO₂ particles. For all experiments, it was observed that the hydrogen and oxygen evolution rates would increase steadily up to a steady-state rate and would remain constant throughout the remaining time of the experiment. In all experiments, the system reached a constant rate of hydrogen output within a relatively short period of time (5 to 15 hours). However, the suspended slurry photocatalyst presented above required more than 200 hours of operation before a steady rate of hydrogen evolution was observed; a similar result was observed by Sayama and Arakawa^{133,134} who reported that a steady state was not achieved until ~70 hours of illumination.

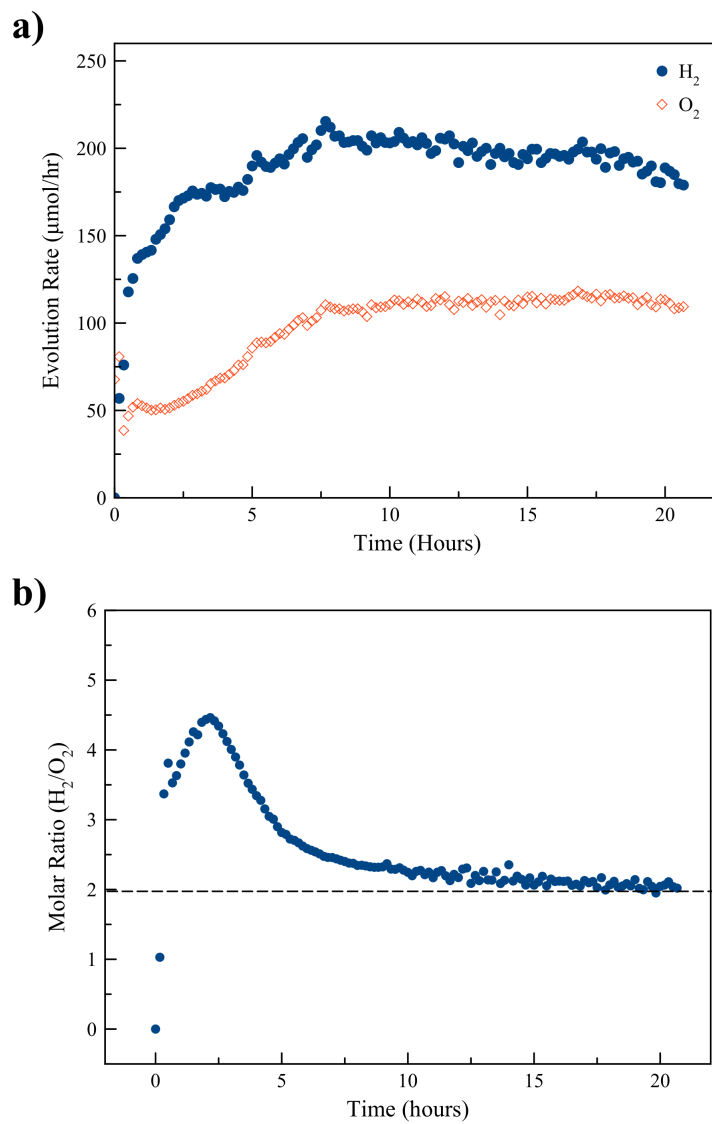


Figure 15: Photocatalytic water splitting performance for 80g of 1.1 mm diameter fluidizable photocatalyst particles. a) The gas evolution rates for hydrogen and oxygen, and b) the stoichiometric ratio of hydrogen to oxygen are shown with respect to time. The particles were fluidized in a 2.2M aqueous Na_2CO_3 solution.

It was also observed in this study that, despite extensive nitrogen purging of the reactor system and the Na_2CO_3 solution, some excess oxygen could be detected during the initial 30-40 minutes of the experiments, which could be seen as large fluctuations in the rate of O_2 evolution. It was determined that the fluctuations in the rate of O_2 evolution were a result of remaining air bubbles trapped in the reactor system being freed as the circulation flow rate was increased to fluidize the photocatalyst particles; no

escaping air bubbles were observed beyond 1 hour of operation. Near stoichiometric H₂ and O₂ evolution were observed in all experiments during steady-state operation; however, in all experiments it was observed that the ratio of hydrogen to oxygen evolution greatly exceeded the expected stoichiometric ratio of 2. As seen in Figure 15b, the molar ratio of hydrogen to oxygen evolution is seen to reach a maximum after 2.5 hours, eventually settling to the expected stoichiometric ratio of 2 after 10 hours of operation. This effect will be discussed further below.

Table 2: Reactor conditions, H₂ evolution rates and Apparent Quantum Efficiencies for various fluidized photocatalyst mass loadings^a.

	1.1 mm TiO ₂ particles				P25 ^b
	60g	80g	100g	120g	1 g/L
Static bed height (cm)	3.6	4.8	6.0	7.2	(-)
Expanded Bed height (cm)	24	24	24	20.0	(-)
Bed Expansion (-)	6.7	5.0	4.0	2.8	(-)
Irradiated Bed Volume (cm ³)	0.30	0.30	0.30	0.21	0.45
Circulation low rate (L min ⁻¹)	8.4	7.6	6.9	5.4	7.6
Approx. # of particles	25,600	32,800	41,000	49,200	(-)
Steady-state H₂ rate (μmol hr ⁻¹)	211	211	202	130	204
H₂ Rate per Irradiated Volume (μmol hr ⁻¹ L ⁻¹)	703	703	672	616	453
Specific H₂ Rate (μmol hr ⁻¹ g ⁻¹)	3.52	2.64	2.02	1.09	204
Apparent Quantum Efficiency	1.33%	1.33%	1.27%	1.16%	0.92%
Steady State Stoichiometric ratio	2.08	2.01	1.96	2.06	2.06

^a 2.2M Na₂CO₃ solution

^b Degussa P25 nanoparticles (containing 0.7 wt% Pt) suspended in 2.2M Na₂CO₃ solution at a rate of 1 g/L

Table 2 shows the reactor conditions, the steady-state hydrogen evolution rates, and the measured hydrogen-to-oxygen molar ratio at steady state for various mass loadings of the 1.1 mm diameter TiO₂ particles in the fluidized bed reactor. The results of the P25 slurry baseline experiment presented in section 2.3.5 are also shown in Table 2 for comparison purposes. For all of the fluidized bed experiments, the photocatalyst particles were fluidized to an expanded bed height of 24 cm, except for experiments utilizing 120 g of photocatalyst particles. The expanded bed height was highly sensitive to slight

fluctuations in the recirculation flow rate at a mass loading of 120 g, with slight increases in flow rate causing the bed to expand dramatically (often to the point where particles would elute from the reactor), thus it was not possible to achieve a stable bed height at 24 cm. By decreasing the flow rate slightly, the expanded bed height settled to a stable bed height of 18 cm and was less sensitive to fluctuations in the recirculation flow rate.

To accurately compare the hydrogen evolution rates for the different photocatalyst types (fluidized versus suspended slurry) it is necessary to normalize the evolution rates based on the irradiated reaction volume (Table 2) because the H₂ evolution rate varies with the total rate of photons entering the reaction volume. Suspended slurry photocatalysts employ the entire reactor volume (and thus cover the full length of the UV lamp), while only a portion of the total reactor volume and lamp length is employed for the fluidized photocatalyst experiments. Moreover, the irradiated volume of a fluidized bed varies with the expanded bed height. It was determined that the lamp irradiance was approximately constant along the length of the lamp and thus it was assumed that the amount of incident UV light entering the reactor volume varied linearly with the irradiated reactor volume. For all fluidized photocatalyst mass loadings, the fluidized particles exhibited a higher rate of hydrogen production per irradiated reactor volume than the suspended slurry photocatalyst, with photocatalyst loadings of 60 g and 80 g exhibiting a 55% increase over that of the suspended P25 photocatalyst particles. It is hypothesized that the increased rate of hydrogen evolution per reactor volume for the fluidized photocatalyst particles (as seen in Figure 16a) is due to the evolved hydrogen and oxygen being quickly separated from the platinum-loaded photocatalyst particles. In contrast, suspended P25 particles were dispersed throughout the entire reactor system, thus P25 particles in non-irradiated regions of the system served only to promote the back reaction of hydrogen and oxygen. This effect is similar to that of increasing the platinum loading on suspended TiO₂ nanoparticles reported in literature^{22,123,136}, where increasing the platinum loading beyond an optimal amount resulted in an increase in the rate of the back reaction and a decrease in the observed rate of hydrogen evolution.

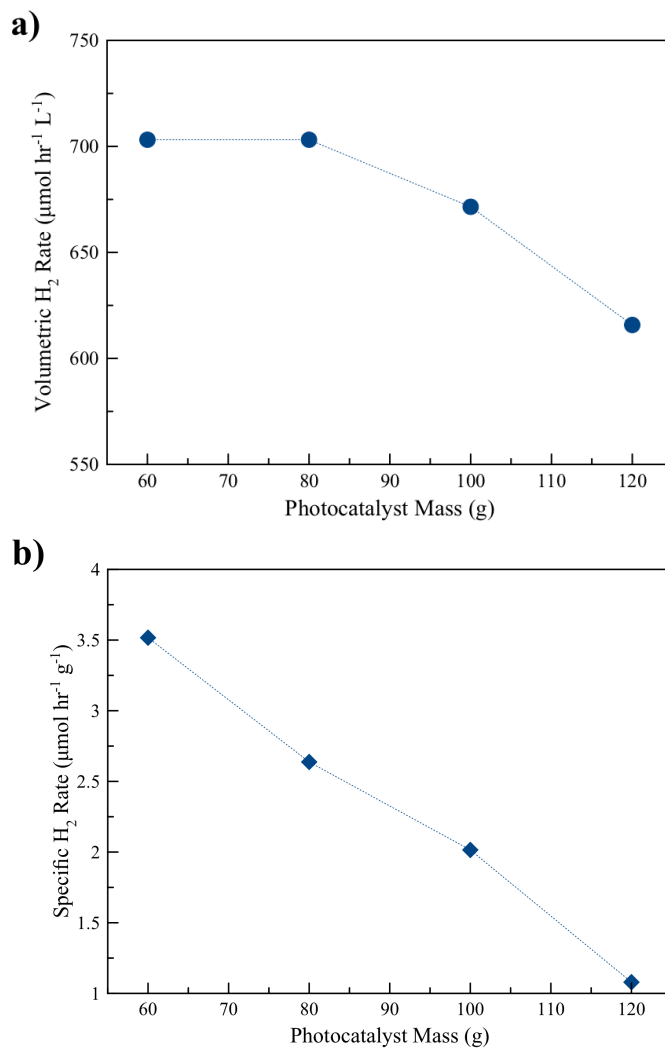


Figure 16: The a) volumetric, and b) specific rates of hydrogen evolution with respect to the mass of photocatalyst particles fluidized in the reactor.

From Figure 16a it can be seen that the rate of hydrogen evolution per irradiated volume decreased for fluidized photocatalyst particle loadings beyond 80 g. Similarly, when the rate of hydrogen evolution is normalized with respect to the mass of fluidized photocatalyst particles (Figure 16b), there is a near linear decrease in the specific rate of hydrogen evolution with increasing photocatalyst mass loadings. It is suspected that the reduction in performance when increasing the photocatalyst loading beyond 80 grams is due, in part, to the increase in bed density. As the bed density increases, the photocatalyst particles near the outer wall of the reactor receive less light and serve only to promote the parasitic back reaction. Other

factors, as discussed later, may also contribute to this observed decrease with increasing photocatalyst mass. It is important to note that the fluidized and suspended slurry photocatalysts cannot be accurately compared on a per weight basis as ~95% of the fluidized photocatalyst particle mass resides within the core of the particle and does not participate in the reaction.

The performance of the fluidized and suspended slurry photocatalysts are best compared through the apparent quantum efficiency (AQE), which is defined as:

$$\Phi_{app} = \frac{2R_{net}}{P_i} \times 100\% \quad (13)$$

where R_{net} and P_i are the net rate of hydrogen evolution measured leaving the separator and the total rate of photons entering the reaction volume, respectively. As discussed previously, the reaction volume for the suspended photocatalyst slurry is that of the entire reactor, whereas for the fluidized photocatalyst particles it is the volume defined by the expanded bed. It was observed that for all fluidized experiments, the apparent quantum efficiency was greater than that observed for the suspended P25 photocatalyst particles. When the AQE for the suspended P25 particles is compared to that observed when 80 g of the 1.1 mm TiO_2 photocatalyst particles are fluidized in the reactor (which employed the same circulation flow rate), it can be seen that the fluidized photocatalyst particles display a 44% increase in the AQE. This effect is, again, likely due to the fluidized particles remaining in the fluidized bed reactor and being quickly separated from the reaction products, thus limiting the extent of the back reaction over the platinum deposits on the photocatalyst particles; whereas, the suspended photocatalyst particles are distributed throughout the reactor volume and exacerbate the parasitic back reaction. This observation demonstrates the importance of minimizing regions of non-irradiated photocatalyst particles, be it

suspended nanoparticles, fluidized photocatalysts or otherwise, when designing and scaling photocatalytic hydrogen production systems that employ platinum as a co-catalyst.

2.3.7 Effect of Na_2CO_3

To observe the effect of Na_2CO_3 on the water splitting performance of the fluidizable photocatalyst particles, 60 g of the photocatalyst particles were first loaded into the reactor and fluidized to an expanded bed height of 24 cm using deionized water only. As seen in Figure 17, the rate of hydrogen evolution rapidly rose to a maximum and then decayed continually with time; if left for an extended period of time, the system would trend toward a pseudo-steady state rate. Negligible oxygen evolution was observed throughout the experiment. This observation is consistent with that of a number of published results that attempt photocatalytic hydrogen production in water (without sacrificial reagents) ^{19,22,55,136,138,192,212,213}.

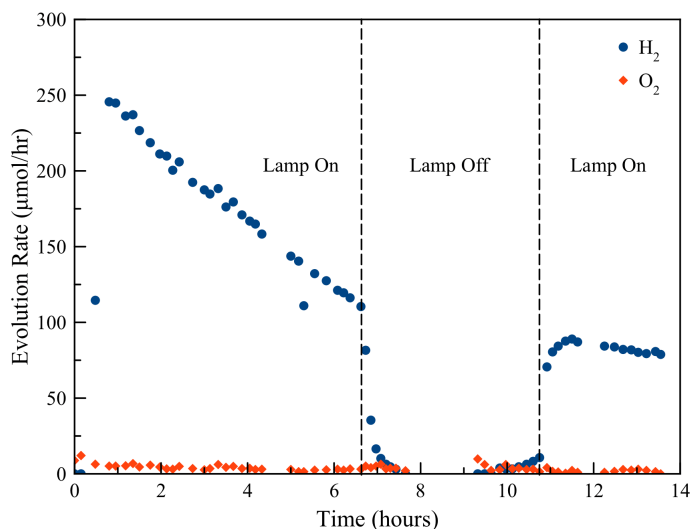


Figure 17: The rate of hydrogen and oxygen evolution over time for 60g of 1.1 mm diameter photocatalyst fluidized in deionized water only. The light was turned on and off to determine whether the photocatalyst deactivation was a photo-induced effect.

In order to ascertain whether the decay in the hydrogen evolution rate with time was a photo-induced effect on the photocatalyst surface, the lamp was shut off for a period of 4 hours while the photocatalyst remained fluidized and the solution was continuously purged with nitrogen. It can be seen in Figure 17

that, when the lamp was turned back on, the hydrogen evolution rate quickly rose back to nearly the same rate before the lamp was turned off and the decay in performance continued in the same fashion.

Furthermore, it was found that the lamp could be shut off at any point during the experiment and the rate would return near to its previous value once the lamp was powered on again, regardless of the amount of time it was off for. These results suggest that the photocatalyst deactivation process is likely a photo-induced effect whose extent is dependent on the cumulative exposure to UV irradiation.

Abe et al.¹³⁹ demonstrated that suspended TiO₂ nanoparticles exhibited a continual decay in the rate of H₂ evolution in combination with an absence of O₂ evolution, and, that after the photocatalyst particles had been irradiated in pure water for 600 hours, they were completely deactivated and could not evolve hydrogen. After further investigation of their deactivated photocatalyst particles, Abe et al. described a shift in the crystalline structure of the TiO₂ when compared to that of fresh photocatalyst particles (as determined by XRD) and the valence state of 35% of the Ti atoms (calculated) had changed from Ti⁴⁺ to Ti⁵⁺ (as measured by XPS analysis). It was postulated that the TiO₂ itself was acting as an electron donor, which led to the formation of a stable (yet photocatalytically inactive) (Ti₂O₅)(TiO₂)₂ mixed-valence structure.

It has also been demonstrated in the literature that oxygen photo-adsorption and peroxy-species formation both readily occur on the surface of TiO₂ under UV irradiation in the presence of water^{139-142,170,214-217} and may account for the absence of O₂ evolution during photocatalytic water splitting. In addition, it has been demonstrated in nearly all reports of hydrogen peroxide generation on TiO₂ surfaces that the formed peroxy-species are not detected in solution, suggesting that the peroxides do not readily desorb from the TiO₂ surface¹⁴⁰⁻¹⁴² and even remain chemically bound to the TiO₂ surface long after the light source has been removed. Harbour et al.¹⁴¹ observed that titanium dioxide nanoparticles were capable of containing over twenty-two chemisorbed H₂O₂ molecules per square nanometer of photocatalyst surface area, which,

for high surface area TiO_2 photocatalysts regularly employed in literature and this work, represents a significant capacity for adsorbed peroxides. The photo-induced deactivation of TiO_2 photocatalyst particles and simultaneous absence of O_2 evolution observed in Figure 17 may be ascribed to either, or a combination of, the two mechanisms described above.

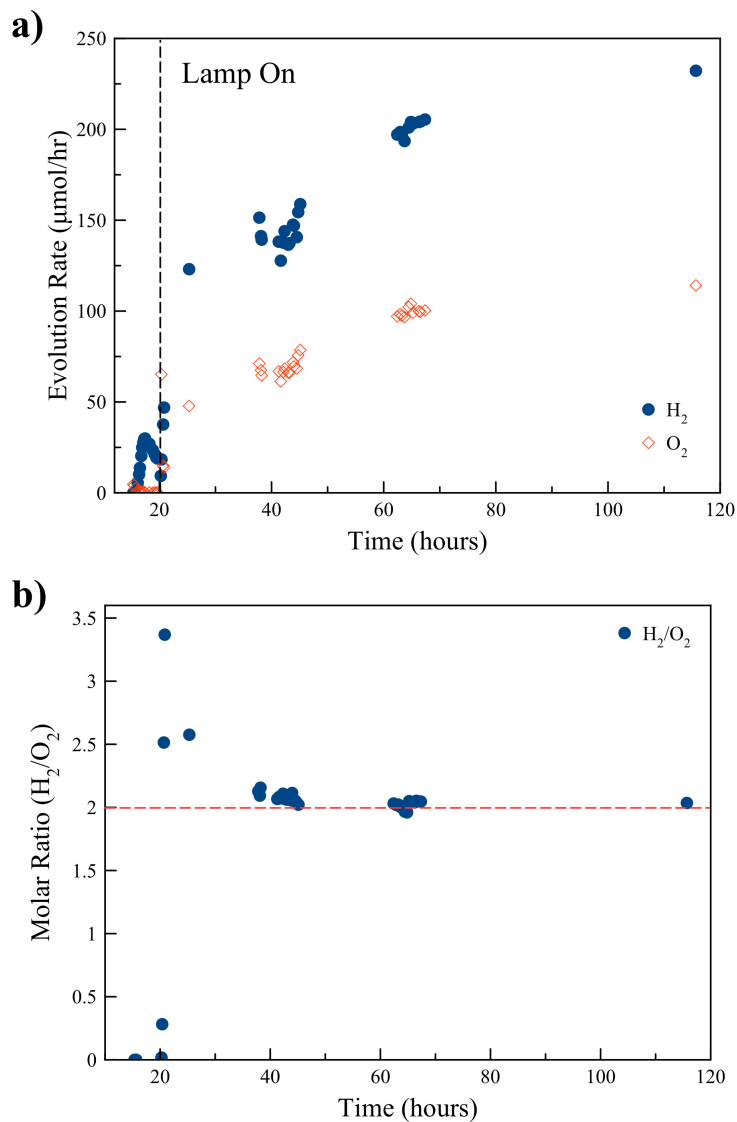


Figure 18: a) The rate of hydrogen and oxygen evolution over time for the same 60 g sample of photocatalyst shown in Figure 17 after dissolving Na_2CO_3 into the solution at a concentration of 2.2M, b) the stoichiometric ratio of hydrogen to oxygen are shown with respect to time.

During the same experiment employing 60 g of the 1.1 mm photocatalyst particles fluidized in deionized water described above, the lamp was shut off after 14 hours of operation and Na_2CO_3 was added to the separator and subsequently allowed to dissolve and mix; the resulting Na_2CO_3 concentration was 2.2M. The reactor was purged continuously during this time to remove any oxygen that was introduced into the system during the addition of Na_2CO_3 . It was observed that a small amount of hydrogen was evolved from the solution following the addition of Na_2CO_3 . The UV lamp was restarted beginning at 20 hours and the liquid-phase flow rate was adjusted slightly to maintain an expanded bed height of 24 cm (adjustment was necessary to compensate for the increased fluid density following the addition of Na_2CO_3); hydrogen and oxygen began to steadily evolve.

As seen in Figure 18a, the rate of gas evolution steadily recovered over the course of 50 hours to reach a pseudo-steady state rate of hydrogen evolution of 203 $\mu\text{mol/hr}$; this result is similar to that achieved in other experiments employing 60 g of the 1.1 mm photocatalyst particles. After a total of 95 hours of operation following the addition of Na_2CO_3 , the rate of hydrogen rose to reach a maximum steady-state rate of 232 $\mu\text{mol/hr}$. During this time, hydrogen and oxygen evolved at the expected stoichiometric ratio of 2 (as shown in Figure 18b), again displaying the characteristic over-stoichiometric evolution of hydrogen during the initial hours of operation.

The results shown in Figure 17 and Figure 18 above suggest that the decay in the rate of hydrogen evolution (and corresponding lack of oxygen evolution) is a photo-induced process – likely due to the formation of peroxy-species on the TiO_2 surface and/or the conversion of TiO_2 to a photocatalytically inactive mixed-valence structure. Furthermore, we demonstrate that the addition of Na_2CO_3 to a solution containing photocatalyst particles that had been previously poisoned by the photo-induced process, be it nanoparticles or large fluidizable particles, is capable of fully recovering the performance back to high, steady rates, and that oxygen evolves at the expected stoichiometric ratio.

Sayama and Arakawa^{133,134} argue that the dramatic increase in water splitting performance in the presence of Na₂CO₃ arises due to: 1) a protective layer of adsorbed Na₂CO₃ covering the platinum surfaces, thus suppressing the back reaction, 2) reduced photoadsorption of O₂ on the TiO₂ surface, and 3) an alternate reaction pathway involving peroxocarbonate species that scavenges holes at the TiO₂ surface and is favorable to the evolution of O₂. Tang et al.⁸⁰ provide evidence that oxygen formation requires 4-hole chemistry, the formation of three possible intermediate species, and that, in the absence of a hole scavenging species, O₂ can be rapidly consumed by photo-excited TiO₂ to form peroxotitanate complexes. The observations presented here in this study and by Tang et al.⁸⁰ suggest that, while Na₂CO₃ may indeed reduce the back reaction at platinum deposits (as Sayama and Arakawa suggest^{133,134}), the Na₂CO₃ may promote stoichiometric water splitting and improve the rate of gas evolution primarily by:

- 1) scavenging holes, thus reducing efficiency lost to e⁻/h⁺ recombination processes,
- 2) preventing or destabilizing surface adsorbed peroxo- species that reduce the available surface area and limit oxygen evolution,
- 3) providing an alternate reaction mechanism that is favorable to oxygen evolution, and
- 4) scavenging holes from the TiO₂ surface, thus preventing TiO₂ from acting as an electron donor, which in turn, prevents (and possibly reverses) the formation of mixed-valence species that lead to deactivation.

While the combination of these effects may all contribute to improved performance, the absence of excess oxygen evolution following the addition of Na₂CO₃ (which would indicate the decomposition of peroxo-species) suggests that the latter effect contributes most to the performance recovery in the deactivated photocatalyst shown in Figure 18. It should be recognized, however, that it is difficult to distinguish

excess oxygen arising from opening the system to add Na_2CO_3 and excess oxygen evolved due to the destabilization and decomposition of peroxy-species on the TiO_2 surface.

2.3.8 Over-stoichiometry

As mentioned previously, it was observed that, for all experiments using the Na_2CO_3 additive, the ratio of hydrogen to oxygen evolution exceeded that of the expected theoretical ratio of 2 during the initial hours of operation, eventually settling to a ratio of 2 during steady state operation, as seen in Figure 19. It was observed that the H_2/O_2 ratio reached a maximum after 2-2.5 hours of operation, with the exception being that for experiments employing 120 g of photocatalyst particles. It was observed that for high photocatalyst loadings at 120 g (which correspond with low recirculation flow rates) the over-stoichiometric peak is not observed until 5 hours of operation and is less pronounced than that of the peaks observed for lower photocatalyst loadings (with correspondingly higher recirculation flow rates).

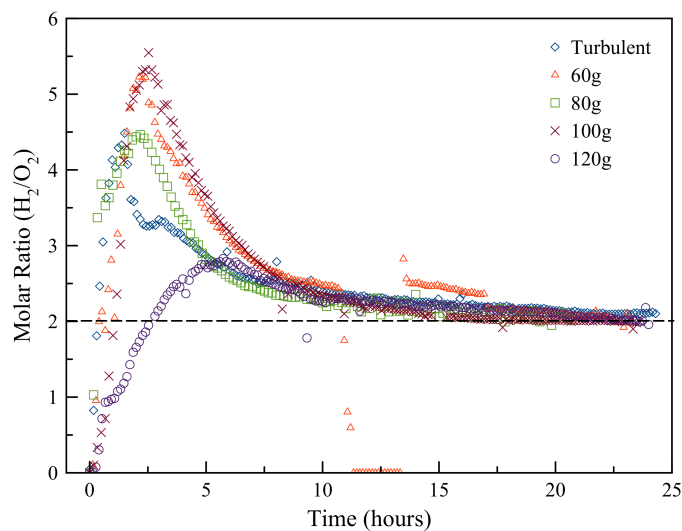


Figure 19: The stoichiometric ratio of hydrogen to oxygen with respect to time for various amounts of 1.1 mm diameter photocatalyst particles fluidized in the photoreactor. The ratio for 100 g of 0.5 mm diameter particles when using a modified separator configuration (denoted as ‘Turbulent’) is discussed in more detail later.

In a similar fashion to the results discussed above, it is possible to ascertain whether the over-stoichiometric effect is photo-induced by extinguishing the UV lamp for a period of time. As observed in Figure 20, when the UV lamp is extinguished for a period of 3 hours and then reignited, the H_2/O_2 ratio almost instantaneously returns to its previous state and continues to settle toward the theoretical ratio of 2. This indicates that, like the hydrogen evolution rate observed in Figure 17, the underlying process leading to stoichiometric evolution of hydrogen and oxygen is a photo-induced effect which is dependent on the cumulative exposure to UV irradiation. The step change observed in the H_2/O_2 ratio between 13.5 and 17 hours of operation in Figure 20 is due to a slight decrease in the fluidized bed height, which was corrected back to a height of 24 cm (at 17 hours of operation) by increasing the recirculation flow rate slightly. This sharp change in the stoichiometric ratio suggests that the photo-induced process leading to the stoichiometric and steady-state evolution of hydrogen and oxygen is also a function of the recirculation flow rate. The possible source of this flow rate dependence is discussed in Chapter 3.

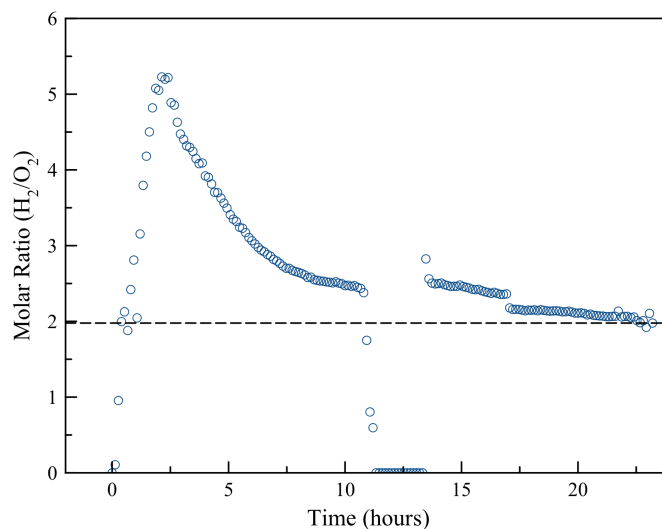


Figure 20: The stoichiometric ratio of hydrogen to oxygen with respect to time for 60 g of the 1.1 mm diameter photocatalyst particles fluidized in the photoreactor. The lamp was turned off and on to observe whether the effect of Na_2CO_3 was photo-induced.

2.4 Conclusions

We herein demonstrate and describe photocatalytic water splitting in a fluidized bed reactor for the first time. From the results of the study, several conclusions may be drawn:

- 1) It was observed that the effective electron diffusion length through the TiO_2 bulk could be estimated by the concentration of photo-deposited platinum co-catalyst sites via D-SIMS analysis.
- 2) When compared to Pt-loaded, suspended slurry type photocatalysts, the fluidized photocatalyst particles yield a 44% increase in the apparent quantum efficiency. It is proposed that this is due, in part, to the reduction of platinum-loaded particles in non-irradiated regions of the reactor that would otherwise serve to promote the parasitic back-reaction of hydrogen and oxygen. This is an important aspect for consideration when designing or scaling photocatalytic hydrogen productions systems – suspended slurry, fluidized particles, or otherwise.
- 3) Photocatalyst deactivation in pure water and the beneficial effect of Na_2CO_3 are both photo-induced processes that depend on the period of time for which the photocatalyst particles are irradiated by UV light.
- 4) The addition of Na_2CO_3 plays a dramatic role in achieving efficient and steady state hydrogen evolution. It is proposed that the Na_2CO_3 additive acts to improve performance by reducing recombination processes, destabilizing surface adsorbed peroxo-species that otherwise lead to photocatalyst deactivation, by providing an alternate reaction mechanism that is favorable to oxygen evolution, and by preventing TiO_2 itself from acting as an electron donor and reversing any deactivation due to the potential formation of mixed-valence titanium oxide species. While the combination of these effects may lead to improved rates of hydrogen evolution, our observations suggest that the latter effect may be the primary contributor to stable, long-term performance by preventing the photo-induced deactivation of TiO_2 .

Chapter 3: Modeling the Behavior of Water Splitting in a Photocatalytic Fluidized Bed System

3.1 Introduction

A fluidized bed reactor was explored in the previous chapter to study its effect on the performance of photocatalytic water splitting. The excellent radiation distribution, reduced mass transfer resistances, and the ability for evolved hydrogen to be quickly separated from the platinum-deposited fluidized bed particles resulted in a large increase in the efficiency of the process. It was observed, however, in Figure 16b (Chapter 2) that as the mass of photocatalyst increases, the specific rate of hydrogen evolution decreases. While it is natural to hypothesize that the decrease in the specific rate of hydrogen production is simply due to increased shading of particles at the outer reactor wall and increased amounts of platinum-loaded photocatalyst promoting the back reaction, it is imperative to also consider the combined effect of both the fluidized bed reactor and the gas-liquid separator. In this chapter we derive a simple, yet powerful, model describing the water splitting system and discuss its application to the experimental results presented in the previous chapter. Relevant nomenclature is shown in Table 3 for convenience.

3.2 Fluidized Bed Theory and Fundamentals

Liquid fluidized bed reactors suspend particles throughout the reactor volume by the upward flow of a liquid phase to create what is known as an expanded bed. The bed expansion for a given mass of photocatalyst particles in a fluidized bed is determined by the terminal velocity and bed voidage of the particles, and the fluid superficial velocity, U , through the fluidized bed. The fluid superficial velocity can be calculated simply by:

$$U = \frac{q}{A_c} \quad (14)$$

Table 3: Nomenclature

a	liquid-gas interfacial area	(cm ² /cm ³)	r _d	H ₂ generation rate	(mol/min.cm ³)
A _c	reactor cross-section area	(cm ²)	r _{net}	net H ₂ evolution rate	(mol/min.cm ³)
Ar	Archimedes number	(-)	R _d	overall H ₂ generation rate	(mol/min)
B _{ex}	bed expansion	(-)	R _{net}	net H ₂ evolution rate	(mol/min)
C _{cat}	photocatalyst mass	(g/cm ³)	RTE	Radiation Transfer Equation	
C _F	H ₂ conc. in the liquid bulk in the fluidized bed reactor	(mol/cm ³)	S	photocatalyst surface area	(cm ² /g)
C _L *	H ₂ conc. at the L-G interface	(mol/m ³)	S _L	rate of photons entering the reactor per lamp length	(ein/min.cm)
C _s	H ₂ conc. in the liquid bulk within the separator	(mol/cm ³)	Sc	Schmidt number	(-)
d _p	particle diameter	(cm)	Sh	Sherwood number	(-)
d _p *	dimensionless particle	(-)	U	superficial velocity	(cm/s)
D	diffusion coefficient	(cm ² /s)	U _e	particle settling velocity	(cm/s)
g	gravitational acceleration	(cm/s ²)	U _t	terminal velocity	(cm/s)
Ga	Galileo number	(-)	U*	dimensionless terminal	(-)
H	Henry constant	(M/atm)	V _{bed}	expanded bed volume	(cm ³)
H _{bed}	static bed height	(cm)	V _s	separator volume	(cm ³)
H _{ex}	expanded bed height	(cm)	W _{cat}	photocatalyst mass	(g)
I	light intensity	(ein/min.cm ²)	W _{max}	maximum mass of catalyst	(g)
k _L	mass transfer coefficient	(cm/min)	α	photon attenuation coefficient	(cm ³ /g)
k _{L,a}	overall mass transfer	(min ⁻¹)	ε	bed voidage	(-)
k' _L	mass transfer constant	(min ⁻¹ cm ⁻³) ^{0.5}	ε ₀	voidage of the static bed	(-)
k'' _L	aggregate mass transfer	(cm ⁻³ min) ^{0.5}	θ _c	“contact time” of a packet of fluid at the liquid-gas interface	(min)
k' _R	back reaction rate constant	(cm ³ /g.min)	μ	fluid viscosity	(cP)
k _s	mass transfer coefficient	(m/s)	ρ _p	bulk particle density	(g/cm ³)
m	constant	(-)	ρ _f	fluid density	(g/cm ³)
M _v	Mass number	(-)	σ	aggregate attenuation cross	(cm ² /g)
n	expansion coefficient	(-)	σ _{abs,l}	probability of photon absorption by the liquid phase	(cm ² /g)
N _G	interface-gas mass transfer rate		σ _{abs,p}	probability of photon absorption by the particles	(cm ² /g)
N _L	liquid-interface mass transfer		σ _{scatter}	probability of photon scattering by the particles	(cm ² /g)
N _S	solid- liquid mass transfer rate		τ _F	fluidized bed residence time	(min)
p _{H₂}	hydrogen partial pressure	(atm)	τ _S	separator residence time	(min)
P _{abs}	overall rate of photon	(ein/min)	φ	sphericity	(-)
P _i	total rate of photons entering the reactor	(ein/min)	Φ	photochemical efficiency	(mol/ein)
r _p	particle radius	(cm)	Φ _{app}	apparent quantum efficiency	(mol/ein)
R _o	radius of outer reactor wall	(cm)	ψ	function of the hydrodynamic parameters of the model	
R _i	radius of the inner annulus	(cm ³ /s)			
q	volumetric flow rate	(cm ³ /s)			
q _e	elutriation flow rate	(cm ³ /s)			
q _{mf}	flow rate at minimum	(mol/min.cm ³)			
r _r	rate of back reaction				

where q is the volumetric fluid flow rate through the reactor and A_c is the reactor cross-section area. The terminal velocity, U_t , may be calculated by the Haider and Levenspiel correlation ²¹⁸ (assuming perfectly spherical particles, $\phi=1$):

$$U_t = U^* \left[\frac{\mu(\rho_p - \rho_f)g}{\rho_f^2} \right]^{1/3} \quad (15)$$

$$U^* = \left[\left(\frac{18}{d_p^*} \right) + \left(\frac{0.591}{\sqrt{d_p^*}} \right) \right]^{-1} \quad (16)$$

$$d_p^* = Ar^{\frac{1}{3}} \quad (17)$$

where U^* and d_p^* are the dimensionless terminal velocity and particle diameter, respectively, and Ar is the Archimedes number. The Archimedes number can be calculated via equation 18:

$$Ar = \frac{\rho_f(\rho_p - \rho_f)g(d_p^3)}{\mu^2} \quad (18)$$

where ρ_p and ρ_f are the particle and fluid densities, respectively, μ is the fluid viscosity, g is the gravitational acceleration constant, and d_p is the particle diameter. The settling velocity of isolated particles, U_e , is then determined by the Kahn and Richardson correlation ²¹⁹:

$$U_e = U_t \left[1 - 1.5 \left(\frac{r_p}{R_o - R_i} \right)^{0.6} \right] \quad (19)$$

where r_p is the particle radius, and R_o and R_i are the outer and inner radii of the annular reaction space of the reactor. The bed voidage, ε , can then be found using the Richardson and Zaki correlation²²⁰ (equation 20), which then allows for the calculation of the bed expansion, B_{ex} :

$$\frac{U}{U_e} = \varepsilon^n \quad (20)$$

$$B_{ex} = \frac{1 - \varepsilon_0}{1 - \varepsilon} \quad (21)$$

where ε_0 is the voidage of the static bed and n is the expansion coefficient determined by:

$$\frac{4.8 - n}{n - 2.4} = 0.043Ar^{0.57} \quad (22)$$

If the reactor cross-section area is constant over the reactor length, equation 20 can be expressed as:

$$\frac{q}{q_e} = \varepsilon^n \quad (23)$$

where q_e , the elutriation flow rate, is the volumetric fluid flow rate through the reactor when the superficial velocity is equal to the settling velocity (i.e., the flow rate required to fluidize a single particle). Flow rates in excess of q_e would result in all particles being eluted from the reactor and thus represents the maximum flow rate through the fluidized bed reactor.

The expanded bed height, H_{ex} , can then be determined given the height of the static bed of particles, H_{bed} :

$$H_{bed} = \frac{W_{cat}}{\rho_p A_c (1 - \varepsilon_0)} \quad (24)$$

$$H_{ex} = H_{bed} B_{ex} \quad (25)$$

where W_{cat} is the total mass of photocatalyst particles in the bed. By substituting equations 21, 23 and 24 into equation 25, it is possible to derive a relationship describing the flow rate required to achieve a desired expanded bed height for a given mass of photocatalyst particles, W :

$$q = q_e \left[1 - \frac{(1 - \varepsilon_0)W}{W_{max}} \right]^n \quad (26)$$

$$W_{max} = H_{ex} A_c \rho_p (1 - \varepsilon_0) \quad (27)$$

$$\varepsilon_0 = \left(\frac{q_{mf}}{q_e} \right)^{1/n} \quad (28)$$

where W_{max} is the maximum amount of catalyst that can be contained in the volume defined by the expanded bed (i.e., the mass of a packed bed of catalyst with the same height as the expanded bed) and q_{mf} is the flow rate at minimum fluidization. From equation 26, it can be seen that the flow rate required to achieve a given expanded bed height decreases with increasing photocatalyst mass in the reactor. Similarly, for a constant flow rate it can be seen that the expanded bed height increases with increasing photocatalyst mass in the reactor. Therefore, it is conceivable that differences in the flow rate through the

fluidized bed/separator system for varying amounts of photocatalyst or bed heights may result in mass transfer related effects that contribute to the inverse relationship between the hydrogen evolution rate and photocatalyst loading observed in Chapter 2.

3.3 Mass Transfer

Escudero et al.⁵⁵ demonstrated that the rate of hydrogen evolution in a bubbling photocatalytic reactor (using a suspended slurry of nanoparticles) is controlled by the rate of mass transfer of hydrogen to the gas phase, and that the rate of hydrogen evolution was proportional to the rate of gas flow bubbled through the reactor solution. This observed effect was due to slow mass transfer rates from the liquid-to-gas phase, which in turn exacerbated the back-reaction over the platinum deposits on the photocatalyst surface. Furthermore, Escudero demonstrated that increasing the gas flow rate through the solution, thus increasing the available area for mass transfer, resulted in an increased rate of hydrogen evolution. To determine the effect of mass transfer in the fluidized bed/separator photocatalytic reactor system described in this work, we herein develop a model describing the overall hydrogen evolution process.

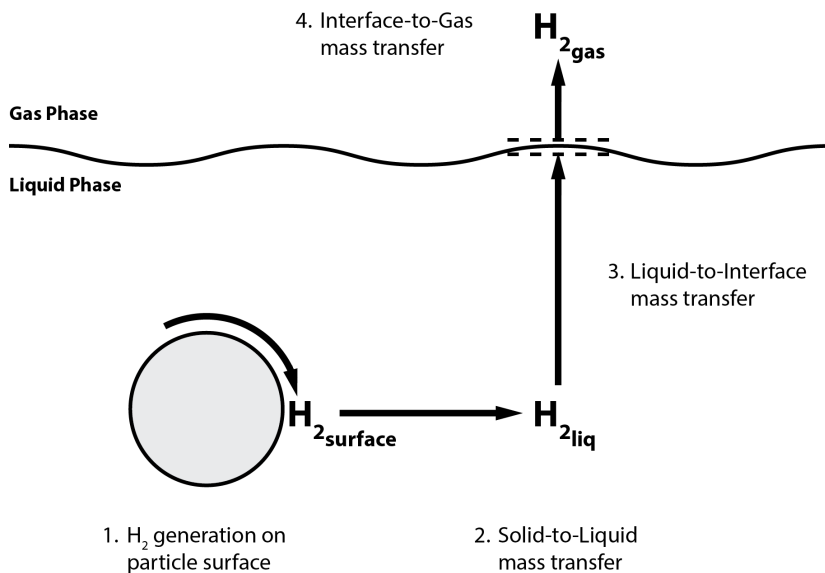


Figure 21: Schematic diagram of photocatalytic hydrogen generation at the fluidized particle surface and the various mass transfer steps involved in the water splitting process.

At steady state, the net rate of hydrogen production is in series with and equal to the solid-to-liquid, liquid-to-interface and interface-to-gas mass transfer rates (illustrated in Figure), and may be described by the following:

$$r_{net} = (C_{cat}S)N_S = aN_L = aN_G \quad (29)$$

where r_{net} is the net rate of hydrogen generation in the fluidized bed reactor, C_{cat} and S are the mass concentration of photocatalyst particles in the fluidized bed volume and specific surface area of the photocatalyst, respectively, and a is the liquid-gas interfacial area. N_S , N_L and N_G are the solid-to-liquid, liquid-to-interface and interface-to-gas mass transfer rates, respectively.

In general, it is well known that fluidized bed reactors exhibit excellent mass transfer between the solid particles and the mobile fluid phase in which they are suspended. While there are a number of correlations describing the mass transfer in solid-liquid fluidized beds^{221,222}, one of the most often employed is that presented by Ballesteros et al.²²³:

$$Sh = 0.245\phi^{1.35}Ga^{0.323}Mv^{0.3}Sc^{0.4} \quad (30)$$

where ϕ is the particle sphericity and Sh , Ga , Mv and Sc are the dimensionless Sherwood, Galileo, Mass and Schmidt numbers, respectively. The Galileo, Mass and Schmidt numbers may be calculated by:

$$Ga = \frac{d_p^3 \rho_f^2 g}{\mu^2} \quad (31)$$

$$Mv = \frac{\rho_p - \rho_f}{\rho_f} \quad (32)$$

$$Sc = \frac{\mu}{\rho_f D} \quad (33)$$

where D is the diffusivity of the solute gas in the liquid phase. The solid-liquid mass transfer coefficient, k_s , may then be calculated from the Sherwood number according to:

$$Sh = \frac{k_s d_p}{D} \quad (34)$$

Given the photocatalyst particle properties presented in Chapter 2, and diffusivity of hydrogen in pure water (which is reported to be $5.5 \times 10^{-4} \text{ cm}^2/\text{s}$ ²²⁴), k_s is estimated to be $2.6 \times 10^{-2} \text{ cm/s}$. From this large value of k_s , it may then be concluded that the mass transfer resistance at the particle-liquid interface is negligible and does not influence the overall process. Furthermore, the liquid-phase hydrogen concentration at the particle surface can therefore be assumed to be equal to that of the liquid-phase hydrogen concentration in the liquid bulk.

In the two-film theory describing mass transfer across a liquid-gas interface, it is supposed that thin films exist on either side of the interface through which mass transfer proceeds solely by molecular diffusion²²⁵. It is generally assumed that all the mass transfer resistance across the interface is centered within the two films and that diffusion through the films is the rate-limiting factor. Thus, according to Fick's Law, the rate of mass transfer across the interface will be proportional to the interfacial surface area and the concentration gradient. For gases such as carbon dioxide, hydrogen and oxygen, it has been

shown that nearly all of the mass transfer resistance exists on the liquid side of the interface²²⁵, thus the interface-to-gas mass transfer resistance can be assumed to be negligible. Furthermore, it can then be said that the gas phase hydrogen concentration is in equilibrium with the liquid-phase hydrogen concentration at the interface, C_L^* , according to Henry's Law:

$$C_L^* = p_{H_2}H \quad (35)$$

where p_{H_2} is the partial pressure of hydrogen and H is the Henry constant for hydrogen in water.

As the solid-to-liquid and interface-to-gas mass transfer resistances may be considered negligible, the net rate of hydrogen production at the photocatalyst surface can therefore be assumed to be in equilibrium with the rate of mass transfer across the liquid-gas interface in the separator unit described in Chapter 2. Given the high degree of turbulence and the strong swirling motion of fluid in the separator, the separator can be approximated as an ideal continually stirred tank reactor (CSTR). The hydrogen mole balance for the separator can therefore be written as:

$$q(C_F - C_S) = k_L a(C_S - C_L^*)V_s \quad (36)$$

where $k_L a$ is the overall mass transfer coefficient, C_s is the liquid-phase hydrogen concentration in the liquid bulk within the separator, and V_s is the volume of the separator. Escudero et al.⁵⁵ demonstrated that the rate of hydrogen evolution was independent of the hydrogen partial pressure, implying that C_L^* is significantly smaller than C_s . In addition, the hydrogen partial pressure in the separator unit employed in this work is significantly diluted by the nitrogen purge gas stream used to carry the reaction products from the separator, thus resulting in C_L^* being so small so as to be considered negligible. Equation 36 can therefore be rewritten as:

$$\frac{(C_F - C_S)}{\tau_s} = k_L a C_A \quad (37)$$

where C_F is the liquid-phase hydrogen concentration in the liquid bulk exiting the fluidized bed reactor and τ_s is the residence time of a fluid parcel in the separator is given by:

$$\tau_s = \frac{V_s}{q} \quad (38)$$

It may be assumed that the overall mass transfer coefficient for the separator, $k_L a$, is dependent solely on the liquid flow rate through the reactor (as the design of the separator provides no means for external agitation). From Higbie's penetration model for mass transfer^{226,227}, the mass transfer coefficient, k_L , can be determined by:

$$k_L = \psi D^m = 2 \sqrt{\frac{1}{\pi \theta_c}} D^m \quad (39)$$

where ψ is a function of the hydrodynamic parameters of the model, m is a constant (for penetration and surface renewal models²²⁶, $m = 1/2$), θ_c is the "contact time" of a packet of fluid at the liquid-gas interface and D is the diffusion coefficient of the solute gas in the liquid phase. It can then be hypothesized that in the separator, the contact time of a parcel of fluid with the liquid-gas interface is proportional to the residence time, τ_s , of a fluid parcel in the separator. The rate of mass transfer from the separator can therefore be written as:

$$\frac{(C_F - C_S)}{\tau_s} = k'_L \sqrt{\frac{q}{V_s}} C_S \quad (40)$$

For simplicity, the V_s term can be incorporated into the mass transfer constant k'_L and equation 40 can be written as:

$$\frac{(C_F - C_S)}{\tau_s} = k'_L \sqrt{q} C_S \quad (41)$$

3.4 Optical Model and Direct Rate of H₂ Evolution

The direct rate of hydrogen generation at the photocatalyst surface is assumed to be zero-order and is proportional to the rate of photon absorption only. Therefore, the rate of hydrogen generation can then assumed to be a function of the rate of photons entering into the fluidized bed reaction volume (which is itself a function of the portion of the UV lamp covered by the expanded fluidized bed), the photochemical efficiency and the concentration of photocatalyst particles in the expanded bed volume.

Accurate modeling of the rate of photon absorption and the optical properties of an expanded fluidized bed (i.e., spectral absorbance, scattering and extinction coefficients) typically requires solving a complex general *radiation transfer equation (RTE)* by Monte Carlo simulation – which is beyond the scope of this work. However, Akehata and Shirai²²⁸ demonstrated that the radiant energy distribution in an annular photocatalytic reactor can be described by a simplified radial emission model when the ratio of the inner reactor radius to lamp length is less than or equal to 0.1 (for the purpose of this work, the effective lamp length is equal to the height of the expanded bed). The radial emission model can be expressed as:

$$I(r, z) = \frac{S_L e^{-\sigma_{cat}(r-R_i)}}{2\pi r} \quad (42)$$

where I is the intensity of light at a point located at a radius, r , and height, z , within the fluidized bed of particles, S_L is the rate of photons with energy equal to greater than the band gap energy entering the

reaction volume per centimeter of lamp length, C_{cat} is the photocatalyst concentration, and σ is an aggregate attenuation cross section:

$$\sigma = \sigma_{abs,p} + \sigma_{abs,l} + \sigma_{scatter} \quad (43)$$

where $\sigma_{abs,p}$, $\sigma_{abs,l}$, and $\sigma_{scatter}$ are the probabilities of absorption by the particles, absorption by the liquid phase, and the probability of scattering, respectively.

As seen in the radial emission model, the light intensity profile is constant in the axial direction and varies only in the radial direction. The output of the UV lamp employed in our work was determined to be largely constant over the length of the lamp (with output decreasing sharply close to the ends) and, as such, it can be reasonably assumed that the total rate of photon absorption in the reaction volume varies linearly with bed height. By integrating the radial emission model over the entire reaction volume defined by a fluidized bed with an expanded bed height H_{ex} , the overall rate of photon absorption, P_{abs} , can be found:

$$P_{abs} = P_i(1 - e^{-\alpha C_{cat}}) \quad (44)$$

$$P_i = H_{ex} S_L \quad (45)$$

where P_i is the total rate of photons entering the reaction volume defined by the expanded bed and α is the photon attenuation coefficient, which is defined as:

$$\alpha = \sigma(R_o - R_i) \quad (46)$$

Though the absorption and scattering properties of a fluidized bed can vary with the bed density, Imoberdorf et al. ⁶² demonstrated through simulation of the RTE and experimental results that photon absorption in an annular fluidized bed reactor follows the behavior described by equation 44. Therefore, the derived expression for the rate of photon absorption can be assumed to be a reasonable first approximation in our case.

As two photons are required to evolve one H₂ molecule, the total rate of hydrogen generation, R_d, by a fluidized bed of photocatalyst particles having a total mass W_{cat} and height H_{ex} can then be expressed as:

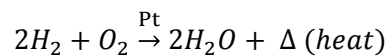
$$R_d = \frac{\Phi H_{ex} S_L}{2} (1 - e^{-\alpha C_{cat}}) \quad (47)$$

where Φ is the photochemical efficiency, which accounts for all e⁻/h⁺ recombination processes and inefficiencies. Alternatively, the rate of hydrogen generation can be expressed on a per volume basis:

$$r_d = \frac{\Phi S_L}{2A_c} (1 - e^{-\alpha C_{cat}}) \quad (48)$$

3.5 Back Reaction

Aside from electron/hole recombination processes, the undesirable platinum-catalyzed back reaction of hydrogen and oxygen is the largest contributor to efficiency losses in photocatalytic water splitting systems. While the back reaction is generally assumed to follow that of the combustion of hydrogen and oxygen over platinum,



few studies have explored the mechanism of the back reaction over Pt-deposited photocatalysts ²²⁹.

Several recent studies, particularly those addressing Pt catalysts in fuel cells, have demonstrated that there are several of pathways through which the back reaction, more correctly referred to as the *hydrogen oxidation reaction (HOR)*, may proceed (a number of possible reaction steps are shown in Table 4).

Table 4: Possible reaction steps for the back reaction of H₂ and O₂ (i.e., hydrogen oxidation reaction, HOR) over platinum surfaces.

Reaction		
a. H ₂ adsorption	$H_2 + * \rightarrow H_2^*$	
b. H ₂ [*] dissociation	$H_2^* + * \rightarrow 2H^*$	
c. O ₂ adsorption	$O_2 + * \rightarrow O_2^*$	
d. O ₂ [*] dissociation	$O_2^* + * \rightarrow 2O^*$	
e. OH [*] formation	$H^* + O^* \rightarrow OH^* + *$	• energetically unfavourable ^{229,230}
f.	$O_2^* + H_2O^* \rightarrow 2OH^*$	• energetically favoured ^{229,230}
g.	$OH^- + * \rightarrow OH^*$	• occurs readily in alkaline media ^{231–233}
h. H ₂ O [*] formation	$H^* + OH^* \rightarrow H_2O^* + *$	
i.	$2H^* + 2OH^- \rightarrow 2H_2O^* + 2e^-$	
j. H ₂ O desorption	$H_2O^* \rightarrow H_2O + *$	

The hydrogen oxidation reaction begins with the adsorption and dissociation of H₂ and O₂ on platinum surfaces to yield surface adsorbed hydrogen and oxygen atoms, H^{*} and O^{*}, respectively (reactions a-d in Table 4). While surface adsorbed O atoms can react directly with H^{*} to form surface hydroxyl groups (reaction e), OH^{*}, the reaction is not energetically favored and HOR is more likely to proceed through O^{*} reacting with surface adsorbed water, H₂O^{*}, to form OH^{*} ^{229,230} (reaction f). The OH^{*} species subsequently react with H^{*} to produce water, which in turn desorbs from the catalyst surface (reactions h and j). It has been shown that OH⁻_{aq} participates in the HOR as a reactant, potentially through H^{*} reacting directly with OH⁻_{aq} in solution (reaction i) ^{234,235}, and that in alkaline solutions the rate of the hydrogen oxidation reaction is governed solely by H^{*} coverage and OH⁻_{aq} activity ^{233,234}. Later results have indicated that OH^{*}

is the primary reactant as opposed to OH^-_{aq} ²³³ and that, in alkaline media, the adsorption of OH^-_{aq} onto the catalyst surface enhances the hydrogen oxidation reaction²³³. Furthermore, it has been established the OH^-_{aq} can readily adsorb onto Pt surfaces (reaction g), especially so in alkaline solutions (such as that employed in our work)²³¹⁻²³³.

For simplicity, the H^* surface coverage is assumed to be proportional to the local concentration of H_2 in solution, which (as discussed previously) will be approximately equal to that of the H_2 concentration in the bulk liquid. As the HOR is determined solely by the H^* surface coverage and OH^* , which in our system will be in great excess with respect to H^* due to the high pH, the back reaction, r_r , can be assumed to behave as a pseudo-first order reaction:

$$-r_r = k'_r C_{\text{cat}} C_F \quad (49)$$

where k'_r is a first order pseudoconstant and C_F is the liquid-phase hydrogen concentration in the liquid bulk within the fluidized bed reactor.

3.6 Overall Rate of H_2 Evolution

To determine the overall rate of hydrogen evolution, the fluidized bed can be modeled (as a first approximation) as a CSTR:

$$q(C_F - C_S) = r_d V_{\text{bed}} - r_r V_{\text{bed}} \quad (50)$$

$$\frac{(C_F - C_S)}{\tau_F} = \frac{\Phi S_L}{2A_c} (1 - e^{-\alpha C_{\text{cat}}}) - k'_r C_{\text{cat}} C_F \quad (51)$$

where V_{bed} is the volume defined by the expanded bed and τ_F is the residence of a fluid parcel in the fluidized bed, which is defined as:

$$\tau_F = \frac{V_{bed}}{q} = \frac{H_{ex}A_c}{q} \quad (52)$$

Once the fluidized bed/separators system reaches steady state operation (i.e., C_F and C_S are constant), it can be seen that the net rate of hydrogen evolution in the fluidized bed is equal the rate of hydrogen removal in the separator, hence:

$$\frac{\Phi S_L}{2A_c} (1 - e^{-\alpha C_{cat}}) \tau_F - k'_r C_{cat} C_F \tau_F = k'_L \sqrt{q} C_S \tau_s \quad (53)$$

From equation 41,

$$C_F = C_S + k'_L \sqrt{q} C_S \tau_s \quad (54)$$

Therefore, equation 53 may be rewritten as:

$$\frac{\Phi S_L}{2A_c} (1 - e^{-\alpha C_{cat}}) \tau_F - k'_r C_{cat} \tau_F C_S [1 + k'_L \sqrt{q} \tau_s] = k'_L \sqrt{q} C_S \tau_s \quad (55)$$

Therefore,

$$C_S = \frac{\frac{\Phi S_L}{2A_c} (1 - e^{-\alpha C_{cat}}) \tau_F}{k'_r C_{cat} \tau_F [1 + k'_L \sqrt{q} \tau_s] + k'_L \sqrt{q} \tau_s} \quad (56)$$

The net rate of hydrogen evolution observed from the separator can then be expressed as:

$$R_{net} = k'_L \sqrt{q} C_S \tau_s q \quad (57)$$

Finally, by substituting equation 56 into equation 57:

$$R_{net} = \frac{\Phi H_{ex} S_L (1 - e^{-\alpha C_{cat}})}{2} \left[\frac{k'_L \sqrt{q} \tau_s}{k'_r C_{cat} \tau_F [1 + k'_L \sqrt{q} \tau_s] + k'_L \sqrt{q} \tau_s} \right] \quad (58)$$

It can be seen that the expression for the net rate of hydrogen evolution (equation 58) has the form

$R_{net} = 0.5 \Phi_{app} P_i$, where Φ_{app} is the apparent quantum efficiency (as per equation 13). Therefore, the apparent quantum efficiency can be written as a function of the photocatalyst concentration and flow rate (which in turn are both functions of W and H_{ex}):

$$\Phi_{app} = \Phi (1 - e^{-\alpha C_{cat}}) \left[\frac{k'_L \sqrt{q} \tau_s}{k'_r C_{cat} \tau_F [1 + k'_L \sqrt{q} \tau_s] + k'_L \sqrt{q} \tau_s} \right] \quad (59)$$

Equation 58 may alternately be rearranged and expressed more simply as:

$$\frac{H_{ex}}{R_{net}} = \left(\frac{2}{\Phi S_L} \right) \left(\frac{1}{1 - e^{-\alpha C_{cat}}} \right) \left[\frac{k'_r W}{k'_L \sqrt{q}} + \frac{k'_r W}{q} + 1 \right] \quad (60)$$

$$k'_L = k'_L V_s \quad (61)$$

While the derived model shown in equation 60 is specific to the annular fluidized bed and separator design employed in our work, the form of the equation will be similar for systems employing different designs. For example, annular fluidized bed reactors having an inner reactor radius to lamp length ratio greater than 0.1, the second term of the right hand side of equation 60 would require modification to account for diffuse or spectral radiation emission models, however, the remainder of the equation would remain the same. Similarly, for separators of different designs, such as hollow fiber membrane separators, the mass transfer coefficient will vary with other powers of flow rate than the square-root, yet the remainder of equation 60 would remain unchanged.

3.7 Discussion

On the right-hand side of equation 60 it can be seen that there are three terms relating to: the maximum rate of hydrogen evolution per centimeter of bed height, the absorption of photons (as a function of photocatalyst concentration), and performance loss due to the back reaction (as a function of flow rate and photocatalyst mass). The parameters of these terms, namely ΦS_L , α , k'_r and k''_L , were fitted to the experimental data reported in Chapter 2 via a non-linear, least squares regression. The fitted parameters for ΦS_L , α , k'_r and k''_L are shown in Table 5 along with the fluidization parameters employed in the model.

Table 5: Fitted parameter values for R_{net} as a function of photocatalyst mass, W , and bed height, H_{ex} , and relevant fluidization parameters.

Fluidization Parameters		Fitted Model Parameters	
ρ_p	3.50 g/cm ³	α	6.29 cm ³ /g
ϵ_0	0.33	ΦS_L	0.68 μ mol/min/cm
A_c	14 cm ²	k'_r	4.0x10 ⁻³ cm ³ /g.min
n	2.72 (<i>calculated</i>)	k''_L	4.5x10 ⁻³ (cm ³ /min) ^{0.5}
q_e	11.15x10 ³ cm ³ /min (<i>calculated</i>)		

While an extensive investigation of each separate parameter is required to generate accurate values, the fitted parameters presented in Table 5 are each within their expected range and thus can be assumed to provide reasonable estimates. The photon attenuation coefficient, α , is in close agreement with that calculated from data presented by Imoberdorf et al.⁶² and Vega²³⁶ ($\alpha \approx 6.3$), both of whom employed photocatalysts of similar size and composition, as well as reactors of similar dimension, to those employed in our work. The rate of photons entering the reaction volume per centimeter of lamp length, S_L , was measured experimentally to be 2.48×10^{-5} einstein/min/cm, therefore the photochemical efficiency, Φ , is estimated to be 2.78%. While there is no known published data for k'_r and k''_l , the fitted rate constants in Table 5 yield estimated liquid-phase hydrogen concentrations in the separator (as per equation 56) that one would expect for hydrogen dissolved in water under an atmosphere having a moderately low hydrogen partial pressure.

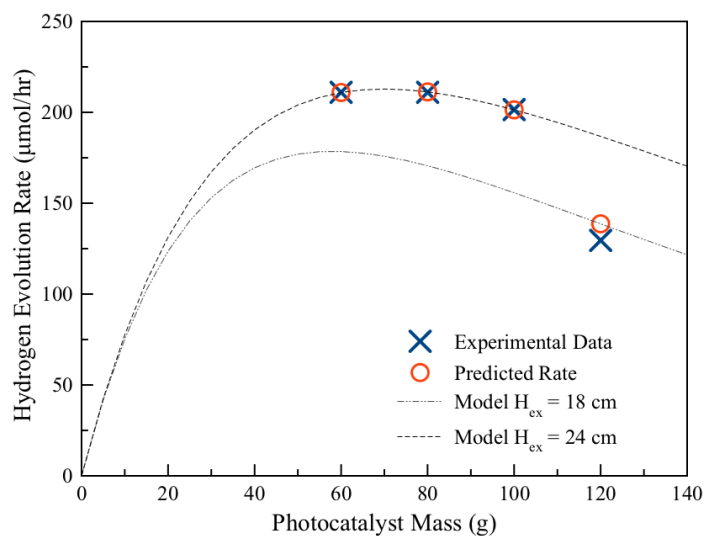


Figure 22: Correlation of predicted hydrogen evolution rates with the experimental data presented in Chapter 2 as a function of photocatalyst mass.

The fitted parameters were used to plot the predicted rate of hydrogen evolution as a function of photocatalyst mass (Figure 22). The hydrogen evolution rates presented the figures of this discussion are displayed with units of $\mu\text{mol/hr}$ to keep consistent with convention. It can be seen that the predicted

hydrogen evolution rates correlate closely with the experimentally measured values for photocatalyst masses of 60 g, 80 g and 100 g (all having an expanded bed height of 24 cm). When 120 g of photocatalyst particles were employed at high recirculation flow rates, the expanded bed height was highly sensitive to slight fluctuations in the flow rate and it was not possible to maintain a steady bed height at 24 cm. As such, it was necessary to reduce the flow rate to achieve steady operation at an expanded bed height of 18 cm. As seen in Figure 22, the model slightly over-estimates the rate of hydrogen evolution for 120 g of photocatalyst; however, the fit is still quite close under this set of conditions. This discrepancy is likely due to error in the measurement of, or fluctuations in, the bed height as the rate of hydrogen evolution is highly dependent on this value (as will be discussed later). However, it must also be considered that the fluidized bed may deviate from CSTR-like behavior at reduced flow rates or that optical properties of the expanded bed may also vary with photocatalyst particle concentration and flow rate. Further experimental investigation and/or solution of a complex radiation transfer equation would be necessary to better understand how the optical properties of an expanded bed may vary with experimental conditions.

3.7.1 General Model Behavior

From equation 58 it can be clearly seen that for a given expanded bed height, the overall rate of hydrogen evolution from the system increases with increasing photocatalyst particle concentration (due to improved photon capture and absorption) and decreases sharply for low photocatalyst particle concentrations. The relative contribution of this effect to the apparent quantum efficiency is demonstrated in Figure 23 where it can be seen that photon absorption trends toward a maximum at a critical photocatalyst concentration. This effect is similar to that reported literature for suspended photocatalyst slurries in that the rate of hydrogen evolution increases with photocatalyst concentration and that there is no further increase beyond a critical photocatalyst loading^{22,136}.

From equation 26, it can be seen that the flow rate required to achieve a given bed height decreases with increasing mass of photocatalyst particles in the fluidized bed. This reduction in flow rate, in turn, reduces the mass transfer coefficient, and thus the rate of hydrogen removal, in the separator (as per equation 41). Simultaneously, as the mass of photocatalyst particles increases, the rate of back reaction increases (as per equation 49). As seen in Figure 22, the combined effect of mass transfer and back reaction results in a reduction in efficiency with increasing photocatalyst mass. Maximizing the rate of hydrogen evolution for a given bed height is, therefore, a balance between maximizing photon absorption while minimizing losses due to mass transfer/back reaction effects. The overall contribution of both photon absorption and mass transfer/back reaction losses to the apparent quantum efficiency is shown in Figure 22 and is seen to display the characteristic curve shape observed in the other figures of this discussion.

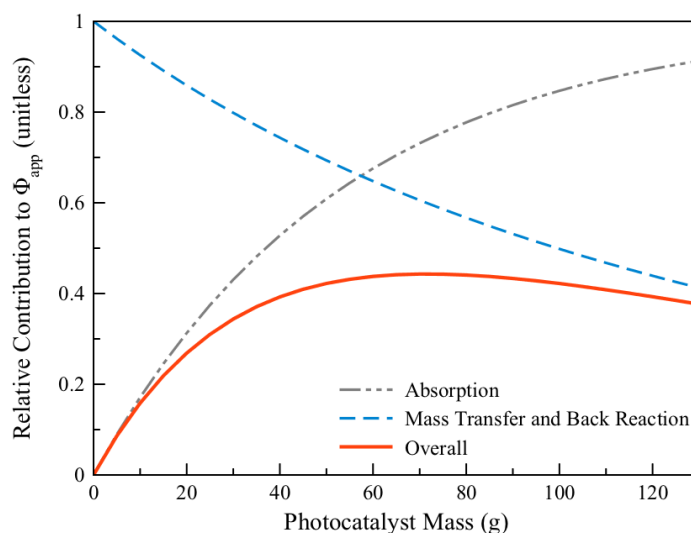


Figure 23: The relative and overall contributions of photon absorption, mass transfer and the back reaction to the apparent quantum efficiency as a function of photocatalyst mass.

3.7.2 Effect of Bed Height

While the maximum achievable rate of hydrogen evolution increases linearly with bed height (i.e. $0.5H_{ex}\Phi_{SL}$), it can be seen in Figure 24a that the overall rate of hydrogen evolution does not. For a given mass of photocatalyst particles, the percentage of photons absorbed by the fluidized bed decreases

with increasing bed height due to a reduction in the photocatalyst particle concentration. In addition, for a given mass of photocatalyst particles there is an exponential relationship between flow rate and bed height (equation 26), meaning that the increase in flow rate required to change the bed height by a given amount decreases with increasing bed expansion. For example, the increase in flow rate required to double the bed height from 5 cm to 10 cm is greater than that required to further double the bed height from 10 cm to 20 cm. The result of this behavior is that the separator mass transfer coefficient increases more dramatically at shorter bed heights; further gains in the mass transfer coefficient diminish as the bed height increases. This observation implies that, for a given mass of photocatalyst particles, the apparent quantum efficiency decreases with increasing bed height, as the diminishing increases in mass transfer do not offset the reduction in photon capture.

Similarly, it can be realized that for shorter bed heights the photocatalyst particle concentration can be greatly increased to maximize photon absorption while minimizing the total mass of photocatalyst particles, thus minimizing the back reaction. Indeed, it can be seen in Figure 24b that the maximum rate of hydrogen evolution per centimeter of bed height (and therefore, maximum efficiency) decreases with increasing bed height. The dashed line in Figure 24b indicates the maximum rate per centimeter of bed height (i.e., maximum efficiency) that can be achieved by a given mass of photocatalyst particles. Conversely, the dashed line may be thought of as the maximum mass of photocatalyst that should be employed for a given bed height. While shorter bed heights yield greater efficiencies, the overall rate of hydrogen evolution is low. Figure 24b should therefore serve as a guide when optimizing the reactor design for cost, efficiency and the overall rate of hydrogen production.

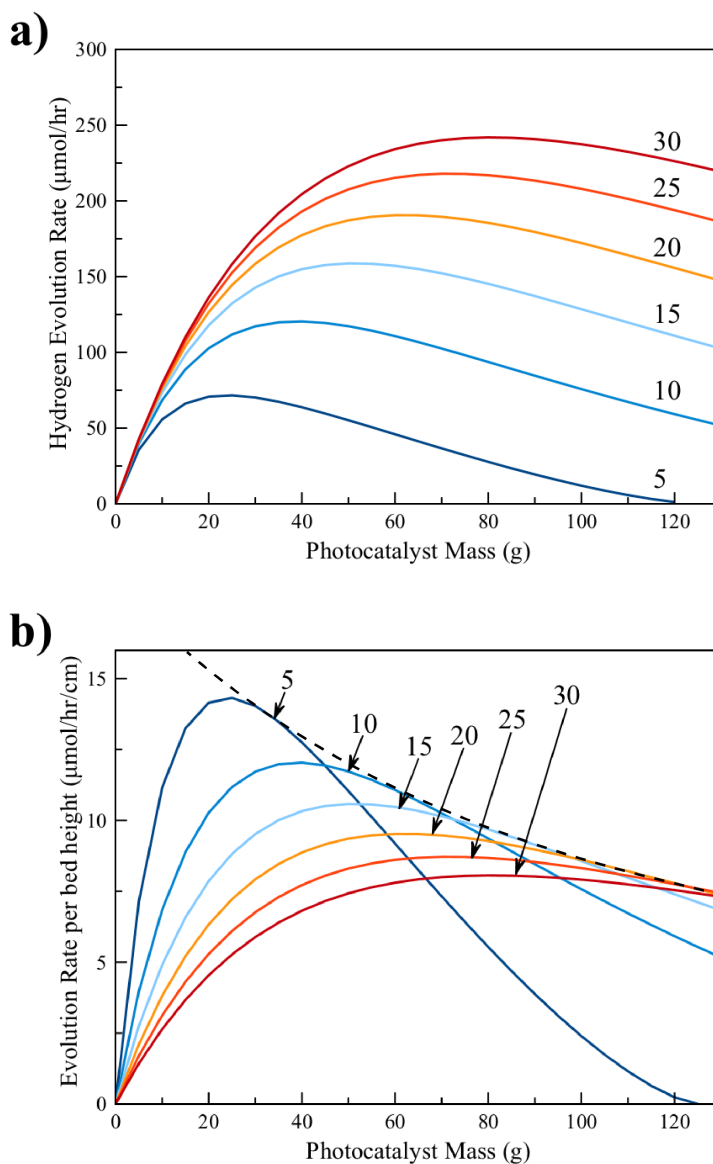


Figure 24: a) The overall rate of hydrogen evolution and b) the rate of evolution per centimeter of bed height as a function of photocatalyst mass, W , and bed height, H_{ex} . All other model parameters are held constant at the values presented in Table 5.

3.7.3 Back Reaction and Mass Transfer Effects

The back reaction is the greatest source of inefficiency in the fluidized bed/separators system apart from electron/hole recombination. Hydrogen is not only lost to the back reaction itself but the need to minimize its effects by reducing the total mass of photocatalyst particles leads to a subsequent reduction in photon capture and efficiency. As shown in Figure 25a, even modest decreases in k'_r can lead to significant

improvements in the overall rate of hydrogen evolution. It should be noted that in the absence of the back reaction ($k'_r = 0$), the behavior of the system is simply that of the photon absorption limited case demonstrated in Figure 23.

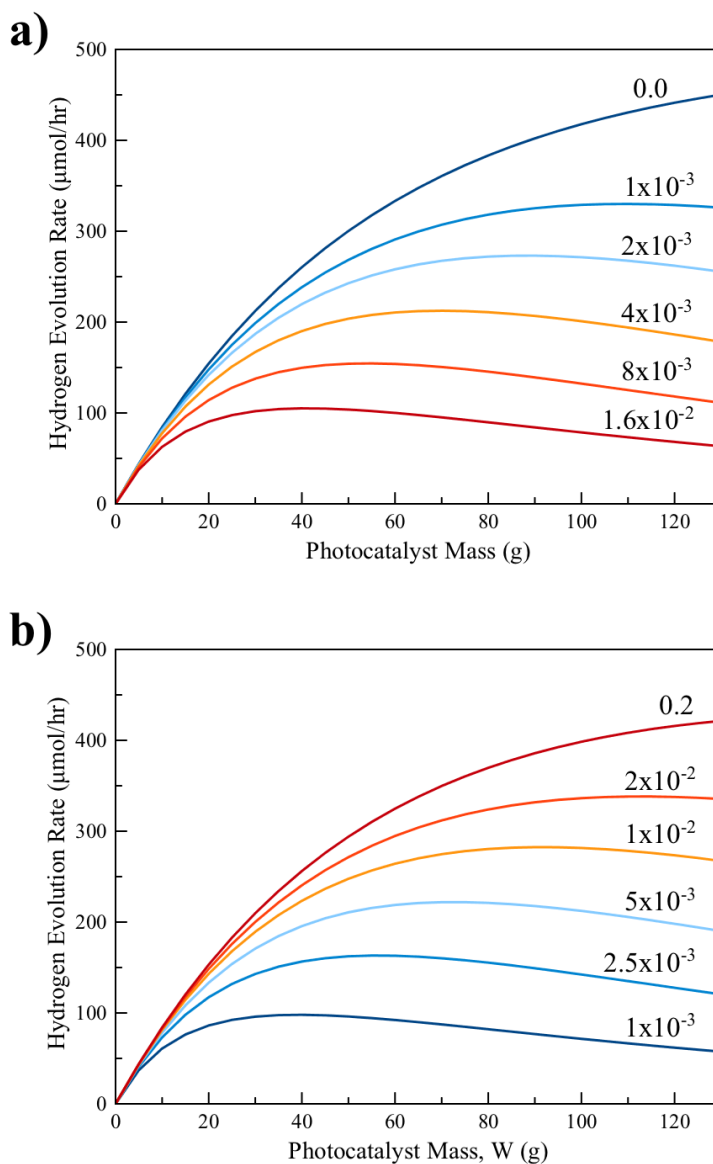


Figure 25: The overall rate of hydrogen evolution as a function of photocatalyst mass for various values of a) the back reaction rate constant, k'_r , and b) the mass transfer constant, k'_L for an expanded bed height, H_{ex} , of 24 cm. All other model parameters are held constant at the values presented in Table 5. The units of k'_r and k'_L are $(\text{cm}^3/\text{g}\cdot\text{min})$ and $(\text{cm}^3/\text{min})^{0.5}$, respectively.

Though a suitable non-noble metal catalyst that avoids the back reaction has yet to demonstrate water splitting performance rivaling that of platinum, it may be possible to greatly minimize the effects of the back reaction by other means. As seen in Figure 25b, increases in k_L'' can counter the effects of the back reaction and yield a notable increase in the overall rate of hydrogen evolution. Optimization of the separator performance, such as through increasing the size or liquid-gas interfacial area of the separator, can improve the mass transfer coefficient. As demonstrated in Figure 25b, if k_L'' were to be made very large the performance of the system would approach that of the back reaction-free case ($k_r' = 0$) shown in Figure 25a. This, herein, demonstrates the potential advantage of a fluidized bed approach over that of suspended slurries. As the fluidized photocatalyst particles are contained only within the volume of the expanded bed, parameters such as the separator volume can be altered without affecting the total mass of photocatalyst particles in the system. Suspended slurry photocatalysts, on the other hand, are distributed throughout the entire system volume and the back reaction occurs at all points in the reactor. Increases in the separator volume of a suspended slurry system would result in an increase in the total photocatalyst mass, along with a subsequent increase in the rate of back reaction. In addition to this, suspended slurries of nanoparticles may be incompatible with improved separator designs such as vacuum-assisted membrane separators.

3.7.4 Effect of Photocatalyst Concentration on Photon Absorption

In order to maximize the overall rate of hydrogen evolution and the apparent quantum efficiency, it is necessary to maximize the photon attenuation coefficient, α . In Figure 26, the predicted rate of hydrogen evolution for an expanded bed height of 24 cm is plotted for various values of α (holding all other parameters constant). It can be seen that the overall rate of hydrogen evolution can be increased significantly with even modest increases in α . In addition, the photocatalyst mass at which the maximum rate of hydrogen evolution is achieved decreases as the photon attenuation coefficient is increased, thus minimizing photocatalyst costs.

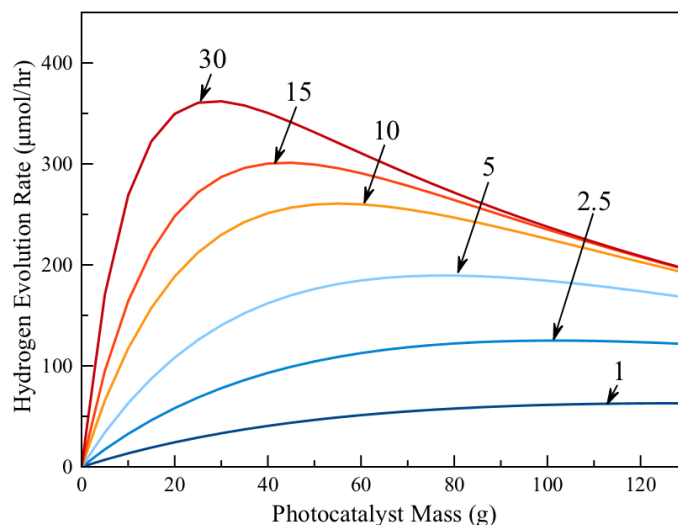


Figure 26: The overall hydrogen evolution rate as a function of photocatalyst mass for various values of the attenuation coefficient, α , for an expanded bed height, H_{ex} , of 24 cm. All other model parameters are held constant at the values presented in Table 5. The units of α are (cm^3/g).

The photon attenuation coefficient may be increased through several means. The first and most facile method to increase α is by increasing the optical path length (i.e.. the distance between the outer reactor wall and the inner annulus, $\Delta R = R_o - R_i$). It should be noted that this is best achieved by decreasing R_i rather than by increasing R_o as the bed volume increases more rapidly with R_o ($dV_B/dR_o = 2\pi R_o H_{ex}$), thus resulting in a large reduction in the photocatalyst particle concentration (for a fixed photocatalyst mass) or an increase in rate of back reaction (for a fix photocatalyst particle concentration). In addition, the volume-averaged rate of hydrogen evolution (equation 48) is increased as the reactor cross-section area, A_c , decreases due to an increase in the average intensity of light incident on each particle. This results in a higher rate of hydrogen evolution per particle, which in turn reduces the amount of photocatalyst required. To maximize the photon attenuation coefficient, the design goal should therefore be to maximize the optical path length while simultaneously minimizing the cross-section area. This dictates that R_i should first be minimized as much as the design of the light source in the inner annulus will allow.

The photon attenuation coefficient may also be increased through modification of the particles or deliberately designing for certain optical behaviors. For perfectly spherical particles, the angle of incidence increases as photons strike the particle surface further from dead center and so will the amount of reflected light. Spherical particles will, therefore, exhibit increased reflection and scattering from their surfaces, which may result in increased rates of photon loss due to absorption by the liquid medium and photons exiting the reactor volume due to scattering. Particles may be designed to have irregular surfaces that can reduce photon scattering and improve photon capture. Similarly, the photocatalyst surface may be modified to have anti-reflective properties, such as through the application of vertically aligned nanostructures⁵⁷. Both of these alternative approaches to photocatalyst design are explored in Chapters 4 and 5.

Finally, by reducing the photocatalyst particle diameter α can be further increased. Small particle diameters result in a large increase in the number of particles per gram of photocatalyst as well as increased surface area for photon absorption. For example, suspended slurries of TiO₂ nanoparticles can achieve maximum photon absorption at concentrations as low as 1 g/L^{22,136}. While reducing the particle diameter is highly effective in increasing the photon attenuation coefficient, the behavior of small particles can introduce other factors that may result in decreased performance and efficiency.

3.7.5 Effect of Particle Size and Density

From equations 15 through 22, it can be seen that a reduction in the photocatalyst particle diameter results in a reduced settling velocity and an increase in the expansion coefficient. While smaller particle diameters are preferred to an extent due to their improved photon capture and lower fluidization velocities (which translate to reduced pumping and equipment costs), the reduction in mass transfer in the separator results in a dramatic decrease in the rate of hydrogen evolution. A similar effect is noted for low-density photocatalyst particles as the required fluidization velocity for a given bed height is reduced, again,

resulting in reduced mass transfer and a low rate of hydrogen evolution. In addition to mass transfer effects, a small particle size also increases the surface area of the platinum-deposited photocatalyst and with it the rate of the back reaction.

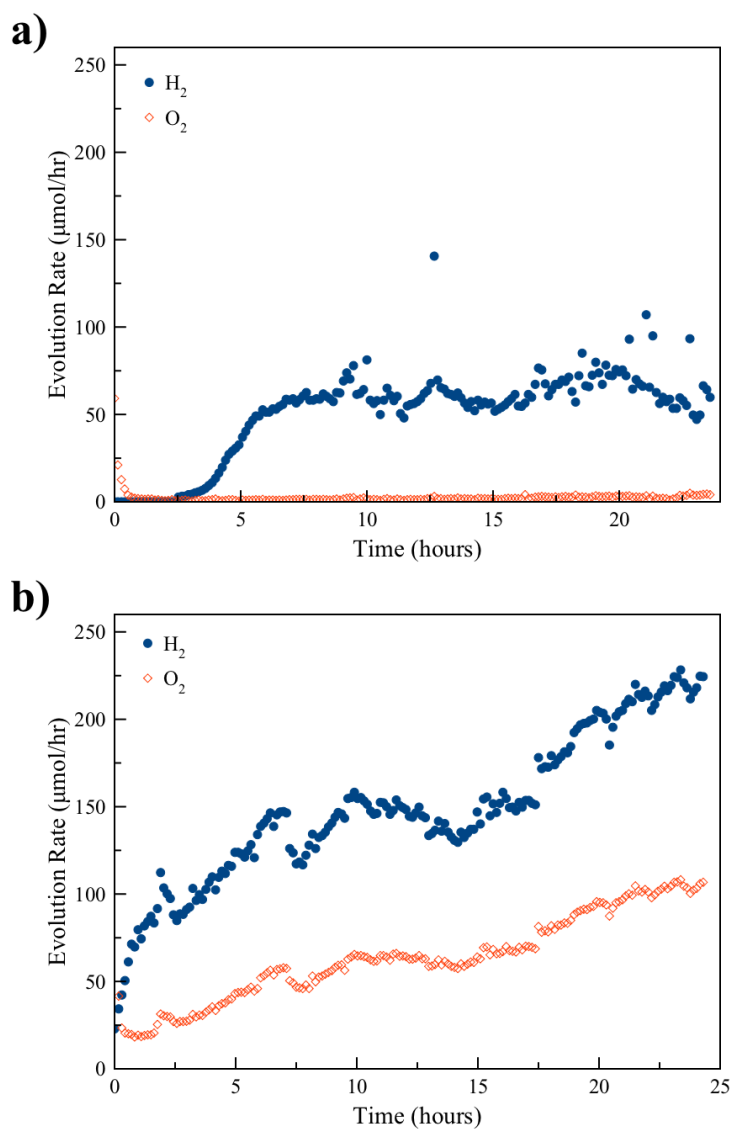


Figure 27: The rate of hydrogen and oxygen evolution over time for a 100 g sample of 0.5 mm photocatalyst particles when using a) the normal separator configuration, and b) the modified separator configuration intended to improve turbulence and liquid-gas contact. The particles were fluidized with the same 2.2M aqueous Na₂CO₃ solution at an expanded bed height of 24 cm.

To examine the effect of small particle diameters, 100 g of 0.5 mm diameter TiO₂ photocatalyst particles were fluidized in a 2.2M Na₂CO₃ solution to an expanded bed height of 24 cm for 24 hours. The reduced

particle diameter significantly reduced the required flow rate from 6.8 L/min to 3 L/min when compared to the exact same conditions for the 1.1 mm particles. As seen in Figure 27a, the rate of hydrogen evolution was depressed and unsteady throughout the experiment. It was also noted that the rate of oxygen evolution was nearly negligible and marginally above the minute background levels.

As discussed previously, it is possible to counteract the effects of low flow rate and the back reaction by increasing k_L'' . To demonstrate this, the previous 0.5 mm particle experiment was stopped after 24 hours and the separator was reconfigured such that the inlet stream entering the unit impinged against the wall of the separator as a jet, causing the jet to break up into fine droplets. This modification significantly improved the liquid-gas interfacial surface area, thus increasing the overall mass transfer coefficient. The experiment was restarted using the same photocatalyst particles and reaction solution and the reactor system was purged with a nitrogen gas stream to remove oxygen that was introduced when the separator was opened. The expanded bed height and flow rate were then set to the same conditions as before.

Figure 27b illustrates the dramatic 350% increase in the rate of hydrogen production (after 24 hours of operation) due to the increase in the overall mass transfer coefficient. It should be noted that the fluctuations in the rate of hydrogen evolution rate seen in Figure 27b and apparent lack of a steady state were due to the difficulty in maintaining a steady bed height at low flow rates as the bed height would vary dramatically with minute changes in flow rate. This sensitivity to flow rate is an effect of the increased expansion coefficient. After modifying the separator, the overall rate of hydrogen evolution actually exceeded the rates observed when using the 1.1 mm particles, despite the smaller particles having a higher platinum-deposited surface area and reduced flow rates. This suggests that the increased performance may not be due to improved mass transfer alone and that the smaller particle size does indeed contribute to improved photon capture.

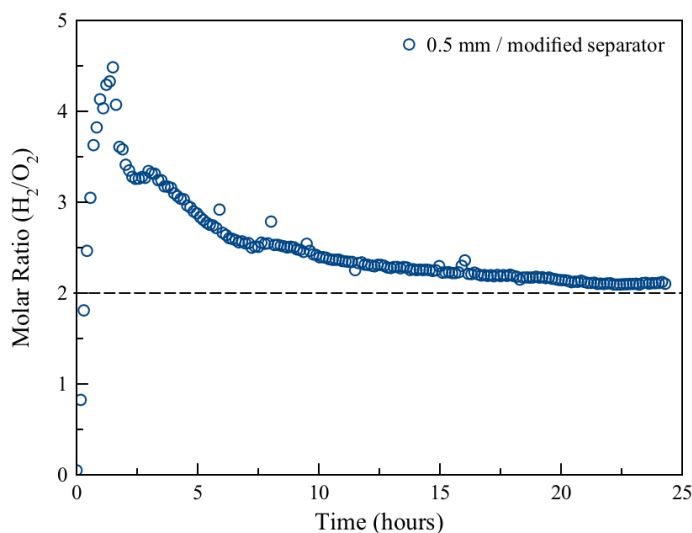


Figure 28: The stoichiometric ratio of hydrogen to oxygen with respect to time when using a modified separator. The particles for 0.5 mm particles were fluidized in a 2.2M aqueous Na_2CO_3 solution at an expanded bed height of 24 cm.

It is also interesting to note that with the increase in the rate of mass transfer oxygen was observed to readily evolve from the separator at the expected stoichiometric ratio with hydrogen (Figure 28). Moreover, the gas evolution rates were observed to climb steadily and reach an eventual pseudo-steady state in the same manner described previously in Chapter 2. This observation may suggest that the (currently unknown) interaction of Na_2CO_3 with TiO_2 may benefit from improved mass transfer and removal of the product gases from the reactor. One hypothesis is that with low rates of mass transfer the concentration of oxygen in the liquid bulk increases. The increased oxygen concentration then promotes the photoabsorption of oxygen and formation of peroxo- compounds on the TiO_2 surface, which may then compete with the beneficial effect of Na_2CO_3 and promote electron/hole recombination at the photocatalyst surface.

3.7.6 Other Fluidization Effects

While large, high density particles may be used to increase the fluidization velocities and maximize mass transfer, one final aspect critical to the operation of fluidized bed reactors, though not accounted for in the

basic optical model, is the fluid behavior of the expanded particle bed. Large particles with high densities typically behave as Geldart Class B or Class D particles²⁰⁶, which result in “bubbling” or “spouted” bed behaviors, respectively. In these bed types, pockets of the fluid phase may travel through the expanded bed, resulting in regions with low or no photocatalyst particles – allowing for photons to escape the reactor, thus reducing efficiency. Modeling of such a system would require the solution of a complex radiation transfer equation and is beyond the capabilities of the model presented here.

3.8 Conclusions

In this study we derived a mathematical model describing the water splitting performance of platinum-deposited photocatalyst particles in a fluidized bed/separator system. The model was fitted to the photocatalyst performances reported in Chapter 2, which provided estimates for the maximum achievable rate of hydrogen evolution, the back reaction rate constant, the mass transfer coefficient and the photon extinction coefficient. It was found that the model is capable of accurately predicting the rate of hydrogen evolution for a given mass of photocatalyst particles and expanded bed height. From this model, several conclusions about the behavior of the system may be drawn:

- 1) The rate of hydrogen evolution and the apparent quantum efficiency of the system are directly controlled by the rate of mass transfer in the separator unit, which in turn is a function of the fluidization flow rate.
- 2) Optimizing the rate of hydrogen evolution is a balance between maximizing the rate of photon absorption while minimizing losses due to the parasitic back reaction. This results in a maximum in the hydrogen evolution rate with respect to the mass loading of photocatalyst particles in the system. If the photocatalyst particle concentration is too low, photons pass through the system without absorption. If the photocatalyst particle concentration is too high, the increased

photocatalyst particle mass and reduced fluidization flow rates promote the parasitic back reaction.

- 3) Optimizing the reactor dimensions and employing shorter expanded bed heights can improve the efficiency of the system, however, the reactor output will be low. Increasing the expanded bed height can increase the overall rate of hydrogen evolution from the system; however, this comes at the expense of reduced efficiency.
- 4) The back reaction is the greatest source of inefficiency in the photocatalytic water splitting system and efforts should be made toward minimizing its effects. It can be seen from equation 60 that if a co-catalyst which avoids the back reaction can be found, the governing equation for the rate of hydrogen evolution collapses to that the photon absorption limited case:

$$\frac{H_{ex}}{R_{net}} = \left(\frac{2}{\Phi S_L} \right) \left(\frac{1}{1 - e^{-\alpha c_{cat}}} \right) \quad (62)$$

- 5) Improving the rate of mass transfer in the separator can counteract the effects of the back reaction. It was demonstrated experimentally that modification of the separator unit to promote mass transfer resulted in significantly improved rates of hydrogen evolution, especially for small photocatalyst particle diameters. If the rate of mass transfer can be made significantly large with respect to the back reaction, the performance of the system can approach that of a system devoid of the parasitic back reaction. For very large values of k'_L , equation 55 can be rewritten as:

$$\frac{H_{ex}}{R_{net}} = \left(\frac{2}{\Phi S_L} \right) \left(\frac{1}{1 - e^{-\alpha c_{cat}}} \right) \left[\frac{k'_r W}{q} + 1 \right] \quad (63)$$

where it can be seen that rate of hydrogen evolution still exhibits a dependence on the flow rate through the fluidized bed. Moreover, the effect of the back reaction decreases with increasing flow rate and, therefore, large or dense particles may yield improved performance over small or low density particles (ignoring differences in photon capture).

- 6) Photocatalyst particles having high bulk densities or large diameters (or both) are typically preferred to small or low density particles as they necessitate the need for high fluidization flow rates. This in turn promotes mass transfer in the separator and results in improved rates of hydrogen evolution. This is contrary to initial expectations as particles with low bulk density or small diameters typically exhibit better photon capture and require less energy for pumping.

- 7) Photocatalytic water splitting in a fluidized bed reactor may provide an advantage over suspended slurry approaches as fluidized photocatalyst particles are contained only within the volume of the expanded bed, whereas suspended photocatalyst slurries are distributed throughout the entire system volume. This yields reduced rates of back reaction when compared to photocatalyst slurries. Moreover, the fluidized bed approach allows for the separator design to be varied without altering the total mass of photocatalyst particles employed in the system and allows for improved separator designs that may not be technically feasible with suspended slurries.

Chapter 4: Scalable Anatase Nanowire Growth for Water Splitting and Photocatalytic Degradation

4.1 Introduction

TiO₂ nanoparticles with one-dimensional (1-D) morphologies - such as nanorods, nanowires and nanoribbons – have garnered a great deal of interest for photocatalytic applications, where they have demonstrated excellent performance for photocatalytic hydrogen production^{59,173–175} and water remediation^{159,176–178}. The advanced performance of 1-D TiO₂ photocatalysts is due, in large part, to their excellent charge transport and separation properties. Their highly ordered structure greatly reduces grain boundaries, which reduces the recombination of photogenerated electrons and holes²³⁷. Moreover, films of vertically aligned nanostructures significantly reduce the reflection of incident light and improve the absorption of photons (which has also led to their use as anti-reflective coatings)⁵⁷.

Nanorods and nanowires have been produced by a number of methods, however, solvo-/hydrothermal methods^{162,184–187,191,238,239} have become most popular due to their relative simplicity. Hydrothermal methods, however, often require specialized equipment, are energy intensive and are difficult to scale beyond the laboratory. Moreover, most hydrothermal methods typically result in the formation of the thermodynamically favored rutile phase. Anatase is often the desired phase for photocatalytic applications as it typically produces greater activities than rutile and its conduction band energy levels are more ideally situated for direct photocatalytic water splitting (i.e., without an applied bias)^{78,90,240,241}.

Protonated or ion-exchanged titanates have been employed as precursors to achieve crystalline TiO₂ of varying phases and shapes through careful selection of the post processing conditions²⁴². Indeed, post-treatment of titanates allows for the facile production of metastable phases such as anatase, brookite and TiO₂(B)⁹⁷, as well as branched nanostructures. Titanate nanorods have been produced via hydrothermal

methods^{189,243,244} and by soft chemical techniques²⁴⁵, which require the controlled hydrolysis of Ti^{4+} as well as the presence of cations to stabilize the titanate layers.

Water-soluble titanium complexes, such as peroxo-titanium complexes (PTC), which have gained popularity as simple and easy to handle alternatives to the more reactive TiCl_4 , TiOSO_4 and Ti-alkoxides precursors^{115,246,247}, can be hydrolyzed in low-temperature systems to produce TiO_2 nanoparticles in solution^{247,248}. Hydrolysis of these water-soluble complexes in peroxide solutions containing a suitable cation results in the formation of layered titanates¹²¹. Cheng et al. have recently demonstrated that hydrolysis of $(\text{NH}_4)_2\text{TiF}_6$ in a urea- H_2O_2 solution produces titanate sheets which spontaneously stack upon aging to form titanate nanowires¹²². Peroxo-titanate complexes have typically been produced by the dissolution of titanium metal in peroxide/ammonia solutions¹¹⁸ or by dissolving titanium hydroxides, produced by precipitation from typical Ti precursors, in H_2O_2 solutions¹²¹. Wu et al. have demonstrated that titanate nanowires can be grown on a Ti substrate in a H_2O_2 solution via a dissolution-precipitation reaction²⁴⁹.

Herein, we present a simple and scalable method for the rapid growth of anatase nanowires. In the presented method (from here on referred to as Chemical Bath Deposition), titanate nanowires were used as intermediate precursors that could be easily converted to crystalline anatase TiO_2 via calcination at temperatures ranging from 350 °C to 750 °C. As *in-situ* phase control during the growth of the nanorods was unnecessary, reaction conditions could be tailored to produce long titanate nanowires quickly and with high yield. By utilizing potassium titanium oxalate - a low-cost, water-soluble titanium salt - to generate the peroxo-titanium complex, the precursor solution and titanate nanowires could be produced in a single step. The resulting anatase nanowires were successfully employed for both the photodegradation of Rhodamine B (RhB) and methanol-assisted photocatalytic hydrogen production, where they demonstrated performance exceeding that of rutile nanorods produce via hydrothermal growth. While the

terms nanowire and nanorod are often used interchangeably in literature, we use the two terms separately to differentiate between two different structures. In this work, nanowire refers to the high aspect ratio (i.e. long and thin) 1-D anatase TiO₂ structures produced via Chemical Bath Deposition whereas nanorod refers to the low aspect ratio (i.e. short and broad) 1-D rutile TiO₂ structures produced via the hydrothermal growth method.

4.2 Experimental

4.2.1 Substrate Preparation

Transparent, conductive fluorine-doped tin oxide glass sheets (FTO, TEC 7, 7 Ω/□, Sigma Aldrich) were cut into individual 13 mm x 47 mm slides. The FTO slides were then ultrasonically degreased and cleaned in a 1:1:1 mixture of acetone, isopropyl alcohol and deionized water for 30 minutes, followed by an additional 30 minutes in deionized water. The slides were then dried with flowing air. For several samples, Kapton® polyimide tape was used to mask a 7 mm x 13 mm portion of one end of the slide to prevent the deposition of nanorods or nanoparticles so that an electrical connection could be made to the conductive FTO layer.

4.2.2 Growth of Anatase Nanorod Arrays via Chemical Bath Deposition

In a typical synthesis, 100 ml 30 wt% hydrogen peroxide (H₂O₂, Fisher) and 2–3 ml nitric acid (HNO₃, Fisher) were placed in a beaker and mixed for 10 minutes before the addition of 300 mg of potassium titanium oxalate (PTO, Sigma Aldrich) and 0-200 mg of melamine (Sigma Aldrich). The solution was gently heated to 40 °C and the solution was stirred until the melamine was completely dissolved. The resulting PTO-H₂O₂ solution was colored an intense red-orange.

FTO slides were placed at an angle, conductive-side down, in glass vials (~20 ml) and 20 ml of the PTO-H₂O₂ solution was added to each. The vials were loosely sealed to reduce evaporation while still allowing

for the release of evolved gases. The sealed vials were placed in an electric oven and maintained at 90°C for 7 hours. The slides were then removed from the vials and thoroughly washed with deionized water to remove any excess solution or loosely bound particles. The samples were briefly dried in air, ensuring to blow remaining water droplets from the deposited surface, and placed into an oven at 80 °C overnight. The slides were calcined in air at temperatures ranging from 350 °C to 800 °C for 1 hour in a furnace. Samples deposited from solutions containing 2 ml or 3 ml HNO₃ are designated CBD-N-*x* and CBD-A-*x*, respectively, where *x* is the calcination temperature.

4.2.3 Hydrothermal Growth of Rutile Nanorod Arrays

Vertically-aligned rutile nanorod arrays were grown on FTO-coated glass slides using a hydrothermal method first presented by Liu and Aydil¹⁶². Briefly, 45 ml hydrochloric acid (Fisher, 37%) and 45 ml of deionized water were added to a beaker and stirred for 15 minutes. Titanium (IV) butoxide (TBOT, 97%, Sigma Aldrich), in the amount of 1.5 ml, was slowly added to the solution and allowed to mix for 15 minutes. Four 13 mm x 47 mm slides were placed at an angle, conductive-side down, in a 150 ml Teflon-line hydrothermal vessel. Several slides were masked with Kapton® tape at one end. The TBOT solution was transferred to the hydrothermal vessel, which was then sealed and placed in an electric oven at 150 °C for 12 hours. The nanorod-deposited slides were then removed from the vessel and thoroughly washed with deionized water. The slides were briefly dried in air, ensuring to blow remaining water droplets from the deposited surface, then placed into an oven at 80°C overnight. The slides were then calcined in air at 550°C for 1 hour in a furnace. The rutile nanorod deposited samples were designated HTV-TB.

4.2.4 TiO₂ Nanoparticle (P25) Deposited Slides

For comparison purposes, ultrasonically cleaned 13 mm x 47 mm FTO slides were deposited with a layer of P25 nanoparticles (Evonik) using a spin-coating method. TiO₂ nanoparticles (4g) were added to a

solution containing 5 ml deionized water, 20 ml ethanol (Sigma Aldrich) and 0.2 ml acetylacetone (as a dispersant, Fisher) and allowed to mix for 1 hour. The solution was then ultrasonicated for 30 minutes. An FTO-coated slide was placed in the spin-coater, conductive-side up, and 0.25 ml of the TiO₂ solution was deposited on the conductive surface. The slide was spun at 3000 rpm for 30 seconds, and then placed into an oven at 80°C for 1 hour to continue drying before being calcined in air at 550°C for 1 hour in a furnace.

4.2.5 Characterization

The various films were characterized by X-ray diffraction (XRD) using a Bruker D2 Phaser desktop X-ray diffractometer using Cu-K α radiation (1.5418 Å). Imaging and energy-dispersive X-ray spectroscopy (EDX) were conducted using a Hitachi S-2600N Variable Pressure Scanning Electron Microscope (VPSEM) and a Hitachi S-4700 Field Emission Scanning Electron Microscope (FE-SEM). X-ray photoelectron spectroscopy (XPS) measurements were recorded with a Leybold MAX200 utilizing Mg K α radiation. UV-Vis Diffuse Reflectance (UV-Vis-DR) spectra of the deposited films were measured using an Ocean Optics Flame UV spectrometer with a tungsten-deuterium light source (DH-2000-BAL) and reflectance probe.

Electrochemical analyses were performed using a standard three-electrode cell and a saturated calomel reference electrode (SCE) and fine platinum mesh (10 mm x 30 mm) as the counter electrode.

Photoanodes were constructed by attaching a copper rod directly to the conductive FTO layer of each sample slide via conductive silver epoxy. The copper rod was cover with heat-shrink tubing and all exposed electrical connections were sealed with non-conductive epoxy. All regions of the sample slides were masked with PTFE film save for a ~ 0.8 cm² exposed region at on end of the slide. All electrochemical measurements were performed in a quartz cell using 1M KOH (pH 13.6), which was purged with Ar to remove dissolved oxygen and reaction products. An ultraviolet (UV) irradiation

system consisting of four 8W low-pressure mercury T5 bulbs (primary output at 254 nm), placed 4 cm from the quartz cell, was used to irradiate the samples during illuminated linear voltage sweeps (10 mV/s). Electrochemical impedance spectroscopy (EIS) measurements were made using the same set-up in the dark with a frequency range of 10^{-1} to 10^5 Hz and an applied AC voltage of 10 mV_{rms}. Both linear sweeps and EIS measurements were conducted using a Bio-Logic VMP3 potentiostat and EC-Lab workstation.

4.2.5.1 Hydrogen Evolution

Prior to all hydrogen evolution experiments, 13 mm x 13 mm samples were cut from the as-deposited slides and placed individually into 10 ml beakers for platinum photodeposition. An appropriate amount of an aqueous 9.2×10^{-4} M chloroplatinic acid solution, such that platinum would be photodeposited on the TiO₂ at a rate of ~1 wt%, was diluted with water and methanol to produce a 30-vol% methanol/water solution, which was then purged with nitrogen for 1 hour to remove dissolved oxygen. Two milliliters (2 ml) of the purged platinum solution was added to each beaker such that each sample was completely covered by solution. The beakers were then placed under a UV irradiation set-up consisting of four 8W low-pressure mercury T5 bulbs and irradiated (254 nm, 5 mW/cm²) for 4 hours. The samples were rinsed thoroughly with deionized water and dried in an oven overnight at 80 °C.

Photocatalytic hydrogen evolution was achieved in a custom-built four-cell reactor. Each reaction cell was 24 mm in diameter, 10 mm deep and individually equipped with a pressure sensor, gas sampling port and connections to allow vacuum- and N₂-purging of each cell. The total head volume of each reaction cell was approximately 6.3 cm³. In a typical experiment, a 30-vol% methanol/water solution was purged with pure nitrogen (50 cc/min) for 1 hour to remove dissolved oxygen. A 13 mm x 13 mm Pt-deposited sample was placed into a 20 mm plastic holder cup, which was then filled with 2 ml of the methanol solution and placed in each cell. Each cell was sealed with a quartz glass window and purged with

flowing N₂ for 30 minutes; following purging, each cell was filled with N₂ to an initial pressure of 141 kPa. The four-cell reactor was placed under the 4x8W UV lamp system and irradiated at an intensity of 5 mW/cm². The quartz window of each cell was covered with a shutter and the reactor was allowed to reach thermal equilibrium, as evidenced by a steady-state cell pressure. The shutters were removed and the samples were irradiated for 1 hour, during which time the pressure of each cell was recorded to monitor the rate of gas evolution. Following each experiment, a 3 ml gas sample was taken from each cell using a syringe and injected into a gas chromatography system (Agilent 7890A, dual TCD, He and N₂ carrier gases) to determine the final hydrogen concentration.

4.2.5.2 Photocatalytic Performance

The photocatalytic performance of the nanorod-deposited samples was evaluated by the degradation of rhodamine B (RhB). The TiO₂-deposited slides were cut into 13mm x 13 mm samples and placed into the bottom of identical 30 ml beakers, TiO₂-side up. The beakers were each filled with 10 ml of a 5-mg/L RhB solution and stored in the dark for 4 hours to allow the dye to reach adsorption equilibrium. The samples were then irradiated by a UV lamp system, consisting of two 40W low-pressure mercury T5 bulbs (primary output at 254 nm); the height of the lamps was adjusted such that the UV irradiance at the samples was measured to be 5 mW/cm². Aliquots (3ml) of solution were collected from each beaker at 20-minute intervals and the RhB concentration was analyzed using a Cary 100 photospectrometer; the aliquots were then returned to their respective beakers. The beakers were agitated gently by hand before and after sampling to remove any concentration gradients. To evaluate the effect of mass transfer on the rate of photodegradation, nanorod- and P25-deposited samples were suspended in 30 ml beakers above magnetic stir bars using stainless steel mesh baskets; the beakers were filled with 20 ml of 5-mg/L RhB solution and the lamp height was adjusted such that the irradiance reaching the samples was measured to be 5 mW/cm². The solutions were stirred at high rate and the samples were allowed to reach equilibrium

with the solution in the dark for 4 hours before following the same experimental procedure described above.

4.3 Results and Discussion

Vertically aligned, high aspect ratio nanowires were successfully grown on FTO substrates via a low temperature chemical bath deposition method. This method utilized the thermal decomposition of a peroxotitanium complex (PTC) in a $\text{H}_2\text{O}_2/\text{HNO}_3$ solution containing ammonium ions to grow titanate nanowires, which are then subsequently transformed to crystalline TiO_2 via calcination in air. Two series of samples were produced via chemical bath deposition using HNO_3 concentrations of 0.31M and 0.46M, and were labeled CBD-N and CBD-A, respectively.

SEM imaging (Figure 29 and Figure 30) revealed that long, high aspect-ratio nanowires were grown from the FTO surface. The nanowires were, on average, $\sim 62 \text{ nm} \times 1.11 \text{ }\mu\text{m}$ and $\sim 52 \text{ nm} \times 2.45 \text{ }\mu\text{m}$ for CBD-N and CBD-A, respectively. During nanowire growth, a large amount of precipitate was observed in the CBD-N solution, while little to any was observed in the CBD-A solution; it is hypothesized that nanowire growth in the CBD-N solution was limited due to the competing nucleation and precipitation of titanate in solution. This effect is examined further in the formation mechanism discussion presented later.

X-ray diffraction analysis of the as-synthesized CBD-A samples (Figure 31a) revealed that the nanowires are layered titanate, as indicated by the low-angle peak at 8.7° and a weak peak at 17.3° . An additional weak peak overlapping the strong FTO background peak could be seen; Reitveld refinement revealed this peak to be located at $\sim 25.9^\circ$. These three peak angles are consistent with the Bragg relationship for layered structures and correspond to lattice spacings of 1.02 nm, 1.02 nm and, 1.03 nm, respectively. Calcination at 250°C for 1 hour resulted in the low-angle peak shifting to 9.31° , indicating a narrowing of the lattice spacing. This is consistent with the deintercalation of water or ammonia from the lattice. After

calcination at 350 °C, the low angle peak disappears completely and is accompanied by the appearance of a weak peak at 25.35° corresponding to the appearance of anatase.

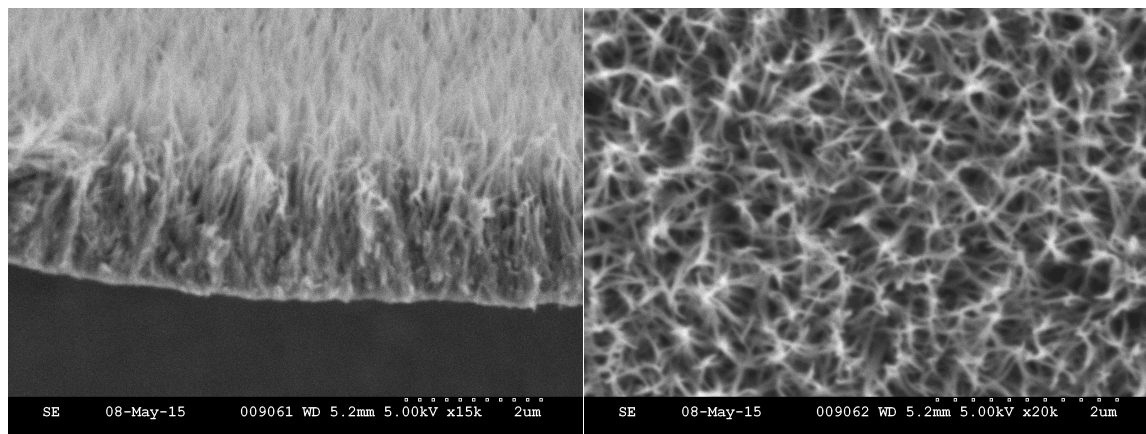


Figure 29: a) cross-section and b) top-view SEM images of CBD-A nanowires grown in peroxotitanium solution containing 0.46M HNO₃

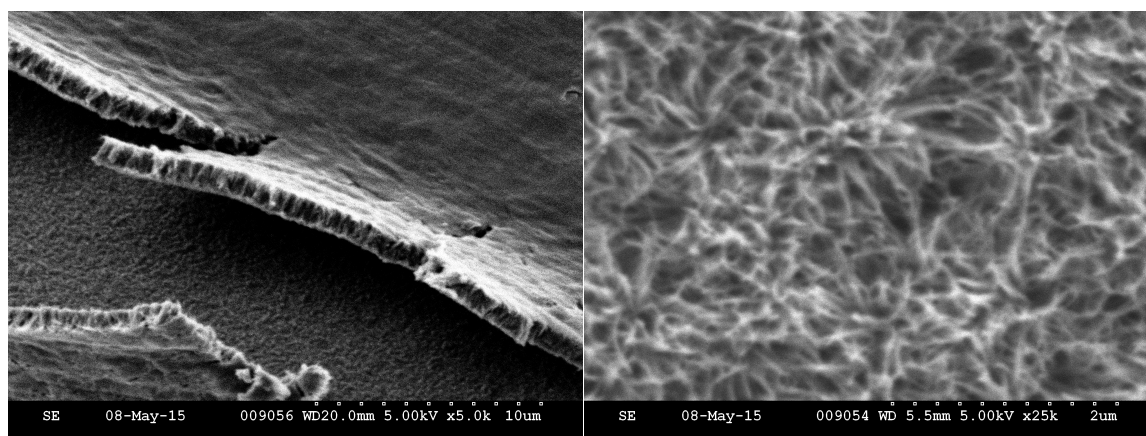


Figure 30: a) cross-section and b) top-view SEM images of CBD-N nanowires grown in peroxotitanium solution containing 0.31M HNO₃

4.3.1 XRD

For CBD-A samples calcined at temperatures ranging from 350 °C to 800 °C (Figure 31b), peaks that index well to anatase (JCPDS 21-1272) can be clearly seen. The intensity of the anatase [101] peak (located at 25.3°) increases up to 650 °C, followed by a subsequent decrease at 750 °C due to the partial conversion of anatase to rutile (JCPDS 21-1276); thus, the titanate nanowires are fully converted to anatase TiO₂ at temperatures between 550-650 °C. The diffraction patterns for the CBD-N samples

(Figure 58 in Appendix C) display the exact same behaviors as those described above for the CBD-A samples, though the peak intensities are reduced in intensity due to the shortened nanowires in the CDB-N films.

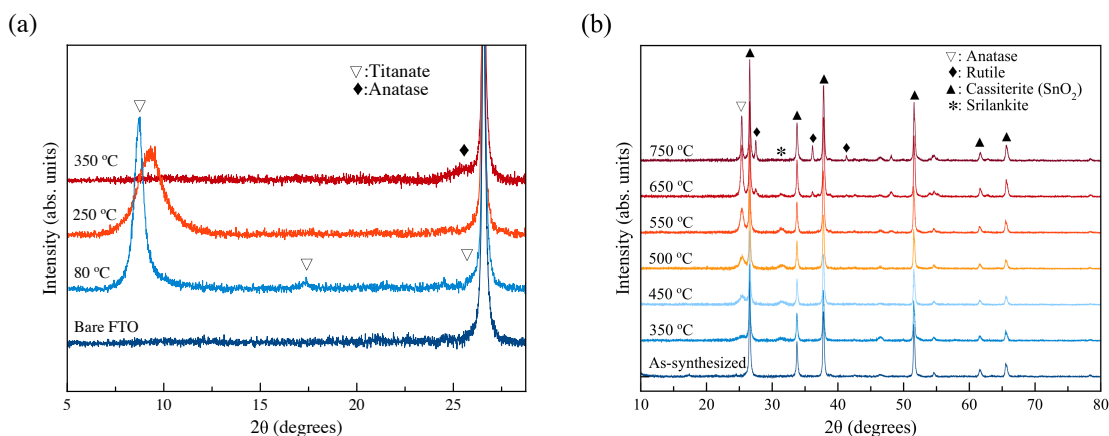


Figure 31: a) Narrow-angle XRD pattern of CBD-A nanowires calcined at 80 °C, 250 °C and 350 °C for 1 hour. b) XRD patterns of CBD-A nanowires calcined at temperatures ranging from 350 °C to 750 °C.

The titanate phase (Figure 31a) was identified as $\text{H}_2\text{Ti}_5\text{O}_{11} \cdot 3\text{H}_2\text{O}$ (JCPDS 44-0130) by other researchers who produced nanowires using a similar approach^{94,250–252}. It has been reported, however, that titanates of the form $\text{H}_2\text{Ti}_n\text{O}_{2n+1} \cdot y\text{H}_2\text{O}$ ($3 \leq n \leq 6$) transform to $\text{TiO}_2(\text{B})$ upon dehydration and calcination⁹⁷, while titanates having the form $\text{H}_x\text{Ti}_{2-x/4}\square_{x/4}\text{O}_4 \cdot y\text{H}_2\text{O}$ (where \square signifies vacant Ti sites) transform to anatase at 450 °C by way of an amorphous intermediate phase upon heating⁹². Given the absence of $\text{TiO}_2(\text{B})$ and the amorphous nature of the samples calcined below 450 °C, we propose that the as-synthesized titanate nanorods have the formula $\text{H}_x\text{Ti}_{2-x/4}\square_{x/4}\text{O}_4 \cdot y\text{H}_2\text{O}$. This is an important distinction as these titanates have straight layers, unlike $\text{H}_2\text{Ti}_n\text{O}_{2n+1} \cdot y\text{H}_2\text{O}$ titanates that have stepped layers; this may provide further insight into the formation of the nanowires. Moreover, Sasaki et al. demonstrated that the interlayer spacing of the $\text{H}_x\text{Ti}_{2-x/4}\square_{x/4}\text{O}_4 \cdot y\text{H}_2\text{O}$ titanates becomes expanded upon intercalation of water and ionic species⁹², yielding interlayer spacing similar to those observed in the uncalcined CBD-A samples.

A small peak situated at 31.4° was observed in the calcined samples. A similar peak reported in nanowires grown from titanate metal was suggested to be srilankite (JCPDS 21-1236)^{249–251,253}, a (Zr,Ti)O₂ mineral with an orthorhombic crystal structure; no zirconia, however, could be detected in our samples by EDX or XPS analysis. Orthorhombic TiO₂ polymorphs exhibiting a crystal structure similar to that of the mineral may alternately be referred to as Srilankite-TiO₂, though are chemically different from the mineral. The srilankite peak increased in intensity up to 550 °C, and then subsequently decreased and disappeared at higher calcination temperatures. As the calcination temperature was increased from 550 °C to 650 °C, a small rutile peak was observed at 27.5°; however, the [001] anatase peak continued to increase in intensity up to 650 °C while the srilankite peak decreased. This observation suggests that the srilankite-like phase is a meta-stable intermediate and begins to transform to rutile at temperatures above 550 °C. The potential cause of the srilankite phase is discussed further later.

4.3.2 UV-Vis-DR Analysis

The absorbance (Figure 32a) and band gap energies (Figure 32b) of the samples were determined via diffuse reflectance spectroscopy. Equivalent absorption spectra were obtained from the measured reflectance values via the Kubelka-Munk function²⁵⁴, which is defined as:

$$F(R) = \frac{(1 - R)^2}{2R} = \frac{k}{s} \quad (64)$$

where R is the percentage of reflected light at a given wavelength, k is the absorption coefficient and s is the scattering coefficient. As the scattering coefficient is largely independent of wavelength, F(R) is directly proportional with the absorption coefficient and is thus commonly employed as a proxy for the actual absorption coefficient. The CBD-A and CBD-N samples were translucent at low calcination temperatures and became notably more opaque as the calcination temperature increased beyond 550 °C;

this can be clearly observed in Figure 32a by the downward shift of the upward inflecting tail in the visible region of the absorption spectrum with increasing calcination temperature.

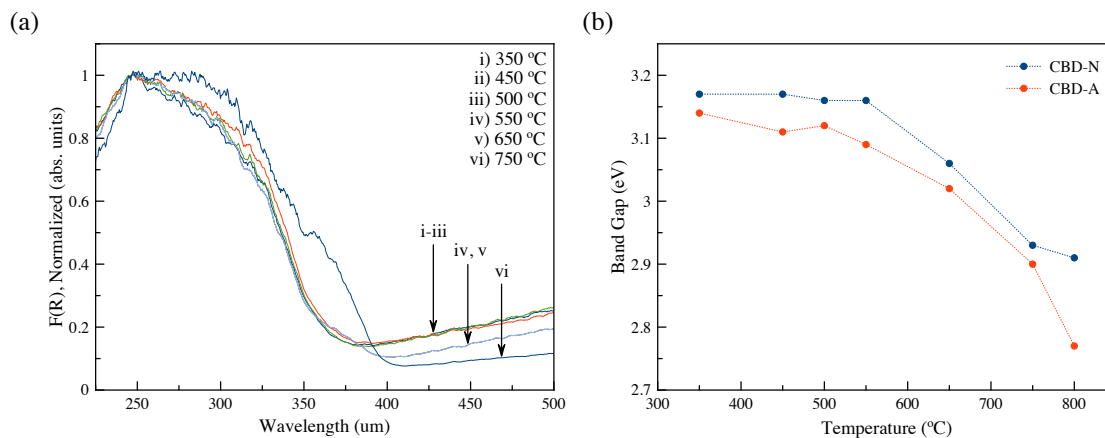


Figure 32: a) Diffuse reflectance UV-Vis absorption spectra for CBD-A samples calcined at temperatures between 350 °C and 750 °C and b) Band gap energies for CBD-A and CBD-N versus temperature.

The optical band gap of the samples was determined via the Tauc method²⁵⁵, where the photon energy, $h\nu$, is plotted on the abscissa and $(kh\nu)^{1/n}$ is plotted on the ordinate (n denotes the nature of the electronic transition and $n = 2$ for indirect semiconductors such as TiO_2). The resulting “Tauc Plot” yields an apparent linear region that indicates the onset of optical absorption; extrapolation of this linear region to the abscissa reveals the band gap energy of the semiconductor. Again, as $F(R)$ is directly proportional with the absorption coefficient, $F(R)$ can be substituted for k in the Tauc equation to yield $(F(R)h\nu)^{1/n}$. The band gap energies of both CBD-A and CBD-N were found to decrease gradually up to 550 °C, beyond which they decreased sharply due to the transformation of anatase to rutile (Figure 32b). For comparison, the band gap energies of P25 powder, P25-deposited film and HTV rutile nanorod films were determined to be 3.23, 3.07 eV and 2.90 eV, respectively (Figure 59 in Appendix C). For all temperatures, the band gap energies of the CBD-A and CBD-N samples were less than the 3.2 eV typically reported for anatase nanrods²³⁹, suggesting the possible doping or sensitization of TiO_2 toward the visible region. Tauc plots for both CBD-A and CBD-N samples display a second linear region beginning in the visible

region (Figure 33). This feature is particularly notable for samples calcined at 550 °C and 650 °C and corresponds to an absorption onset at 2.60 eV. As the absorption of this feature is weak, it is not likely to be due to a band-to-band transition but rather due to transitions to or from defect states in the band gap.

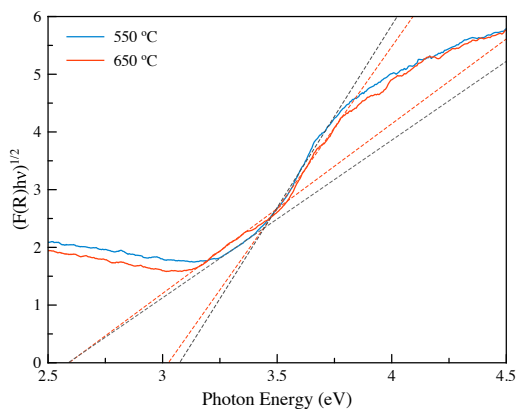


Figure 33: Tauc plots for CBD-A samples calcined at 550 °C and 650 °C

4.3.3 XPS Analysis

XPS analysis of Pt-deposited CBD-A films revealed the presence of nitrogen, a well-known dopant that yields visible light activity in TiO₂. The nitrogen content of the CBD-A samples calcined at 350 °C contained a significant amount of nitrogen in the amount of 2.8 at%, which decreased to 1.1 at% at 550 °C. Increasing the temperature to 650 °C resulted in a slight increase in the nitrogen content to 1.5 at%.

High-resolution XPS spectra over the Ti 2p binding energies (BE) (Figure 34a) displayed Ti 2p_{3/2} and Ti 2p_{1/2} peaks located at 458.7 eV and 464.4 eV, respectively, with a peak separation of 5.7 eV. These can be identified as those belonging to anatase TiO₂²⁵⁶. No notable Ti 2p doublets associated with Ti³⁺, which would result from interstitial N-doping, could be observed.

The O 1s XPS spectrum was fit by three peaks (Figure 34b). The BE peak at 530.0 corresponded to Ti-O bonds in the lattice²⁵⁷; the position of Ti-O peak for the sample calcined at 350 °C was shifted to

530.2 eV which was assumed to be due to N-containing species bound to the surface which were desorbed or decomposed at higher temperatures. Accurate identification of the 531.7 eV peak is difficult as a number of species, such as O=C-N^{258,259}, C-O^{257,260}, Ti-N²⁶¹, Ti-O-C²⁶¹ and -OH groups^{256,262-265} have all been shown to have binding energies in this region. The 533.2 eV O 1s peak can be ascribed to C-O(H)²⁶⁶ and -C-O-²⁶⁰.

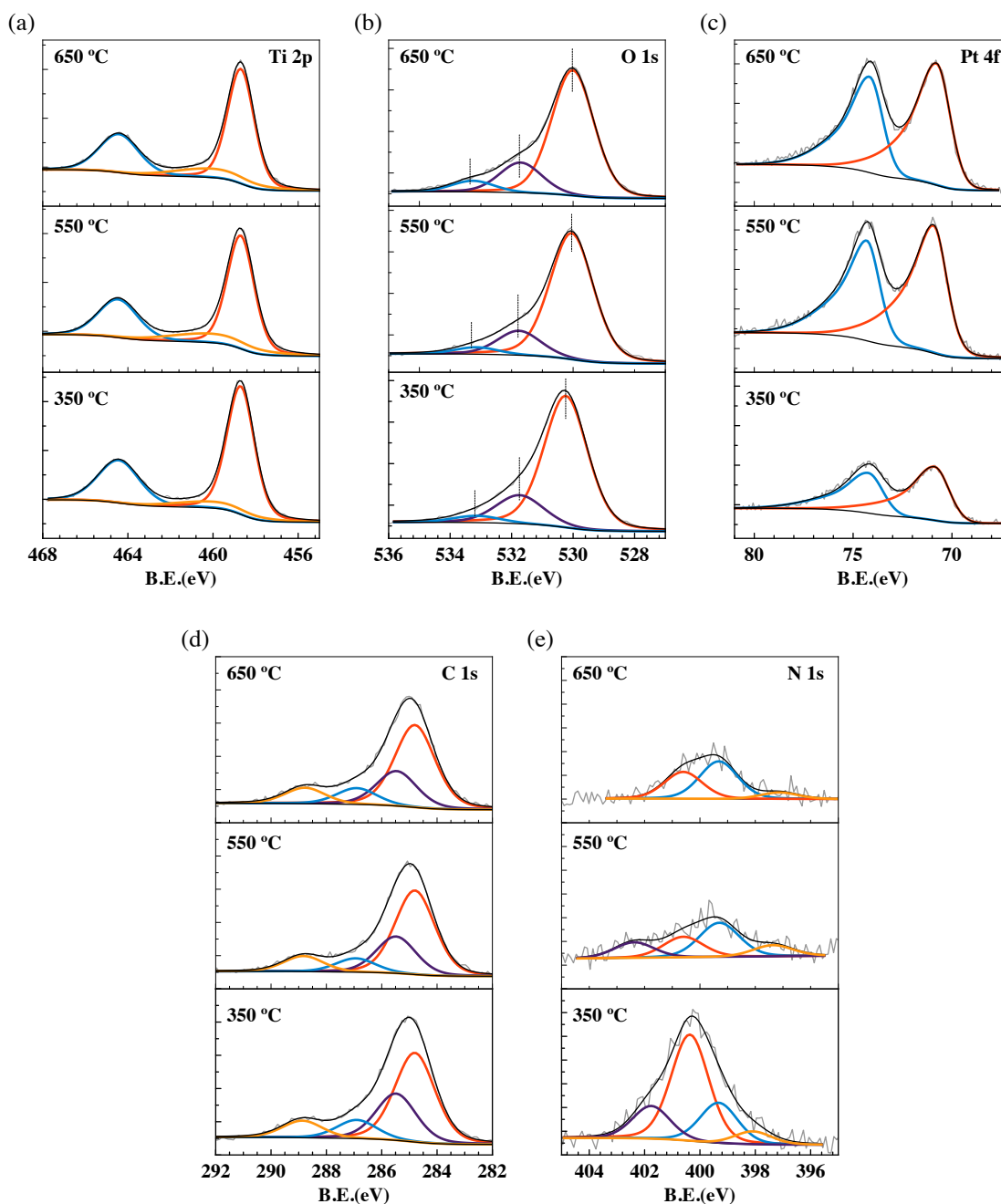


Figure 34: High resolution XPS spectra for a) Ti 2p, b) O 1s, c) Pt 4f, d) C 1s, and e) N 1s

Photodeposited platinum was detected on the samples in the amount of 0.7, 1.6 and 1.6 at% for CBD-A samples calcined at 350 °C, 550 °C and 650 °C, respectively. The Pt 4f peaks were fit with asymmetric curves (Figure 34c) and were found to be located at 70.9 and 74.2 eV, indicating that the platinum was reduced completely to Pt⁰.

Four peaks can be distinguished in the C 1s spectrum (Figure 34d). The first two peaks may be assigned to adventitious carbon at 284.8 eV, and C-C^{56,267,268} and C=N²⁶⁹⁻²⁷¹ at 285.5 eV. The peak observed at 286.9 eV is due to the presence of C-O^{56,257} and C-N^{267,272}. The high energy C 1s peak at 288.8 eV is due to C=O²⁶², Ti-O-C or Ti-OCO^{262,273}.

The high-resolution N 1s spectra (Figure 34e) could be fit with four peaks centered at 398, 399.3, 400.6 and 401.7 eV. Binding energy peaks located at 285.5 eV and 400.6 eV have been shown to be due to the presence of C=C-N-^{36,274} and polycyanogen (-C=N-)_x²⁷⁵, while the 399.3 eV peak can be assigned to C-N=C²⁶⁵, (-C=N-)_x²⁷⁵, =N-²⁶⁹, and N atoms bound to three C atoms in a heptazine ring²⁷¹. The 400.6 eV peak may also be due to -NH₂²⁶⁹, graphite-like N-Csp² bonds³⁶ or oxidized N species such as Ti-O-N or Ti-N-O linkages^{276,277}.

These binding energies are consistent with typical values for triazine compounds such as melamine^{269,278}, and for TiO₂ that has been doped with graphitic-carbon nitride (g-C₃N₄) or poly-s-triazine species, such as melem or melon^{36,274-276,279}. It has been reported that heating TiO₂ in the presence of urea, melamine or other triazine species results in the polycondensation of triazine species on the TiO₂ surface. Thermal decomposition of urea forms melamine^{36,275,280}, which then undergoes polycondensation to form poly-s-triazine/heptazine (i.e., melem/ melam/melon) between 360 °C and 500 °C²⁸¹⁻²⁸³. The chemical structure of melamine and its poly-s-triazine condensation products are shown in Figure 35. Heating poly-s-triazines above 550 °C results in the formation of g-C₃N₄²⁸². Poly-s-triazine and g-C₃N₄ doped onto the

surface of TiO_2 (herein collectively referred to as $\text{TiO}_2\text{-N,C}$) have been shown to act as sensitizers that extend the activity of TiO_2 into the visible region and may thus explain the reduced band gap values shown in Figure 32b. Indeed, the weak absorption feature noted in Figure 32a having an absorption onset beginning at 2.6 eV, corresponds with common band gap values for s-heptazine (i.e., melon) and carbon nitrides^{283–285} and may be due to HOMO-LUMO transitions in these compounds or due to defect states induced by their presence.

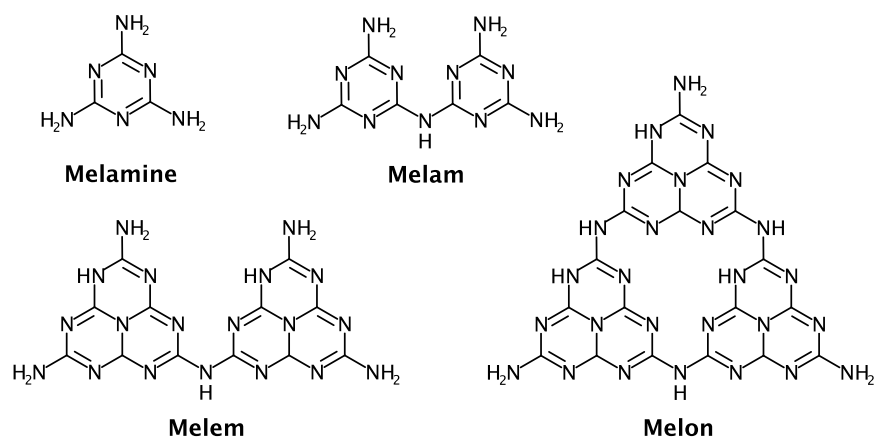


Figure 35: Chemical structures of melamine and its condensation products: melam, melem and melon

It can be seen in the N 1s spectra that as the calcination temperature increases from 350 °C to 550 °C, there is a significant decrease in the peak centered around 400.3–400.6 eV, as well as decrease in the peak centered at 401.7–402 eV. As the calcination temperature increases from 550 °C to 650 °C, the peaks at 398 and 401.7 largely disappear. The low binding energy N 1s peak at 398 eV is due to -NH- ²⁶⁵ and C-NH_2 ²⁶⁹, while 401.7–402 eV peak has been assigned to N species in higher oxidation states, such as NH_4^+ ^{286,287}, as well -NH_x groups^{265,288}. The initial large decrease in these peaks may be assumed to be due to the reaction of -NH_2 groups during the polycondensation of triazine, decomposition of melamine/triazine species and the removal of any remaining NH_4^+ , which may be intercalated between the titanate layers. It has been shown that heating melamine in the presence of TiO_2 results in N-H bond breakage in the amine groups due to nucleophilic attack by surface -OH groups, resulting in the

formation of Ti-(NH)- bonds^{36,275,282,289}. Moreover, it has been shown that titanates calcined in the presence of urea and melamine formed TiO₂-N,C^{279,289}, and that the high –OH content of titanates promoted the polycondensation of triazine. This resulted in a higher poly-s-triazine content for TiO₂-N,C produced from titanates than those produced using TiO₂²⁸⁹. The reduction, and eventual disappearance, of the 398 eV and 401.7 eV peaks as the calcination temperature is increased may then be attributed to the consumption –NH₂ groups via reaction with surface –OH groups and the polycondensation of triazine.

4.3.4 Thermogravimetric Analysis

Thermogravimetric analysis (TG/DTGA) for CBD-A and CBD-N (Figure 36) revealed that the nanowires undergo two weight loss stages. The first weight loss stage occurred between 100 and 525 °C, where CBD-A and CBD-N exhibit weight losses of 24.8% and 25.0%, respectively, and was followed by a smaller secondary weight loss of 0.6% and 1.3%, respectively, between 525 °C and 670 °C. This first mass loss is consistent with the dehydration and collapse of the titanate layers to form TiO₂, however, the mass lost over this range is greater than the expected 7-15% from protonated layered titanates^{92,97,290}.

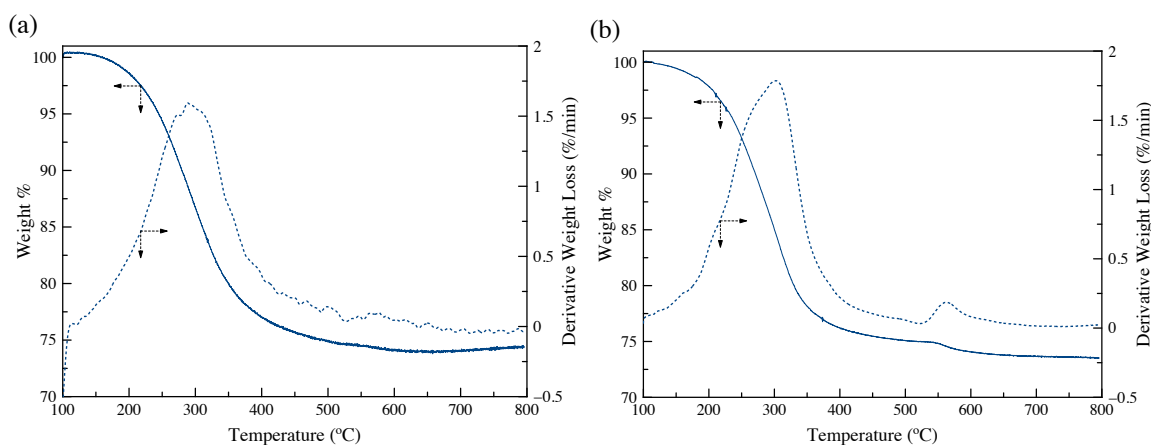


Figure 36: TGA/DTGA curves for a) CBD-A and b) CBD-N

The polycondensation of melamine on the surface of TiO₂ has been shown to occur between 360 °C and 500 °C^{281–283}, evolving ammonia with each polymerization step. The resulting poly-s-triazine species,

such as melem and melon, have been reported to be stable in air up to 550 °C^{281,291,292}. Indeed, it has been reported that TiO₂-N,C exhibits rapid weight loss between 500 °C and 650 °C, which was attributed to the decomposition or desorption of poly-s-triazine compounds^{281,282,293,294}. Gong et al.²⁸⁹, however, reported a sharp weight loss occurring at lower temperatures, between 350 °C and 500 °C, for TiO₂-N,C heated in air; this was ascribed to the depolymerization, oxidation and volatilization of melon. Gong et al. observed a second, smaller weight loss between 550 °C and 800 °C. Similarly, it has been demonstrated that the thermal decomposition of melamine on TiO₂ may occur around 325 °C²⁸².

The skewed peak shape of the derivative weight loss curves between 100 °C and 525 °C appears to be due to two overlapping weight loss peaks. Deconvolution of the DTG peak between 100 and 525 °C yields two peaks, located at 260 °C and 310 °C for both CBD-A and CBD-N; these peaks correspond approximately with the expected maximum rate of weight loss for the dehydration of titanates^{92,97} and the decomposition/ deammonation of melamine^{12,280,282,283,293}, respectively. The additional weight lost in the first stage can, therefore, be attributed to the evolution ammonia (during polycondensation), the decomposition of melamine and partial decomposition of poly-s-triazine; while the second weight loss stage can be attributed to the decomposition or desorption of poly-s-triazine compounds.

4.3.5 Growth Mechanism

4.3.5.1 Effect of Acid Concentration

The formation of the various TiO₂ polymorphs is known to follow the Ostwald step rule^{93,98}, whereby the least stable phase is precipitated first, followed by subsequent reformation of the crystal lattice to produce the next stable phase. As such, slow particle formation or long aging times at moderate temperatures is necessary for the formation of layered titanates; low temperatures (<80 °C) or fast hydrolysis typically yield amorphous TiO₂, whereas high temperatures (>150 °C) typically result in anatase or rutile^{93,98,99,121,295,296}. It is known that increasing [H⁺] acts to slow the rate of hydrolysis and condensation;

as such HNO_3 was employed at concentrations of 0.31M and 0.46M, and were labeled CBD-N and CBD-A, respectively.

Initially, the CBD-N solution was colored an intense orange, whereas the CBD-A solution was a deep red-orange; as the reaction progressed, the color of each solution lightened to a pale yellow/orange. The temporal color shift of each solution can be seen in Figure 60 in Appendix C. It was observed that during nanowire growth there was a critical point at which nanowires began to deposit rapidly, which was accompanied by an intense evolution of gas bubbles. It is hypothesized that deposited nanowires catalyze the decomposition of H_2O_2 , thus the rapid gas evolution corresponds with the onset of nanowire growth. The onset of rapid nanowire growth was delayed in the CBD-A solution due to the slower rate of hydrolysis and nucleation.

The CBD-N solution produced significant amounts of precipitated titanate during nanowire growth while the CBD-A solution displayed negligible amounts. The slower rate of hydrolysis in the CBD-A solution reduced homogeneous nucleation in solution and promoted heterogeneous nucleation on the substrate surface, whereas nucleation and precipitation in solution competed with nanowire growth in the CBD-N solution. This resulted in the growth of 2.45 μm long nanowires in the CBD-A solution versus the 1.11 μm nanowires formed in the CBD-N solution. It was also noted that the increase in $[\text{HNO}_3]$ resulted in a slight decrease in the nanowire diameter from 62 nm in the CBD-N samples to 52 nm in the CBD-A samples. It has been demonstrated that NO_3^- ions adsorb to TiO_2 surfaces²⁹⁷⁻²⁹⁹, thus the adsorption of NO_3^- onto certain facets of the nanowires may promote anisotropic growth and result in narrower, well-defined nanowires. Wu et al.²⁴⁹ noted a similar result that peroxy-titanium solutions without HNO_3 resulted in broad, flake-like titanate growths, while the addition of HNO_3 resulted in separated nanowires.

4.3.5.2 Role of Melamine

It has been reported that cations, such as Na^+ , K^+ or NH_4^+ present in solution act to stabilize the negatively charged titanate layers, thus preventing layer collapse and crystallization^{93,98,99,245,295,296}. In the absence of a suitable cation, charge neutrality can only be maintained by layers collapsing through destabilization and recombination of TiO_6 octahedra³⁰⁰. Several researchers have produced ammonium ions *in-situ* by the acidic hydrolysis of urea^{245,301,302}, hexamethylenetetramine (HMT)^{303–308} and melamine^{94,249–253,309} in heated (>80 °C) solutions. The evolution of NH_4^+ through hydrolysis not only acts to stabilize titanates but also serves to neutralize H^+ liberated through hydrolysis of Ti^{4+} ions¹¹⁷, thus allowing *in situ* control of the solution pH. As such, both melamine and urea were investigated for their effect on nanowire formation.

CBD-A solutions with and without melamine were heated at 90 °C for 7 hours. It was observed that the solution without melamine quickly produced precipitate in solution with little-to-no nanowire growth and, what little film that was deposit quickly delaminated from the FTO substrate upon drying. The solution containing melamine produced 2.45 μm -thick nanowire films with little precipitate (as discussed earlier). It has been demonstrated that urea, triazine compounds (such as melamine), SO_4^{2-} and F^- ions act to slow hydrolysis by coordinating with Ti^{4+} centers^{246,293,310–313}, which in turn slows homogeneous nucleation in solution. This simultaneously leads to increased heterogeneous nucleation on both hydrophobic and hydrophilic surfaces, which reduces precipitate formation, and improves adhesion and film growth. Indeed, for CBD-A solutions containing melamine, nanowires could be seen growing not only from the FTO substrate but also from the sides of the glass vials used to contain the reaction.

Solutions without melamine were initially colored pale orange, whereas the melamine-containing solutions were a deep red-orange. This increasing color intensity suggests an increase in coordination with the Ti^{4+} , further supporting the hypothesis that melamine (or one of its decomposition products)

coordinates with the Ti^{4+} centers (likely through the lone electron pairs of an amino groups or through carbonyl/hydroxyl groups attached to the triazine ring). During nanowire growth, the solution containing melamine noticeably lightened to a pale yellow while the solution without melamine remained bright orange, indicating that a large amount of the peroxy-titanium complex remained unreacted in the absence of melamine. For both solutions, the initial pH was measured to be ~ 0.1 ; however, after nanowire growth, the pH of the solution with melamine increased to 0.55 whereas the pH of solution without only increased to 0.2. The pH increase due to hydrolysis of melamine may drive the hydrolysis of the peroxy-titanium complex, promoting the nucleation and growth of nanowires.

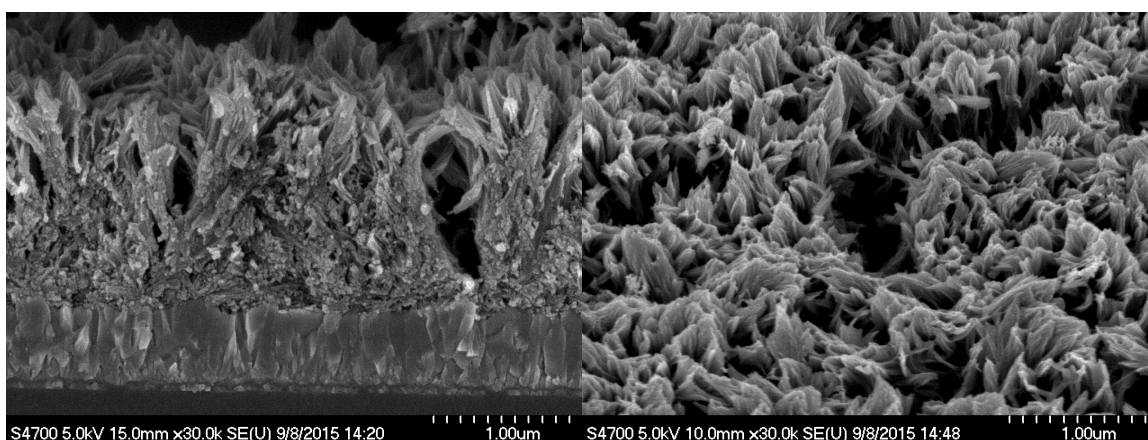


Figure 37: FESEM a) cross-section and b) top-view images of nanowires grown in peroxy-titanium solution containing 45 mM urea

Urea was substituted for melamine in the amount of 45 mM (such that similar amounts of NH_4^+ liberated by melamine hydrolysis would be achieved), producing an intense orange solution. The behavior of nanowire growth from the urea-containing solution was much the same as that observed for melamine-containing solutions; however, large quantities of precipitate were produced, in similar fashion to the CBD-N solution (0.31M HNO_3) described earlier. The less intensely colored solution and increased amount of precipitate formed in-solution indicated that urea coordinates with Ti^{4+} less strongly than melamine, thus increasing the rate of hydrolysis. As seen in Figure 37, the nanowire growth was stunted

to 1.49 μm due to competing nucleation-precipitation in solution, again, in similar behavior to films grown in the CBD-N solutions.

Also shown in Figure 37, films grown from urea-containing solutions are more densely structured than those produced from melamine-containing solutions and consist of blade-like nanowire bundles 100-200 nm wide. These blade-like bundles are formed by narrow nanowires ~ 26 nm in diameter attached via their vertical faces. The isoelectric point of TiO_2 is typically reported to be $\sim \text{pH } 6$, thus TiO_2 surfaces in highly acid solutions will be protonated and have a positive charge. NO_3^- ^{297–299}, HMT^{242,314,315} and urea^{301,311} all may adsorb electrostatically to positively charged TiO_2 surfaces (urea likely adsorbing as a bidentate species via its amine groups). As discussed earlier, adsorption of NO_3^- onto the deposited nanowires decreases nanowire diameter and improves nanowire dispersion, thereby preventing aggregation of the nanowires. Adamu²⁹⁹ demonstrated that the presence of 2 mM oxalic acid (which adsorbs as a bidentate species) was sufficient to inhibit NO_3^- adsorption onto TiO_2 surfaces. Moreover, Yamabi³¹⁶ concluded that urea was preferentially adsorbed onto TiO_2 nanorods, displacing SO_4^{2-} anions (which are known to adsorb strongly to metal oxide surfaces). The observed agglomeration of nanowires into larger blade-like structures may, therefore, be the result of a reduction of surface adsorbed NO_3^- anions due to competitive adsorption by urea. In contrast, melamine has been shown to only adsorb on TiO_2 for $\text{pH} > 5$ ³¹⁷ and cyanuric acid displays nearly negligible adsorption on TiO_2 ¹² at all pH, thus the adsorption of nitric acid on the surface of the nanowires remains unaffected and long, individually separated nanowires are produced. This effect may offer an explanation as to why reports utilizing peroxide solutions with^{94,249–253,309,318} or without^{307,319,320} melamine produce individually separated nanowires, whereas reports utilizing HMT (which adsorbs onto TiO_2) produce nanoflower-like structures, where smaller nanorods fuse together to form the nanoflower “petals”^{305,306,315}. It is not expected that oxalate ions from the PTO precursor adsorb to the nanowire surface during growth as it has been shown that oxalate readily decomposes in $\text{H}_2\text{O}_2/\text{HNO}_3$ solutions^{321,322}.

Lai and Wu²⁵¹ reported that the addition of 50-100 mM potassium titanium oxalate (PTO) to H₂O₂/HNO₃ solutions containing 2.4 mM melamine during the growth of nanowires from Ti metal sheets resulted in the formation of rutile nanoflowers forming on top of an initial layer of titanate nanowires. While no explanation for this behavior was offered, the [Ti⁴⁺]/[melamine] ratio was overlooked. As the PTO begins to hydrolyze, the [Ti⁴⁺]/[melamine] ratio may potentially exceed 50:1 and thus there is insufficient NH₄⁺ present to stabilize the titanate layers, resulting in the formation of crystalline rutile TiO₂. Similarly, Lin et al.²⁴⁵ demonstrated the importance of NH₄⁺ concentration during the hydrolysis of TBOT in an aqueous urea solution. It was reported that [urea]/[TBOT] >100 resulted in the formation of amorphous titania which then formed layered titanates upon aging, while [urea]/[TBOT] < 100 resulted in the formation of anatase TiO₂. A [Ti⁴⁺]/[melamine] ratio of 1:2 was employed in our work to ensure sufficient NH₄⁺ concentration to stabilize the titanate layers.

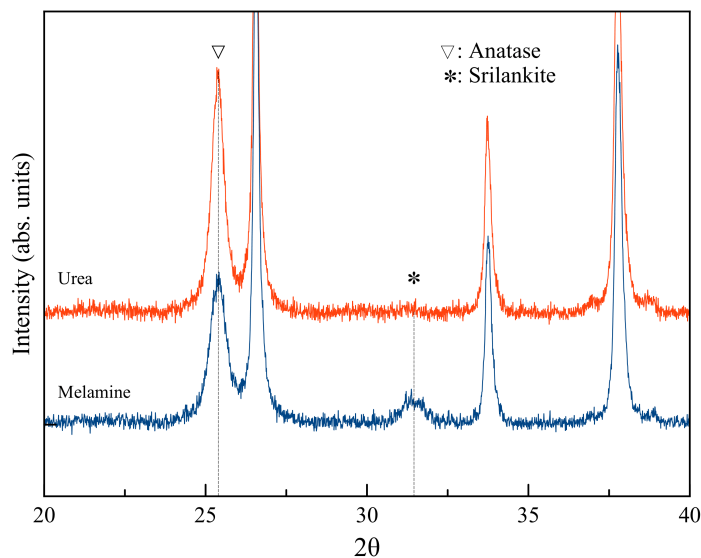


Figure 38: Narrow-angle XRD pattern for nanowires grown in peroxo-titanium solutions containing 15 mM melamine and 45 mM urea

One of the more interesting observations revealed by XRD analysis is the disappearance of the srilankite peak located at 31.4° when urea is substituted for melamine (Figure 38). This is in agreement with literature, where films grown in melamine-peroxide solutions contain a small amount of

srilankite^{94,235-239}, while srilankite is absent in films grown in HMT-peroxide solutions^{253,305,306}. It can therefore be concluded that melamine or one of its decomposition products is responsible for the appearance of the srilankite phase. Cyanuric acid is known to be highly chemically- and thermally-stable, due to its triazine ring, and is resistant to hydrolysis in acid conditions³²³, whereas urea and HMT may be hydrolyzed completely to NH_4^+ and CO_2 . Moreover, melamine derivatives make particularly good ligands toward Ti^{4+} in solution^{246,293,310,313} and have been shown to form complexes that are highly stable toward hydrolysis²⁴⁶.

Cheng et al. demonstrated through FTIR measurements that urea interacts with the Ti-O network during hydrolysis, where urea coordinated with the Ti^{4+} centers via carbonyl groups, forming a Ti-O-C bond³²⁴. Similarly, it may be expected that hydrolyzed melamine derivatives coordinate with Ti^{4+} via carbonyl or hydroxyl groups. As such, each melamine molecule may bond with up to three Ti^{4+} through Ti-O-C bonds, depending on the degree of hydrolysis. These highly stable ligands may then be incorporated into the titanate layers, with the triazine rings substituting for a Ti in the Ti-O network; the 288.8 eV peak found by XPS analysis may be a result of Ti-O-C- bonds arising from melamine derivatives being incorporated into the titanate layers. Indeed, triazine compounds have been shown to act as linking units between metal centers to form metal-organic frameworks³²⁵. Germain et al.³²⁶ demonstrated that partial substitution of Ti by Zr in hydrothermally produced nanowires leads to the formation of the orthorhombic srilankite crystal structure, which displays a dominant (111) XRD peak at $\sim 31.4^\circ$. The srilankite crystal structure arises due to the large ionic radius of Zr (compared to that of the Ti it substitutes). The radius of the triazine ring is similar to that of the ionic radius of the large Zr atoms, thus the incorporation of triazine compounds into the titanate layers may then result in the formation of a srilankite-like phase upon calcination. Alternatively, Zhao et al. noted that layered titanates that were either fully protonated or fully intercalated by NH_4^+ would produce anatase TiO_2 upon calcination or hydrothermal treatment, whereas titanates partially intercalated by both NH_4^+ and Na^+ would result in the formation of brookite^{93,98,99},

which was a result of a lattice shear due to different deintercalation rates of NH_4^+ and Na^+ . Similarly, melamine derivatives, which do not decompose until 320-650 °C^{281–283,291–294}, intercalated into the titanate lattice may induce a lattice shear during dehydration and calcination, thus leading to an orthorhombic intermediate phase. Further investigation into the connection between melamine and the srilankite phase is required, however, results suggest that the hydrolyzed melamine products may be incorporated into or between the titanate layers.

4.3.5.3 Effect of H_2O_2 ratio

Several samples were grown in solutions employing the same PTO, melamine and HNO_3 concentrations as the CBD-A films, however, the $[\text{H}_2\text{O}_2]/[\text{Ti}]$ ratio was varied by diluting the stock H_2O_2 solution with deionized water. The samples were then calcined at 550 °C for 1 hour. The XRD results of the resulting films are shown in Figure 39. It was observed that, in general, reducing the $[\text{H}_2\text{O}_2]/[\text{Ti}]$ ratio lead to faster formation and increased precipitation. For $[\text{H}_2\text{O}_2]/[\text{Ti}] = 100$, the as-synthesized films still develop as titanate, however, the srilankite phase increased considerably upon calcination at 550 °C. Decreasing the $[\text{H}_2\text{O}_2]/[\text{Ti}]$ ratio further (≤ 10), resulted in rapid precipitation which severely limited growth. Moreover, the films did not form as titanate, but rather as rutile TiO_2 . Several researchers have demonstrated that, for a given pH, the $[\text{H}_2\text{O}_2]/[\text{Ti}]$ ratio is critical for controlling both the rate of particle formation and the resulting phase in peroxo-titanium systems^{119,278,327}. It was reported that low $[\text{H}_2\text{O}_2]/[\text{Ti}]$ ratios result in fast particle growth and the formation of crystalline anatase and brookite, while intermediate ratios reduce growth and produce crystalline rutile. High ratios retarded crystal formation entirely (resulting an amorphous TiO_2). Therefore, the high $[\text{H}_2\text{O}_2]/[\text{Ti}]$ ratio employed in the growth of the CBD-A and CBD-N films slowed hydrolysis and nanowire formation, thus favoring the titanate phase and reducing homogeneous nucleation/precipitation in solution. Given that melamine derivatives form highly stable ligands toward Ti^{4+} centers^{246,310}, the slower nanowire growth afforded by high H_2O_2 concentrations may allow for more of these ligands to be hydrolyzed and removed from titanate layers, during the formation

thus reducing the incorporation of melamine into the lattice, as evidenced by the reduction of the srilankite phase.

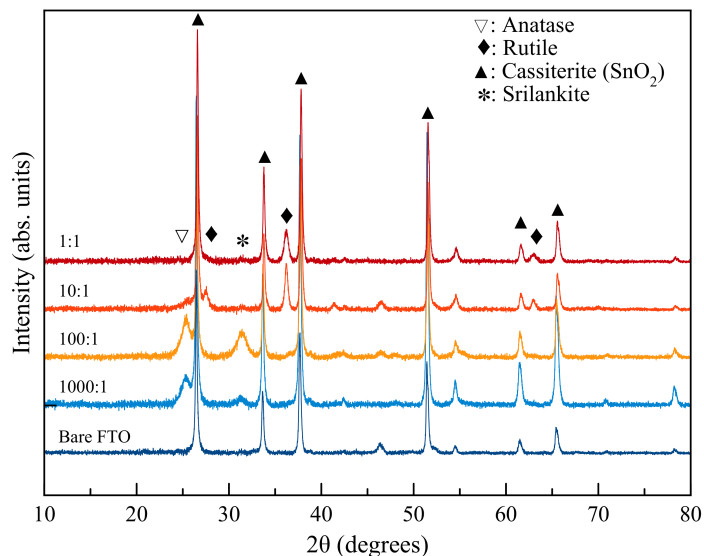


Figure 39: XRD patterns of CBD-A nanowires grown in peroxo-titanium solutions of varying H_2O_2 concentrations, with $[\text{H}_2\text{O}_2]/[\text{Ti}]$ ratios ranging from 1:1 to 1000:1

4.3.6 Photoelectrochemical Characterization

The current-voltage behaviors of CBD-A-550, HTV and P25 films were measured in both dark and UV-illuminated conditions (Figure 40). At high bias potentials, the photocurrent of the anatase CBD-A nanowires exceeds that of both the rutile HTV nanorods and P25 film. The CBD-A-550, HTV and P25 films achieved maximum photocurrents of 1.14 mA/cm^2 , 0.83 mA/cm^2 and 0.53 mA/cm^2 , respectively. The potential at which photocurrent onset was observed (V_{onset}) for both the CBD-A nanowire and HTV nanorod films is shifted anodically with respect to that of P25. While the photocurrent onset for rutile TiO_2 is generally regarded to be at more anodic potentials than the anatase phase, the anodic shift of V_{onset} for CBD-A (with respect to P25), however, suggests the presence of surface states which promote recombination.

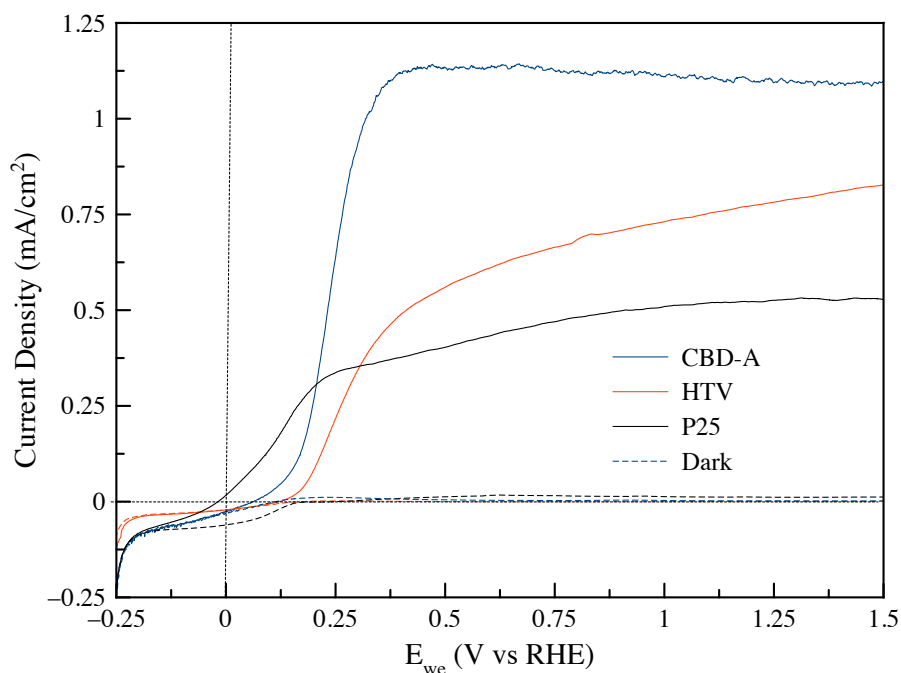


Figure 40: Comparison of the I-V characteristics of CBD-A-550 nanowire, HTV nanorod and P25 films irradiated with 254 nm irradiation in 1M KOH electrolyte

The chopped photocurrent response for both the CBD-A and HTV films are shown in Figure 41.

Significant photocurrent transients that decay rapidly with time can be seen in Figure 41a. Photocurrent transients are due to the electro-oxidation and –reduction of surface states (i.e., trapped holes)^{140,171,328} as the CBD-A sample is alternated between light and dark conditions, respectively; the rapid decay of the photocurrent peak indicates a high density of surface states. It can be seen that as the applied bias increases, the photocurrent transient behavior is reduced and becomes largely negligible by 0.35 V (vs RHE). By applying a bias voltage the Fermi Energy (E_F) of the TiO_2 may be shifted to potentials lower (i.e., more positive) than the redox potential of the surface states (E_{SS}) and thus conduction band electrons can no longer fill the surface states. Therefore, 0.35 V (vs RHE) can be said to be the lowest energy state of E_{SS} and the surface state energy levels are situated below the conduction band. Trapping of holes in surface state below the conduction band drastically enhance recombination as the water oxidation potential is more positive than the surface state energy level, meaning the surface trapped holes can only

be quenched by conduction band electrons^{294,329} and not through water oxidation. Surface states, which occur naturally to a small degree, can also be observed as small photocurrent transients for the HTV nanorods (Figure 41b), though are significantly reduced compared to those seen in Figure 41a. Due to the high density of surface states in CBD-A, V_{onset} cannot be used as a reliable measure for the flat band potential (V_{FB})³³⁰.

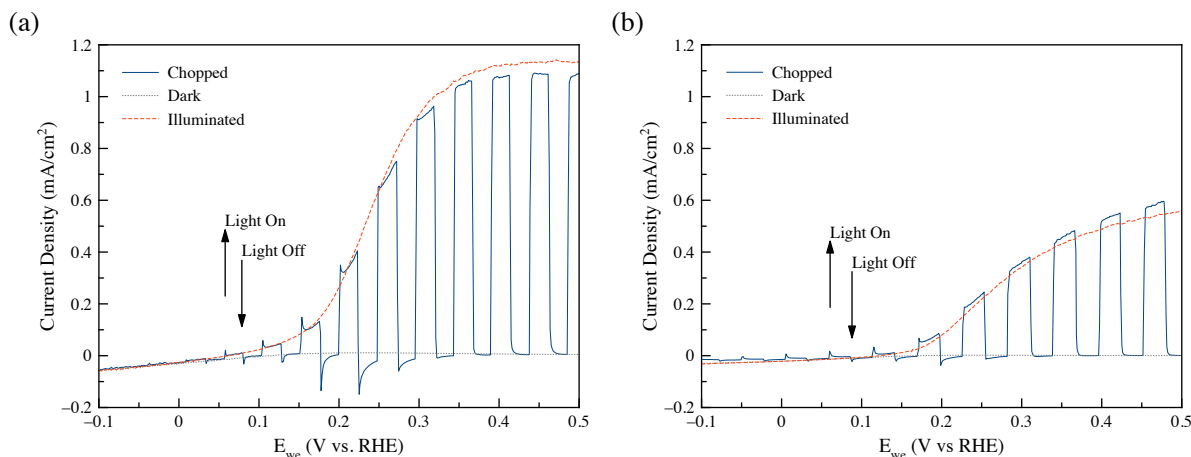


Figure 41: Chopped-light I-V curves for a) anatase CBD-A-550 nanowires and b) rutile HTV nanowires. Samples were irradiated with 254 nm irradiation in 1M KOH electrolyte. The light was chopped at a frequency of 0.5 Hz. Linear voltage sweeps in light and dark conditions are included for clarity.

CBD-A (Figure 41a) shows a small standing photocurrent beginning at -0.02V (vs RHE), however, no photoresponse at potentials negative of this value can be observed. In contrast, the HTV film (Figure 41b) exhibits notable photoresponse up to -0.2V, albeit with no standing photocurrent at potentials less than -0.03 V (vs RHE). As photon adsorption in the low wavelength region is very high (Figure 32a), photons are absorbed in a narrow region near the semiconductor surface (the majority being absorbed within 10 nm from the TiO₂ surface), which, in turn, increases the probability of electron recombination with holes trapped in surface states. The lack of photoresponse at negative potentials for CBD-A, therefore, can be explained by the use of 254 nm radiation and negligible band bending at potentials near V_{FB} to separate conduction band electrons from the TiO₂ surface, which results in high recombination and quenching of any photoresponse. Similar results have been reported for N- and C-doped TiO₂^{294,331–335}, where

photocurrents and photocatalytic performance were seen to decrease drastically at shorter wavelengths due to increased recombination with holes trapped in surface states. The presence of shallow surface states situated below the conduction band cannot be readily attributed to O^{2-} surface vacancies or N-substitution doping in the TiO_2 lattice, as XPS analysis did not reveal any discernable Ti^{3+} $2p_{3/2}$ peaks or a 396 eV peak, respectively, though such species may be below the detection limits of the XPS apparatus. Peaks observed in the C 1s, N 1s and O 1s spectra - the 288.8 eV peak in particular - suggest the presence of Ti-O-C ^{262,273,335} bonds which may result from linkages between the TiO_2 surface and triazine rings. It has been suggested that Ti-O-C bonds result in the formation of surface states below the conduction band ^{334,335}.

Electrical impedance spectra for CBD-A, HTV and P25 were taken in the dark (to avoid generation of photoinduced surface states) at a bias of 0.4 V vs RHE (Figure 42a) and were fit according to the equivalent circuit shown in Table 6. In this model, R_s is the series resistance of the cell, CPE_{DL} and R_{DL} are the capacitance and depletion layer resistance, respectively. The Helmholtz layer is represented by CPE_H and R_H , the Helmholtz layer capacitance and charge transfer resistance, respectively, and a Warburg diffusion resistance, W_H .

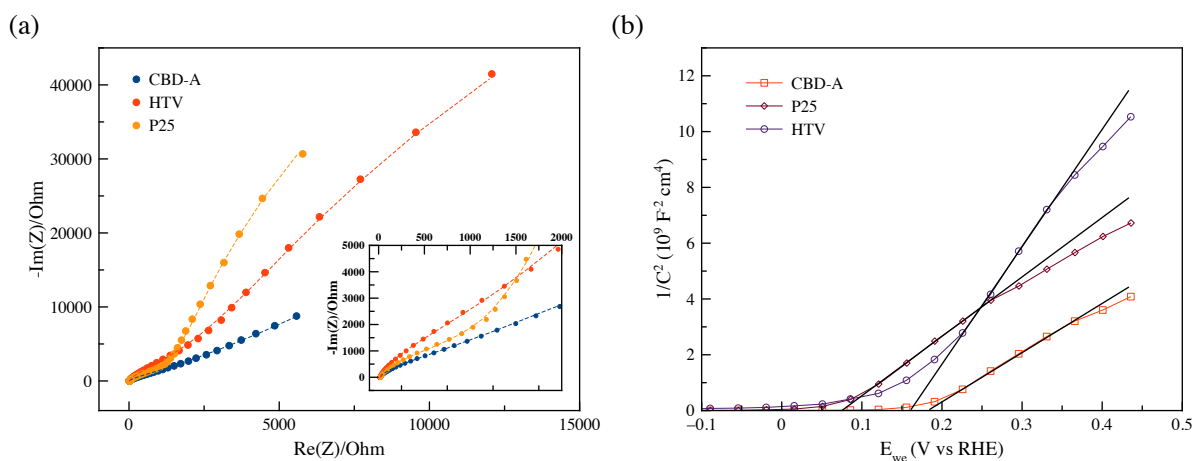
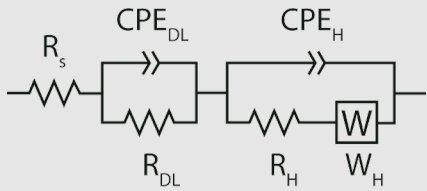


Figure 42: a) Nyquist plots of CBD-A, HTV and P25 taken in dark at 0.4V vs RHE and b) Mott-Schottky plots for CBD-A, HTV and P25 at 4.8 kHz



	R_s (Ω)	R_{DL} (Ω)	CPE_{DL} (F)	n_{DL}	R_H (Ω)	W_H ($\Omega s^{-1/2}$)	CPE_H (F)	n_H
CBD-A	19.06	2.10×10^5	5.05×10^{-4}	0.95	622.7	4533	2.53×10^{-5}	0.92
HTV	16.43	2.31×10^5	4.77×10^{-5}	1.00	1855.8	6250	2.20×10^{-5}	0.93
P25	21.43	3.39×10^5	5.54×10^{-5}	1.00	1230.1	1792	2.73×10^{-5}	0.91

Table 6: Equivalent circuit used for modeling the photoanode in 3-electrode configuration and corresponding fitting parameters for dark conditions at 0.4V vs RHE.

From the given model, it was found that the charge transfer resistance in the Helmholtz layer was significantly reduced compared to the other samples. More surprisingly, the double layer capacitance of CBD-A was an order of magnitude larger than that of the HTV nanorods and the P25 film. The large double layer capacitance arises due to the combined bulk resistance/ capacitance of the nanowires and the parallel resistance/capacitance of the recombination process with the surface states. Moreover, the results indicate that the surface states are not due to photoinduced species, such as surface adsorbed peroxide or –OH groups, and are likely due to intrinsic defects, doping or absorbed species such as poly-s-triazines. Though an attempt was made to model the parallel bulk and surface state recombination, it was not possible to distinguish the relative contribution of each process at this time. Mott-Schottky analysis of the CBD-A nanowires revealed a high frequency-dependent dispersion due to the presence of surface states and, as such, could not be used to provide a reliable estimate of the flatband potential. It was observed by Mott-Schottky analysis (Figure 42b), however, that the CBD-A nanowires and the P25 films have similar dopant densities as indicated by their nearly identical slopes³³⁶. This observation suggests that dopants were not introduced into the TiO₂ lattice, and that the high double layer capacitance and high recombination rates are due to the presence of a surface species.

4.3.7 Photocatalytic Water Splitting

Methanol-assisted water splitting was carried out in a specially designed reactor. Methanol was employed as a hole scavenger to minimize the effect of surface states, accelerate hydrogen production (thus increasing the sensitivity of the measurements), and to suppress O₂ evolution via water oxidation (which would promote the back reaction of H₂ and O₂ over the deposited platinum sites). Each reaction cell was fitted with a pressure sensor to measure the time-course of gas evolution. The pressure was observed to increase linearly with time (Figure 43a), indicating a constant rate of H₂ evolution, and the change in pressure correlated well with the final H₂ concentrations determined by GC measurement. The H₂ evolution rate for CBD-A was found, in general, to increase with calcination temperature, while CBD-N displays no appreciable increase up to 550 °C (Figure 43b). Both, however, exhibit a rapid increase at 650 °C to a maximum H₂ evolution rate of 4.15 and 2.89 μmol/hr for CBD-A and CBD-N, respectively. The rutile HTV nanorod and P25 films displayed maximum H₂ evolution rates of 1.21 and 7.12 μmol/hr, respectively.

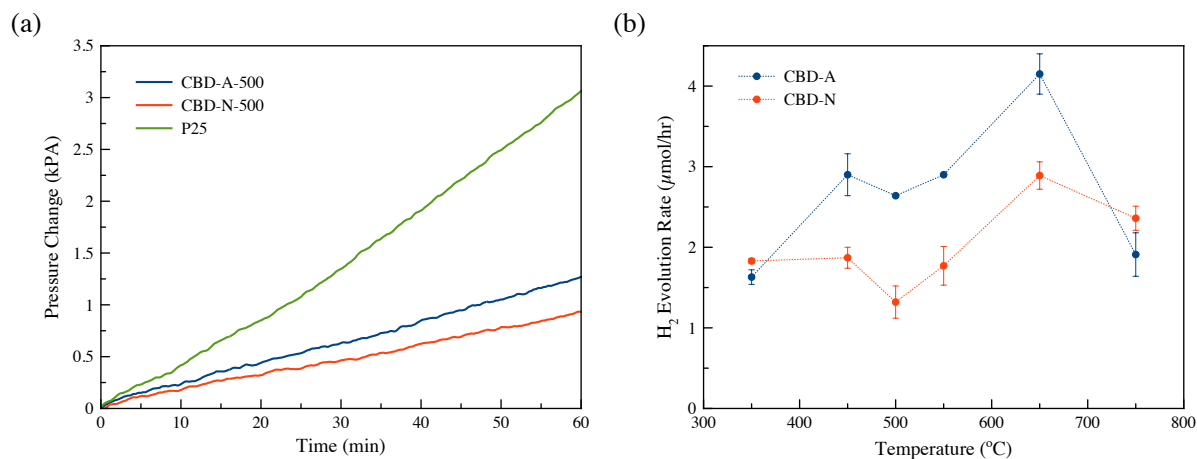


Figure 43: a) Pressure increase with time due H₂ evolution and b) H₂ evolution rates for CBD-A and CBD-N nanowire films calcined at temperatures ranging from 350 °C to 750 °C.

Interestingly, both CBD-A and CBD-N display a slight depression in performance when calcined at 500 °C; this may be due to formation of surface species such as poly-*s*-triazines, resulting from the polycondensation of melamine^{36,275,280–282}, which promote electron/hole recombination.

Thermogravimetric analysis revealed a small mass loss between 550 and 650 °C, which is consistent with the desorption or decomposition of poly-s-triazine species that form surface states^{281,293,294}; the desorption of these species would yield decreased e^-/h^+ recombination and a subsequent increase in performance. The maximum in H₂ evolution at 650 °C may also be explained by coexisting anatase and rutile phases, which would improve charge separation and reduce recombination^{337,338}, or conversion of the srilankite phase (whose effect on performance is not yet understood). It is suspected, however, that the former is the more likely cause due to the observed increase in photodeposited platinum with calcination temperature, as a reduction in surface state density would result in an increase in surface e^- density and the rate of reduction of Pt⁴⁺ at the semiconductor at surface. Both CBD-A and CBD-N exhibit a significant decrease in H₂ evolution at 750 °C due to particle ripening and increased formation of the rutile phase. The observed peak in hydrogen evolution at 650 °C may also be due to a larger concentration of surface Pt deposits. The potential of the Pt deposits will be approximately equal to the hydrogen evolution potential and, therefore, electron transfer to the Pt deposits will be energetically comparable or favored compared to electron transfer to the surface states.

4.3.8 Photocatalytic Degradation of Model Organic Compound

Photocatalytic activities of the nanowire samples prepared at various temperatures were compared with P25 and HTV nanorods by the photocatalytic decomposition of RhB under UV illumination. All samples were coated or grown on to FTO glass, which was then cut into small samples (~ 13 mm x 13 mm). Mass transfer effects were first investigated by supporting P25 and CBD-A-550 films above magnetic stir bars, coated-side facing up, in identical beakers. The solution volume and lamp position were adjusted such that incident power and solution depth above the films was identical to samples investigated without stirring; the photodegradation rate of RhB rate was then measured with and without vigorous stirring. As seen in Figure 44a, the photodegradation rate for the P25 film increased from 0.0023 min⁻¹ to 0.0048 min⁻¹ with stirring, whereas the CBD-A-550 film (0.0018 min⁻¹) showed negligible change in

performance. This same insensitivity to mass transfer was observed with several nanowire samples; it was, therefore, concluded that the nanowire films were not mass transfer limited and it was possible to conduct the photodegradation experiments without stirring. It is believed that the open structure of the nanowire films, as opposed to the porous structure of the P25 films, yields reduced mass transfer resistance.

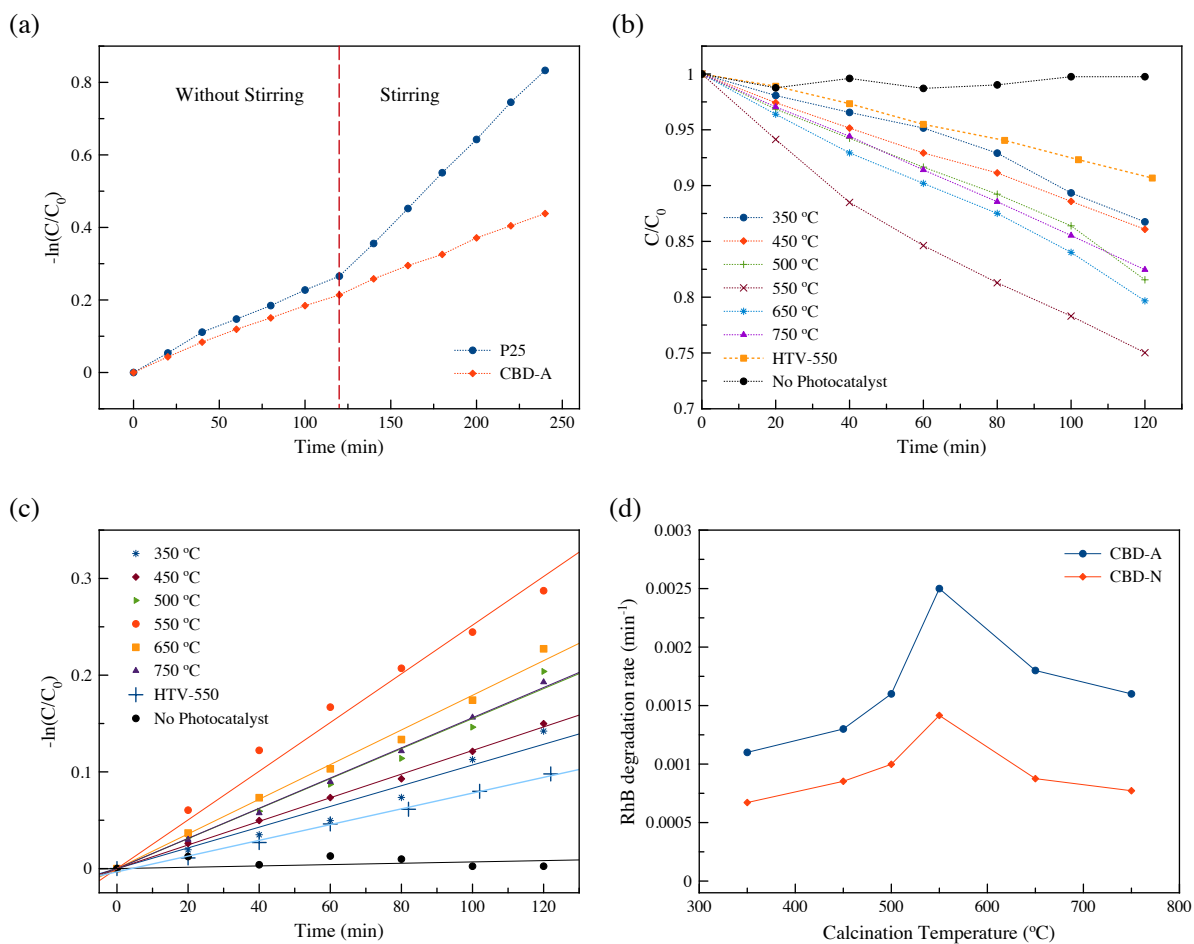


Figure 44: a) Photodegradation of Rhodamine B (RhB) in the presence of P25 and CBD-A-550 films with and without stirring, b) Photodegradation of RhB in the presence of CBD-A films calcined at temperatures varying from 350 °C to 750 °C and c) the corresponding pseudo-first order fits, and d) Comparison of the photodegradation performance of CBD-A and CBD-N nanowires calcined at temperatures varying from 350 °C to 750 °C.

It was observed that the photodegradation rate using the CBD-A nanowires (Figure 44b) increased with calcination temperature to a maximum for samples calcined at 550 °C and that calcination temperatures

beyond this resulted in a reduction in performance. The photodegradation of RhB could be fit as a pseudo-first order reaction (Figure 44c); the CBD-A nanowire films were found to have a maximum rate of 0.0023 min^{-1} at $550 \text{ }^\circ\text{C}$, a nearly 3x increase in performance over the rutile HTV nanorod films ($7.8 \times 10^{-3} \text{ min}^{-1}$). The observed increase in photodegradation rate with calcination temperature is a result of complete transformation of titanate to anatase at $550 \text{ }^\circ\text{C}$, as well as the thermal degradation of triazine species incorporated on the nanowire surface (which largely decompose between $400\text{-}550 \text{ }^\circ\text{C}$). Higher calcination temperatures result in the formation of rutile, which is known to have a lower photocatalytic performance than anatase, as well as coarsening of the nanowires, resulting in a decrease in surface area. The performance of the CBD-A samples were found to be $\sim 1.5\text{-}2$ times as great as that of the CBD-N samples (Figure 44d); this is in agreement with the difference in nanowire length, suggesting that the difference in performance is primarily due to surface area alone.

4.4 Conclusions

Titanate nanowires were grown on FTO substrates using a simple chemical bath deposition method. These titanate nanowires were then easily transformed to anatase by calcination. It was found that calcination temperatures between $550 \text{ }^\circ\text{C}$ and $650 \text{ }^\circ\text{C}$ yield the highest activities for photocatalytic hydrogen production and photodegradation of Rhodamine B. It was demonstrated that increased $[\text{HNO}_3]$, high $[\text{H}_2\text{O}_2]/[\text{Ti}]$ ratios, and the presence of precursors, such as urea and melamine, in the correct amount are necessary for the slow hydrolysis of Ti^{4+} and the stabilization of the titanate phase during growth. Moreover, it was demonstrated that urea and melamine precursors, intended for the evolution of NH_4^+ cations via hydrolysis, also behave as ligands that complex with Ti^{4+} in solution and slow the rate of hydrolysis. Melamine was found to be an excellent ligand that is highly resistant toward hydrolysis, resulting in the growth of $2.45 \text{ }\mu\text{m}$ nanowires in high yields. The high stability of melamine, however, may also result in its incorporation on the surface of the titanate nanowires. Melamine then forms polycondensation products (such as melem and melon), during calcination of the titanate nanowires,

resulting in the presence of hole trap surface states which result in increased recombination and reduced recombination. The anatase nanowires were observed to have greater photocatalytic hydrogen production and photodegradation performance than rutile nanorods produced by hydrothermal growth. Moreover, it was found that in photoelectrochemical applications, where a bias potential may be applied, the performance of the anatase nanowires as a photoanode far exceeded that of both the rutile nanorods and P25 TiO₂.

Chapter 5: Advanced Fluidizable Nanowire Photocatalysts for Water

Splitting and Water Decontamination

5.1 Introduction

Growing global energy concerns and an increasing public environmental awareness has been fueling the adoption of clean energy technologies, particularly in the automotive and household power sectors, which has resulted in an increased demand for clean hydrogen fuels. Photocatalytic water splitting has long been sought after as an emissions-free, sustainable, direct solar-to-chemical energy conversion method to replace or augment current hydrogen production from conventional energy sources.

Titanium dioxide (TiO_2) has been one of the most heavily researched photocatalyst materials for both water splitting and water treatment due to its low-cost, high stability and large band gap^{136,137,192}. While excellent photocatalytic water splitting research has been carried out over several decades, there have been few reported attempts toward creating a scalable process. We recently demonstrated that photocatalytic water splitting in a UV-irradiated fluidized bed reactor resulted in a marked increase in the efficiency of the process, while simultaneously minimizing mass-transfer effects, poor radiation distribution, parasitic back-reactions and photocatalyst handling difficulties which limit scalability of immobilized-film and suspended slurry photocatalysts. The inherent nature of fluidized bed reactors also allows for relatively simple scaling of the process. Moreover, we have presented a model describing a fluidized water splitting reactor that provides further insight into the optimization and scaling of such systems.

While the fluidization of TiO_2 photocatalysts yields excellent performance and a scalable process, the rigors of fluidization induce a great deal of mechanical stress, resulting in the rapid attrition of the particles, thus limiting the exploration of advanced photocatalyst designs. One-dimensional TiO_2 photocatalyst particles, such as nanorods, -wires and -ribbons, are highly desired as they have

demonstrated excellent performance for both water splitting^{19,34,59,339} and photocatalytic water treatment^{94,159,320,340} due, largely, to their excellent charge transport and separation properties. The highly ordered nanostructure of 1-D photocatalyst arrays greatly reduces grain boundaries, which reduces the recombination of photogenerated electrons and holes²³⁷, and serves to reduce the reflection of incident light and improve the absorption of photons⁵⁷. The harsh physical environment of a fluidized bed reactor does not readily allow for nanostructured TiO₂ photocatalysts, as the fine features would be quickly removed from the particle surface. Several researchers have successfully deposited TiO₂ photocatalysts onto porous, fluidizable particles to protect photocatalyst coatings from particle-to-particle and particle-to-wall collisions, which greatly reduced the mechanical ablation of the photocatalyst layer^{65,72,157,158}. The research group of Langford and Kantzas^{71-73,157,158} aptly described the structure of the porous support particles as being “golf ball”-like, wherein the rough surface of the particles created many indentations (much like the “dimples” of a golf ball) in which the deposited TiO₂ photocatalyst coating could reside and remain protected from mechanical ablation during fluidization. Such porous, “golf ball”-like particles may provide sufficient protection to allow the use of 1-D nanostructured films on their surface.

One-dimensional nanostructured TiO₂ films have been synthesized via a number of methods^{86,159,179}, however, hydrothermal growth has proven to be of the most facile and popular methods^{167,174,180-188}. The hydrothermal growth method presented by Liu and Aydil¹⁶² has become one of the most popular and highly cited methods due to its relative simplicity. This method, however, results in nanorods with the rutile crystalline structure, which typically has been shown to be less active than anatase TiO₂, particularly so for water splitting^{11,15-21}. The solution-based hydrothermal nanorod growth method, however, allows for all surfaces of the porous particles to be deposited with nanorods or nanowires in a single processing step. In spite of its great potential, only a few examples of hydrothermal growth of TiO₂ nanorods and nanowires on porous or high surface-area substrates have been published^{94,341,342}. Further,

there has there been any work, to our knowledge, describing the scale-up of a hydrothermal method to allow for the volume production of TiO₂ nanorods.

Several researchers and ourselves have presented several low-temperature chemical bath deposition (CBD) techniques that allow for long titanate nanowires to be deposited easy on a wide variety of substrates⁹⁴; these titanate nanowires are then converted to anatase TiO₂ nanowires by calcination or crystallization in acidic hydrothermal baths^{94,252,253}. As these low-temperature methods do not require specialized reaction vessels like the hydrothermal methods, they offer a greater degree if flexibility when attempting to scale the production of nanowire deposited substrates.

We, to our knowledge, present here for the first time the production of TiO₂ nanorod and nanowire photocatalysts on porous, fluidizable substrates for use in a UV-irradiated fluidized bed reactor. Moreover, we present two methods that expand upon both our own CBD nanowire process and the popular hydrothermal nanorod method to allow for scalable production of fluidizable nanorod photocatalysts. It should be noted that the terms nanowire and nanorod are employed to differentiate between the 1-D structures produced by the two growth methods. In this work, nanowire refers to the high aspect ratio (i.e. long and thin) 1-D anatase TiO₂ structures produced via Chemical Bath Deposition whereas nanorod refers to the low aspect ratio (i.e. short and broad) 1-D rutile TiO₂ structures produced via the hydrothermal growth method.

5.2 Experimental

5.2.1 Materials

Porous glass beads (Siran™ #4711, 1-2 mm diameter, Jaeger Biotech), shown in Figure 45, were employed as porous substrates for the production of the fluidizable nanowire/nanorod-deposited particles. The porous particles were measured to have a dry bulk density of 568 kg/m³ and a mean diameter of 1.6

mm. The manufacturer-supplied specifications report the pore diameters $<120\ \mu\text{m}$, pore volume to be 55-60% and surface area as $87,056\ \text{m}^2/\text{m}^3$ ($\sim 1.53\ \text{m}^2/\text{g}$).

Before use, the as-received porous glass beads were first cleaned by ultrasonication in a 1:1:1 mixture of acetone, isopropyl alcohol and water for 30 minutes, followed by ultrasonication in deionized water for 30 minutes. The particles were then drained and dried in an oven at $80\ ^\circ\text{C}$.

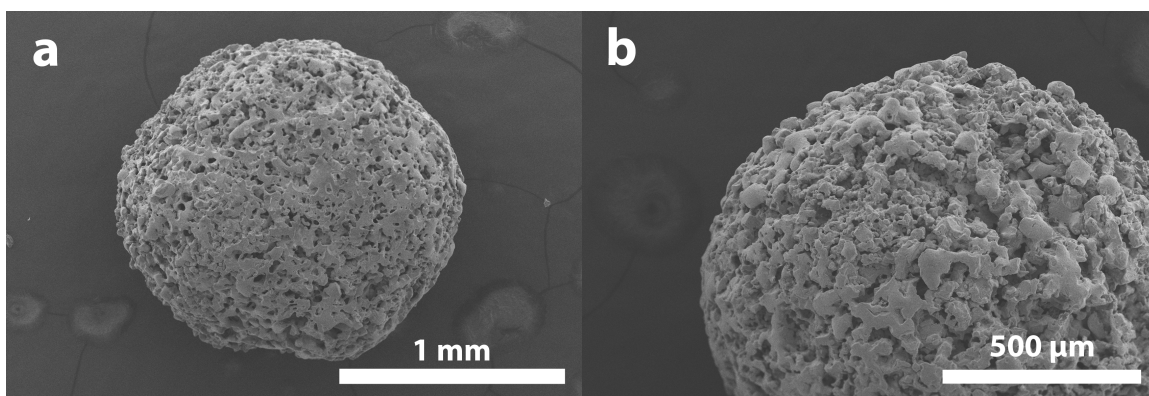


Figure 45: SEM images of the porous Siran glass particles

5.2.2 Anatase Nanowire-coated Particles

The porous glass beads were first deposited with a TiO_2 seed layer by placing 20 g of the bare substrate into 80 ml of a 0.2M aqueous TiCl_4 solution. The porous beads were allowed to soak in the solution for 12 hours, then rinsed with deionized water to remove excess solution and dried at $80\ ^\circ\text{C}$. The TiO_2 seed-deposited beads were then calcined in air at $450\ ^\circ\text{C}$ for 1 hour in an oven.

A growth solution was prepared according to the method we have described in detail in Chapter 4. In brief, a growth solution was prepared by mixing 800 ml 30 wt% hydrogen peroxide (H_2O_2 , Fisher) and 24 ml nitric acid (HNO_3 , Fisher) for 10 minutes, followed by 2.4 g of potassium titanium oxalate (PTO, Sigma Aldrich) and 1.6 g of melamine (Sigma Aldrich). The solution was gently heated to $40\ ^\circ\text{C}$ while stirring stirred to aid the complete dissolution of melamine, yielding an intense red-orange PTO- H_2O_2

solution. The solution was then transferred to a 1-liter glass vessel containing 0–40 g of the seed-deposited porous beads. The glass vessel was sealed loosely to minimize evaporation while avoiding pressurization of the vessel by gases evolved during nanowire growth, and then placed in an oven at 80 °C for 7 hours. The titanate nanowire-deposited beads were first rinsed with deionized water, and then placed in a 1M HCl solution for 15 minutes. The particles were then decanted from the solutions and rinsed thoroughly with deionized water until the wash water measured a pH of 6–7; the particles were then dried at 80 °C in an oven. The titanate nanowires were converted to anatase TiO₂ nanowires by calcining the nanowire-deposited beads in air at 550 °C for 1 hour in a furnace. This temperature was found to yield complete conversion of the titanate to anatase and excellent performance in our previous study.

5.2.3 Rutile Nanorod-coated Particles

It was observed that highly acid hydrothermal conditions occasionally resulted in the dissolution of the TiO₂ seed layer formed by the TiCl₄ treatment described above, resulting in delamination of the nanorod layer, therefore an alternative seed layer method was developed based on a TiO₂/sol-gel composite method described by Keshmiri et al ¹¹². A solution containing 17.6 ml ethanol, 1.2 ml H₂O and 2.9 ml HCl was mixed in a beaker for 10 minutes. Titanium tetraisopropoxide (TTIP, 22 ml, Sigma Aldrich) was added drop-wise to the solution while stirring and allowed to mix for 1 hr. Commercial TiO₂ powder (7 g, Evonik P25) was added to the solution and left to stir overnight. The solution was then diluted with 81.3 ml ethanol and allowed to mix for 1 hour. The composite solution was transferred to a 250 ml beaker. Porous glass beads (100 g) were placed in a stainless steel mesh basket and immersed in the composite solution and allowed to soak for 10 minutes; the beads were stirred occasionally with a glass rod to dislodge any air bubbles trapped on the surface of the beads. The basket was withdrawn from the solution slowly, allowing excess solution to drain away. The coated beads were spread on a tray in a single layer and allowed to dry at room temperature over night. The beads were then calcined at 500 °C

for 1 hour. This process was repeated twice to achieve a strong, even TiO₂ layer over the entire particle surface.

In a large beaker, 50–150 ml deionized water and 50–150 ml concentrated hydrochloric acid were mixed to yield a total volume of 200 ml. TTIP was added to the solution in varying amounts (0–20 ml) and mixed for 10 minutes. The solution was then transferred to a 500 ml Teflon-lined hydrothermal vessel containing 0–20 g of the TiO₂-composite coated porous beads. The sealed vessel was then placed in an oven at 150 °C for up to 18 hours. The vessel was then cooled under running water to room temperature. The growth solution was carefully decanted from the vessel and the nanorod-coated beads were recovered in a fine mesh basket. The beads were then gently washed with in a 50:50 water/HCl bath to remove excess solution (while avoiding hydrolysis), followed by gentle rinsing with deionized water until the wash water measured a pH of 6–7. The nanorod-coated beads were dried in an oven at 80 °C overnight, followed by calcining in an oven at 550 °C for 1 hour.

5.2.4 UV-irradiated Fluidized Bed Reactor System

The UV-irradiated fluidized bed system and its operation has been described in detail in Chapter 2. In brief, an annular fluidized bed, with a quartz glass tube inner annulus, containing a low-pressure mercury vapor ultraviolet (UV) lamp (Emperor Aquatics, 50W, 254 nm), and a polycarbonate outer annulus, was employed. The UV lamp was not employed in this study. The photocatalytic reaction zone between the quartz glass tube and the outer polycarbonate wall has an inner radius of 1.41 cm, an outer radius of 2.54 cm and an effective length of 32.76 cm, yielding a total fluidized reactor volume of 0.45 L. The inlet of the fluidized bed reactor was comprised of a conical flow distributor designed to avoid jetting. The outlet ports of the fluidized bed reactor were connected directly to a separator unit having a volume of 0.40 L. The reaction solution was circulated from the separator back to the fluidized bed reactor inlet by a PanWorld NH-100PX centrifugal pump. A stainless steel mesh filter was placed over the outlet of the

separator to avoid entrainment of any eluted particles into the pump (where they would be macerated by the impeller). A National Instruments USB-6212 Data Acquisition (DAQ) card was used to provide direct control of the UV lamp and centrifugal circulation pump.

5.2.5 Attrition Resistance

The rate of attrition was determined using a spectrophotometric technique¹⁴³. Briefly, 70 ml of photocatalyst particles are loaded into the fluidized bed reactor system, which was then filled with 1L deionized water. The photocatalyst particles were then fluidized to an expanded bed height of 24 cm and 10 ml samples of the liquid phase were taken at several intervals. The UV lamp was not employed during the attrition tests.

A solution (Solution A) was prepared by dissolving $(\text{NH}_4)_2\text{SO}_4$ (3M) in concentrated H_2SO_4 . Solution B consisted of a 1.8M aqueous H_2SO_4 solution. The 10 ml aliquots containing TiO_2 were transferred to a ceramic dish, to which was then added 10 ml of Solution A. The mixture was then heated over a Bunsen burner until boiling and the TiO_2 dissolved (~10-20 minutes). The mixture was then qualitatively transferred to a 25 ml volumetric flask using 5 ml deionized water. The volumetric flask was then filled to 25 ml with Solution B, then 200 μl H_2O_2 was added. The flask was then inverted and agitated to form a yellow-orange peroxo-titanium complex. The concentration of Ti^{4+} was then measured using a Cary 100 photospectrometer by measuring the absorbance at 410 nm.

5.2.6 Characterization

The particles were characterized by X-ray diffraction (XRD) using a Bruker D2 Phaser desktop X-ray diffractometer using $\text{Cu-K}\alpha$ radiation (1.5418 Å). As the nanowire/-rod surface layer on the porous glass particles was minute compared to the total bulk of the particles, it was often not possible to detect the peaks arising from the 1-D nanoparticles once the nanowire/-rod deposited glass particles were finely

ground and prepared for analysis. An alternate method was devised and a custom sample holder that could hold a sufficient depth of whole particles was produced. Whole particles were then loaded into the sample holder and leveled as flat as possible. The loaded sample holder was placed into the diffractometer and XRD measurements were then made while rotating the sample holder at a speed of 2 rpm. This approach averaged irregularities in the sample surface exposed to the detector and produced diffractograms displaying peaks that indexed well with diffractograms of the 1-D nanoparticles grown on flat indium–tin oxide (ITO) coated glass slides. It should be noted that while this method was sufficient to identify the TiO₂ phases present on the porous glass particle surface, the results may be inadequate for further analyses requiring peak intensities (i.e. elemental and phase composition).

SEM imaging and energy-dispersive X-ray spectroscopy (EDX) were conducted on both the Hitachi S-2600N Variable Pressure Scanning Electron Microscope (VPSEM) and the Hitachi S3000N VP-SEM with EDX. The samples were mounted on adhesive carbon tape and coated with a 5 nm platinum layer. Imaging was carried out at 5 kV to avoid electrostatic distortion of the images due to charging of the TiO₂ and glass particles. Transmission Electron Microscopy (TEM) imaging was conducted on a FEI Tecnai G2 200kV Transmission Electron Microscope. The nanowire and nanorod rod deposited particles were ground in an agate mortar, then sonicated in pure ethanol. The fine TiO₂ particles dispersed in ethanol were then dropped on to TEM grids and allowed to dry at 80 °C for 5 hours before imaging. ImageJ software was used to manually measure the nanowire and nanorod dimensions from the SEM and TEM images, as well as to determine the crystal lattice interlayer distances by Fast Fourier Transform (FFT) analysis of the TEM images. UV-Vis Diffuse Reflectance (UV-Vis-DR) spectra of the deposited films were measured by using an Ocean Optics Flame UV spectrometer with a tungsten-deuterium light source (DH-2000-BAL) and reflectance probe.

5.3 Results and Discussion

5.3.1 Anatase Nanowire Growth

Titanate nanowires were grown on the porous TiCl_4 -seeded particles via a low-temperature chemical bath deposition (CBD) method, which was presented in detail in Chapter 4. Unlike the hydrothermal growth method, the CBD process does not require a specialized reaction vessel, thus the reactor vessel size could be easily varied to produce desired batch sizes. As this method employs the use of a water-soluble peroxy-titanium complex, the initial $[\text{Ti}^{4+}]$ concentration could be easily varied; however, $[\text{Ti}^{4+}]$ was held constant at 8 mM for these experiments.

While titanate nanowires could be grown on the same TiO_2 -composite seeded particles employed for the hydrothermally grown samples, it was found that the presence of the thick TiO_2 seed layer catalyzed the decomposition of H_2O_2 . This in turn led to a rapid evolution of gas, making the reaction violent; this was especially prevalent for high $[M_{cat}]/[V_{sol}]$ ratios, where M_{cat} and V_{sol} are the mass of seed particles and the growth solution volume, respectively. The use of TiCl_4 -seeded porous particles resulted in a reduced rate of gas evolution and a gentler nanowire growth phase. As such, the TiCl_4 -seeded particles were preferred from a safety and practicality standpoint. It was observed that the gas bubbles evolved during nanowire growth caused the porous particles to fluidize and tumble in the reaction vessel. In contrast to the hydrothermal growth of nanorods, where the particles form a packed bed, it is believed that this mixing resulted in improved nanowire growth and particle-to-particle consistency, as well as served to minimize the accumulation of nanoparticles precipitated in solution (through homogeneous nucleation) on the particles surface.

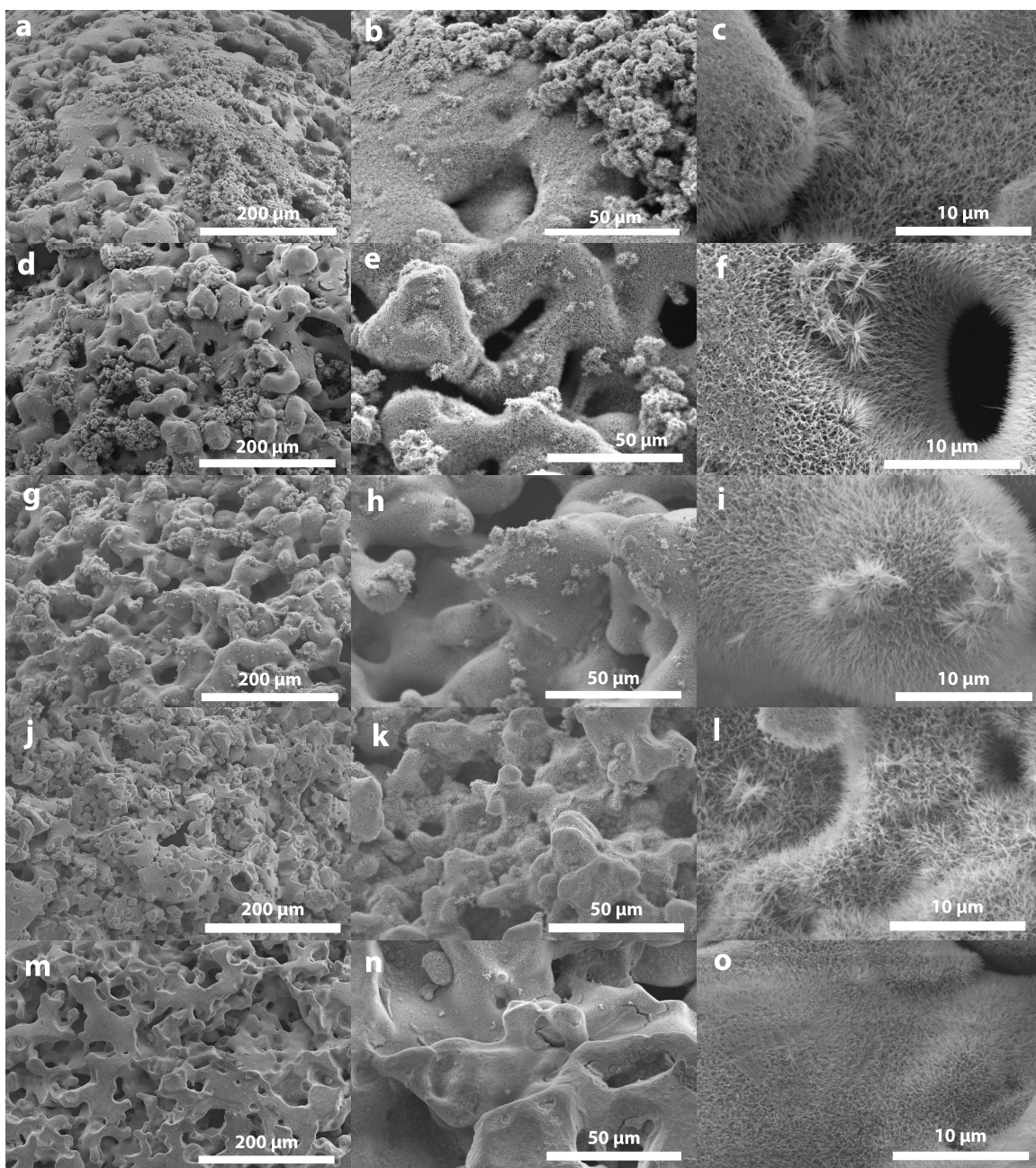


Figure 46: SEM images of nanowire-deposited particles grown at $[M_{cat}]/[V_{sol}]$ ratios of (a-c) 5×10^{-4} , (d-f) 2.5×10^{-3} , (g-i) 5×10^{-3} , (j-l) 0.025 and (m-o) 0.05 g/ml.

Titanate nanowires were grown on the porous seeded particles at $[M_{cat}]/[V_{sol}]$ ratios of 5×10^{-4} , 2.5×10^{-3} , 5×10^{-3} , 0.025 and 0.05 g/ml in an oven at 80 °C for 7 hours. The nanowire-deposited particles were then calcined at 550 °C for 1 hour to convert the titanate nanowires to anatase. For all $[M_{cat}]/[V_{sol}]$ ratios,

dense films of vertically aligned nanowires were observed covering all surfaces of the porous particles (Figure 46). In Figure 46, it can be seen that for low $[M_{cat}]/[V_{sol}]$ ratios, the surface of the particles are covered with flower-like nanowire “balls”, which are the result of homogeneous nucleation, growth and precipitation of nanowires in solution. It can be seen that as the $[M_{cat}]/[V_{sol}]$ ratio increases, the quantity of nanoflower balls decreases and are largely absent for samples grown at $[M_{cat}]/[V_{sol}]$ ratios of 0.025 g/ml and 0.05 g/ml. This observation indicates that increasing the total surface area on which nanowires can grow promotes heterogeneous nucleation and reduces homogeneous nucleation in solution.

In Figure 46k and Figure 46n, regions of flattened nanowires can be seen on the apex points of the particle surface that are the result of the vigorous tumbling during nanowire growth and subsequent handling. Meanwhile, the majority of the nanowires (which reside in recesses below the apex points) remain intact; this demonstrates the effectiveness of the porous particle shape in protecting the nanowires during fluidization and from other mechanical damage.

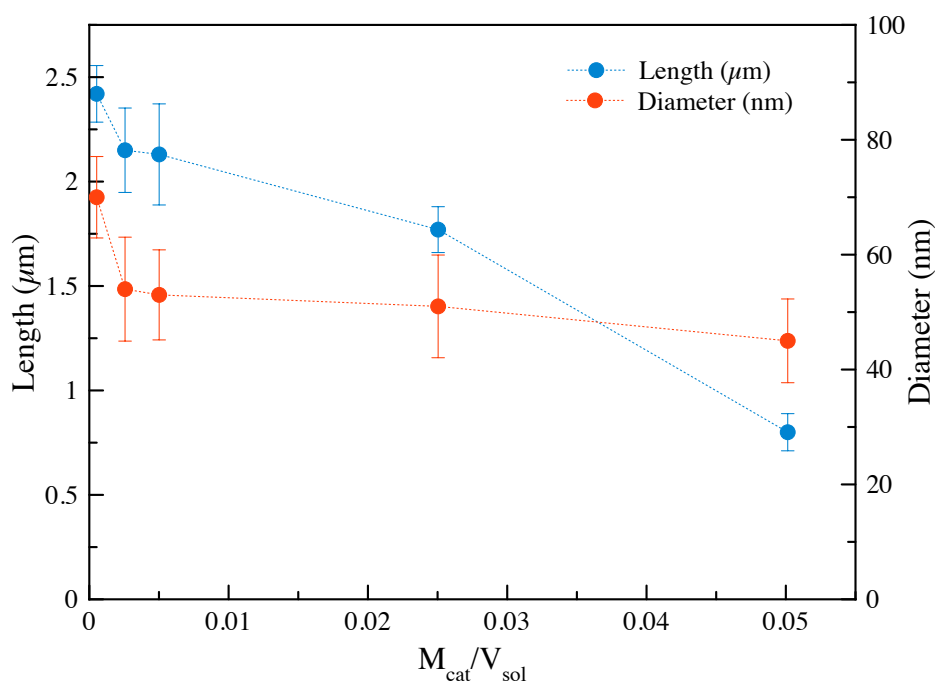


Figure 47: Nanowire length and diameter dependence on $[M_{cat}]/[V_{sol}]$

As seen in Figure 47, a $[M_{cat}]/[V_{sol}]$ ratio of 5×10^{-4} g/ml yielded 2.42 μm long, 70 nm wide nanowires as a result of rapid nanowire growth. Increasing the ratio to 2.5×10^{-3} g/ml resulted in a sharp drop in both the nanowire diameter and length. From 2.5×10^{-3} g/ml to 0.025 g/ml the nanowire length decreased slightly while the diameter remained largely unchanged. Further increasing the $[M_{cat}]/[V_{sol}]$ ratio to 0.05 g/ml, however, resulted in the nanowire length decreasing sharply to 0.8 μm . The ideal $[M_{cat}]/[V_{sol}]$ ratio was thus chosen to be 0.025 g/ml to minimize the presence of nanowire balls (which may be easily ablated from the particle surface during fluidization) while maximizing the nanowire aspect ratio and maximizing the amount of nanowire-deposited photocatalyst particles that can be produced in a given batch.

5.3.2 Rutile Nanorod Growth

Rutile TiO_2 nanorods were grown on the TiO_2 -composite coated porous glass particles using a modified hydrothermal growth (HTV) method based on that originally presented by Liu and Aydil¹⁶². Early attempts to scale the hydrothermal process to grow nanorods on porous particles in any substantial amount resulted in sporadic, inconsistent growth with high particle-to-particle variability where some particles were covered entirely with nanorods while others were completely devoid of nanorod growth. It was observed that particles at the top of the bed had better nanorod growth with those at the bottom typically had poor or no growth. Moreover, it was observed that, under certain conditions, the nanorods would delaminate or slough off the particle surface in sheets. Liu and Aydil observed a similar delamination issue for treatment times beyond 24 hours, where it was hypothesized that when the system reached an equilibrium between dissolution and growth processes (due to decreasing $[\text{Ti}^{4+}]$), dissolution at the glass/ TiO_2 interface resulted in delamination of the deposited nanorod layer. We observed that the TiCl_4 -treated particles were particularly prone to delamination, especially at high acid concentrations or high $[M_{cat}]/[V_{sol}]$ ratios. By employing the TiO_2 -composite seed layer, which has been shown to be mechanically strong^{112,156}, this delamination effect could be minimized.

The HCl/H₂O ratio, the amount of TTIP and the amount of porous substrate employed in the hydrothermal vessel were varied to determine conditions under which nanorods could be successfully grown on significant amounts of the porous particles. The various trials are summarized in Table 7. While the dimensions of the resulting nanorods could be easily described quantitatively, the extent of surface coverage, the nanorod film quality and the particle-to-particle variability could only be described in qualitative terms. The quality of the resulting nanorod-deposited particles were classified into the following three categories:

Class I (Good):

- Dense, vertically aligned nanorod growth on all sampled particles.
- Little particle-to-particle variability
- Few, if any, regions devoid of nanorods
- No delamination of the nanorod films

Class II (Moderate):

- Nanorod growth on all sampled particles with some variability in nanorod density across particle surface.
- Little particle-to-particle variability
- Few bare regions or regions with low nanorod density
- No delamination of the nanorod films

Class III (Poor):

- Patchy, sporadic or no nanorod growth
- Moderate to high particle to particle variability
- Significant delamination of the nanorod films

Examples of Class I (good), Class II (moderate) and Class III (poor) quality nanorod films are shown in Figure 48.

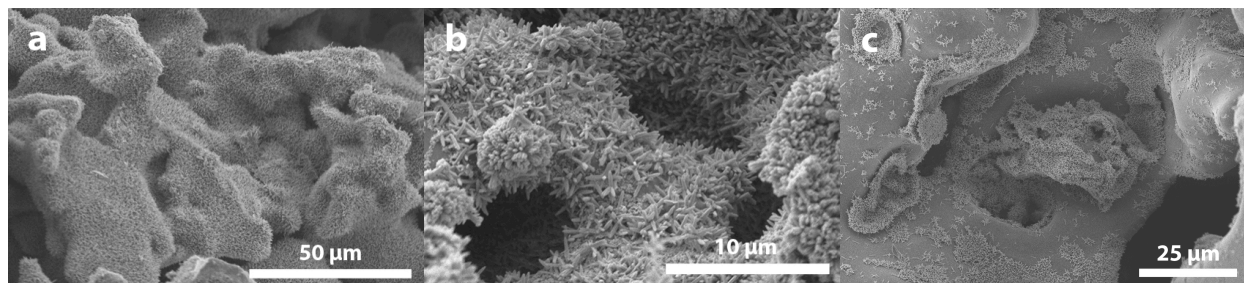


Figure 48: Examples of nanorod films exhibiting (a) Class I (good), (b) Class II (moderate) and (c) Class III (poor) quality

Table 7: Summary of hydrothermal growth conditions and resulting nanorod dimensions

Sample #	Initial Hydrothermal Reactor Conditions						R_q	Resulting Nanorod Dimensions		
	V_{H_2O} (ml)	V_{HCl} (ml)	V_{TIP} (ml)	M_{KCl} (g)	M_{cat} (g)	Time (hours)		Growth Quality	Width (nm)	Length (μm)
HTV-1	100	100	3.3	0	0.5	7	0.3	Good	257	1.72
HTV-2	100	100	3.3	0	5	17	2.6	Moderate	129	1.30
HTV-3	100	100	3.3	0	10	17	5.3	Poor	274	2.51
HTV-4	100	100	3.3	0	15	17	7.9	Poor	152	1.40
HTV-5	100	100	3.3	5	10	17	5.3	Poor	146	1.65
HTV-6	100	100	3.3	5	15	17	7.9	Poor	115	1.41
HTV-7	100	100	3.3	0	20	7	10.5	Poor	127	1.10
HTV-8	100	100	3.3	0	20	17	10.5	Poor	76	1.14
HTV-9	100	100	6.6	0	20	7	5.2	Poor	143	1.29
HTV-10	100	100	6.6	5	20	8.5	5.1	Poor	85	1.15
HTV-11	100	100	6.6	5	20	12	5.2	Poor	166	1.62
HTV-12	100	100	10	0	20	7	3.4	Moderate	322	1.18
HTV-13	100	100	10	5	20	7	3.4	Moderate	223	1.10
HTV-14	100	100	12	5	20	7	2.8	Good	302	1.13
HTV-15	100	100	12	8	20	7	2.8	Good	223	1.16
HTV-16	100	100	12	12	20	7	2.8	Good	228	1.15
HTV-17	100	100	12	5	25	7	3.5	Moderate	226	0.97
HTV-18	50	150	20	0	20	7	2.4	Good	257	2.83
HTV-19	50	150	20	3.5	20	7	2.4	Good	182	2.14
HTV-20 ^a	45	45	1.5	0	1	7	1.2	Good	240	1.65

^a grown in 180 ml hydrothermal vessel at 150 °C

It was found that this classification followed a trend with a ratio, R_q , which was defined as:

$$R_q = \frac{[H^+] M_{cat}}{[TTIP] V_{sol}} \quad (65)$$

where $[H^+]$ and $[TTIP]$ are the initial H^+ and TTIP concentrations (mol/L), while M_{cat} and V_{sol} are the mass of porous particles and the total solution volume employed in the hydrothermal vessels. A clear trend in the quality of the nanorod-deposited particles can be seen in Figure 49, where R_q was plotted versus $[H^+]/[TTIP]$ for each trial and the markers were labeled according to the corresponding classification. It was observed that for constant (V_{sol}/M_{cat}) (corresponding to the slope of the diagonal lines) that the quality of the particles increases with decreasing R_q (Class I). This may be viewed either as the particle quality increasing with lower $[H^+]/[TTIP]$ ratios, where higher $[TTIP]$ results in higher rate nanorod nucleation and growth, or increasing with lower $M_{cat}/([TTIP] V_{sol})$ ratios, where a minimum total number of moles of TTIP is required for proper nanorod growth. Similarly, for constant $[H^+]/[TTIP]$, corresponding to the horizontal lines in Figure 49, the quality of the particles increases with decreasing R_q , implying an ideal $[M_{cat}]/[V_{sol}]$ ratio. The range of R_q values defining the Class II (moderate) region were not constant but rather appear to have a dependence on the $[H^+]/[TTIP]$ ratio, however, it was not possible to derive an explanation for this relationship. The observed relationship between R_q and the particle quality could be reliably reproduced in a smaller 180 ml hydrothermal vessel, indicating that the relationship is independent of the vessel size (at least for vessels less than 500 ml). It should be noted that the same fill percentage, $V_{sol}/V_{reactor}$, was employed for both vessels.

No clear relationship between R_q and the nanorod dimensions could be observed; however, it was noted that for solutions employing 1:1 volume ratios of HCl/H₂O, the nanorods typically grew to lengths between 1.1 and 1.4 μm . It was simultaneously observed that in 1:1 HCl/H₂O solutions, the amount of

TTIP could not be easily increased beyond 12 ml (0.187 mol/L) without the formation of significant amounts of precipitate, both during preparation of the growth solution and during nanorod growth in the hydrothermal vessel. It is hypothesized that the high H₂O content of these solutions leads to rapid hydrolysis of the TTIP, especially so as the TTIP concentration increases, which results in the homogeneous nucleation and precipitation of TiO₂ in solution. This homogeneous nucleation and precipitation competes with the heterogeneous nucleation and growth of nanorods, resulting in shortened nanorod lengths.

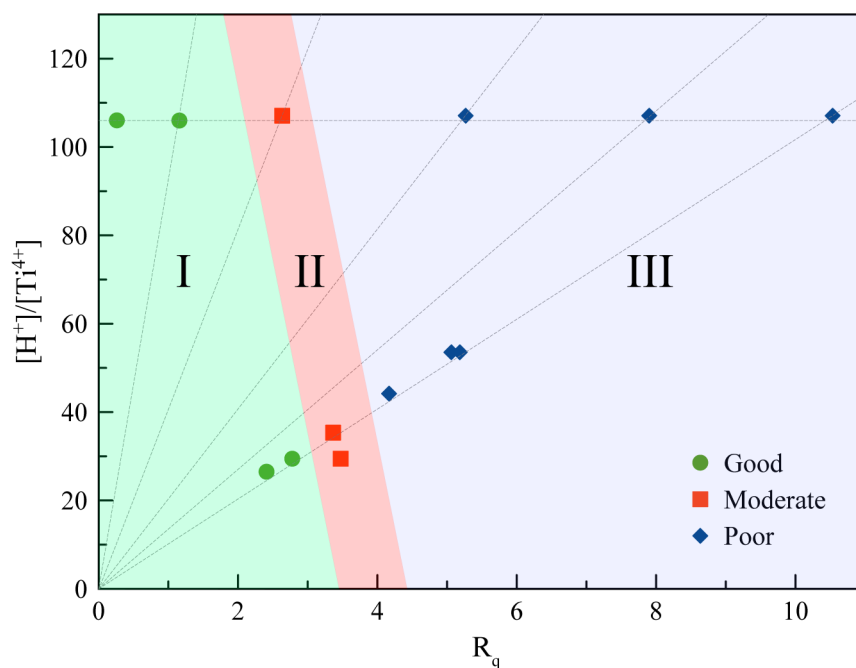


Figure 49: Nanorod film quality classification versus R_q

It was found that by increasing the HCl/H₂O ratio to 3:1, the amount of TTIP could be increased to 20 ml (0.3 mol/L) without the formation of precipitate, which in turn resulted in a ~200% increase in the nanorod length to 2.8 μ m. It should be noted, however, that by increasing the HCl/H₂O ratio to 3:1, the minimum amount of TTIP is required to achieve nanorod growth increases (as R_q increases); indeed, it was observed that for a 3:1 HCl/H₂O solution, 12 ml (0.187 mol/L) of TTIP resulted in little-to-no nanorod growth. It is hypothesized that the increased $[H^+]$ and reduced H₂O content of these solutions

slows the rate of hydrolysis, reduces homogeneous nucleation and allows for a greater amount of TTIP to be dissolved in solution, the combination of which resulting in the growth of longer nanowires; however, the high $[H^+]$ may result in the inhibition of nanorod growth entirely if $[TTIP]$ is not sufficiently high. It was noted that increasing the HCl/H₂O ratio resulted in a notable change of the nanorod shape; nanorods grown at lower HCl/H₂O ratios typically had straight sides and square ends, whereas nanorods formed in high HCl/H₂O ratio solutions had a pronounced tapered shape (Figure 50). This may be a result of the higher $[H^+]$ having a more pronounced effect on growth rate where, as the concentration of Ti in solution decreases during the course of nanorod growth, the rate of growth will reduce more sharply than solutions with lower H^+ concentrations, resulting in the tapered shape.

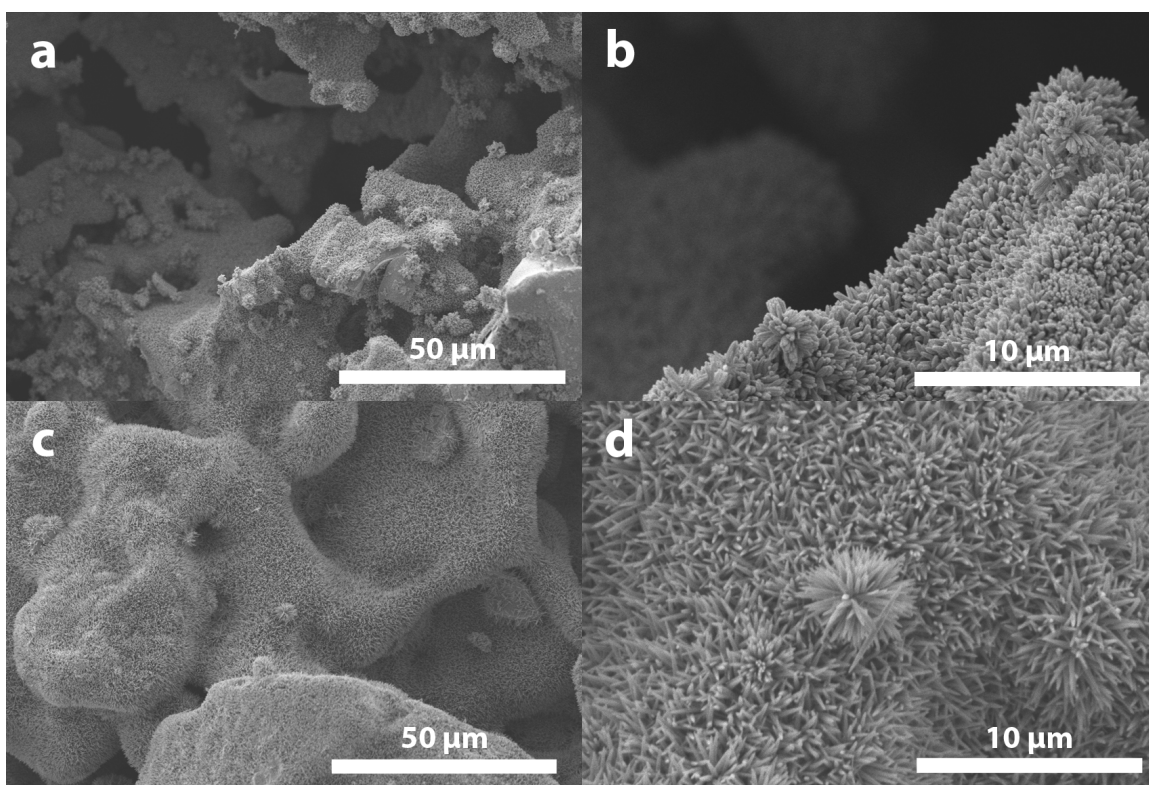


Figure 50: Nanorod-deposited particles grown in (a,b) 1:1 HCl/H₂O solution with 12 ml TTIP and (c,d) 3:1 HCl/H₂O solution with 20 ml TTIP (corresponding to HTV-14 and HTV-18 in Table 7, respectively)

For nearly all growth conditions, the nanorods were observed to consist of bundles of smaller diameter nanorods. It was found that the addition of KCl (up to 12 g) lead to a slight reduction in both the average diameter of the bundles and the smaller nanorods that comprise them. A similar effect has been reported where the addition of NaCl led to reduced nanorod diameters^{162,343}; this effect was discussed to be due to selective adsorption of Cl⁻ on certain facets or due to electrostatic screening. The relative increase in [Cl⁻] due to the addition of KCl, however, is small, as will be any increase in Cl⁻ adsorption, thus it is suspected that the reduction in nanorod diameter was due primarily to the latter effect.

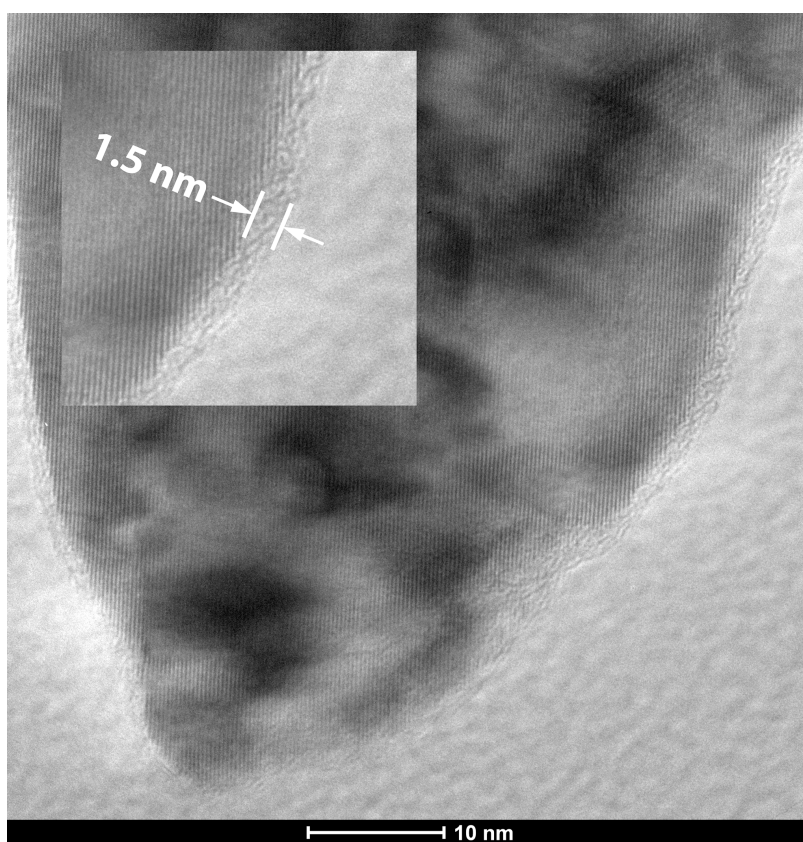


Figure 51: TEM image of graphitic contamination layer of nanorod surface

It was observed that the addition of KCl resulted in an increase of an immiscible organic phase suspended on top of the growth solution; this immiscible phase is presumed to be an isopropoxide species resulting from the hydrolysis of TTIP. It was necessary to carefully decant the immiscible organic layer before

removing the particles from the hydrothermal vessel as the organic layer would easily contaminate the surface of the nanorod-deposited particles and impart a hydrophobic behavior after drying and calcination. Calcining organic-contaminated particles in air resulted in the formation of a graphite-like layer on the surface of the nanorods. TEM imaging (Figure 51) shows that the graphitic layer was 1.5 nm thick. The interplanar spacing of the graphitic layer was 3.3 Å, which is in agreement with (002) d-spacing values reported in literature^{344–346}. The ideal hydrothermal growth conditions were chosen to be those corresponding with HTV-18 (Table 7) as these conditions yielded dense growth of 2.8 µm nanorods over the entire particle surface. Moreover, KCl was not added to the solution to over exacerbation of the organic phase to avoid contamination of the particle surface.

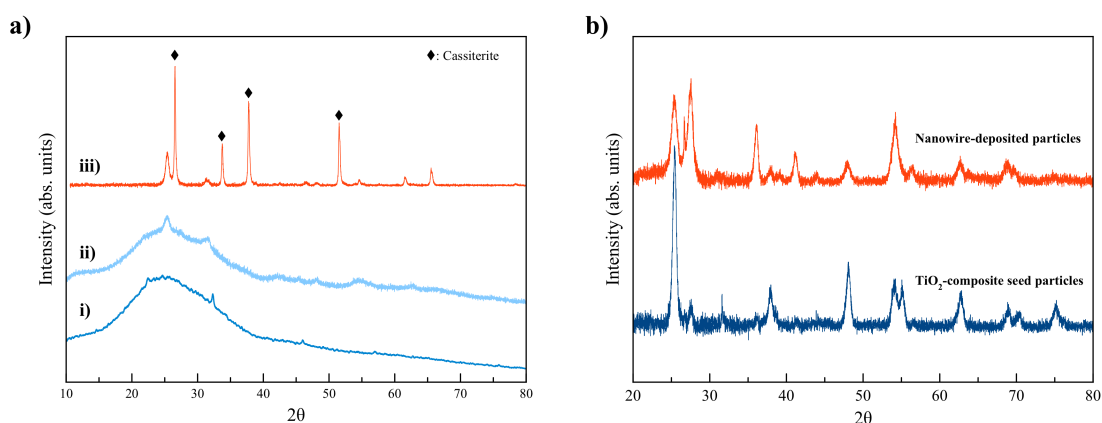


Figure 52: (a) X-Ray diffraction patterns of (i) TiCl_4 -treated seed particles, (ii) nanowire-deposited particles and (iii) nanowires grown on FTO glass slides. (b) X-Ray diffraction patterns of the TiO_2 -composite seed particles and the nanorod-deposited particles.

5.3.3 Characterization

Titanate nanowires were grown on the porous, seeded particles at a $[M_{cat}]/[V_{sol}]$ ratio of 0.025 g/ml in an oven at 80 °C for 7 hours, then calcined at 550 °C in air for 1 hour to convert the titanate nanowires to anatase. XRD analysis of the calcined particles (Figure 52a) revealed the nanowires to be anatase (JCPDS 00-021-1272) with the addition of a small peak located at 31.4°. This small peak has been discussed to be due to the presence of srilankite-like TiO_2 (JCPDS 21-1236)^{249–251,253}. We hypothesized in Chapter 4 that the appearance of srilankite TiO_2 may be due to the incorporation of triazine compounds into the titanate

structure during nanowire growth as a result of the presence of melamine (which was employed as an in-situ source of NH_4^+). As the glass particle substrate created a large background signal, nanowire samples were also grown from fluorine-doped tin oxide (FTO) coated glass slides in order to provide a more detailed XRD pattern for reference (shown in Figure 52a).

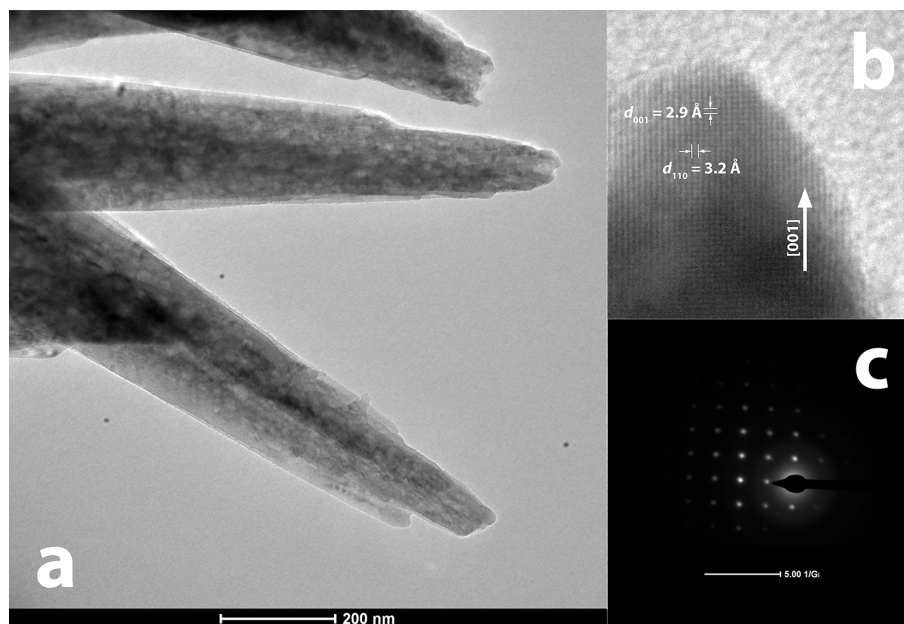


Figure 53: TEM images of (a) hydrothermally grown nanorods and (b) the lattice fringes. (c) The SAED pattern for the nanorod shown in (b).

Nanorod-rod deposited particles were produced in a hydrothermal vessel employing growth conditions corresponding to HTV-18 (Table 7). Figure 52b shows that the TiO_2 -composite seed particles were primarily anatase. Minor rutile content was observed due to the P25 particles incorporated into the film. It can be seen in Figure 52b that, following hydrothermal treatment, the particle surface is covered with rutile (JCPDS 21-1276) nanorods. A small, sharp peak observed at 26.65° in Figure 52 was indexed to $\text{SiO}_2/\text{quartz}$, presumably arising from the glass particle substrate, which may develop a crystalline content after multiple calcination steps at high temperatures. TEM imaging revealed that the nanorods consist of narrow nanorods ($\sim 50\text{-}60 \text{ nm}$ diameter) that have fused together via their vertical faces (Figure 53a). Lattice fringes with interplanar spacing of 2.9 \AA and 3.2 \AA (Figure 53b) correspond with those of the rutile (110) and (001) planes, respectively. As the [110] axis is perpendicular to the vertical sides of the

nanorods, it can be concluded that the nanorods grow with their [001] axis normal to the surface of the porous particles. The select-area electron diffraction (SAED) pattern (Figure 53c) indicates that the nanorods are largely single crystalline throughout their length.

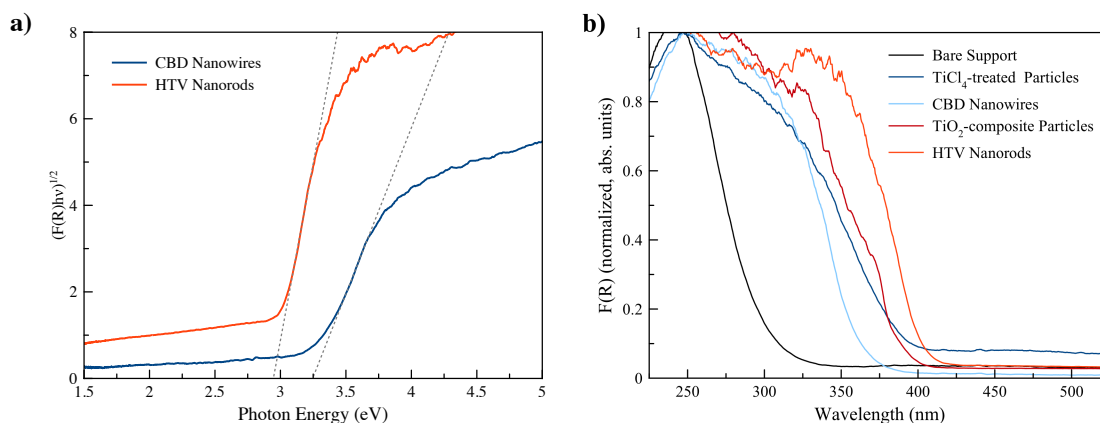


Figure 54: (a) Tauc plots for the nanowire- and nanorod-deposited particles and (b) UV-Vis diffuse reflectance absorption spectra for bare, seeded and nanowire-/nanorod-deposited particles

The band gap energies and absorbance of the CBD nanowire- and HTV nanorod-deposited particles were determined from the diffuse reflectance spectra. The nanowire- and nanorod-deposited particles were found to have band gap energies of 3.25 eV and 2.95 eV (Figure 54a), respectively, which are in close agreement with band gap values reported for anatase and rutile TiO₂ in literature^{91,347,348}. It can be seen in Figure 54b that the optical absorption onset for the TiCl₄-treated seed particles is similar to that of rutile TiO₂, indicating that the TiCl₄ treatment yields rutile crystallites on the porous glass particle surface which act as nucleation sites for nanowire growth. It can therefore be concluded that the phase of the TiO₂ seed layer on porous particles does not effect the product phase of the nanowires or nanorods.

The anatase nanowire-deposited particles were measured to have a skeletal density of 2460 kg/m³ while the rutile nanorod-deposited particles have a skeletal density of 2540 kg/m³, thus yielding effective densities of 1700 and 1790 kg/m³, respectively, when the particles are fluidized in a 2.2M aqueous Na₂CO₃ solution (~1200 kg/m³) for water splitting. The nanowire- and nanorod-deposited particles were

measured to have dry packed bed densities of 570 kg/m^3 and 620 kg/m^3 , respectively, each having a voidage of 0.42. These physical characteristics place both particle types in Geldart class D (spoutable)²⁰⁶, and yield estimated minimum fluidization velocities of 0.0038 m/s ($\sim 0.32 \text{ L/min}$) and 0.0044 m/s ($\sim 0.37 \text{ L/min}$), respectively.

The low bulk particle densities and reduced fluidization velocities observed for both the nanowire- and nanorod-deposited particles yields several desirable and beneficial effects. The low bulk particle densities reduce the mass and, therefore, the momentum of individual particles, which, in turn, reduces the force of impact in particle-to-particle and particle-to-wall collisions. These reduced forces can serve to minimize any damage sustained during impact and significantly reduce the rate of attrition. Similarly, the low fluidization velocities typically provide gentler fluidization conditions and slower particle velocities, which helps to further reduce the rate of attrition. Finally, the low fluidization velocities also serve to reduce the total recirculation rate of the liquid phase. This, in turn, minimizes the energy required for pumping (thereby improving the overall energy efficiency of the process) and minimizes the capital cost of equipment as a smaller pump can be employed.

5.3.4 Attrition Resistance

The large surface pores of the glass particles employed in this work create networks of “valley”- and “dimple”-like indentations surrounded by “peaks” and other large features (Figure 55). These deep indentations provided large areas in which the mechanically weak TiO_2 photocatalyst coating could reside and remain protected from mechanical ablation during fluidization. Similarly, the outermost peaks served to minimize the contact area in particle-to-particle and particle-to-wall collisions, as well as to bear the force of impact. These effects are clearly demonstrated in Figure 55, which shows an anatase nanowire-deposited photocatalyst particle that was fluidized for 40 hours. As seen in Figure 55, the nanowires on the outermost points were compressed into a flat film or ablated from the particle surface (leaving a small

bare area) due to collisions with other particles or the reactor wall, yet the nanowires residing in the deep indentations on the surface remain entirely intact. The small, damaged regions observed at the outermost points represent only a small portion of the visible nanostructure-deposited surface and are only observed under moderate-to-high magnification of select areas (thus making visual estimates of active surface area lost to mechanical attrition challenging).

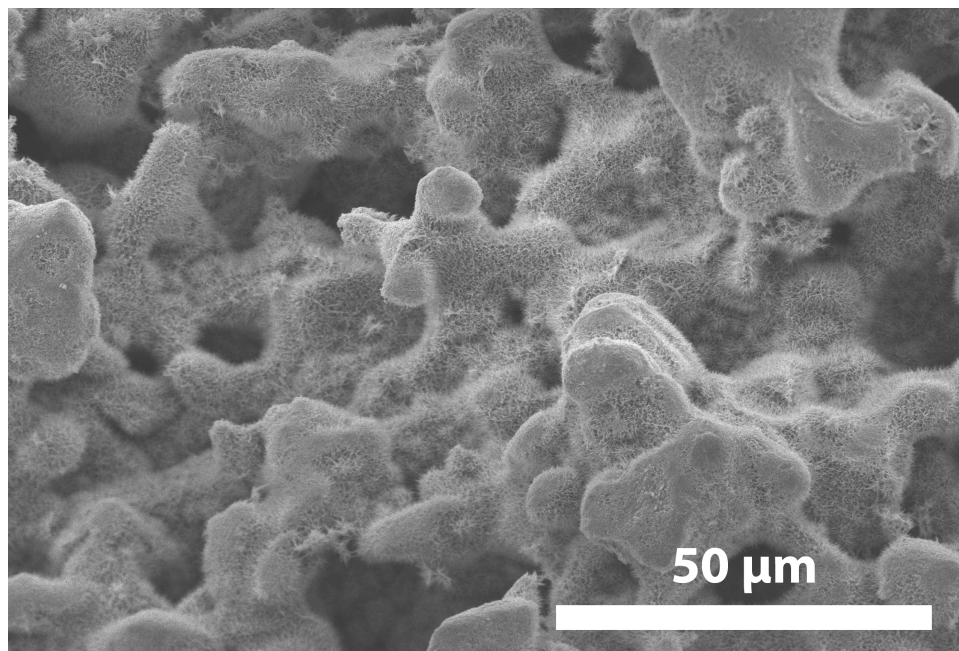


Figure 55: SEM image of an anatase nanowire-deposited particle after 40 hours of fluidization. Nanowires were grown on the porous particles using a $[M_{\text{cat}}]/[V_{\text{sol}}]$ ratio of 0.025 g/ml.

To determine the attrition resistance of the porous glass design, a measured amount of nanorod-deposited particles (70 ml/42.82 g) and solid TiO_2 -composite spheres (70 ml/81.32 g) (which were developed previously in Chapter 2) were individually placed the fluidized bed. The particles were fluidized in the reactor (no UV illumination) using deionized water to an expanded bed height of 24 cm for over 40 hours and the concentration of ablated TiO_2 particles suspended in solution was monitored. It can be seen in Figure 56 that both particle types exhibit a ‘break-in’ period with a high initial rate of attrition as loosely bound or weak features are ablated from the particle surface. After 3.5 hours, most weakly bound TiO_2 is removed from the surface of the nanorod-deposited porous particles, however, this process continues for

up to 5.5 hours for the solid TiO₂-composite spheres. Following the initial break-in period, the TiO₂-composite spheres continue to erode at a constant 0.011 g/(L.hr) while the rate of TiO₂ ablated from the nanorod-deposited particles decreases significantly to a low 0.0011 g/(L.hr). The amount of TiO₂ ablated from the nanorod-deposited particles after 46 hours of fluidization was estimated to less than 1% of the total mass of TiO₂ deposited on the porous particles.

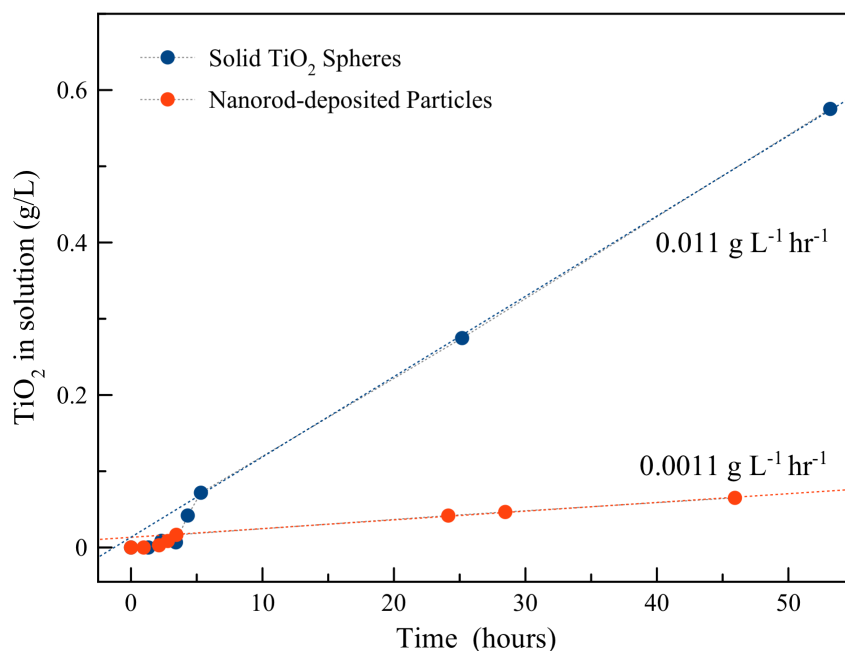


Figure 56: Attrition resistance as determined by the concentration of ablated TiO₂ in solution (g_{TiO₂}/L) for TiO₂ Solid Spheres (•) and Nanorod-deposited samples (•)

5.3.5 Comments on H₂ Evolution Performance

While it was possible to successfully produce 1-D TiO₂ nanostructures on the surface of the porous glass particles, which in turn were shown to be highly effective in preventing the attrition of the nanostructures during fluidization, it was not possible to successfully demonstrate photocatalytic water splitting in the UV-irradiated fluidized bed with these photocatalysts at this time. As discussed in Chapter 3, the low density of the porous particles results in very low flow rates required for fluidization (2-5 L/min), resulting in poor mass transfer in the separator and a long residence time in the fluidized bed and thus causing the back reaction to dominate. This in turn resulted in negligible rates of hydrogen evolution

being evolved from the UV-irradiated fluidized bed reactor system. Attempts were made to increase the required flow rate by decreasing the mass of photocatalyst particles in the reactor and increasing the expanded bed height, however, this resulted in low photocatalyst particle concentrations (and thus poor rates of photon capture). Furthermore, the highly expanded bed made controlling the height of challenging. Similarly, it was attempted to reconfigure the separator to improve the rate of mass transfer; however, none of the modifications yielded a noticeable difference at such low flow rates.

To correct for the low fluidization flow rates and allow the nanowire- and nanorod-deposited porous glass particles to function without significant back-reaction and mass transfer effects, the separator unit would require significant design revisions, optimization and remanufacturing. This is, unfortunately, beyond the scope and time of this thesis. Revisions to the design of the system and further investigation of the water splitting performance of the nanowire- and nanorod-deposited photocatalysts will be carried out in future work.

5.4 Conclusions

- Two separate methods have been developed that allow for the fabrication of fluidizable nanowire and nanorod photocatalysts in large quantities.
- Anatase TiO₂ nanowires were grown onto porous particles using a Chemical Bath Deposition (CDB) process. For $[M_{\text{cat}}]/[M_{\text{sol}}] = 0.025 \text{ g}_{\text{cat}}/\text{ml}$, nanowires 53 nm x 2 μm long were reliably produced in batches sizes up to 30 g of the porous particles. Batch sizes were easily varied by using the appropriate volume of growth solution for the desire amount of porous glass particles. The nanowires were observed to grow in high density over the entire particle surface for all conditions studied.

- Rutile TiO₂ nanorods were produced using a modified hydrothermal method (500 ml reaction vessel) in batches up to 25 g of particles. The quality of the resulting nanorod films was observed to vary according to the initial reactor conditions. A growth quality factor, R_q, was defined that allowed for the quick calculation of the hydrothermal reactor conditions necessary to produce good quality films. R_q allowed for good quality films to be grown on varying different batch amounts and even different hydrothermal reactor sizes. For an initial growth solution having 150 ml HCl/50 ml H₂O/20 ml TTIP, high-density nanorod films 2.8 μm thick could be easily grown.
- It was found that the porous glass beads were highly effective in reducing the rate of photocatalyst attrition. The protective features of the particles reduced the rate of attrition by 10x to near negligible levels.

Chapter 6: Conclusions and Recommendations

6.1 Conclusions

The objectives of this research were to: develop a photocatalytic fluidized bed reactor for hydrogen production, to produce water splitting photocatalysts suitable for fluidization, and to identify the primary factors determining the operation and performance of the system. The following sections provide a discussion on the significance of the various outcomes and their impact on the wider contribution to knowledge.

6.1.1 Photocatalytic Water Splitting in a UV-irradiated Fluidized Bed Reactor

In this work we developed a UV-irradiated fluidized bed reactor system employing an annular fluidized bed design and a liquid-gas separator unit. It was found that by fluidizing platinum-loaded TiO₂-composite spheres in a 2.2M Na₂CO₃ solution, the system was capable of evolving hydrogen at steady rates as high as 211 μmol/hr with an apparent quantum efficiency of 1.33%. When compared to the performance of a platinum-loaded P25 TiO₂ suspended slurry (1 g/L) in the same reactor, it was found that the fluidized photocatalysts exhibit a 44% increase in the apparent quantum efficiency.

As the fluidized platinum-loaded photocatalyst particles remain in the irradiated volume of the reactor only, the evolved H₂/O₂ is quickly carried from the reactor by the flowing liquid phase and is thus separated from the photocatalyst. This is in contrast to the platinum-loaded P25 TiO₂ suspended slurry, which is circulated throughout the reactor system and remains in contact with the evolved H₂/O₂ for extended periods of time. It is known that the presence of platinum deposits on the photocatalyst surface catalyzes the back reaction of H₂ and O₂ to form water, resulting in a loss of efficiency. It is believed that the more effective separation of H₂/O₂ from the Pt-loaded photocatalyst in the fluidized bed design gives rise to the observed increase in efficiency.

While there are several alternatives to platinum catalysts that can be applied for water splitting – such as Au, Pd, Rh, Ni/NiO, Ag and Cu – many of the precious metals also catalyze the back reaction of H₂/O₂ and few have demonstrated performance comparable to or better than platinum^{10,127}. Several approaches, such as Cr₂O₃-coated noble metals²⁷ or molecular electrocatalysts³⁴⁹, are being explored as means to reduce or eliminate the back reaction over the metal deposits; however, most of these technologies are still in their infancy. Our finding is significant as the use of a fluidized bed reactor design, with its improved catalyst/product separation, may allow for the realization of increased efficiencies from existing photocatalyst materials and potentially allowing for economically-viable water splitting in the near future.

6.1.2 Mathematical Model and Understanding of Performance Determining Factors

One of the most significant outcomes of this research was the derivation of a mathematical model describing the behavior of the fluidized bed/separator system. From this model, it became apparent that the performances of the fluidized photocatalysts employed in this thesis were largely dictated by mass transfer in the gas-liquid separator (which, in turn, is a function of the fluidization flow rate) and the capture of photons in the reactor (as a function of particle concentration and expanded bed height). The parameters of this model were fitted to our experimental data and were found to be within their expected range of values. The model and fitted parameters were used to predict the expected rates of hydrogen evolution for the photocatalyst masses and bed heights employed in our experiments and it was found that the predicted values closely matched the experimentally measured rates. By studying the model, it was possible to understand how various parameters – such as the photocatalyst properties, separator performance and reactor dimensions – affect the rate of hydrogen evolution.

From our model, it was seen that increasing amounts of photocatalyst in the reactor result in an increase in photon capture and, subsequently, the hydrogen evolution rate. Increasing the photocatalyst amount beyond a certain amount, however, resulted in a decrease in performance. While it may be first assumed

that an excess of platinum-loaded photocatalyst simply promotes the back reaction of H_2/O_2 , it was found that the decreasing fluidization velocities required for higher photocatalyst loadings (at a fixed bed height) had the most pronounced effect. As the rate of liquid-to-gas mass transfer in the separator was controlled by the flow rate of solution through it, high photocatalyst loadings resulted in reduced mass transfer, which in turn exacerbated the back reaction. The implications of this finding were surprising as it suggested that large, heavy photocatalyst particles requiring high fluidization velocities would yield increased performance, while particles with smaller diameters or reduced density would result in a significant reduction in performance.

This model and its implications, unfortunately, eluded us until the end of our work, so it was not possible to use it as a guide toward the design of the photocatalyst particles or the reactor system itself. The behavior of decreasing performance with decreasing flow rate ran contrary to a number of the efforts we made toward improving the photocatalyst design in this thesis (many of which were not reported). Small particles and particles with reduced bulk density were sought for better distribution/adsorption of light, as well as reduced flow rates (which would yield reduced pumping-related energy and equipment costs in a scaled system). However, the behavior of the system when using these alternative particles was similar to effects seen with contaminated or poor quality photocatalysts, resulting in a number of designs being disregarded and considerable time being spent analyzing and “troubleshooting”.

The impact of this model on the understanding of water splitting in fluidized bed reactors has wide-ranging significance on the design and operation of both the reactor system and the photocatalyst. One of the most critical facts revealed by the model is the importance of the design of the separator as even small improvements in the mass transfer coefficient for a given flow rate bring about significant improvements in the rate of hydrogen evolution. We demonstrated this in Chapter 3 where a slight reconfiguration of the separator yielded a 350% increase in the rate of hydrogen evolution. If a fluidized bed water splitting

system can be used in conjunction with efficient gas/liquid separation, the result may bring economically viable water splitting with existing materials within reach.

From the model derived in Chapter 3, it was observed that optimization of the hydrogen evolution rate requires a balance between optimizing photon capture while minimizing the effects of the back reaction. These constraints, in turn, led to the understanding that the water splitting performance of the fluidized bed can be improved by increasing the particle concentration in the fluidized bed while simultaneously decreasing both the inner and out diameters of the reactor. This understanding suggests that a scaled system consisting of several small diameter reactors is preferred over that of a system having a single, large reactor. This has several implications on the design of a scaled, solar water splitting system:

1. The greatest performance might be achieved by employing an externally situated light source focused on a narrow, tubular fluidized bed reactor as opposed to an annular reactor design.
2. The narrow, single tube reactor is ideally suited to be used with a concave parabolic concentrating (CPC) mirror which can focus solar irradiation along the length of the reactor tube. This is a simple and efficient alternative to the “light pipe” system that would be required to deliver solar radiation to an annular fluidized bed reactor.
3. A number of tubular fluidized bed reactor/CPC mirror units can be arranged into a panel-like array and connected by common inlet and outlet manifolds.
4. These panelized arrays can be easily manipulated by a heliostat to maintain maximum performance through out the day and year.. While it is not yet understood how water splitting fluidized bed reactors would behave when held at an incline, the ability to reorient the reactors to maximize performance would allow the reactors to function in winter months and at higher latitudes where the sun is positioned lower toward the horizon. This presents an

advantage over “solar pond” concepts (which employ shallow suspended photocatalyst slurry ponds) whose performance will vary with the sun’s azimuth throughout the day and year.

5. High quality, optically transparent tube materials (such as quartz) are commonly produced in a range of small diameters and can be obtained at a relatively low cost; however, the price of these materials can increase significantly with the diameter of the tube. As such, the narrow, tubular fluidized bed reactors present a cost advantage over large or annular reactor designs.

6.1.3 Effect of Na₂CO₃ on the Performance of Photocatalytic Water Splitting

We demonstrate that carrying out water splitting in a sodium carbonate solution (2.2M) is vital both for long term stability and high rates of hydrogen evolution. In the absence of Na₂CO₃, the performance of the photocatalyst decays steadily with time toward a low steady state and does not evolve oxygen. We then demonstrate that adding Na₂CO₃ to the system results not only the stoichiometric evolution of H₂/O₂ but also a recovery to high rates of H₂ evolution.

While the significance of Na₂CO₃ is known in literature, little is understood about the mechanism by which it acts. The current hypotheses in literature regarding of the effect induced by Na₂CO₃ is that it: 1) forms a layer over platinum surfaces and suppresses the back reaction, 2) improves desorption of O₂ or destabilizes peroxo species that deactivate the TiO₂ surface, and 3) provides an alternate reaction pathway involving that is favorable to the evolution of O₂. In our work we demonstrate that the Na₂CO₃ effect is photoinduced and the degree to which it affects the performance is dependent on the period of illumination. Moreover, it is shown that removing the illumination source for several hours does not alter this effect and that performance returns immediately to the same rate before the light source was removed.

While a complete understanding of the Na_2CO_3 effect remains elusive, our observations provide further insight into its behavior. The observed results run contrary to the existing belief that its presence simply alters the performance of the system but rather shows that the underlying mechanism involves a complex relationship between photoactivated TiO_2 and the Na_2CO_3 solution.

6.1.4 Fluidizable Photocatalyst Design and Manufacturing

In an attempt to improve both the mechanical stability and performance of the photocatalyst, we sought to explore several variations of the photocatalyst design. While, ultimately, it was discovered that the reduced flow rates (and thus reduced liquid-to-gas mass transfer in the separator) associated with the size and density of the particles led to poor or negligible water splitting performance, the outcomes are no less significant.

One design of particular note employs an entirely new photocatalyst architecture that combined attrition resistant photocatalyst supports employed for water treatment and advanced nanostructured (yet mechanically weak) photocatalysts found in photoelectrochemical cell research. This photocatalyst design achieved the objective of being attrition resistant and allowing for aligned nanowire structures to be used in physically demanding environments. While the low-density of the particles results in them being unsuitable for water splitting at this time, the photocatalyst design may be adapted to other processes, such as water treatment, and the methods we developed for their manufacture may find widespread application.

To our knowledge, there are few methods that may be scaled easily for the production of nanowires and nanorods in large volumes. In this thesis, we developed a novel method to produce long, vertically aligned titanate nanowires that are then converted to anatase. This method was found to be remarkably simple and scaled in a very simple manner, with the only limitation being the size of the glass containers that could

be fit into our lab oven. Moreover, it was observed in electrochemical measurements that these anatase nanowires could exceed both P25 TiO₂ and rutile nanorods in terms of performance, both of which are highly popular for the production of dye-sensitized solar cells.

In addition to the nanowire method, we expanded on the most widely used method for the production of rutile nanorods to allow for nanowire growth onto high surface area substrates. Through this work we developed a parameter that allows one to predict the growth conditions necessary for certain applications. Through our own application of this parameter, we were able to not only grow nanorods in highly acidic conditions (which until now was thought to be impossible due to inhibited growth at low pH) but were also able to do so with great success, producing dense films of long nanorods over a high surface area porous substrate.

6.2 Future Work and Recommendations

1. While the mathematical model developed was effective for our purposes, several simplifications regarding the dynamic and optical behaviors of the fluidized bed were made. Developing a more complex model that accounts for different fluidization regimes in the reactor, such as bubbling or spouted beds, and their effect on the scattering and absorption of light, is recommended.
2. In order for the mathematical model to be employed with a high degree of confidence, it is necessary to obtain accurate values for each of the model parameters. As such, each of the parameters should be investigated independently. To facilitate investigation of the parameters, several modifications to the system design are recommended:
 - a. Commercially available dissolved hydrogen and dissolved oxygen meters, or custom-made Clark electrodes, should be situated at the inlets of both the fluidized bed reactor and the separator in order to measure the real-time concentrations of hydrogen and

oxygen in the liquid bulk. Similarly, a pH probe will allow for real-time pH monitoring. These measurements will allow for the back reaction rate constant, k'_r , and the separator mass transfer constant, k''_L , to be studied independently and accurately. To our knowledge, such a study of a water splitting system has not been demonstrated in literature.

- b. A plethora of sample ports should be located along the length of the reactor body to allow for optical and liquid sampling. By connecting long and short collimating tubes to each of these sample ports, it is possible to measure the amount of specular and scattered light reaching the out reactor wall, respectively. This will allow the optical behavior of the fluidized bed under varying conditions and fluidization regimes to be easily studied. In addition, the more rigorous optical measurements will provide more accurate calculation of the quantum efficiency as well as support the modeling of the optical properties of the bed through a complex radiation transfer equation.
- c. Sodium carbonate can be notoriously challenging to work with due to its corrosive nature and its tendency to “salt creep” (wherein dried Na_2CO_3 solution wicks more solution from the system, which in turn dries and perpetuates the wicking/drying process). The latter issue is particularly troublesome as the salt creep can produce significant leakage of the Na_2CO_3 solution, particularly so at sampling ports. It is recommended that the optical sample ports be permanently sealed with quartz glass windows and to minimize the number of liquid sampling ports to avoid this issue.
- d. Similarly, residual Na_2CO_3 solution can make cleaning the reactor system very challenging as it can be difficult to remove all traces completely and any dried solution present at fluid connections and seals during reassembly of the system results in salt creep. Employing a highly modular system with Tri-clamp sanitary fittings (as opposed to flanged connections with o-rings held together with bolts or machine screws) will

allow for fast and complete disassembly of the system for thorough cleaning between experiments. A vinegar or dilute HCl rinsing solution is highly effective for ensuring complete removal of Na_2CO_3 during cleaning. Employing several drain valves at the lowest points in the system will further facilitate the cleaning processes.

- e. In order to study the effect of temperature on each of the parameters and the overall rate of hydrogen evolution, it is recommended that a heat exchange unit be placed in series between the pump and fluidized bed reactor. If suspended slurry photocatalysts are to be employed in the system during future studies, it is highly recommended that the heat exchange unit be a flat plate exchanger designed for easy disassembly and cleaning (such as those designed for brewing or biological applications) as the photocatalyst nanoparticles can be notoriously challenging to eliminate from a system completely (particularly so for equipment having high surface area and complex geometry).
3. As the performance of the fluidized bed water-splitting reactor was highly dependent on the rate of mass transfer in the separator, the performance of the system and the range of possible photocatalyst designs can be greatly enhanced by a more efficient separator. Moreover, significant improvements to the separator performance are required in order to achieve appreciable rates of hydrogen evolution from the nanowire- and nanorod-deposited photocatalyst particles presented in Chapter 5. In addition, more in-depth studies of the system parameters can be made if the separator performance can be made largely independent of the flow rate.

Hollow-fiber membrane separators should be investigated as suitable design alternatives due to their high contact area and ability to apply a vacuum to facilitate hydrogen removal. Moreover, the performance of hollow-fiber membrane separators may exhibit a reduced dependence on flow rate through the unit. Alternatively, a drum-type gas-liquid separator with a volume larger than

the unit employed in this work (so as to provide an increased residence time) may also be employed. The drum-type separator may be modified further such that the liquid stream entering the separator is sprayed as a fine mist to maximize the gas-liquid interfacial area.

4. **The primary design objective of any fluidized bed water splitting system employing precious metal-loaded photocatalysts should be to first maximize the design and performance of the separator.** Any efforts to enhance the performance of the photocatalyst are mostly futile while the separator is the limiting factor.

5. Fluidization of small photocatalyst particles offers enhanced photon absorption and more effective bed behavior (i.e., no bubbling or spouting). If a more efficient separator can be realized, such that flow rate no longer limits the performance of the small particles, the development of small diameter photocatalyst particles should be made a priority to:
 - Improve fluidization behavior
 - Improve photon capture
 - Reduce flow rates (thus reducing energy and capital costs)

6. Once the separator has been optimized to minimize the back reaction, greater focus should then be placed on developing photocatalyst particles that exhibit visible light activity so that the solar-to-hydrogen conversion efficiency may be improved. Recent visible light active photocatalysts in literature have begun displaying improved efficiencies, though many still fall short of the efficiencies needed to yield an economically viable solution. These photocatalysts should be investigated for use in the fluidized bed system as the reduction in the back reaction achieved by the fluidized bed/separator approach may yield the efficiency increases necessary to achieve an economically viable process.

7. Similarly, once the separator has been optimized to remove mass transfer limitations and minimize the back reaction, efforts should be directed toward maximizing photon capture and minimizing charge recombination. This can be achieved through the design of the fluidized bed reactor (by optimizing the reactor dimensions, reflective surface coatings to minimize photon loss from the reactor, etc.) and the particles themselves (such through particle size, surface texture, material selection, etc.). However, care should be taken to avoid increasing the back reaction in the process. The fluidizable nanowire- and nanorod-deposited photocatalysts presented in Chapter 5 demand further investigation once the mass transfer related issues can be resolved.

8. As the fluidized bed system yields improved performance through enhanced separation of the platinum-loaded photocatalyst and the evolved H_2/O_2 , the question remains: Does the use of a fluidized bed design yield any net benefit for noble metal-free photocatalysts? If so, how will its performance compare to slurry photocatalyst systems? While there are few alternative co-catalysts that can match the performance of Pt, metal oxide catalyst such as NiO, PtO and Cr_2O_3/Pt have demonstrated in literature promising hydrogen evolution performance while simultaneously significantly reducing the parasitic back reaction. Titanium dioxide photocatalysts deposited with these co-catalysts may be suitable for the exploration of the behavior of the fluidized bed system in the absence of recombination.

9. If the back reaction can be significantly reduced or eliminated entirely through the development of a suitable co-catalyst, fluidizing small photocatalyst particles with gas bubbles in a three-phase reactor should be explored. This approach offers several advantages such as requiring no pumps (the upward motion of the gas bubbles agitates the solution and fluidizes the particles) and allowing for the gas to be easily collected at the top of the reactor. Moreover, fluidizing with

nitrogen gas will aid in the dilution of the H₂/O₂ product gases such that the composition is no longer within the explosive limit, thus improving safety. Fluidizing with CO₂ would be an interesting alternative to investigate, as it would be an effective means for photocatalytic CO₂ reduction to methane or higher carbons.

10. While the photocatalysts employed in this work demonstrated significant resistance to attrition over a period of 20–50 hours (particularly so for the porous glass-based particles), only a small number of exploratory experiments were made to investigate the very long-term performance of the system (the longest being ~250 hours). A dedicated fluidized bed system should be constructed to investigate the long-term performance over the course of several months of operation. Ideally, the highly attrition resistant porous glass particles would be employed for this test provided the mass transfer issues stemming from their low fluidization flow rates can be resolved. This system would require a cold-trap on the product gas line exiting the separator to condense and return any water vapor back to the system, or the system may be fitted with an automatic top-off system that can supply deionized water to make up for water lost to the water splitting reaction and evaporation. Thermocouples and a compressed air source can be employed to measure and maintain the operating temperature of the UV lamp so as to preserve lamp life and avoid accelerated aging due to excessive heat. An optical sensor is required to monitor the lamp output over the course of the experiment so that any changes in the rate of hydrogen evolution can be ascribed to changes in the behavior of the UV lamp or photocatalyst particles.
11. The mechanism behind the dramatic effect that Na₂CO₃ has on TiO₂ photocatalysts is poorly understood and demands a thorough investigation such that it may be optimized or that principles behind its operation may be engineered into future generations of photocatalysts. While this effect may be studied in the fluidized bed system by observing its effect on the rate of back reaction,

electrochemical analysis of the Na_2CO_3 effect on TiO_2 photoelectrodes will provide a greater depth of detail and insight. Electrochemical analyses such as cyclic voltammetry and electrochemical impedance spectroscopy may provide insight into the mechanism, the active chemical species, whether the effects acts on the TiO_2 surface or over platinum deposits, and whether Na_2CO_3 effects the anodic or cathodic portion of the water splitting reaction. The recovery of a previously poorly performing photocatalyst upon addition of Na_2CO_3 to the solution (such as that demonstrated in Chapter 2) can be investigated in the same electrochemical set-up. No focused electrochemical study of the Na_2CO_3 effect has been presented in literature and thus represents a significant gap in knowledge.

12. While the current method for the scalable growth of anatase nanowires presented in this thesis is effective, the melamine employed to control hydrolysis and supply NH_4^+ *in-situ* may be incorporated into the nanowires or may result in a poly-s-triazine/heptane/graphitic carbon nitride film on the nanowire surface. Both of these effects will lead to enhanced charge recombination. Recent results suggest that substituting urea for melamine may eliminate this issue, and thus should be explored in greater detail.
13. Currently high acid concentrations are employed to retard homogeneous nucleation in solution and enhance the heterogeneous nucleation and growth of nanowires on a substrate surface. Using peroxotitanate precursors containing chelating ligands – such as citrate or lactate ions – may allow for the acid concentration to be reduced considerably, thus expanding the range of substrates to which the process can be applied.
14. Though the fluidizable, nanowire- and nanorod-deposited photocatalysts were developed for the purposes of water splitting, these advanced photocatalyst designs may also be applied to other

photocatalytic processes such as water treatment. The nanostructured photocatalysts presented in Chapters 4 and 5 should be investigated for the degradation of a model organic contaminant in both fluidized bed and immobilized film reactors. The anatase nanowire films discussed in Chapter 4 demonstrated insensitivity to mass transfer effects, whereas the degradation rate of P25 films was nearly halved in the absence of a well-stirred solution. These nanowire films may address mass transfer limitations observed in other photocatalytic system designs.

Bibliography

1. IEA. *World Energy Outlook 2014*. (2014). doi:10.1787/weo-2014-en
2. EIA. *World Energy Outlook 2015*. (OECD Publishing, 2015). doi:10.1787/weo-2015-en
3. IEA. *World Energy Outlook Special Report 2015: Energy and Climate Change*. (2015).
4. Freedomia Focus. *World Hydrogen*. (2014). at <Retrieved from Freedomia Focus database>
5. Bockris, J. O. Hydrogen economy in the future. *Int. J. Hydrogen Energy* **22**, 1–15 (1999).
6. Contreras, A. Solar–hydrogen: an energy system for sustainable development in Spain. *Int. J. Hydrogen Energy* **24**, 1041–1052 (1999).
7. Nowotny, J., Sorrell, C. C., Sheppard, L. R. & Bak, T. Solar-hydrogen: Environmentally safe fuel for the future. *Int. J. Hydrogen Energy* **30**, 521–544 (2005).
8. Lee, D.-H. Toward the clean production of hydrogen: Competition among renewable energy sources and nuclear power. *Int. J. Hydrogen Energy* **37**, 15726–15735 (2012).
9. Lee, D.-H. & Hung, C.P. Toward a clean energy economy: With discussion on role of hydrogen sectors. *Int. J. Hydrogen Energy* **37**, 15753–15765 (2012).
10. Ni, M., Leung, M. K. H., Leung, D. Y. C. & Sumathy, K. A review and recent developments in photocatalytic water-splitting using TiO₂ for hydrogen production. *Renew. Sustain. Energy Rev.* **11**, 401–425 (2007).
11. Chen, X., Shen, S., Guo, L. & Mao, S. S. Semiconductor-based photocatalytic hydrogen generation. *Chem. Rev.* **110**, 6503–70 (2010).
12. Oh, Y. C. & Jenks, W. S. Photocatalytic degradation of a cyanuric acid, a recalcitrant species. *J. Photochem. Photobiol. A Chem.* **162**, 323–328 (2004).
13. Galińska, A. & Walendziewski, J. Photocatalytic Water Splitting over Pt–TiO₂ in the Presence of Sacrificial Reagents. *Energy & Fuels* **19**, 1143–1147 (2005).
14. Escobedo Salas, S., Serrano Rosales, B. & De Lasa, H. Quantum yield with platinum modified TiO₂ photocatalyst for hydrogen production. *Appl. Catal. B Environ.* **140–141**, 523–536 (2013).
15. Karakitsou, K. E. & Verykios, X. E. Effects of altermvalent cation doping of titania on its performance as a photocatalyst for water cleavage. *J. Phys. Chem.* **97**, 1184–1189 (1993).
16. Ding, Z., Lu, G. Q. & Greenfield, P. F. Role of the Crystallite Phase of TiO₂ in Heterogeneous Photocatalysis for Phenol Oxidation in Water. *J. Phys. Chem. B* **104**, 4815–4820 (2000).
17. Sreethawong, T., Suzuki, Y. & Yoshikawa, S. Synthesis, characterization, and photocatalytic activity for hydrogen evolution of nanocrystalline mesoporous titania prepared by surfactant-assisted templating sol–gel process. *J. Solid State Chem.* **178**, 329–338 (2005).
18. Jitputti, J., Pavasupree, S., Suzuki, Y. & Yoshikawa, S. Synthesis and photocatalytic activity for water-splitting reaction of nanocrystalline mesoporous titania prepared by hydrothermal method. *J. Solid State Chem.* **180**, 1743–1749 (2007).
19. Jitputti, J., Suzuki, Y. & Yoshikawa, S. Synthesis of TiO₂ nanowires and their photocatalytic activity for hydrogen evolution. *Catal. Commun.* **9**, 1265–1271 (2008).
20. Leung, D. Y. C. *et al.* Hydrogen production over titania-based photocatalysts. *ChemSusChem* **3**, 681–694 (2010).
21. Luttrell, T. *et al.* Why is anatase a better photocatalyst than rutile?--Model studies on epitaxial

- TiO₂ films. *Sci. Rep.* **4**, 4043 (2014).
22. Kiwi, J. & Grätzel, M. Optimization of conditions for photochemical water cleavage. Aqueous Pt/TiO₂ (anatase) dispersions under ultraviolet light. *J. Phys. Chem.* **88**, 1302–1307 (1984).
 23. Kemppainen, E. *et al.* Scalability and feasibility of photoelectrochemical H₂ evolution: the ultimate limit of Pt nanoparticle as an HER catalyst. *Energy Environ. Sci.* **8**, 2991–2999 (2015).
 24. Subramanian, V., Wolf, E. & Kamat, P. V. Semiconductor-metal composite nanostructures. To what extent do metal nanoparticles improve the photocatalytic activity of TiO₂ films? *J. Phys. Chem. B* **105**, 11439–11446 (2001).
 25. Shockley, W. & Queisser, H. J. Detailed balance limit of efficiency of p-n junction solar cells. *J. Appl. Phys.* **32**, 510–519 (1961).
 26. Kudo, A. & Miseki, Y. Heterogeneous photocatalyst materials for water splitting. *Chem. Soc. Rev.* **38**, 253–278 (2009).
 27. Maeda, K. & Domen, K. Photocatalytic Water Splitting: Recent Progress and Future Challenges. *J. Phys. Chem. Lett.* **1**, 2655–2661 (2010).
 28. Osterloh, F. E. & Parkinson, B. A. Recent developments in solar water-splitting photocatalysis. *MRS Bull.* **36**, 17–22 (2011).
 29. Liu, C., Tang, J., Chen, H. M., Liu, B. & Yang, P. A fully integrated nanosystem of semiconductor nanowires for direct solar water splitting. *Nano Lett* **13**, 2989–2992 (2013).
 30. Takata, T., Pan, C. & Domen, K. Recent progress in oxynitride photocatalysts for visible-light-driven water splitting. *Sci. Technol. Adv. Mater.* **16**, 033506 (2015).
 31. Moniz, S. J. A., Shevlin, S. a., Martin, D. J., Guo, Z.-X. & Tang, J. Visible-light driven heterojunction photocatalysts for water splitting – a critical review. *Energy Environ. Sci.* **00**, 1–29 (2015).
 32. Osterloh, F. E. Inorganic nanostructures for photoelectrochemical and photocatalytic water splitting. *Chem. Soc. Rev.* **42**, 2294–2320 (2013).
 33. Burda, C. *et al.* Enhanced Nitrogen Doping in TiO₂ Nanoparticles. *Nano Lett.* **3**, 1049–1051 (2003).
 34. Wang, G. *et al.* Hydrogen-treated TiO₂ nanowire arrays for photoelectrochemical water splitting. *Nano Lett.* **11**, 3026–33 (2011).
 35. Kitano, M., Matsuoka, M., Ueshima, M. & Anpo, M. Recent developments in titanium oxide-based photocatalysts. *Appl. Catal. A Gen.* **325**, 1–14 (2007).
 36. Mitoraj, D. & Kisch, H. The Nature of Nitrogen-Modified Titanium Dioxide Photocatalysts Active in Visible Light. *Angew. Chemie Int. Ed.* **47**, 9975–9978 (2008).
 37. Walter, M. G. *et al.* Solar Water Splitting Cells. *Chem. Rev.* **110**, 6446–6473 (2010).
 38. Jingshan, L. *et al.* Water photolysis at 12.3% efficiency via perovskite photovoltaics and Earth-abundant catalysts. *Science (80-.)*. **345**, 1593–1596 (2014).
 39. May, M. M., Lewerenz, H., Lackner, D., Dimroth, F. & Hannappel, T. Efficient direct solar-to-hydrogen conversion by in situ interface transformation of a tandem structure. *Nat. Commun.* **6**, 8286 (2015).
 40. Abe, R., Sayama, K., Domen, K. & Arakawa, H. A new type of water splitting system composed of two different TiO₂ photocatalysts (anatase, rutile) and a IO₃⁻/I⁻ shuttle redox mediator. *Chem. Phys. Lett.* **344**, 339–344 (2001).

41. Sayama, K., Mukasa, K., Abe, R., Abe, Y. & Arakawa, H. A new photocatalytic water splitting system under visible light irradiation mimicking a Z-scheme mechanism in photosynthesis. *J. Photochem. Photobiol. A* **148**, 71–77 (2002).
42. Lee, K., Nam, W. S. & Han, G. Y. Photocatalytic water-splitting in alkaline solution using redox mediator. 1: Parameter study. *Int. J. Hydrogen Energy* **29**, 1343–1347 (2004).
43. Sayama, K., Abe, R., Arakawa, H. & Sugihara, H. Decomposition of water into H₂ and O₂ by a two-step photoexcitation reaction over a Pt–TiO₂ photocatalyst in NaNO₂ and Na₂CO₃ aqueous solution. *Catal. Commun.* **7**, 96–99 (2006).
44. Linkous, C., Muradov, N. & Ramser, S. Consideration of reactor design for solar hydrogen production from hydrogen sulfide using semiconductor particulates. *Int. J. Hydrog.* **20**, 701–709 (1995).
45. Baniyadi, E., Dincer, I. & Naterer, G. F. Exergy and environmental impact assessment of solar photoreactors for catalytic hydrogen production. *Chem. Eng. J.* **213**, 330–337 (2012).
46. Villa, K., Domènech, X., Malato, S., Maldonado, M. I. & Peral, J. Heterogeneous photocatalytic hydrogen generation in a solar pilot plant. *Int. J. Hydrogen Energy* **38**, 12718–12724 (2013).
47. Priya, R. & Kanmani, S. Design of pilot-scale solar photocatalytic reactor for the generation of hydrogen from alkaline sulfide wastewater of sewage treatment plant. *Environ. Technol.* **34**, 2817–2823 (2013).
48. Singh, A., Alam, Z., Sahu, N. & Sinha, A. S. K. *Photocatalytic Hydrogen Production using Solar Radiation in Photo Reactor: Reactor Design and Preliminary Results*. Paper presented at Chemcon 2013: The 66th Annual Session of the Indian Institute of Chemical Engineers, Mumbai (2013). doi:10.13140/2.1.2544.0642
49. James, B. D., Baum, G. N., Perez, J. & Baum, K. N. Technoeconomic analysis of photoelectrochemical (PEC) hydrogen production. *DOE Contract Number GS-10F-009J 22201*, 1–128 (2009).
50. Pinaud, B. A. *et al.* Technical and economic feasibility of centralized facilities for solar hydrogen production via photocatalysis and photoelectrochemistry. *Energy Environ. Sci.* **6**, 1983 (2013).
51. Fabian, D. M. *et al.* Particle Suspension Reactors and Materials for Solar-Driven Water Splitting. *Energy Environ. Sci.* **8**, 2825–2850 (2015).
52. Mukherjee, P. S. & Ray, A. K. Major Challenges in the Design of a Large-Scale Photocatalytic Reactor for Water Treatment. *Chem. Eng. Technol.* **22**, 253–260 (1999).
53. Chen, D., Li, F. & Ray, A. K. Effect of mass transfer and catalyst layer thickness on photocatalytic reaction. *AIChE J.* **46**, 1034–1045 (2000).
54. Turchi, C. & Ollis, D. Comment. Photocatalytic reactor design: an example of mass-transfer limitations with an immobilized catalyst. *J. Phys. Chem.* **92**, 6852–6853 (1988).
55. Escudero, J. C., Simarro, R., Cervera-March, S. & Giménez, J. Rate-controlling steps in a three-phase (solid–liquid–gas) photoreactor: a phenomenological approach applied to hydrogen photoproduction using Pt–TiO₂ aqueous suspensions. *Chemical Engineering Science* **44**, 583–593 (1989).
56. Grimes, C. A., Mor, G. K., *TiO₂ Nanotube Arrays*. (Springer US, 2009). doi:10.1007/978-1-4419-0068-5
57. Cai, J. *et al.* Self-cleaning, broadband and quasi-omnidirectional antireflective structures based on mesocrystalline rutile TiO₂ nanorod arrays. *Energy Environ. Sci.* **5**, 7575 (2012).

58. Yun, H. J., Lee, H., Joo, J. B., Kim, W. & Yi, J. Influence of Aspect Ratio of TiO₂ Nanorods on the Photocatalytic Decomposition of Formic Acid. *J. Phys. Chem. C* **113**, 3050–3055 (2009).
59. Yun, H. J., Lee, H., Joo, J. B., Kim, N. D. & Yi, J. Effect of TiO₂ Nanoparticle Shape on Hydrogen Evolution via Water Splitting. *J. Nanosci. Nanotechnol.* **11**, 1688–1691 (2011).
60. Murakami, N., Katayama, S., Nakamura, M., Tsubota, T. & Ohno, T. Dependence of Photocatalytic Activity on Aspect Ratio of Shape-Controlled Rutile Titanium(IV) Oxide Nanorods. *J. Phys. Chem. C* **115**, 419–424 (2011).
61. Schwarze, M. *et al.* Quantification of photocatalytic hydrogen evolution. *Phys. Chem. Chem. Phys.* **15**, 3466 (2013).
62. Imoberdorf, G. E., Taghipour, F., Keshmiri, M. & Mohseni, M. Predictive radiation field modeling for fluidized bed photocatalytic reactors. *Chem. Eng. Sci.* **63**, 4228–4238 (2008).
63. Braham, R. J. & Harris, A. T. A complete multi-scale simulation of light absorption within a fluidized bed photoreactor using integrated particle, fluid and photon behaviour models. *Phys. Chem. Chem. Phys.* 12373–12385 (2013). doi:10.1039/c3cp50328c
64. Rachel, A., Subrahmanyam, M. & Boule, P. Comparison of photocatalytic efficiencies of TiO₂ in suspended and immobilised form for the photocatalytic degradation of nitrobenzenesulfonic acids. *Appl. Catal. B Environ.* **37**, 301–308 (2002).
65. Kanki, T., Hamasaki, S., Sano, N., Toyoda, A. & Hirano, K. Water purification in a fluidized bed photocatalytic reactor using TiO₂-coated ceramic particles. *Chem. Eng. J.* **108**, 155–160 (2005).
66. Pozzo, R. L., Brandi, R. J., Giombi, J. L., Cassano, A. E. & Baltanás, M. A. Fluidized bed photoreactors using composites of titania CVD-coated onto quartz sand as photocatalyst: Assessment of photochemical efficiency. *Chem. Eng. J.* **118**, 153–159 (2006).
67. Braham, R. J. & Harris, A. T. Review of major design and scale-up considerations for solar photocatalytic reactors. *Ind. Eng. Chem. Res.* **48**, 8890–8905 (2009).
68. Cassano, A. E. & Alfano, O. M. Reaction engineering of suspended solid heterogeneous photocatalytic reactors. *Catal. Today* **58**, 167–197 (2000).
69. Imoberdorf, G. E., Cassano, A. E., Alfano, O. M. & Irazoqui, H. A. Modeling of a multiannular photocatalytic reactor for perchloroethylene degradation in air. *AIChE J.* **52**, 1814–1823 (2006).
70. Liang, Z. *et al.* Study on the Radiation Distribution in A Fluidized Tubular Reactor for Heterogeneous Photocatalytic Hydrogen Production. *Procedia Environ. Sci.* **12**, 285–292 (2012).
71. Kabir, M. F., Haque, F., Vaisman, E., Langford, C. H. & Kantzas, A. Disinfecting E.coli Bacteria In Drinking Water Using A Novel Fluidized Bed Reactor. *Int. J. Chem. React. Eng.* **1**, (2003).
72. Bhargava, A., Kabir, M. F., Vaisman, E., Langford, C. H. & Kantzas, A. Novel Technique to Characterize the Hydrodynamics and Analyze the Performance of a Fluidized-Bed Photocatalytic Reactor for Wastewater Treatment. *Ind. Eng. Chem. Res.* **43**, 980–989 (2004).
73. Vaisman, E., Kabir, M. F., Kantzas, a. & Langford, C. H. A fluidized bed photoreactor exploiting a supported photocatalyst with adsorption pre-concentration capacity. *J. Appl. Electrochem.* **35**, 675–681 (2005).
74. Malato, S., Blanco, J., Vidal, A. & Richter, C. Photocatalysis with solar energy at a pilot-plant scale: An overview. *Appl. Catal. B Environ.* **37**, 1–15 (2002).
75. Jing, D., Jing, L., Liu, H., Yao, S. & Guo, L. Photocatalytic hydrogen production from refinery gas over a fluidized-bed reactor I: Numerical simulation. *Ind. Eng. Chem. Res.* **52**, 1982–1991 (2013).
76. Jing, D., Jing, L., Liu, H., Yao, S. & Guo, L. Photocatalytic hydrogen production from refinery gas

- over a fluidized-bed reactor II: Parametric Study. *Ind. Eng. Chem. Res.* **52**, 1982–1991 (2013).
77. Fujishima, A. & Honda, K. Electrochemical Evidence for the Mechanism of the Primary Stage of Photosynthesis. *Bulletin of the Chemical Society of Japan* **44**, 1148–1150 (1971).
 78. Fujishima, A. & Honda, K. Electrochemical photolysis of water at a semiconductor electrode. *Nature* **238**, 37–38 (1972).
 79. Hoffmann, M. R., Martin, S. T., Choi, W. & Bahnemann, D. W. Environmental Applications of Semiconductor Photocatalysis. *Chem. Rev.* **95**, 69–96 (1995).
 80. Tang, J., Durrant, J. R. & Klug, D. R. Mechanism of photocatalytic water splitting in TiO₂. Reaction of water with photoholes, importance of charge carrier dynamics, and evidence for four-hole chemistry. *J. Am. Chem. Soc.* **130**, 13885–91 (2008).
 81. McNaught, A. D. & Wilkinson, A. *IUPAC Compendium of Chemical Terminology (The 'Gold Book')*. Book (2014). doi:10.1351/goldbook
 82. Linsebigler, A. L., Lu, G. & Yates, J. T. Photocatalysis on TiO₂ Surfaces: Principles, Mechanisms, and Selected Results. *Chem. Rev.* **95**, 735–758 (1995).
 83. Fujishima, A., Rao, T. & Tryk, D. Titanium dioxide photocatalysis. *J. Photochem. Photobiol. C* **1**, 1–21 (2000).
 84. Hashimoto, K., Irie, H. & Fujishima, A. TiO₂ Photocatalysis: A Historical Overview and Future Prospects. *Jpn. J. Appl. Phys.* **44**, 8269–8285 (2005).
 85. Fujishima, A., Zhang, X. & Tryk, D. TiO₂ photocatalysis and related surface phenomena. *Surf. Sci. Rep.* **63**, 515–582 (2008).
 86. Banerjee, A. N. The design, fabrication, and photocatalytic utility of nanostructured semiconductors: focus on TiO₂-based nanostructures. *Nanotechnol. Sci. Appl.* **4**, 35–65 (2011).
 87. Hanaor, D. & Sorrell, C. Review of the anatase to rutile phase transformation. *Journal of Materials Science* **46**, 855–874 (2011).
 88. Kumar, S. G. & Rao, K. S. R. K. Polymorphic phase transition among the titania crystal structures using a solution-based approach: from precursor chemistry to nucleation process. *Nanoscale* **6**, 11574–11632 (2014).
 89. Di Paola, A., Bellardita, M. & Palmisano, L. Brookite, the Least Known TiO₂ Photocatalyst. *Catalysts* **3**, 36–73 (2013).
 90. Kavan, L., Grätzel, M., Gilbert, S. E., Klemenz, C. & Scheel, H. J. Electrochemical and photoelectrochemical investigation of single-crystal anatase. *J. Am. Chem. Soc.* **118**, 6716–6723 (1996).
 91. Scanlon, D. O. *et al.* Band alignment of rutile and anatase TiO₂. *Nat. Mater.* **12**, 798–801 (2013).
 92. Sasaki, T. *et al.* Preparation and Acid-Base Properties of a Protonated Titanate with the Lepidocrocite-like Layer Structure. *Chem. Mater.* **7**, 1001–1007 (1995).
 93. Zhao, B., Chen, F., Jiao, Y. & Zhang, J. Phase transition and morphological evolution of titania/titanate nanomaterials under alkaline hydrothermal treatment. *Journal of Materials Chemistry* **20**, 7990 (2010).
 94. Li, B., Wu, J.-M., Guo, T.-T., Tang, M.-Z. & Wen, W. A facile solution route to deposit TiO₂ nanowire arrays on arbitrary substrates. *Nanoscale* **6**, 3046–50 (2014).
 95. Morgado, E. *et al.* A study on the structure and thermal stability of titanate nanotubes as a function of sodium content. *Solid State Sci.* **8**, 888–900 (2006).

96. Armstrong, A. R., Armstrong, G., Canales, J. & Bruce, P. G. TiO₂-B nanowires. *Angew. Chemie - Int. Ed.* **43**, 2286–2288 (2004).
97. Feist, T. P. & Davies, P. K. The soft chemical synthesis of TiO₂(B) from layered titanates. *Journal of Solid State Chemistry* **101**, 275–295 (1992).
98. Zhao, B., Chen, F., Gu, X. & Zhang, J. Organic-stabilizer-free synthesis of layered protonic titanate nanosheets. *Chem. - An Asian J.* **5**, 1546–1549 (2010).
99. Zhao, B., Lin, L. & He, D. Phase and morphological transitions of titania/titanate nanostructures from an acid to an alkali hydrothermal environment. *J. Mater. Chem. A* **1**, 1659 (2013).
100. Hench, L. L. & West, J. K. The sol-gel process. *Chem. Rev.* **90**, 33–72 (1990).
101. Brinker, C. J. & Scherer, G. W. *Sol-gel science: the physics and chemistry of sol-gel processing*. Academic Press London **8**, (1990).
102. *Sol-Gel Optics*. (Springer US, 1994). doi:10.1007/978-1-4615-2750-3
103. Mackenzie, J. D. Applications of the sol-gel process. *J. Non. Cryst. Solids* **100**, 162–168 (1988).
104. Guglielmi, M. Sol-gel coatings on metals. *J. Sol-Gel Sci. Technol.* **8**, 443–449 (1997).
105. Lu, Y. *et al.* Continuous formation of supported cubic and hexagonal mesoporous films by sol-gel dip-coating. *Nature* **389**, 364–368 (1997).
106. Wen, J. & Wilkes, G. L. Organic/Inorganic Hybrid Network Materials by the Sol-Gel Approach. *Chem. Mater.* **8**, 1667–1681 (1996).
107. Livage, J., Henry, M. & Sanchez, C. Sol-gel chemistry of transition metal oxides. *Prog. Solid State Chem.* **18**, 259–341 (1988).
108. Kessler, V. G. in *The Sol-Gel Handbook* 195–224 (2015). doi:10.1002/9783527670819.ch06
109. Livage, J. & Sanchez, C. Sol-gel chemistry. *J. Non. Cryst. Solids* **145**, 11–19 (1992).
110. Su, C., Hong, B.-Y. & Tseng, C.-M. Sol-gel preparation and photocatalysis of titanium dioxide. *Catal. Today* **96**, 119–126 (2004).
111. Macwan, D. P., Dave, P. N. & Chaturvedi, S. A review on nano-TiO₂ sol-gel type syntheses and its applications. *J. Mater. Sci.* **46**, 3669–3686 (2011).
112. Keshmiri, M., Mohseni, M. & Troczynski, T. Development of novel TiO₂ sol-gel-derived composite and its photocatalytic activities for trichloroethylene oxidation. *Appl. Catal. B Environ.* **53**, 209–219 (2004).
113. Qiu, W. & Zheng, Y. A comprehensive assessment of supported titania photocatalysts in a fluidized bed photoreactor: Photocatalytic activity and adherence stability. *Appl. Catal. B Environ.* **71**, 151–162 (2007).
114. Kobayashi, M., Petrykin, V., Kakihana, M. & Tomita, K. Morphology Control of Rutile Nanoparticles in a Hydrothermal Synthesis from Water-Soluble Titanium Complex Aqueous Solution. *J. Ceram. Soc. Japan* **115**, 835–839 (2007).
115. Kakihana, M., Kobayashi, M., Tomita, K. & Petrykin, V. Application of water-soluble titanium complexes as precursors for synthesis of titanium-containing oxides via aqueous solution processes. *Bull. Chem. Soc. Jpn.* **83**, 1285–1308 (2010).
116. Kobayashi, M., Petrykin, V. & Kakihana, M. One-Step Synthesis of TiO₂ (B) Nanoparticles from a Water-Soluble Titanium Complex. *Chem. Mater.* **2**, 5373–5376 (2007).
117. Lu, J. *et al.* Synthesis and characterization of TiO₂ nanopowders from peroxotitanium solutions.

- Mater. Chem. Phys.* **115**, 142–146 (2009).
118. Kobayashi, M., Kato, H. & Kakihana, M. Synthesis of Titanium Dioxide Nanocrystals with Controlled Crystal- and Micro-structures from Titanium Complexes. *Nanomater. Nanotechnol.* **3**, 1–10 (2013).
 119. Nag, M., Ghosh, S., Rana, R. K. & Manorama, S. V. Controlling phase, crystallinity, and morphology of titania nanoparticles with peroxotitanium complex: Experimental and theoretical insights. *J. Phys. Chem. Lett.* **1**, 2881–2885 (2010).
 120. Kobayashi, M., Osada, M., Kato, H. & Kakihana, M. Design of crystal structures, morphologies and functionalities of titanium oxide using water-soluble complexes and molecular control agents. *Polym. J.* **47**, 78–83 (2014).
 121. Sutradhar, N., Sinhamahapatra, A., Pahari, S. K., Bajaj, H. C. & Panda, A. B. Room temperature synthesis of protonated layered titanate sheets using peroxy titanium carbonate complex solution. *Chem. Commun. (Camb)*. **47**, 7731–7733 (2011).
 122. Cheng, H. *et al.* A novel hydrolytic reaction to morphology-controlled TiO₂ micro/nanostructures for enhanced photocatalytic performances. *RSC Adv.* **5**, 43630–43638 (2015).
 123. Ikuma, Y. & Bessho, H. Effect of Pt concentration on the production of hydrogen by a TiO₂ photocatalyst. *Int. J. Hydrogen Energy* **32**, 2689–2692 (2007).
 124. Mills, A. & Lee, S. K. Platinum group metals and their oxides in semiconductor photosensitisation. *Platin. Met. Rev.* **47**, 2–12 (2003).
 125. Subramanian, V., Wolf, E. E. & Kamat, P. V. Catalysis with TiO₂/gold nanocomposites. Effect of metal particle size on the Fermi level equilibration. *J. Am. Chem. Soc.* **126**, 4943–50 (2004).
 126. Bamwenda, G. R., Tsubota, S., Nakamura, T. & Haruta, M. Photoassisted hydrogen production from a water-ethanol solution: a comparison of activities of Au-TiO₂ and Pt-TiO₂. *J. Photoch. Photobiol. A* **89**, 177–189 (1995).
 127. Bamwenda, G. R., Tsubota, S., Nakamura, T. & Haruta, M. The influence of the preparation methods on the catalytic activity of platinum and gold supported on TiO₂ for CO oxidation. *Catal. Letters* **44**, 83–87 (1997).
 128. Senevirathna, M. K. I., Pitigala, P. K. D. D. P. & Tennakone, K. High quantum efficiency Pt/TiO₂ catalyst for sacrificial water reduction. *Sol. Energy Mater. Sol. Cells* **90**, 2918–2923 (2006).
 129. Millon, C., Riassetto, D., Berthomé, G., Roussel, F. & Langlet, M. The photocatalytic activity of sol-gel derived photo-platinized TiO₂ films. *J. Photochem. Photobiol. A Chem.* **189**, 334–348 (2007).
 130. Riassetto, D. *et al.* Mechanisms involved in the platinization of sol-gel-derived TiO₂ thin films. *J. Photochem. Photobiol. A Chem.* **202**, 214–220 (2009).
 131. Kowalska, E., Rau, S. & Ohtani, B. Plasmonic Titania Photocatalysts Active under UV and Visible-Light Irradiation: Influence of Gold Amount, Size, and Shape. *J. Nanotechnol.* **2012**, 1–11 (2012).
 132. Sayama, K. & Arakawa, H. Effect of carbonate addition on the photocatalytic decomposition of liquid water over a ZrO₂ catalyst. *J. Photochem. Photobiol. A Chem.* **94**, 67–76 (1996).
 133. Sayama, K. & Arakawa, H. Effect of carbonate salt addition on the photocatalytic decomposition of liquid water over Pt-TiO₂ catalyst. *J. Chem. Soc. Faraday ...* **93**, 1647–1654 (1997).
 134. Arakawa, H. & Sayama, K. Solar hydrogen production. Significant effect of Na₂CO₃ addition on water splitting using simple oxide semiconductor photocatalysts. *Catal. Surv. from Japan* **4**, 75–80

- (2000).
135. Abe, R., Sayama, K. & Arakawa, H. Significant effect of iodide addition on water splitting into H₂ and O₂ over Pt-loaded TiO₂ photocatalyst: suppression of backward reaction. *Chem. Phys. Lett.* **371**, 360–364 (2003).
 136. Karakitsou, K. E. & Verykios, X. E. Influence of catalyst parameters and operational variables on the photocatalytic cleavage of water. *J. Catal.* **134**, 629–643 (1992).
 137. Muraki, H., Saji, T., Fujihira, M. & Aoyagui, S. Photocatalytic oxidation of water to hydrogen peroxide by irradiation of aqueous suspensions of TiO₂. *Journal of Electroanalytical Chemistry and Interfacial Electrochemistry* **169**, 319–323 (1984).
 138. Escudero, J. C., Cervera-March, S., Giménez, J. & Simarro, R. Preparation and characterization of Pt(RuO₂)/TiO₂ catalysts: Test in a continuous water photolysis system. *J. Catal.* **123**, 319–332 (1990).
 139. Abe, T., Suzuki, E., Nagoshi, K., Miyashita, K. & Kaneko, M. Electron source in photoinduced hydrogen production on Pt-supported TiO₂ particles. *J. Phys. Chem. B* **103**, 1119–1123 (1999).
 140. Salvador, P. Kinetic approach to the photocurrent transients in water photoelectrolysis at n-titanium dioxide electrodes. I. Analysis of the ratio of the instantaneous to steady-state photocurrent. *J. Phys. Chem.* **89**, 3863–3869 (1985).
 141. Harbour, J. R., Tromp, J. & Hair, M. L. Photogeneration of hydrogen peroxide in aqueous TiO₂ dispersions. *Canadian Journal of Chemistry* **63**, 204–208 (1985).
 142. Shiraishi, F. & Kawanishi, C. Effect of diffusional film on formation of hydrogen peroxide in photocatalytic reactions. *J. Phys. Chem. A* **108**, 10491–10496 (2004).
 143. Jackson, N. & Wang, C. Attachment of TiO₂ Powders to Hollow Glass Microbeads: Activity of the TiO₂-Coated Beads in the Photoassisted Oxidation of Ethanol to Acetaldehyde. *J. Electrochem. Soc.* **138**, 3660–3664 (1991).
 144. Pozzo, R. L., Brandi, R. J., Giombi, J. L., Baltanás, M. a. & Cassano, A. E. Design of fluidized bed photoreactors: Optical properties of photocatalytic composites of titania CVD-coated onto quartz sand. *Chem. Eng. Sci.* **60**, 2785–2794 (2005).
 145. Bideau, M., Claudel, B., Dubien, C., Faure, L. & Kazouan, H. On the ‘immobilization’ of titanium dioxide in the photocatalytic oxidation of spent waters. *J. Photochem. Photobiol. A Chem.* **91**, 137–144 (1995).
 146. Pozzo, R. L., Baltanás, M. A. & Cassano, A. E. Towards a precise assessment of the performance of supported photocatalysts for water detoxification processes. *Catal. Today* **54**, 143–157 (1999).
 147. Pozzo, R. L., Giombi, J. L., Baltanás, M. A. & Cassano, A. E. The performance in a fluidized bed reactor of photocatalysts immobilized onto inert supports. *Catal. Today* **62**, 175–187 (2000).
 148. Rodriguez, P., Meille, V., Pallier, S. & Ali Al Sawah, M. Deposition and characterisation of TiO₂ coatings on various supports for structured (photo)catalytic reactors. *Appl. Catal. A Gen.* **360**, 154–162 (2009).
 149. Fernandez, A., Lassaletta, G. & Jimenez, V. Preparation and characterization of TiO₂ photocatalysts supported on various rigid supports (glass, quartz and stainless steel). Comparative studies of photocatalytic activity in water purification. *Appl. Catal. B* **7**, 49–63 (1995).
 150. Ma, Y. *et al.* Photocatalytic activity of TiO₂ films grown on different substrates. *Chemosphere* **44**, 1087–92 (2001).
 151. Balasubramanian, G. *et al.* Titania powder modified sol-gel process for photocatalytic

- applications. *J. Mater. Sci.* **38**, 823–831 (2003).
152. Balasubramanian, G., Dionysiou, D. D., Suidan, M. T., Baudin, I. & Laine, J. M. Evaluating the activities of immobilized TiO₂ powder films for the photocatalytic degradation of organic contaminants in water. *Appl. Catal. B Environ.* **47**, 73–84 (2004).
 153. Chen, Y. & Dionysiou, D. D. Correlation of structural properties and film thickness to photocatalytic activity of thick TiO₂ films coated on stainless steel. *Appl. Catal. B Environ.* **69**, 24–33 (2006).
 154. Chen, Y. & Dionysiou, D. D. TiO₂ photocatalytic films on stainless steel: The role of Degussa P-25 in modified sol-gel methods. *Appl. Catal. B Environ.* **62**, 255–264 (2006).
 155. Chen, Y. & Dionysiou, D. D. Effect of calcination temperature on the photocatalytic activity and adhesion of TiO₂ films prepared by the P-25 powder-modified sol-gel method. *J. Mol. Catal. A Chem.* **244**, 73–82 (2006).
 156. Vega, A., Keshmiri, M. & Mohseni, M. Composite template-free TiO₂ photocatalyst: Synthesis, characteristics and photocatalytic activity. *Appl. Catal. B Environ.* **104**, 127–135 (2011).
 157. Haque, F., Vaisman, E., Langford, C. H. & Kantzas, A. Preparation and performance of integrated photocatalyst adsorbent (IPCA) employed to degrade model organic compounds in synthetic wastewater. *J. Photochem. Photobiol. A Chem.* **169**, 21–27 (2005).
 158. Kabir, M. F., Vaisman, E., Langford, C. H. & Kantzas, A. Effects of hydrogen peroxide in a fluidized bed photocatalytic reactor for wastewater purification. *Chem. Eng. J.* **118**, 207–212 (2006).
 159. Wang, X., Li, Z., Shi, J. & Yu, Y. One-Dimensional Titanium Dioxide Nanomaterials: Nanowires, Nanorods, and Nanobelts. *Chem. Rev.* **114**, 9346–9384 (2014).
 160. Kelzenberg, M. D. *et al.* Enhanced absorption and carrier collection in Si wire arrays for photovoltaic applications. *Nat. Mater.* **9**, 239–244 (2010).
 161. Foley, J. M., Price, M. J., Feldblyum, J. I. & Maldonado, S. Analysis of the operation of thin nanowire photoelectrodes for solar energy conversion. *Energy Environ. Sci.* **5**, 5203–5220 (2012).
 162. Liu, B. & Aydil, E. S. Growth of oriented single-crystalline rutile TiO₂ nanorods on transparent conducting substrates for dye-sensitized solar cells. *J. Am. Chem. Soc.* **131**, 3985–90 (2009).
 163. Feng, X., Zhu, K., Frank, A. J., Grimes, C. A. & Mallouk, T. E. Rapid Charge Transport in Dye-Sensitized Solar Cells Made from Vertically Aligned Single-Crystal Rutile TiO₂ Nanowires. *Angew. Chemie* **124**, 2781–2784 (2012).
 164. Cao, G. & Liu, D. Template-based synthesis of nanorod, nanowire, and nanotube arrays. *Adv. Colloid Interface Sci.* **136**, 45–64 (2008).
 165. Rajeshwar, K. Fundamentals of Semiconductors Electrochemistry and Photoelectrochemistry. *Encycl. Electrochem.* 1–51 (2007). doi:10.1002/9783527610426.bard060001
 166. Fitch, A., Strandwitz, N. C., Brunschwig, B. S. & Lewis, N. S. A comparison of the behavior of single crystalline and nanowire array ZnO photoanodes. *J. Phys. Chem. C* **117**, 2008–2015 (2013).
 167. Qin, D.-D. *et al.* Hydrothermal Growth and Photoelectrochemistry of Highly Oriented, Crystalline Anatase TiO₂ Nanorods on Transparent Conducting Electrodes. *Chem. Mater.* 150603072845009 (2015). doi:10.1021/acs.chemmater.5b00782
 168. Wilson, R. H. Observation and Analysis of Surface States on TiO₂ Electrodes in Aqueous Electrolytes. *Journal of The Electrochemical Society* **127**, 228 (1980).
 169. Rajeshwar, K. Charge Transfer in Photoelectrochemical Devices via Interface States: Unified

- Model and Comparison with Experimental Data. *J. Electrochem. Soc.* **129**, 1003–1008 (1982).
170. Salvador, P. & Decker, F. The generation of hydrogen peroxide during water photoelectrolysis at n-titanium dioxide. *J. Phys. Chem.* **88**, 6116–6120 (1984).
171. Peter, L. M., Li, J. & Peat, R. Surface recombination at semiconductor electrodes: Part I. Transient and steady-state photocurrents. *J. Electroanal. Chem. Interfacial Electrochem.* **165**, 29–40 (1984).
172. Li, J., Peat, R. & Peter, L. M. Surface recombination at semiconductor electrodes: Part II. Photoinduced ‘near-surface’ recombination centres in p-GaP. *J. Electroanal. Chem. Interfacial Electrochem.* **165**, 41–59 (1984).
173. Wolcott, A., Smith, W. A., Kuykendall, T. R., Zhao, Y. & Zhang, J. Z. Photoelectrochemical water splitting using dense and aligned TiO₂ nanorod arrays. *Small* **5**, 104–11 (2009).
174. Cho, I. S. *et al.* Branched TiO₂ nanorods for photoelectrochemical hydrogen production. *Nano Lett.* **11**, 4978–84 (2011).
175. Huang, C.-W., Liao, C.-H. & Wu, J. C. S. Photocatalytic Separate Evolution of Hydrogen and Oxygen over Highly Ordered Nanorods and Bulk TiO₂ Thin Films. *J. Clean Energy Technol.* **1**, 1–5 (2013).
176. Wang, Y., Zhang, L., Deng, K., Chen, X. & Zou, Z. Low Temperature Synthesis and Photocatalytic Activity of Rutile TiO₂ Nanorod Superstructures. *J. Phys. Chem. C* **111**, 2709–2714 (2007).
177. Zhang, G., Wu, J., Liu, S. & Yan, M. Fabrication of titania thin film with composite nanostructure and its ability to photodegrade rhodamine B in water. *Front. Chem. Eng. China* **2**, 44–48 (2008).
178. Jia, H., Zheng, Z., Zhao, H., Zhang, L. & Zou, Z. Nonaqueous sol–gel synthesis and growth mechanism of single crystalline TiO₂ nanorods with high photocatalytic activity. *Mater. Res. Bull.* **44**, 1312–1316 (2009).
179. Bao, N., Feng, X. & Grimes, C. A. Self-organized one-dimensional TiO₂ nanotube/nanowire array films for use in excitonic solar cells: A review. *Journal of Nanotechnology* **2012**, (2012).
180. Liu, B., Boercker, J. E. & Aydil, E. S. Oriented single crystalline titanium dioxide nanowires. *Nanotechnology* **19**, 505604 (2008).
181. Li, Y., Guo, M., Zhang, M. & Wang, X. Hydrothermal synthesis and characterization of TiO₂ nanorod arrays on glass substrates. *Mater. Res. Bull.* **44**, 1232–1237 (2009).
182. Li, Y., Zhang, M., Guo, M. & Wang, X. Hydrothermal growth of well-aligned TiO₂ nanorod arrays: Dependence of morphology upon hydrothermal reaction conditions. *Rare Met.* **29**, 286–291 (2010).
183. Wei, Z., Yao, Y., Huang, T. & Yu, A. Solvothermal growth of well-aligned TiO₂ nanowire arrays for dye-sensitized solar cell: Dependence of morphology and vertical orientation upon substrate pretreatment. *Int. J. Electrochem. Sci.* **6**, 1871–1879 (2011).
184. Wu, W.-Q. *et al.* Hydrothermal fabrication of hierarchically anatase TiO₂ nanowire arrays on FTO glass for dye-sensitized solar cells. *Sci. Rep.* **3**, 1352 (2013).
185. Wu, W.-Q. *et al.* Hierarchical oriented anatase TiO₂ nanostructure arrays on flexible substrate for efficient dye-sensitized solar cells. *Sci. Rep.* **3**, 1892 (2013).
186. Wu, W.-Q., Xu, Y.-F., Su, C.-Y. & Kuang, D.-B. Ultra-long anatase TiO₂ nanowire arrays with multi-layered configuration on FTO glass for high-efficiency dye-sensitized solar cells. *Energy Environ. Sci.* **7**, 644–649 (2014).
187. Wu, W.-Q. *et al.* A family of vertically aligned nanowires with smooth, hierarchical and

- hyperbranched architectures for efficient energy conversion. *Nano Energy* **9**, 15–24 (2014).
188. Chu, L. *et al.* A general method for preparing anatase TiO₂ treelike-nanoarrays on various metal wires for fiber dye-sensitized solar cells. *Sci. Rep.* **4**, 4420 (2014).
 189. Kasuga, T., Hiramatsu, M., Hoson, A., Sekino, T. & Niihara, K. Titania Nanotubes Prepared by Chemical Processing. *Adv. Mater.* **11**, 1307–1311 (1999).
 190. Kumar, A., Madaria, A. R. & Zhou, C. Growth of Aligned Single-Crystalline Rutile TiO₂ Nanowires on Arbitrary Substrates and Their Application in Dye-Sensitized Solar Cells. *J. Phys. Chem. C* **114**, 7787–7792 (2010).
 191. Wu, W.-Q., Feng, H.-L., Rao, H.-S., Kuang, D.-B. & Su, C.-Y. Rational surface engineering of anatase titania core-shell nanowire arrays: full-solution processed synthesis and remarkable photovoltaic performance. *ACS Appl. Mater. Interfaces* **6**, 19100–8 (2014).
 192. Karakitsou, K. E. & Verykios, X. E. Definition of the Intrinsic Rate of Photocatalytic Cleavage of Water Over Pt-RuO₂/TiO₂ Catalysts. *J. Catal.* **152**, 360–367 (1995).
 193. Ramsden, C. S., Smith, T. J., Shaw, B. J. & Handy, R. D. Dietary exposure to titanium dioxide nanoparticles in rainbow trout, (*Oncorhynchus mykiss*): No effect on growth, but subtle biochemical disturbances in the brain. *Ecotoxicology* **18**, 939–951 (2009).
 194. Kwon, J. M. *et al.* Novel immobilization of titanium dioxide (TiO₂) on the fluidizing carrier and its application to the degradation of azo-dye. *J. Hazard. Mater.* **134**, 230–6 (2006).
 195. Lee, D.-K., Kim, S.-C., Cho, I.-C., Kim, S.-J. & Kim, S.-W. Photocatalytic oxidation of microcystin-LR in a fluidized bed reactor having TiO₂-coated activated carbon. *Sep. Purif. Technol.* **34**, 59–66 (2004).
 196. Lim, T. & Kim, S. Photocatalytic degradation of trichloroethylene over TiO₂/SiO₂ in an annulus fluidized bed reactor. *Korean J. Chem. Eng.* **19**, 1072–1077 (2002).
 197. Nelson, R. J., Flakker, C. L. & Muggli, D. S. Photocatalytic oxidation of methanol using titania-based fluidized beds. *Appl. Catal. B Environ.* **69**, 189–195 (2007).
 198. Lee, S., Park, J. & Joo, H. Visible light-sensitized photocatalyst immobilized on beads by CVD in a fluidizing bed. *Sol. Energy Mater. Sol. Cells* **90**, 1905–1914 (2006).
 199. Rahn, R. O. Potassium Iodide as a Chemical Actinometer for 254 nm Radiation: Use of Iodate as an Electron Scavenger. *Photochem. Photobiol.* **66**, 450–455 (1997).
 200. Rahn, R. O. *et al.* Quantum Yield of the Iodide–Iodate Chemical Actinometer: Dependence on Wavelength and Concentration. *Photochem. Photobiol.* **78**, 146–152 (2003).
 201. Rahn, R. O., Bolton, J. & Stefan, M. I. The iodide/iodate actinometer in UV disinfection: determination of the fluence rate distribution in UV reactors. *Photochem. Photobiol.* **82**, 611–5 (2006).
 202. Spurr, R. a. & Myers, H. Quantitative Analysis of Anatase-Rutile Mixtures with an X-Ray Diffractometer. *Anal. Chem.* **29**, 760–762 (1957).
 203. Suttiponparnit, K. *et al.* Role of Surface Area, Primary Particle Size, and Crystal Phase on Titanium Dioxide Nanoparticle Dispersion Properties. *Nanoscale Res. Lett.* **6**, 27 (2010).
 204. Ohtani, B. Preparing Articles on Photocatalysis—Beyond the Illusions, Misconceptions, and Speculation. *Chem. Lett.* **37**, 216–229 (2008).
 205. Cullity, B. & Stock, S. Elements of X-ray diffraction, 3rd edition. *Prentice Hall* Chapter 1 (2001).
 206. Geldart, D. Types of gas fluidization. *Powder Technology* **7**, 285–292 (1973).

207. Disdier, J., Herrmann, J.-M. & Pichat, P. Platinum/titanium dioxide catalysts. A photoconductivity study of electron transfer from the ultraviolet-illuminated support to the metal and of the influence of hydrogen. *Journal of the Chemical Society, Faraday Transactions 1* **79**, 651 (1983).
208. Herrmann, J. M., Disdier, J. & Pichat, P. Photoassisted platinum deposition on TiO₂ powder using various platinum complexes. *J. Phys. Chem.* **90**, 6028–6034 (1986).
209. Amaldi, E. & Fermi, E. On the absorption and the diffusion of slow neutrons. *Phys. Rev.* **50**, 899–928 (1936).
210. Gonzalez-Vazquez, J. P., Anta, J. A. & Bisquert, J. Determination of the electron diffusion length in dye-sensitized solar cells by random walk simulation: Compensation effects and voltage dependence. *J. Phys. Chem. C* **114**, 8552–8558 (2010).
211. Leng, W. H., Barnes, P. R. F., Juozapavicius, M., O'Regan, B. C. & Durrant, J. R. Electron Diffusion Length in Mesoporous Nanocrystalline TiO₂ Photoelectrodes during Water Oxidation. *J. Phys. Chem. Lett.* **1**, 967–972 (2010).
212. D'Elia, D. *et al.* Impact of three different TiO₂ morphologies on hydrogen evolution by methanol assisted water splitting: Nanoparticles, nanotubes and aerogels. *Int. J. Hydrogen Energy* **36**, 14360–14373 (2011).
213. Maeda, K. Photocatalytic properties of rutile TiO₂ powder for overall water splitting. *Catal. Sci. Technol.* **4**, 1949 (2014).
214. Salvador, P. & Gutierrez, C. On the Nature of Surface States Involved in the Photo- and Electroluminescence Spectra of n-TiO₂ Electrodes. *J. Phys. Chem.* **88**, 3696–3698 (1984).
215. Ferrer, I. J., Muraki, H. & Salvador, P. Detection of surface states associated with adsorbed hydrogen peroxide on titanium dioxide by impedance and electrolyte electroreflectance measurements. *J. Phys.* **90**, 2805–2807 (1986).
216. Tafalla, D. & Salvador, P. Kinetic Approach to the Photocurrent Transients in Water Photoelectrolysis at n-TiO₂ Electrodes. II. Analysis of the Photocurrent-Time Dependence. *Journal of The Electrochemical Society* **137**, 1810 (1990).
217. Shiraishi, F., Nakasako, T. & Hua, Z. Formation of Hydrogen Peroxide in Photocatalytic Reactions. *J. Phys. Chem.* **107**, 11072–11081 (2003).
218. Haider, A. & Levenspiel, O. Drag coefficient and terminal velocity of spherical and nonspherical particles. *Powder Technology* **58**, 63–70 (1989).
219. Khan, A. R. & Richardson, J. F. The Resistance to Motion of a Solid Sphere in a Fluid. *Chemical Engineering Communications* **62**, 135–150 (1987).
220. Richardson, J. F. & Zaki, W. N. The sedimentation of a suspension of uniform spheres under conditions of viscous flow. *Chemical Engineering Science* **3**, 65–73 (1954).
221. Tournié, P., Laguerie, C. & Couderc, J. P. Correlations for mass transfer between fluidized spheres and a liquid. *Chem. Eng. Sci.* **34**, 1247–1255 (1979).
222. Arters, D. C. & Fan, L.-S. Solid-liquid mass transfer in a gas-liquid-solid fluidized bed. *Chem. Eng. Sci.* **41**, 107–115 (1986).
223. Ballesteros, R. L., Riba, J. P. & Couderc, J. P. Dissolution of non-spherical particles in solid-liquid fluidization. *Chem. Eng. Sci.* **37**, 1639–1644 (1982).
224. Verhallen, P. T. H. M., Oomen, L. J. P., Elsen, A. J. J. M. v. d., Kruger, J. & Fortuin, J. M. H. The diffusion coefficients of helium, hydrogen, oxygen and nitrogen in water determined from the permeability of a stagnant liquid layer in the quasi-steady state. *Chem. Eng. Sci.* **39**, 1535–1541

- (1984).
225. Richardson, J. F., Harker, J. H. & Backhurst, J. R. *Coulson and Richardson's Chemical Engineering Volume 2 - Particle Technology and Separation Processes (5th Edition)*. (Elsevier, 2002). at <<http://app.knovel.com/hotlink/toc/id:kpCRCEVPT2/coulson-richardsons-chemical-3/coulson-richardsons-chemical-3>>
 226. Linek, V., Mayrhoferová, J. & Mošnerová, J. The influence of diffusivity on liquid phase mass transfer in solutions of electrolytes. *Chem. Eng. Sci.* **25**, 1033–1045 (1970).
 227. Carberry, J. J. *Chemical and Catalytic Reaction Engineering*. (Dover Publications, 2001).
 228. Akehata, T. & Shirai, T. Effect of light-source characteristics performance of circular annular photochemical reactor. *J. Chem. Eng. Japan* 59–65 (1972). doi:10.1252/jcej.5.385
 229. Hang Li, Y. *et al.* Unidirectional suppression of hydrogen oxidation on oxidized platinum clusters. *Nat. Commun.* **4**, (2013).
 230. Michaelides, a. & Hu, P. Catalytic water formation on platinum: A first-principles study. *J. Am. Chem. Soc.* **123**, 4235–4242 (2001).
 231. Gileadi, E., Argade, S. D. & Bockris, J. O. The Potential of Zero Charge of Platinum and Its pH Dependence. *J. Phys. Chem* **586**, 2044 (1992).
 232. Kucernak, A. R. & Offer, G. J. The role of adsorbed hydroxyl species in the electrocatalytic carbon monoxide oxidation reaction on platinum. *Phys. Chem. Chem. Phys.* **10**, 3699–3711 (2008).
 233. Strmcnik, D. *et al.* Improving the hydrogen oxidation reaction rate by promotion of hydroxyl adsorption. *Nat. Chem.* **5**, 300–306 (2013).
 234. Sheng, W., Gasteiger, H. a. & Shao-Horn, Y. Hydrogen Oxidation and Evolution Reaction Kinetics on Platinum: Acid vs Alkaline Electrolytes. *J. Electrochem. Soc.* **157**, B1529 (2010).
 235. Vega, J. A., Smith, S. & Mustain, W. E. Hydrogen and Methanol Oxidation Reaction in Hydroxide and Carbonate Alkaline Media. *J. Electrochem. Soc.* **158**, B349–B354 (2011).
 236. Vega, A. A. Development and evaluation of a composite photocatalyst for water treatment processes. (University of British Columbia, 2009). doi:10.14288/1.0058900
 237. Shankar, K. *et al.* Recent Advances in the Use of TiO₂ Nanotube and Nanowire Arrays for Oxidative Photoelectrochemistry. *J. Phys. Chem. C* **113**, 6327–6359 (2009).
 238. Feng, X. *et al.* Vertically aligned single crystal TiO₂ nanowire arrays grown directly on transparent conducting oxide coated glass: synthesis details and applications. *Nano Lett.* **8**, 3781–6 (2008).
 239. Shalan, A. E., Rashad, M. M., Yu, Y., Lira-Cantú, M. & Abdel-Mottaleb, M. S. A. A facile low temperature synthesis of TiO₂ nanorods for high efficiency dye sensitized solar cells. *Applied Physics A* 111–122 (2012). doi:10.1007/s00339-012-7368-6
 240. Radecka, M., Rekas, M., Trenczek-Zajac, A. & Zakrzewska, K. Importance of the band gap energy and flat band potential for application of modified TiO₂ photoanodes in water photolysis. *J. Power Sources* **181**, 46–55 (2008).
 241. Mikami, M., Nakamura, S., Kitao, O., Arakawa, H. & Gonze, X. First-Principles Study of Titanium Dioxide: Rutile and Anatase. *Jpn. J. Appl. Phys.* **39**, L847–L850 (2000).
 242. Li, J., Yu, Y., Chen, Q., Li, J. & Xu, D. Controllable Synthesis of TiO₂ Single Crystals with Tunable Shapes Using Ammonium-Exchanged Titanate Nanowires as Precursors. *Cryst. Growth Des.* **10**, 2111–2115 (2010).

243. Kolen'ko, Y. V. *et al.* Hydrothermal Synthesis and Characterization of Nanorods of Various Titanates and Titanium Dioxide. *J. Phys. Chem. B* **110**, 4030–4038 (2006).
244. Xie, J., Wang, X. & Zhou, Y. Understanding Formation Mechanism of Titanate Nanowires through Hydrothermal Treatment of Various Ti-Containing Precursors in Basic Solutions. *J. Mater. Sci. Technol.* **28**, 488–494 (2012).
245. Lin, C., Wong, D. S. & Lu, S. Layered Protonated Titanate Nanosheets Synthesized with a Simple One-Step, Low-Temperature, Urea-Modulated Method as an Effective Pollutant Adsorbent. (2014).
246. Peri, D., Alexander, J. S., Tshuva, E. Y. & Melman, A. Distinctive structural features of hydroxyamino-1,3,5-triazine ligands leading to enhanced hydrolytic stability of their titanium complexes. *Dalton Trans.* 4169–4172 (2006). doi:10.1039/b606072b
247. Truong, Q. D., Le, T. H., Liu, J.-Y., Chung, C.-C. & Ling, Y.-C. Synthesis of TiO₂ nanoparticles using novel titanium oxalate complex towards visible light-driven photocatalytic reduction of CO₂ to CH₃OH. *Applied Catalysis A: General* **437-438**, 28–35 (2012).
248. Kandiel, T. A., Feldhoff, A., Robben, L., Dillert, R. & Bahnemann, D. W. Tailored Titanium Dioxide Nanomaterials: Anatase Nanoparticles and Brookite Nanorods as Highly Active Photocatalysts. *Chem. Mater.* **22**, 2050–2060 (2010).
249. Wu, J.-M. & Xue, H. X. Photocatalytic active titania nanowire arrays on Ti substrates. *J. Am. Ceram. Soc.* **92**, 2139–2143 (2009).
250. Lai, L.-L. & Wu, J.-M. A facile synthesis of hierarchical TiO₂ for dye adsorption and photocatalysis. *RSC Adv.* **4**, 36212 (2014).
251. Lai, L.-L., Huang, L.-L. & Wu, J.-M. K₂TiO(C₂O₄)₂-mediated synthesis of rutile TiO₂ mesocrystals and their ability to assist photodegradation of sulfosalicylic acid in water. *RSC Adv.* **4**, 49280–49286 (2014).
252. Wu, J.-M. & Yin, J.-X. A facile solution-based approach to a photocatalytic active branched one-dimensional TiO₂ array. *RSC Adv.* **5**, 3465–3469 (2015).
253. Sun, J., Wen, W. & Wu, J.-M. Low-temperature transformation of titania thin films from amorphous nanowires to crystallized nanoflowers for heterogeneous photocatalysis. *J. Am. Ceram. Soc.* **96**, 2109–2116 (2013).
254. Hecht, H. G. The Interpretation of Diffuse Reflectance Spectra. *J. Res. NBS A Phys. Ch.* **80**, 567–583 (1976).
255. Tauc, J. in *Optical Properties of Solids* **198**, 123–136 (Springer US, 1969).
256. Biesinger, M. C. *et al.* Resolving surface chemical states in XPS analysis of first row transition metals, oxides and hydroxides: Cr, Mn, Fe, Co and Ni. *Appl. Surf. Sci.* **257**, 2717–2730 (2011).
257. Sarma, B. K., Pal, A. R., Bailung, H. & Chutia, J. A hybrid heterojunction with reverse rectifying characteristics fabricated by magnetron sputtered TiO_x and plasma polymerized aniline structure. *Journal of Physics D: Applied Physics* **45**, 275401 (2012).
258. Rong, M. *et al.* A Label-Free Fluorescence Sensing Approach for Selective and Sensitive Detection of 2,4,6-Trinitrophenol (TNP) in Aqueous Solution Using Graphitic Carbon Nitride Nanosheets. *Anal. Chem.* **87**, 1288–1296 (2015).
259. Tong, X., Yang, P., Wang, Y., Qin, Y. & Guo, X. Enhanced photoelectrochemical water splitting performance of TiO₂ nanotube arrays coated with an ultrathin nitrogen-doped carbon film by molecular layer deposition. *Nanoscale* **6**, 6692 (2014).

260. Jun, J., Shin, J. H. & Dhayal, M. Surface state of TiO₂ treated with low ion energy plasma. *Appl. Surf. Sci.* **252**, 3871–3877 (2006).
261. Kuznetsov, M. V., Zhuravlev, Ju. F. & Gubanov, V. A. XPS analysis of adsorption of oxygen molecules on the surface of Ti and TiN_x films in vacuum. *J. Electron Spectros. Relat. Phenomena* **58**, 169–176 (1992).
262. Dong, F., Zhao, W. & Wu, Z. Characterization and photocatalytic activities of C, N and S co-doped TiO₂ with 1D nanostructure prepared by the nano-confinement effect. *Nanotechnology* **19**, 365607 (2008).
263. Yang, L. L. *et al.* Effective suppression of surface recombination in ZnO nanorods arrays during the growth process. *Cryst. Growth Des.* **10**, 1904–1910 (2010).
264. Anil Kumar Reddy, P. *et al.* Photocatalytic Degradation of Isoproturon Pesticide on C, N and S Doped TiO₂. *J. Water Resour. Prot.* **02**, 235–244 (2010).
265. Fettkenhauer, C., Weber, J., Antonietti, M. & Dontsova, D. Novel carbon nitride composites with improved visible light absorption synthesized in ZnCl₂-based salt melts. *RSC Adv.* **4**, 40803–40811 (2014).
266. Silversmit, G. *et al.* A comparative XPS and UPS study of VO_x layers on mineral TiO₂ (001)-anatase supports. *Surf. Interface Anal.* **38**, 1257–1265 (2006).
267. Roy, S. S., McCann, R., Papakonstantinou, P., Maguire, P. & McLaughlin, J. A. The structure of amorphous carbon nitride films using a combined study of NEXAFS, XPS and Raman spectroscopies. *Thin Solid Films* **482**, 145–150 (2005).
268. Ameen, S., Akhtar, M. S., Kim, Y. S. & Shin, H. S. Controlled synthesis and photoelectrochemical properties of highly ordered TiO₂ nanorods. *RSC Advances* **2**, 4807 (2012).
269. Dementjev, A.P. *et al.* X-Ray photoelectron spectroscopy reference data for identification of the C₃N₄ phase in carbon–nitrogen films. *Diam. Relat. Mater.* **9**, 1904–1907 (2000).
270. Zhang, W., Huang, H., Li, F., Deng, K. & Wang, X. Palladium nanoparticles supported on graphitic carbon nitride-modified reduced graphene oxide as highly efficient catalysts for formic acid and methanol electrooxidation. *J. Mater. Chem. A* **2**, 19084–19094 (2014).
271. Ma, W. *et al.* Ultrathin g-C₃N₄/TiO₂ composites as photoelectrochemical elements for the real-time evaluation of global antioxidant capacity. *Chem. Sci.* **5**, 3946 (2014).
272. Choukourov, A. *et al.* Properties of amine-containing coatings prepared by plasma polymerization. *J. Appl. Polym. Sci.* **92**, 979–990 (2004).
273. Kisch, H. Semiconductor Photocatalysis-Mechanistic and Synthetic Aspects. *Angew. Chemie Int. Ed.* **52**, 812–847 (2013).
274. Komatsu, T. & Nakamura, T. Polycondensation/pyrolysis of tris-s-triazine derivatives leading to graphite-like carbon nitrides. *J. Mater. Chem.* **11**, 474–478 (2001).
275. Mitoraj, D. & Kisch, H. On the Mechanism of Urea-Induced Titania Modification. *Chem. - A Eur. J.* **16**, 261–269 (2010).
276. Qiao, Y. *et al.* Conformal N-doped carbon on nanoporous TiO₂ spheres as a high-performance anode material for lithium-ion batteries. *J. Mater. Chem. A* **1**, 10375 (2013).
277. Jiang, Z. *et al.* Solvothermal synthesis of N-doped TiO₂ nanotubes for visible-light-responsive photocatalysis. *Chem. Commun.* **1**, 6372 (2008).
278. Sasirekha, N., Rajesh, B. & Chen, Y. W. Synthesis of TiO₂ sol in a neutral solution using TiCl₄ as a precursor and H₂O₂ as an oxidizing agent. *Thin Solid Films* **518**, 43–48 (2009).

279. Wang, J., Huang, B., Wang, Z., Qin, X. & Zhang, X. Synthesis and characterization of C,N-codoped TiO₂ nanotubes/nanorods with visible-light activity. *Rare Met.* **30**, 161–165 (2011).
280. Bernhard, A. M., Peitz, D., Elsener, M., Wokaun, A. & Kröcher, O. Hydrolysis and thermolysis of urea and its decomposition byproducts biuret, cyanuric acid and melamine over anatase TiO₂. *Appl. Catal. B Environ.* **115-116**, 129–137 (2012).
281. Costa, L. & Camino, G. Thermal behaviour of melamine. *J. Therm. Anal.* **34**, 423–429 (1988).
282. Lin, Y.-C., Chien, T.-E., Li, K.-L. & Lin, J.-L. Comparison of the Thermal and Photochemical Reaction Pathways of Melamine on TiO₂. *J. Phys. Chem. C* **119**, 8645–8651 (2015).
283. Schwarzer, A., Saplinova, T. & Kroke, E. Tri-s-triazines (s-heptazines)—From a ‘mystery molecule’ to industrially relevant carbon nitride materials. *Coord. Chem. Rev.* **257**, 2032–2062 (2013).
284. Zhang, J. *et al.* Synthesis of a Carbon Nitride Structure for Visible-Light Catalysis by Copolymerization. *Angew. Chemie Int. Ed.* **49**, 441–444 (2010).
285. Xu, Y. & Gao, S. P. Band gap of C₃N₄ in the GW approximation. *Int. J. Hydrogen Energy* **37**, 11072–11080 (2012).
286. Qian, J. *et al.* Hydrothermal Synthesis of Nitrogen-Doped Titanium Dioxide and Evaluation of Its Visible Light Photocatalytic Activity. *Int. J. Photoenergy* **2012**, 1–6 (2012).
287. Rutar, M. *et al.* Transformation of hydrogen titanate nanoribbons to TiO₂ nanoribbons and the influence of the transformation strategies on the photocatalytic performance. *Beilstein J. Nanotechnol.* **6**, 831–844 (2015).
288. Guo, Q. *et al.* Synthesis of carbon nitride nanotubes with the C₃N₄ stoichiometry via a benzene-thermal process at low temperatures. *Chem. Commun. (Camb).* **1**, 26–27 (2004).
289. Gong, D. *et al.* Poly Tri-s-triazines as Visible Light Sensitizers in Titania-Based Composite Photocatalysts: Promotion of Melon Development from Urea over Acid Titanates. *ACS Sustain. Chem. Eng.* **2**, 149–157 (2014).
290. Lai, L.-L. & Wu, J.-M. A facile synthesis of hierarchical TiO₂ for dye adsorption and photocatalysis. *RSC Adv.* **4**, 36212 (2014).
291. Thomas, Y., Taravel, B., Fromage, F. & Delorme, P. Etude des produits de decomposition thermique de l’ion guanidinium par spectrometrie infrarouge. *Mater. Chem.* **5**, 117–123 (1980).
292. Komatsu, T. The first synthesis and characterization of cyameluric high polymers. *Macromol. Chem. Phys.* **202**, 19–25 (2001).
293. Sathish, M., Viswanathan, B. & Viswanath, R. P. Characterization and photocatalytic activity of N-doped TiO₂ prepared by thermal decomposition of Ti-melamine complex. *Appl. Catal. B Environ.* **74**, 307–312 (2007).
294. Beranek, R. & Kisch, H. Tuning the optical and photoelectrochemical properties of surface-modified TiO₂. *Photochem. Photobiol. Sci.* **7**, 40–48 (2008).
295. Zhao, B., Chen, F., Huang, Q. & Zhang, J. Brookite TiO₂ nanoflowers. *Chem. Commun. (Camb).* 5115–5117 (2009). doi:10.1039/b909883f
296. Jiao, Y., Zhao, B., Chen, F. & Zhang, J. Insight into the crystal lattice formation of brookite in aqueous ammonia media: the electrolyte effect. *CrystEngComm* **13**, 4167 (2011).
297. Guillard, C., Puzenat, E., Lachheb, H., Houas, A. & Herrmann, J.-M. Why inorganic salts decrease the TiO₂ photocatalytic efficiency. *Int. J. Photoenergy* **7**, 1–9 (2005).

298. Jung, H. S., Lee, J., Lee, S., Hong, K. S. & Shin, H. Acid Adsorption on TiO₂ Nanoparticles - An Electrochemical Properties Study. *J Phys Chem C* **112**, 8476–8480 (2008).
299. Adamu, H. & Anderson, J. A. Insights into Competitive Adsorption Between Nitrate and Oxalic Acid Over TiO₂ and Consequences for Photocatalytic Remediation. (2015).
300. Hu, W., Li, L., Li, G., Liu, Y. & Withers, R. L. Atomic-scale control of TiO₆ octahedra through solution chemistry towards giant dielectric response. *Sci. Rep.* **4**, 6582 (2014).
301. Miao, Y. & Gao, J. Synthesis of {010}-faceted cuboid-like anatase TiO₂ nanorods by the hydrothermal method. *Micro Nano Lett.* **6**, 848 (2011).
302. Miao, Y. & Gao, J. Preparation of {010}-faceted anatase TiO₂ nanocuboids from peroxotitanium complex solution. *J. Solid State Chem.* **196**, 372–378 (2012).
303. Vayssieres, L. Growth of arrayed nanorods and nanowires of ZnO from aqueous solutions. *Adv. Mater.* **15**, 464–466 (2003).
304. Yin, S. & Sato, T. Mild solution synthesis of zinc oxide films with superhydrophobicity and superhydrophilicity. *J. Mater. Chem.* **15**, 4584 (2005).
305. Wu, J.-M., Huang, B., Wang, M. & Osaka, A. Titania Nanoflowers with High Photocatalytic Activity. *J. Am. Ceram. Soc.* **89**, 2660–2663 (2006).
306. Wu, J.-M. & Qi, B. Low-temperature growth of a nitrogen-doped titania nanoflower film and its ability to assist photodegradation of rhodamine B in water. *J. Phys. Chem. C* **111**, 666–673 (2007).
307. Wu, J.-M. & Huang, B. Enhanced ability of nanostructured titania film to assist photodegradation of rhodamine B in water through natural aging. *J. Am. Ceram. Soc.* **90**, 283–286 (2007).
308. Gateshki, M., Yin, S., Ren, Y. & Petkov, V. Titania polymorphs by soft chemistry: Is there a common structural pattern? *Chem. Mater.* **19**, 2512–2518 (2007).
309. Tao, R. H. *et al.* A novel approach to titania nanowire arrays as photoanodes of back-illuminated dye-sensitized solar cells. *J. Power Sources* **195**, 2989–2995 (2010).
310. Ballesteros, R., Fajardo, M., Sierra, I. & del Hierro, I. Synthesis of titanium-triazine based MCM-41 hybrid materials as catalyst for the asymmetric epoxidation of cinammyl alcohol. *J. Mol. Catal. A Chem.* **310**, 83–92 (2009).
311. Yamabi, S. & Imai, H. Synthesis of rutile and anatase films with high surface areas in aqueous solutions containing urea. *Thin Solid Films* **434**, 86–93 (2003).
312. Yamabi, S. & Imai, H. Crystal Phase Control for Titanium Dioxide Films by Direct Deposition in Aqueous Solutions. *Chem. Mater.* **14**, 609–614 (2005).
313. Hermon, T. & Tshuva, E. Y. Synthesis and conformational analysis of constrained ethylene-bridged bis(hydroxylamino-1,3,5-triazine) compounds as tetradentate ligands; structure of rigid dinuclear Ti(IV) complex. *J. Org. Chem.* **73**, 5953–8 (2008).
314. Yin, Y., Tan, X., Hou, F. & Zhao, L. Efficient synthesis of titania nanotubes and enhanced photoresponse of Pt decorated TiO₂ for water splitting. *Front. Chem. Eng. China* **3**, 298–304 (2009).
315. Rahman, M. Y. a, Umar, A. A., Roza, L. & Salleh, M. M. Effect of TiO₂ nanostructure morphology on the performance of a photoelectrochemical cell of ITO/TiO₂/electrolyte/platinum. *J. Solid State Electrochem.* **16**, 3947–3952 (2012).
316. Yura, K., Fredrikson, K. C. & Matijević, E. Preparation and properties of uniform colloidal indium compounds of different morphologies. *Colloids and Surfaces* **50**, 281–293 (1990).

317. Bozzi, A. *et al.* Evolution of toxicity during melamine photocatalysis with TiO₂ suspensions. *J. Photochem. Photobiol. A Chem.* **162**, 179–185 (2004).
318. Tao, R. H. *et al.* Conformal growth of ZnO on TiO₂ nanowire array for enhanced photocatalytic activity. *Appl. Surf. Sci.* **279**, 324–328 (2013).
319. Wu, J.-M. Low-temperature preparation of titania nanorods through direct oxidation of titanium with hydrogen peroxide. *J. Cryst. Growth* **269**, 347–355 (2004).
320. Wu, J.-M. *et al.* Large-scale preparation of ordered titania nanorods with enhanced photocatalytic activity. *Langmuir* **21**, 6995–7002 (2005).
321. Mailen, J. C., Tallent, O. K. & Arwood, P. C. *Destruction of Oxalate by Reaction with Hydrogen Peroxide [Hydrazine oxalate]. No. ORNL/TM-7474.* (1981). at <<http://www.osti.gov/scitech/biblio/6229619>>
322. Kim, E.-H., Chung, D.-Y., Park, J.-H. & Yoo, J.-H. Dissolution of Oxalate Precipitate and Destruction of Oxalate Ion by Hydrogen Peroxide in Nitric Acid Solution. *J. Nucl. Sci. Technol.* **37**, 601–607 (2000).
323. in *Chemistry of Heterocyclic Compounds: s-Triazines and Derivatives* (eds. Smolin, E. M. & Rapoport, L.) **13**, 545–596 (John Wiley & Sons, Inc., 1959).
324. Cheng, P., Qiu, J., Gu, M., Jin, Y. & Shangguan, W. Synthesis of shape-controlled titania particles from a precursor solution containing urea. *Mater. Lett.* **58**, 3751–3755 (2004).
325. Kitagawa, S. & Kondo, M. Functional Micropore Chemistry of Crystalline Metal Complex-Assembled Compounds. *Bulletin of the Chemical Society of Japan* **71**, 1739–1753 (1998).
326. Germain, M. *et al.* Synthesis and characterization of srilankite nanowires. *J. Nanosci. Nanotechnol.* **8**, 1481–1488 (2008).
327. Zhang, Y., Wu, L., Zeng, Q. & Zhi, J. An approach for controllable synthesis of different-phase titanium dioxide nanocomposites with peroxotitanium complex as precursor. *J. Phys. Chem. C* **112**, 16457–16462 (2008).
328. Salvador, P. & Gutiérrez, C. Analysis of the transient photocurrent-time behaviour of a sintered n-SrTiO₃ electrode in water photoelectrolysis. *J. Electroanal. Chem. Interfacial Electrochem.* **160**, 117–130 (1984).
329. Beranek, R. *et al.* Exploring the electronic structure of nitrogen-modified TiO₂ photocatalysts through photocurrent and surface photovoltage studies. *Chem. Phys.* **339**, 11–19 (2007).
330. Ge, H. *et al.* Influence of surface states on the evaluation of the flat band potential of TiO₂. *ACS Appl. Mater. Interfaces* **6**, 2401–2406 (2014).
331. Wang, L., Bledowski, M., Ramakrishnan, A. & Beranek, R. TiO₂-Polyheptazine Hybrid Photoelectrodes: Dynamics of Photogenerated Holes. *ECS Trans.* **35**, 173–182 (2011).
332. Wang, L. *et al.* Dynamics of Photogenerated Holes in TiO₂-Polyheptazine Hybrid Photoanodes for Visible Light-Driven Water Splitting. *J. Electrochem. Soc.* **159**, H616–H622 (2012).
333. Beranek, R. & Kisch, H. Surface-modified anodic TiO₂ films for visible light photocurrent response. *Electrochem. commun.* **9**, 761–766 (2007).
334. Sakthivel, S. & Kisch, H. Daylight Photocatalysis by Carbon-Modified Titanium Dioxide. *Angew. Chemie Int. Ed.* **42**, 4908–4911 (2003).
335. Qiu, B. *et al.* Facile synthesis of the Ti³⁺ self-doped TiO₂-graphene nanosheet composites with enhanced photocatalysis. *Sci. Rep.* **5**, 8591 (2015).

336. Fabregat-Santiago, F., Garcia-Belmonte, G., Bisquert, J., Bogdanoff, P. & Zaban, A. Mott-Schottky Analysis of Nanoporous Semiconductor Electrodes in Dielectric State Deposited on SnO₂(F) Conducting Substrates. *Journal of The Electrochemical Society* **150**, E293 (2003).
337. Hurum, D. C., Gray, K. A., Rajh, T. & Thurnauer, M. C. Recombination Pathways in the Degussa P25 Formulation of TiO₂: Surface versus Lattice Mechanisms. *J. Phys. Chem. B* **109**, 977–980 (2005).
338. Kho, Y., Iwase, A. & Teoh, W. Photocatalytic H₂ evolution over TiO₂ nanoparticles. The synergistic effect of anatase and rutile. *J. J. Phys. Chem. C* **114**, 2821–2829 (2010).
339. Chuangchote, S., Jitputti, J., Sagawa, T. & Yoshikawa, S. Photocatalytic activity for hydrogen evolution of electrospun TiO₂ nanofibers. *ACS Appl. Mater. Interfaces* **1**, 1140–3 (2009).
340. Yang, Z. *et al.* Factors influencing the photocatalytic activity of rutile TiO₂ nanorods with different aspect ratios for dye degradation and Cr(VI) photoreduction. *Phys. Chem. Chem. Phys.* **17**, 18670–18676 (2015).
341. Guo, Y., Liu, G., Ren, Z., Piyadasa, A. & Gao, P.X. Single crystalline brookite titanium dioxide nanorod arrays rooted on ceramic monoliths: a hybrid nanocatalyst support with ultra-high surface area and thermal stability. *CrystEngComm* **15**, 8345 (2013).
342. Cai, X. *et al.* Dye-sensitized solar cells with vertically aligned TiO₂ nanowire arrays grown on carbon fibers. *ChemSusChem* **7**, 474–482 (2014).
343. Rajabi, M., Shogh, S. & Irajizad, A. Defect study of TiO₂ nanorods grown by a hydrothermal method through photoluminescence spectroscopy. *J. Lumin.* **157**, 235–242 (2015).
344. Shanmugam, S., Gabashvili, A., Jacob, D. S., Yu, J. C. & Gedanken, A. Synthesis and Characterization of TiO₂@C Core–Shell Composite Nanoparticles and Evaluation of Their Photocatalytic Activities. *Chem. Mater.* **18**, 2275–2282 (2006).
345. Zhang, L. W., Fu, H. B. & Zhu, Y. F. Efficient TiO₂ photocatalysts from surface hybridization of TiO₂ particles with graphite-like carbon. *Adv. Funct. Mater.* **18**, 2180–2189 (2008).
346. Zhong, J., Chen, F. & Zhang, J. Carbon-Deposited TiO₂: Synthesis, Characterization, and Visible Photocatalytic Performance. *J. Phys. Chem. C* **114**, 933–939 (2010).
347. Madhusudan Reddy, K., Manorama, S. V & Ramachandra Reddy, A. Bandgap studies on anatase titanium dioxide nanoparticles. *Mater. Chem. Phys.* **78**, 239–245 (2002).
348. Reyes-Coronado, D. *et al.* Phase-pure TiO₂ nanoparticles: anatase, brookite and rutile. *Nanotechnology* **19**, 145605 (2008).
349. Yang, J. Y., Bullock, R. M., DuBois, M. R. & DuBois, D. L. Fast and efficient molecular electrocatalysts for H₂ production: Using hydrogenase enzymes as guides. *MRS Bull.* **36**, 39–47 (2011).

Appendices

Appendix A – Publications

- Reilly, K., Wilkinson, D. P. & Taghipour, F., (2016). Anatase Nanowire Growth on Rugged, Fluidizable Media. (To be submitted, 2016)
- Reilly, K., Taghipour, F., & Wilkinson, D. P. (2016). Scalable Hydrothermal Rutile Nanorod Production on Fluidizable Media. (To be submitted, 2016)
- Reilly, K., Taghipour, F., & Wilkinson, D. P. (2016). Scalable Nanowire growth for Water Splitting and Photocatalytic Degradation. (To be submitted, 2016)
- Reilly, K., Wilkinson, D. P., & Taghipour, F. (2016). Photocatalytic water splitting in a UV-irradiated fluidized bed reactor. (To be submitted, 2016)
- Reilly, K., Wilkinson, D. P., & Taghipour, F. (2016). Photocatalytic Water Splitting in a Fluidized Bed System: Predictive Model and Comparison with Experimental Data. (To be submitted, 2016)
- Fang, B., Bonakdarpour, A., Reilly, K., Xing, Y., Taghipour, F., & Wilkinson, D. P. (2014). Large-Scale Synthesis of TiO₂ Microspheres with Hierarchical Nanostructure for Highly Efficient Photodriven Reduction of CO₂ to CH₄. *ACS applied materials & interfaces*, 6 (17), 15488-15498.
- Reilly, K., Taghipour, F., & Wilkinson, D. P. (2012). Photocatalytic hydrogen production in a UV-irradiated fluidized bed reactor. *Energy Procedia*, 29, 513-521.

Appendix B - Engineered Drawings

B.1 Fluidized Bed Reactor

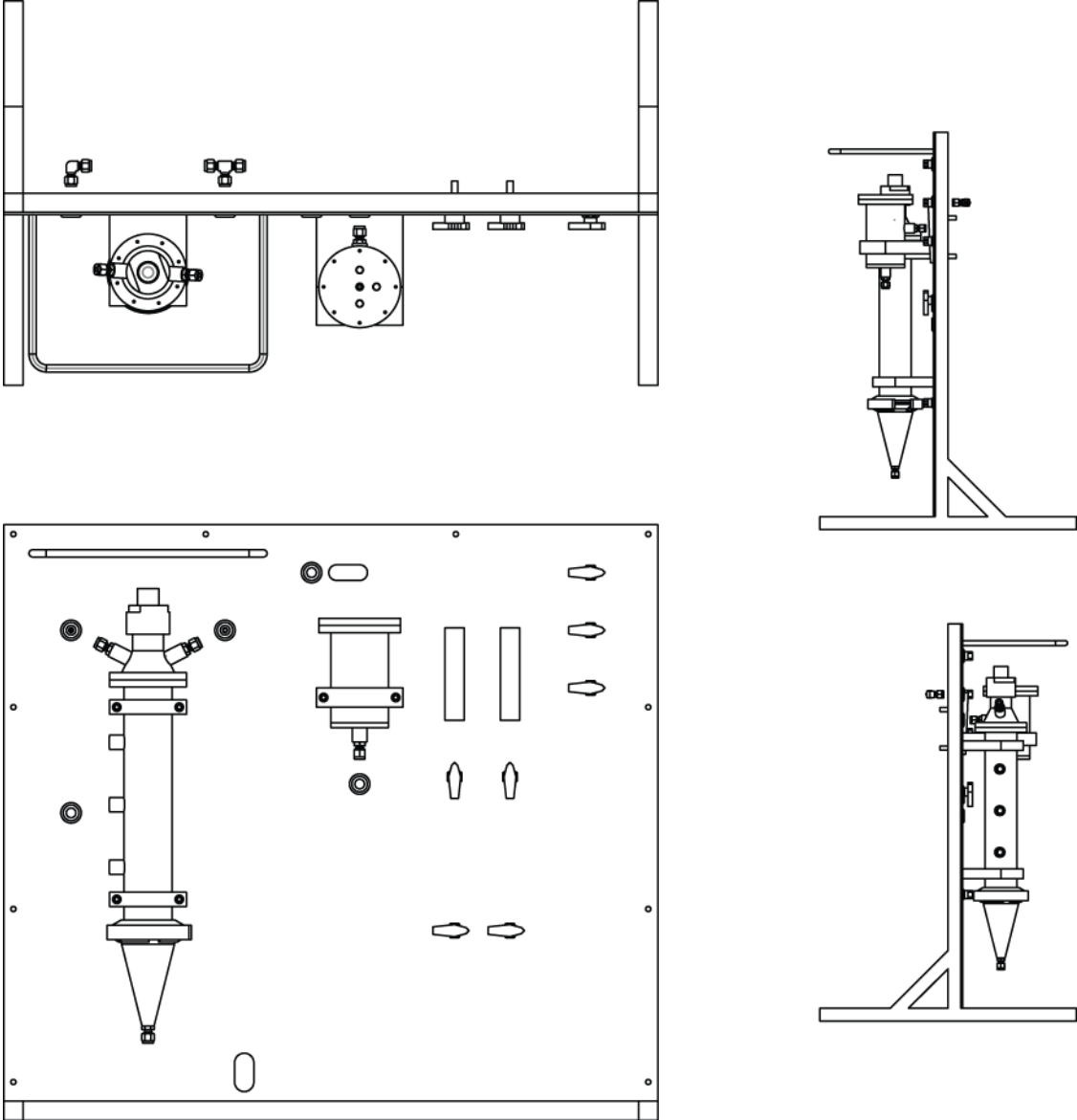
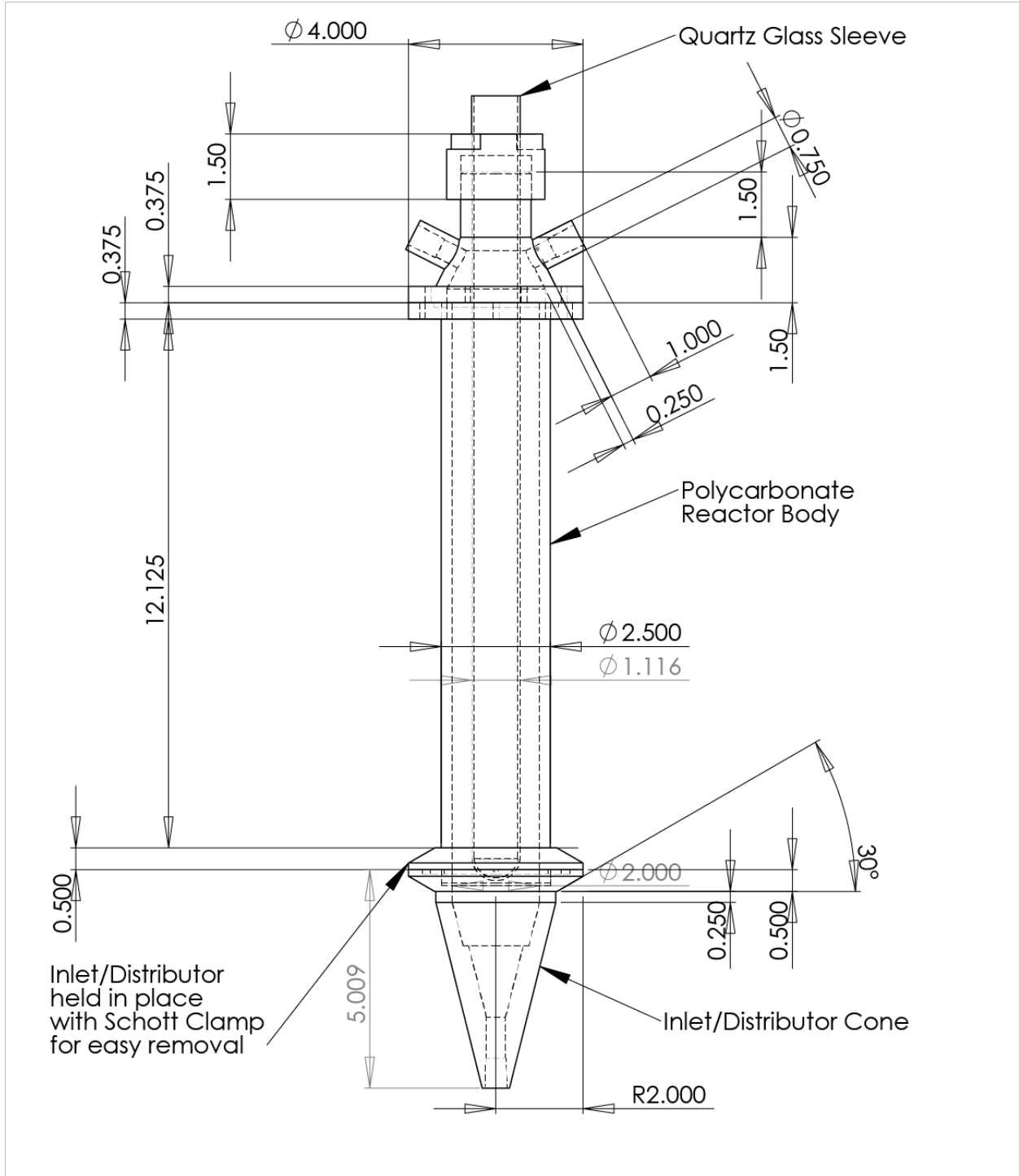
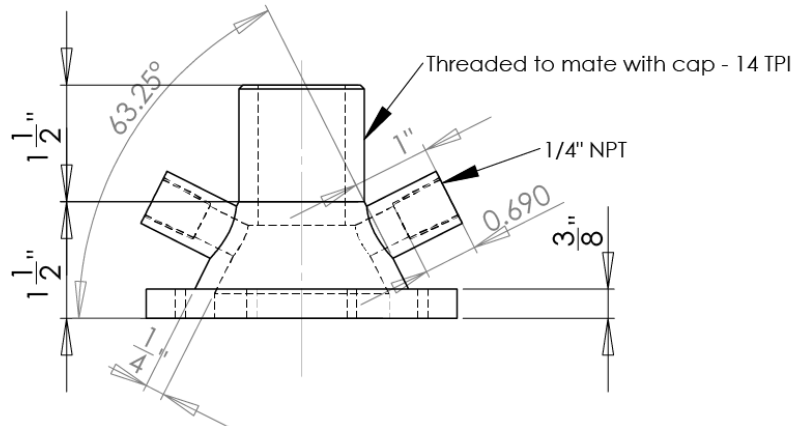
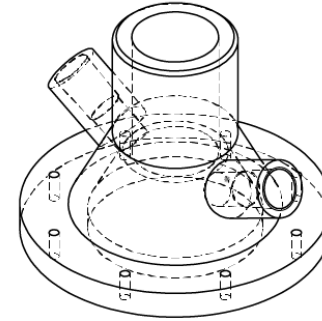
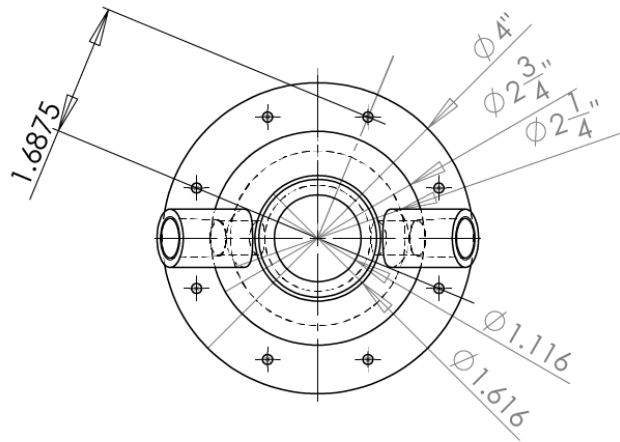


Figure 57: Schematic view of assembled fluidized bed test station



PROPRIETARY AND CONFIDENTIAL
 THE INFORMATION CONTAINED IN THIS
 DRAWING IS THE SOLE PROPERTY OF
 THE UNIVERSITY OF BRITISH COLUMBIA.
 ANY REPRODUCTION IN PART OR AS A
 WHOLE WITHOUT THE WRITTEN PERMISSION
 OF THE UNIVERSITY OF BRITISH COLUMBIA IS
 PROHIBITED.

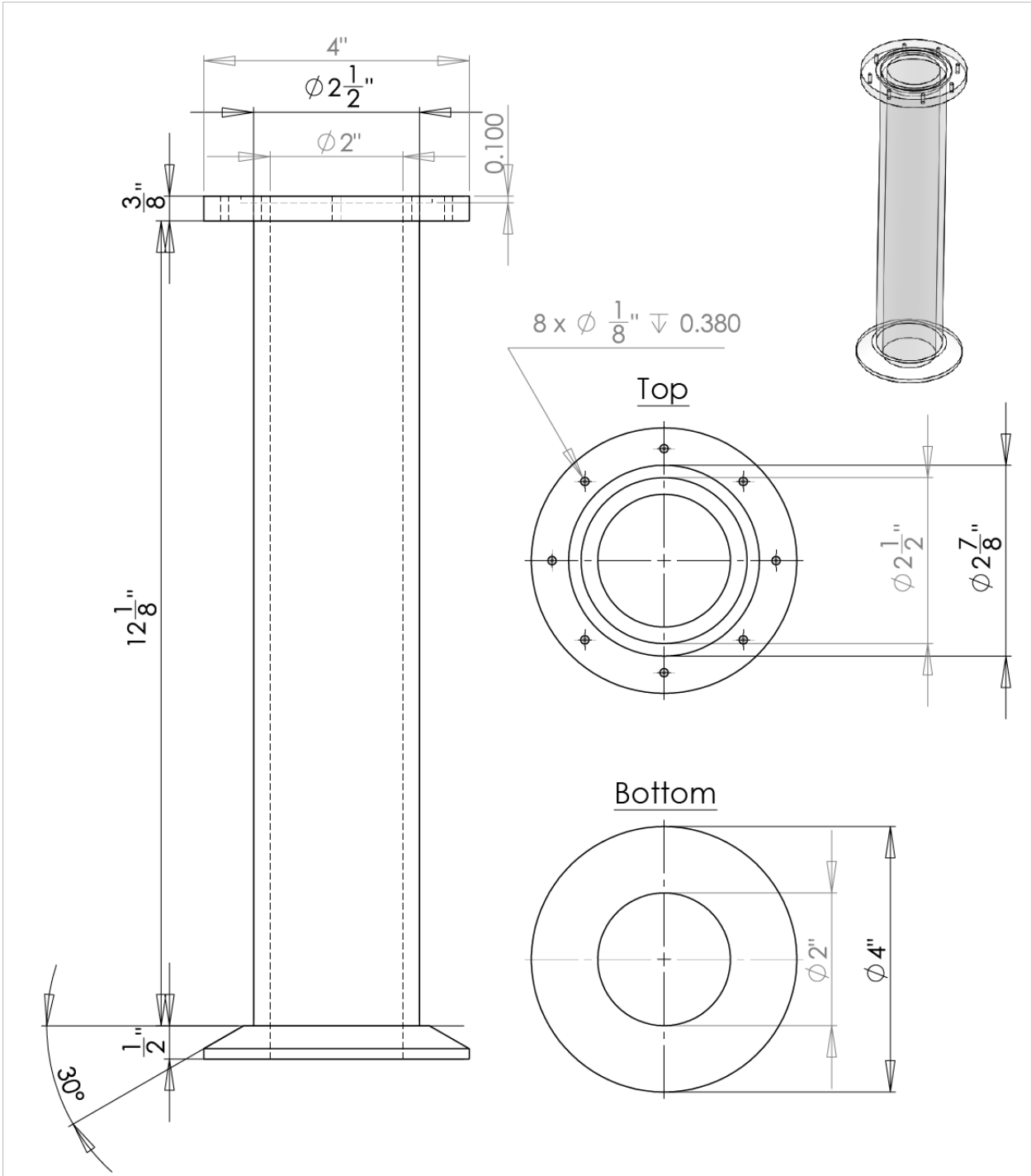
		DIMENSIONS ARE IN INCHES		NAME	DATE
		TOLERANCES:		DRAWN	
		FRACTIONAL \pm		CHECKED	
		ANGULAR: MACH \pm BEND \pm		ENG APPR.	
		TWO PLACE DECIMAL \pm		MFG APPR.	
		THREE PLACE DECIMAL \pm		Q.A.	
		MATERIAL		COMMENTS:	
NEXT ASSY	USED ON	FINISH			
APPLICATION		DO NOT SCALE DRAWING			
				SIZE	DWG. NO.
				A Fluidized Bed Assembly	
				SCALE: 1:3	WEIGHT:
				SHEET 1 OF 1	
				REV.	



PROPRIETARY AND CONFIDENTIAL
 THE INFORMATION CONTAINED IN THIS DRAWING IS THE SOLE PROPERTY OF THE UNIVERSITY OF BRITISH COLUMBIA. ANY REPRODUCTION IN PART OR AS A WHOLE WITHOUT THE WRITTEN PERMISSION OF THE UNIVERSITY OF BRITISH COLUMBIA IS PROHIBITED.

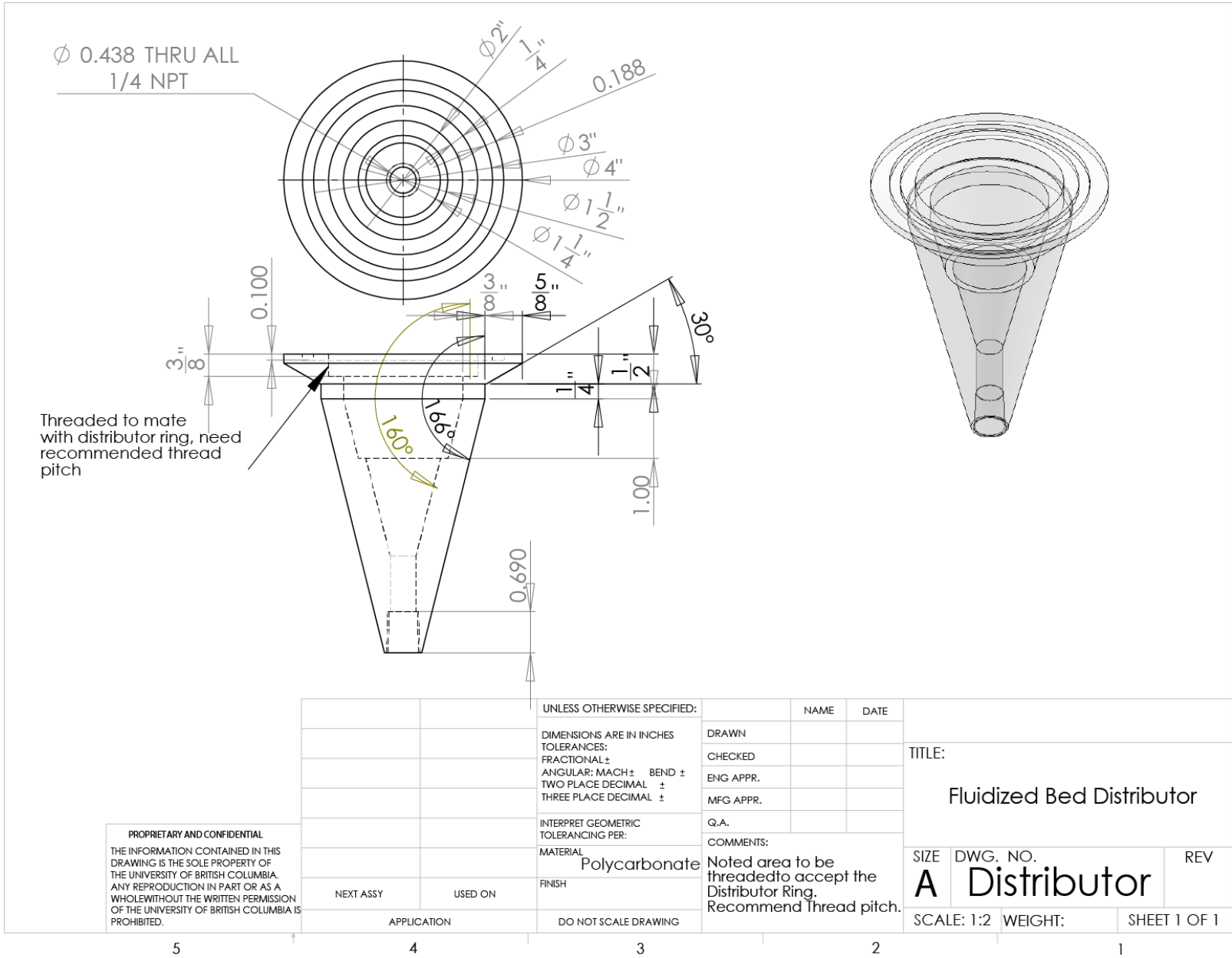
		UNLESS OTHERWISE SPECIFIED:	NAME	DATE	
		DIMENSIONS ARE IN INCHES	DRAWN		TITLE: Fluidized Bed Top
		TOLERANCES:	CHECKED		
		FRACTIONAL ±	ENG APPR.		
		ANGULAR: MACH ± BEND ±	MFG APPR.		
		TWO PLACE DECIMAL ±	Q.A.		
		THREE PLACE DECIMAL ±	COMMENTS:		
		INTERPRET GEOMETRIC TOLERANCING PER:	Threaded to mate with top cap.		SIZE DWG. NO. REV
		MATERIAL	Recommend thread pitch.		A Top
		FINISH			SCALE: 1:2 WEIGHT: SHEET 1 OF 1
	NEXT ASSY	USED ON			
	APPLICATION	DO NOT SCALE DRAWING			

5 4 3 2 1



PROPRIETARY AND CONFIDENTIAL
 THE INFORMATION CONTAINED IN THIS
 DRAWING IS THE SOLE PROPERTY OF
 THE UNIVERSITY OF BRITISH COLUMBIA.
 ANY REPRODUCTION IN PART OR AS A
 WHOLE WITHOUT THE WRITTEN PERMISSION
 OF THE UNIVERSITY OF BRITISH COLUMBIA IS
 PROHIBITED.

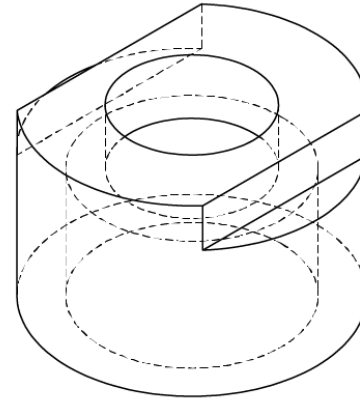
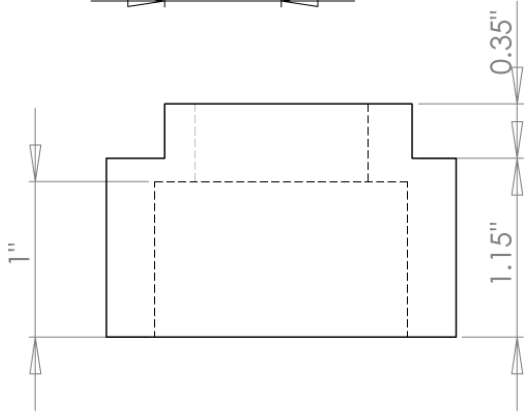
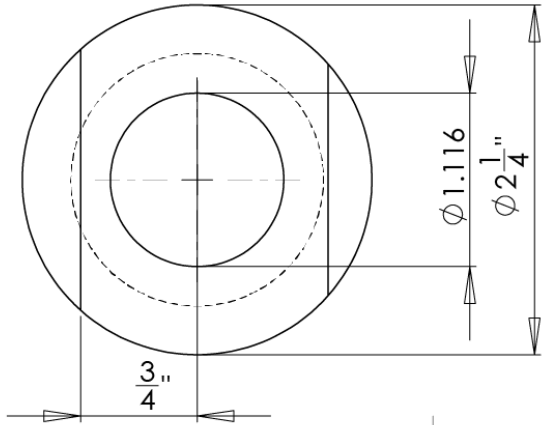
		DIMENSIONS ARE IN INCHES		NAME	DATE
		TOLERANCES:		DRAWN	
		FRACTIONAL ±		CHECKED	
		ANGULAR: MACH ± BEND ±		ENG APPR.	
		TWO PLACE DECIMAL ±		MFG APPR.	
		THREE PLACE DECIMAL ±		Q.A.	
		MATERIAL Polycarbonate		COMMENTS:	
NEXT ASSY	USED ON	FINISH			
APPLICATION		DO NOT SCALE DRAWING		Fluidized Bed Column Body	
				SIZE A	DWG. NO. ColumnBody
				SCALE: 1:5	WEIGHT:
				REV.	
				SHEET 1 OF 1	



Threaded to mate with distributor ring, need recommended thread pitch

PROPRIETARY AND CONFIDENTIAL
 THE INFORMATION CONTAINED IN THIS DRAWING IS THE SOLE PROPERTY OF THE UNIVERSITY OF BRITISH COLUMBIA. ANY REPRODUCTION IN PART OR AS A WHOLE WITHOUT THE WRITTEN PERMISSION OF THE UNIVERSITY OF BRITISH COLUMBIA IS PROHIBITED.

		UNLESS OTHERWISE SPECIFIED:		NAME	DATE	TITLE: Fluidized Bed Distributor	
		DIMENSIONS ARE IN INCHES	DRAWN				SIZE DWG. NO. REV A Distributor
		TOLERANCES: FRACTIONAL ± ANGULAR: MACH ± BEND ± TWO PLACE DECIMAL ± THREE PLACE DECIMAL ±	CHECKED				
		INTERPRET GEOMETRIC TOLERANCING PER:	ENG APPR.				
NEXT ASSY	USED ON	MATERIAL Polycarbonate	MFG APPR.				
	APPLICATION	FINISH	Q.A.				
		DO NOT SCALE DRAWING	COMMENTS: Noted area to be threaded to accept the Distributor Ring. Recommend Thread pitch.				



PROPRIETARY AND CONFIDENTIAL
 THE INFORMATION CONTAINED IN THIS DRAWING IS THE SOLE PROPERTY OF THE UNIVERSITY OF BRITISH COLUMBIA. ANY REPRODUCTION IN PART OR AS A WHOLE WITHOUT THE WRITTEN PERMISSION OF THE UNIVERSITY OF BRITISH COLUMBIA IS PROHIBITED.

		UNLESS OTHERWISE SPECIFIED:		NAME	DATE		
		DIMENSIONS ARE IN INCHES		DRAWN		TITLE: Fluidized Bed Top Cap	
		TOLERANCES:		CHECKED			
		FRACTIONAL ±		ENG APPR.			
		ANGULAR: MACH ± BEND ±		MFG APPR.			
		TWO PLACE DECIMAL ±		Q.A.		SIZE DWG. NO. REV	
		THREE PLACE DECIMAL ±		COMMENTS:			
		INTERPRET GEOMETRIC TOLERANCING PER:		Cap is to be threaded to mate with the Fluidized Bed Top. Please recommend thread pitch.		A Cap	
		MATERIAL					
		Polycarbonate					
		FINISH					
		DO NOT SCALE DRAWING					
		APPLICATION					
		NEXT ASSY USED ON					

5

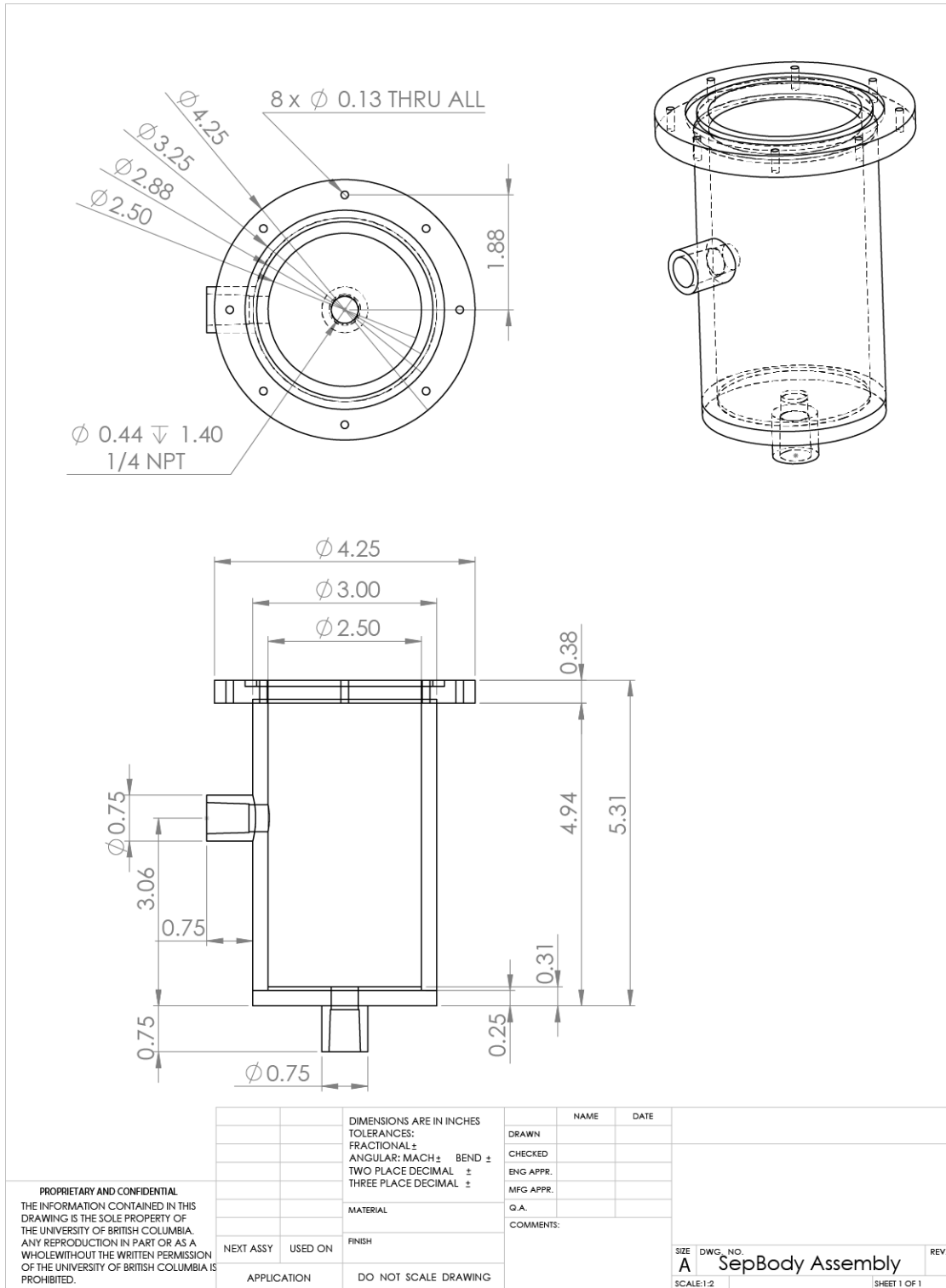
4

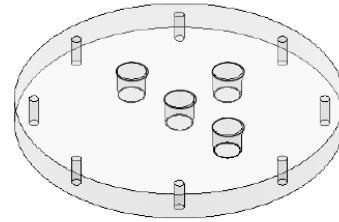
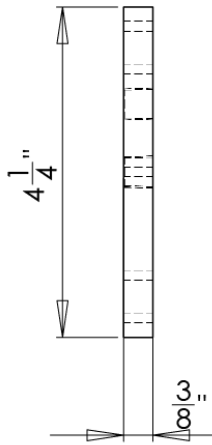
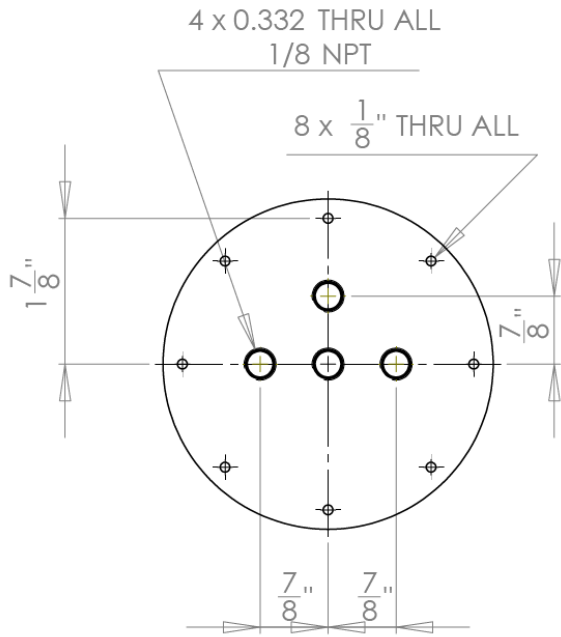
3

2

1

B.2 Gas-Liquid Separator





PROPRIETARY AND CONFIDENTIAL
 THE INFORMATION CONTAINED IN THIS DRAWING IS THE SOLE PROPERTY OF THE UNIVERSITY OF BRITISH COLUMBIA. ANY REPRODUCTION IN PART OR AS A WHOLE WITHOUT THE WRITTEN PERMISSION OF THE UNIVERSITY OF BRITISH COLUMBIA IS PROHIBITED.

		UNLESS OTHERWISE SPECIFIED:		NAME	DATE	
		DIMENSIONS ARE IN INCHES	DRAWN			TITLE:
		TOLERANCES:	CHECKED			
		FRACTIONAL ±	ENG APPR.			
		ANGULAR: MACH ± BEND ±	MFG APPR.			
		TWO PLACE DECIMAL ±	Q.A.			
		THREE PLACE DECIMAL ±	COMMENTS:			
		INTERPRET GEOMETRIC TOLERANCING PER:				SIZE DWG. NO. REV
		MATERIAL				A SepTop
	NEXT ASSY	USED ON				SCALE: 1:2 WEIGHT: SHEET 1 OF 1
	APPLICATION	DO NOT SCALE DRAWING				

5 4 3 2 1

Appendix C – Supplementary Figures

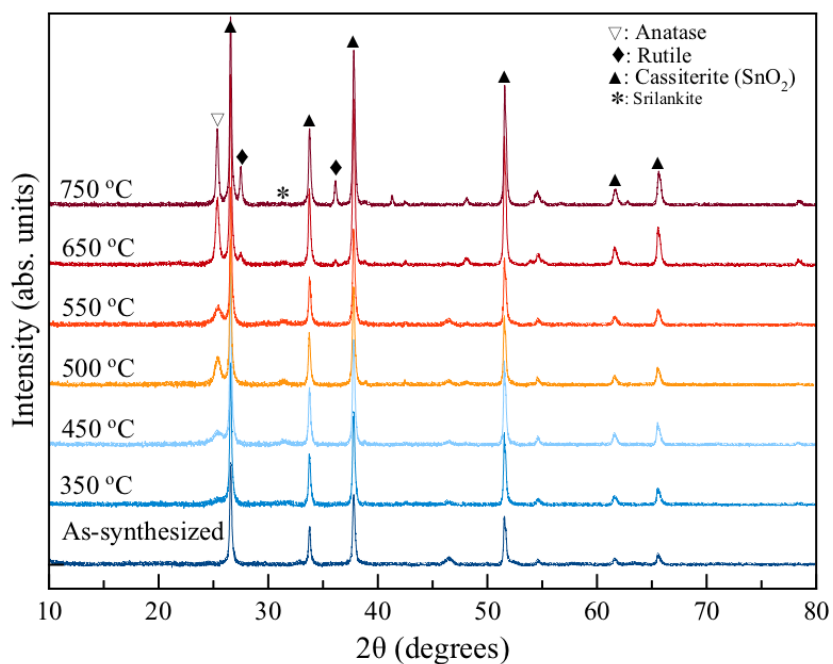


Figure 58: XRD patterns of CBD-N nanowires calcined at temperatures ranging from 350 °C to 750 °C.

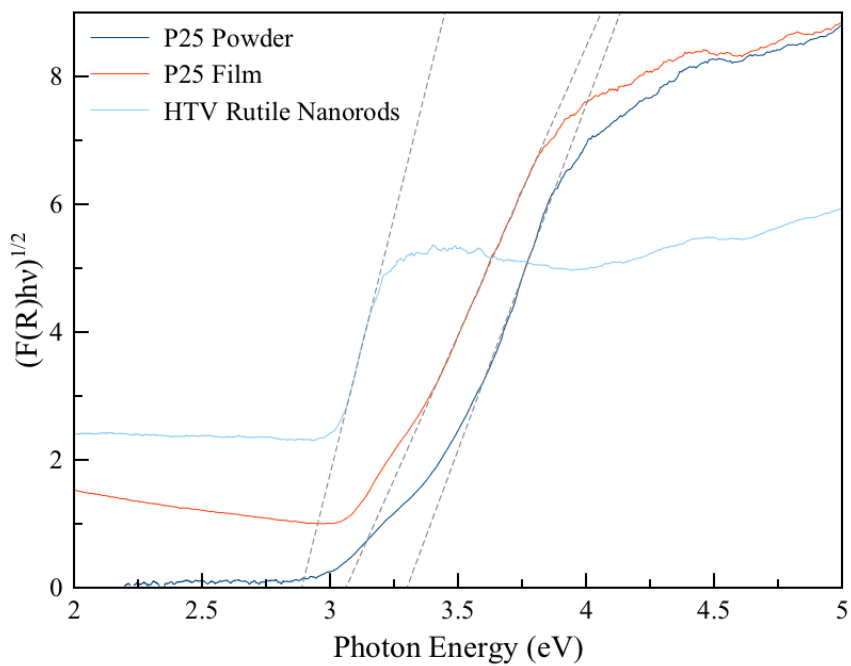


Figure 59: Tauc plots for P25 powder, P25 film and HTV rutile nanorods

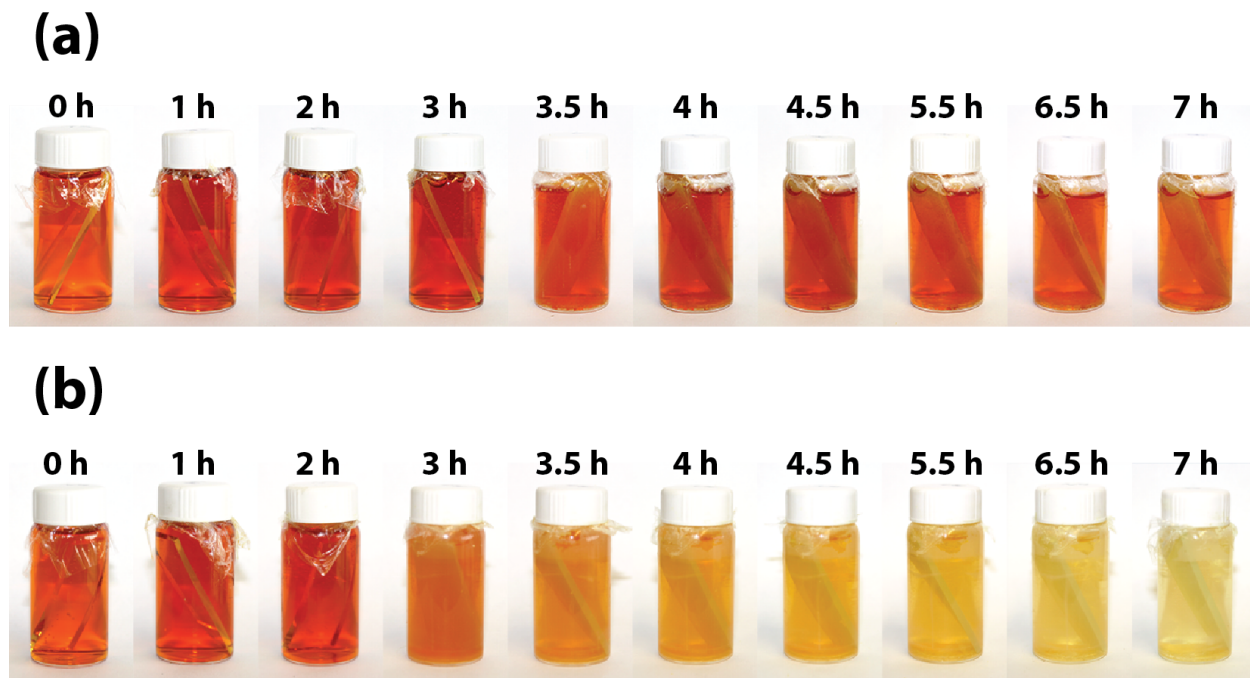


Figure 60: Color shift of the growth solution during the growth of nanowires in a) 0.46M HNO_3 and b) 0.31M HNO_3 solutions